Non-Gaussian States and Measurements in Quantum Information Science

Rajveer Nehra
Jhunjhunu, Rajasthan, India

Integrated BS-MS, 2014
Indian Institute of Science Education and Research, Mohali, India

A Thesis presented to the Graduate Faculty of the University of Virginia in Candidacy for the Degree of Doctor of Philosophy

Department of Physics
University of Virginia

August, 2020

Abstract

With the rapid advances in quantum information science and technology, it is of paramount importance to efficiently characterize and develop resources that are capable of offering quantum advantages. Continuous-variable quantum computation is the most scalable implementation of quantum computation to date, but it requires non-Gaussian resources to allow for exponential speedup and fault tolerance. This can be accomplished with non-Gaussian states such as Fock states or non-Gaussian measurements by photon-number-resolved detection. Therefore, it becomes a key task to devise techniques to, (a) efficiently characterize these non-Gaussian states and measurements and (b) perform non-Gaussian measurements via photon-number-resolved detection. This thesis is a step toward this goal.

The work presented in this thesis is two-fold. The first part focuses on characterizing quantum states with non-Gaussian Wigner quasi-probability distribution functions using photon-number-resolving (PNR) measurements performed with the superconducting transition-edge sensor. The second part focuses on characterizing quantum detectors by Wigner functions, and designing room temperature PNR detectors using "click detectors" such as single-photon avalanche-photodiodes (SPADs).

Within the state characterization, we first demonstrate a scheme proposed by Wallentowitz-Vogel [1] and Banaszek-Wódkiewicz [2] (WVBW) that allows the *direct* reconstruction of the Wigner function using PNR

measurements. We observe the negativity of the single-photon Wigner function in the raw data without any inference or correction for decoherence.

We then propose and experimentally demonstrate a novel scheme that generalizes and improves upon the WVBW scheme. The proposed scheme reconstructs the density operator, as opposed to probing the Wigner function, of an arbitrary quantum state in the Fock space from the state overlap measurements with a small set of calibrated coherent states. We devise computationally efficient and physically reliable techniques to deconvolve the deleterious effects of experimental imperfections.

In the second part of this thesis, we first investigate the feasibility and performance of a segmented waveguide detector consisting of SPADs with low dark count noise for PNR measurements. We characterize its performance by evaluating the purities of photon-count positive-operator-valued measures (POVMs) in terms of the number of SPADs, photon loss, dark counts, and electrical cross-talk. We find that the number of integrated SPADs is the dominant factor for high-quality PNR detection. Next, we propose an experimentally feasible noise-robust method to characterize a quantum detector by reconstructing the Wigner functions of the detector POVMs corresponding to the measurement outcomes.

Finally, we study a Heisenberg-limited quantum interferometer with indistinguishably photon-subtracted twin beams as an input state. We show that such an interferometer achieves Quantum Cramér-Rao bound with the intensity difference measurements and can yield a direct fringe unlike the Holland-Burnett interferometer with twin beams.

List of Publications

- **Rajveer Nehra**, Aye Win, Miller Eaton, Niranjan Sridhar, Reihaneh Shahrokhshahi, Thomas Gerrits, Adriana Lita, Sae Woo Nam, and Olivier Pfister, "State-independent quantum state tomography by photon-number-resolving measurements," Optica, 6(10), pp.1356-1360.
- **Rajveer Nehra**, Chun-Hung Chang, Qianhuan Yu, Andreas Beling, and Olivier Pfister, "Photon-number-resolving segmented detectors based on single-photon avalanche-photodiodes," Opt. Express 28, 3660-3675 (2020).
- **Rajveer Nehra**, Miller Eaton, Carlos González-Arciniegas, M. S. Kim, and Olivier Pfister, "Generalized overlap quantum state tomography," arXiv:1911.00173v2 [quant-ph] (Submitted).
- **Rajveer Nehra** and Kevin Valson Jacob, "Characterizing quantum detectors by Wigner functions," arXiv:1909.10628 [quant-ph], (Submitted).
- **Rajveer Nehra**, Aye Win, and Olivier Pfister, "Heisenberg-limited quantum interferometry with photon-subtracted twin beams," arXiv:1707.07641 [quant-ph]

The other published work contribution by the author which is not written in the thesis

Miller Eaton, **Rajveer Nehra**, and Olivier Pfister, "Non-Gaussian and Gottesman-Kitaev-Preskill state preparation by photon catalysis," New J. Phys. 21 113034.

Acknowledgements

Graduate school has been a great learning experience, which would not have been possible without the continuous help and support of many people. These acknowledgements are my attempt to express how grateful I am to have these wonderful people by my side throughout my Ph.D. journey.

First and foremost, I would like to express my deepest gratitude to my advisor, Professor Olivier Pfister, for his constant guidance throughout my time at UVA. My time in Olivier's lab can be *accurately and efficiently* characterized as a series of diverse learning experiences. This was only possible because of his scientific brilliance, *coherent* kindness, *dual* research vision, and *continuous* wholehearted support for these past five years. Olivier has created a perfect research environment in his lab where everyone can thrive and grow as a researcher.

When things did not go as planned and I found myself stressed, Olivier was always available for discussions and worked with me to solve the problem in-hand. His systematic approach to resolving technical issues in both theory and experiments has been very helpful to me. I hope to be carry this approach forward in my research career. Olivier has this magical power of lightening the stress through his many impressions and humorous stories which made every meeting fun.

Moreover, Olivier was always excited about my ideas and allowed me to pursue them, which gave me a sense of independence in my research

and has been a key component in my growth as a researcher. I deeply enjoyed going to grant meetings with you and seeing you presenting our work helped me to develop my presentation skills. Thanks for being such a source of inspiration, Olivier!

I would like to thank Profs. Peter Schauss, Israel Klich, and Andreas Beling for being on my Ph.D. committee. I highly appreciate you taking time to read my thesis and giving me very constructive feedback.

I am grateful to Profs. Michael Fowler and Thomas Gallagher for being on my research committee. Your feedback in the annual research meetings has been very fruitful for my research progress.

I must thank Prof. Myungshik Kim from Imperial College London for being a great collaborator on the last project of my thesis. Discussions with him were always intellectually stimulating.

I am grateful to our collaborators at NIST: Drs. Thomas Gerrits, Adriana Lita, and Sae Woo Nam for their help in reviewing our papers and giving us feedback. Dr. Thomas has been very helpful whenever we had issues with the TES. I would also like to thank Dr. Aaron Miller for his help in fixing the TES.

I would also like to thank my labmates for their lovely company and all the technical and non-technical discussions we have had over the years. I was fortunate enough to learn from Dr. Aye Lu Win, who introduced me to the experimental side of quantum optics. Thanks for being so patient with my questions and teaching me many technical skills at the beginning of my Ph.D.

Working with Miller Eaton has been one of the greatest experiences in the lab. Together, we explored many exciting things in the quantum optics wonderland on both experimental and theoretical fronts. I am amazed by your curiosity-driven nature, and am looking forward to the exciting things you will be doing on the photon counting side of the lab. I am glad that you are going to see the end of the non-Gaussian trail with beautiful views (Wigner function negativity), I hope that you will employ the Heisenberg picture of optical alignment invented by us in the state engineering experiments[1]. Thanks for all the fun we had in the lab, I am surely going to miss it. I am sure about having CLEO round 2 some day, so that you will be able to prove your navigation skills.

I am extremely thankful to Chun-Hung Chang for being a constant companion for all these years. Chun-Hung has done it all, ranging from designing the room-temperature photon-number-resolving detectors, to setting up a new lab, to quantum engineering for massively entangled states. And most importantly, bearing with me for all these years, particularly my not-so-funny puns, and picking the perfect time to have a good coffee. I enjoyed our walks to Starbucks, there hasn't been anything we haven't discussed, although you might disagree to that. I will say it here again that you might be a great dribbler, but I am slightly better at shooting. Thanks for all the good times and working with me on the detector project. We finally got it published!

I am glad that my time overlapped with Catherine Zhu, I thoroughly enjoyed our late night discussions in the lab. Catherine is the calm one in the lab and has been very successful settling our debates (technical or non-technical), especially between Chun-Hung and me. Catherine's direct, yet very empathetic and kind nature is second to none. I look forward to the exciting results on graph state engineering experiments you and Chun-Hung are working on. Thanks for your help!

[1] In the Heisenberg picture of optical alignment, the detector is physically aligned to the light source as opposed to aligning the light source to the detector.

Dr. Carlos González-Arciniegas has been a great friend and a collaborator, who guided me through life as a graduate student. Carlos patiently listened to my ideas and his profound questions gave me clarity about many things. Thanks Carlos for teaching me how to have a balanced research life, and also forcefully (or with his not-so-subtle ways) dragging me out of the lab to the climbing wall. I am going to reiterate that you might be a better $V_{5/6}$ climber (for now), but I can run a full-marathon. So, there is that! And Yoga is good for you. I will always remember you saying, "That's what quantum mechanics does," every time I am awestruck by a new concept or insight.

I would also like to thank Benjamin Godek, Zack Carson, Jacob Higgins, Rocio Rivera, and Manon Jerger for the time we spent together working in the lab.

I must offer my sincere gratitude to Dr. Rafael (Raf) N. Alexander for many technical discussions and (physics-y) gossip we have had over the years. I learned many things from Raf, including losses modeling in quantum optics experiments, writing research proposals, and most importantly how to survive when research goes through some rough patches. I am amazed by your very broad knowledge in physics and I am sure that you will do great things in your research career. Thanks for introducing me to many great people in the quantum optics research community!

I am immensely grateful to Reihaneh Shahrokhshahi and Niranjan Sridhar who worked on the photon counting experiments before I joined Olivier's lab. Because of your solid experimental foundation, I was able to go faster and attempt new things. Although we never worked together, our email conversations were very helpful. I would also like to thank you both for your help when I was trying to figure out my post Ph.D. plans.

I would also like to thank Prof. Nicolas (Nick) Menicucci for inviting me to participate in "Cluster State Mini Workshop - 2019" and "BBQ - 2019", I learned a lot about bosonic quantum error correction there. I enjoyed our discussions during your visits to UVA and remote ones this year. During my time in Australia, I visited Prof. Mirko Lobino at the Griffith University. I greatly enjoyed visiting your labs and having discussions with you and your group. I am glad that we started a collaboration on quantum state engineering experiments. I look forward to the exciting results from your lab. Thank you for hosting me!

I must thank the late Prof. Jonathan Dowling who invited me to visit his group at LSU for a couple of weeks during QCMC - 2018. I enjoyed working with his graduate student Kevin Valson Jacob on characterizing quantum detectors by Wigner functions. It was a short visit but it helped me gain new insights on characterizing quantum resources.

I would like to extend my gratitude to the physics staff (in no particular order)– Peter Cline, Dawn Shifflett, Vicky Ingram, Tammie Shifflett, Al Tobias, Bryan Wright, Jeff Behrend, Mike Beverage, William Fariss, Ashley Haddox, Beth Guyton, Rick Marshall, Faye Safley, and Beverly Martyn for their help throughout my time at UVA.

I consider myself very lucky to have met amazing friends in Charlottesville. It made graduate school full of joy. I enjoyed taking classes and discussing research with the graduate students from my year: Serdar(ji) Kurbanov, a Russian physicist turned banker, turned back to physics, and now finally settling in software engineering, was my first friend in C'ville. Thanks for all the thanksgiving lunches, Christmas Eves, and New Years we celebrated together, I am going to cherish it. I must thank Cristiana Principato, Sina Tafti, Zack Carson, Aaron Wegner, Sanjay Khatri, Jing Luo, David Keder, Edward Moan, and Depei Zhang for all the discussions

and good times. I would like to extend my gratitude to graduate students above and below my year - Charlie Glaser, a great physicist and wonderful friend. Thanks Charlie for always being there for me, I am glad that we have similar perspectives on many things in science and technology. Although we still need to settle our debates on capitalism and what it means to have economic growth in the most humane sense. In no particular order, many thanks are due to Evan Wolfe, Abha Rajan, Sharmistha Sahoo, Ajinkya Kamat, Preetha Saha, Grace Cummings, Marybeth Beydler, Adam Fallon, Kapila Wijayaratne, Saikat Bera, and Robin Smith. I am truly grateful to Sharon Santhamma Philip for being a wonderful friend in last 4 years, you have always been by my side during good and bad times. I appreciate your support. Thanks for all the random lunch and coffee breaks! Now that I am moving away, I am going to again remind you that we human beings are social animals by nature and are inherently capable of making homes wherever we go.

I would also like to thank Pallavi Patil, Mitra Menon, Abhiraj Deshpande, Mrugen Deshmukh, Vishaal Saraiya, Gandhi Dontu, Mandi Das, Arun Kumar Subramaniam, Oshin Jakhete, Mohan Kumar, Haritha Bhairavabhatla, Tara George, Krishna Makhija, Rachna Bhave, and Anchit Arora for their lovely company in all these years. I couldn't have asked for better friends. Arielle Shaindel Boguslav deserves a special mention. She been a great support and a critical investigator of my wild adventures and writings. I learned a lot about pedagogy, communicating science, and most importantly the difference between "lighting" and "lightening" from you. I look forward to your exciting research on inclusive methods to train teachers at all levels of teaching. By now, Arielle understands that the characterization of quantum states must be a state-independent approach and if one assumes some prior information, it defeats the very purpose of state characterization.

I must thank frequency-multiplexing expert Chaitali Joshi, whom I met in the 2017 single photon workshop in Boulder, Colorado. I thoroughly enjoyed our conversations on the subject matter and beyond that. While you decided not to climb Mt. Katahdin, it was quite an experience to climb Mt. Washington with you[2]. Although you decided to move to microwave photons, I hope that we continue to discuss research at Caltech! I would also like to thank Avik Dutt for many technical and non-technical discussions. I look forward to working together in the future.

I am immensely beholden to the Indian Student Community in Charlottesville for their lovely company during all these years. In particular, I cherish the time spent during the long "Relishing" Barbecue nights, and Diwali celebrations (R. Bhave *et al.*); it made Charlottesville feel like home. I thank you all for supporting my fundraiser for the KALAP Foundation: it makes me deeply believe that you all are going to make a global impact while pursuing your personal dreams. I am grateful to the SPIC-MACAY team at UVA for organizing the Indian Classical music concerts, which have been helpful for keeping my sanity in stressful times.

Last but definitely not least, I am deeply grateful to my beloved parents and family for their unconditional love and constant support. They taught me to always stay open-minded and believe in myself no matter how tough it gets. Although we have spent very little time together in last six years, their love and continuous guidance has always been with me. I would not be where I am today without their sacrifices and tremendous support. I promise to continue making you proud. Thanks for believing in me even when I doubted myself.

[2]Someday I will write a book about it, and also our quantum optics version of the great Mirza Ghalib

Contents

List of Figures

I dedicate this thesis to my parents for their unconditional love and support.

Chapter 1

Introduction

> "The light in me honors the
> light in you."

The beginning of the 20th century was the golden age for quantum physics. New fundamental theories developed by the brilliant minds, to name a few, Max Planck, Niels Bohr, Louis de Broglie, Albert Einstein, Werner Heisenberg, and Erwin Schrödinger, led to the first quantum revolution, spurring the development of technologies such as transistors, magnetic resonance imaging (MRI), and lasers in the mid 20th century, which have had a huge impact on society since their inception [5]. The technologies were based on the quantum understanding of the natural world around us. The advent of transistors and their subsequent miniaturization by the current state-of-the-art nanotechnology has enabled the semiconductor industries to embed billions of transistors on a single chip, transforming computers from vacuum-tube based room-sized to pocket-sized devices with enormous computational power. The number of transistors in a dense integrated circuit (IC) has doubled every 18 months since the invention of the very first IC at 10 μm scale in 1970 [6]. This was predicted by Gordon Moore and is known as Moore's law [1]

[1]Moore's law is not a *physical* law, it is rather an empirical observation.

Today the size of a transistor is comparable to that of an atom, i.e., at the nanometer scale. At this scale, undesired quantum effects start to interfere in the functioning of these nanometer scale electronic devices, limiting any further shrinkage in the near future. Therefore, the semiconductor industries have run into their fundamental limit of device fabrication. To further improve the computational power, other architectures based on two-dimensional Graphene [7] and genetic circuits (biological computing) [8] have been explored.

The other promising avenue is to move to a new paradigm of information processing based on the laws of quantum physics, in place of classical physics laws. Using truly quantum phenomenon such as quantum superposition and quantum entanglement, it is believed to perform certain information processing tasks with far superior performance than the current classical technology. These tasks spans into a variety of fields including quantum simulation, quantum computing, quantum sensing and quantum communication.

Before we delve into these fields, let's briefly discuss how a classical information processor, for instance, a classical computer (PC) works. The fundamental unit to encode and process information on a classical computer is a "bit" which is physically realized using transistor-transistor logic (TTL). A bit is a binary system that can be either in *zero (0V)* or *one (5V)* state. A classical computer with n bits has access to only one state at a given time out of all 2^n possible states of n bits. Any certain function is then *sequentially* evaluated on these states, one state at a time. In the physical sense, these logical operations are implemented by controlling the current and voltages across these electronic units by using laws of classical electromagnetic theory.

On the other hand, a quantum computer uses "quantum bits (qubits)" as a fundamental unit to store and process information. Rather than just being in either *zero* or *one* state, a qubit can also be in the linear combination of them, which is one of the key features of quantum systems and is known as quantum superposition. Mathematically, a qubit is described by a state vector in a 2-dimensional Hilbert space as

$$|\psi\rangle = \alpha|0\rangle + \beta|1\rangle, \tag{1.1}$$

where α and β are complex probability amplitudes such that $|\alpha|^2$ and $|\beta|^2$ are the probabilities of collapsing the state vector to *zero* and *one* states respectively when a measurement is performed. One can further create a large quantum system by using a process called quantum entanglement, a physical phenomenon when two quantum systems are correlated in some physical degree of freedom, and whenever the state of one system is measured, it instantaneously changes the physical state of the other system regardless of how far they are from each other. Consequently, a quantum computer with n entangled qubits has access to 2^n states *simultaneously*, and a function is then evaluated using unitary operators acting on this quantum superposition. This is known as quantum parallelism which is one of the key routines for any quantum algorithm. To be more specific, a quantum algorithm is carefully designed such that *quantum inferences* among probability amplitudes increase the probability of right solution while decreasing the probabilities of wrong solutions. This is somewhat analogues to constructive and destructive inference phenomenon of the light waves. When a measurement is performed at the end of the processing (or the sequence of unitary transformations), the quantum superposition collapses to the solution of the computational problem with high probability and the amount of resources needed for this entire physics process have *polynomial scaling*. For concreteness, let us consider an action of the Hadamard gate (H-gate) on a state defined by Eq. (1.1) for a particular case of $\alpha = \beta$. The H-gate is given as

$$H = \frac{1}{\sqrt{2}} \begin{bmatrix} 1 & 1 \\ -1 & 1 \end{bmatrix} \tag{1.2}$$

And its action on the basis states leads to

$$\begin{aligned} H|0\rangle &= \frac{1}{\sqrt{2}}(|0\rangle + |1\rangle) \\ H|1\rangle &= \frac{1}{\sqrt{2}}(|0\rangle - |1\rangle) \end{aligned} \tag{1.3}$$

After the H-gate operation, the qubit state is

$$H|\psi\rangle = \frac{1}{2}[(|0\rangle + |1\rangle) + (|0\rangle - |1\rangle))] = |0\rangle \tag{1.4}$$

From Eq. (1.4), we can see that the probability amplitudes for the basis state $|1\rangle$ destructively interfere which results in only $|0\rangle$ state. The idea of building a computer based on the laws of quantum physics was originally proposed by Richard Feynman in 1982. He proposed:

"Let the computer itself be built of quantum mechanical elements which obey quantum mechanical laws."

Feynman conceived the original idea of a quantum simulator, which is a fully controllable well-known quantum system to simulate the Hamiltonian dynamics of an unknown quantum system [9]. Quantum simulation is computationally hard, particularly for systems of many particles with exponentially large Hilbert space of d^N, where N is the number of particles and d is the size of the Hilbert space of each particle. Simulation of a physical system consisting of n particles requires exponentially large resources on a classical computer while a quantum computer would only require polynomial resources, thereby making it computationally efficient [10]. In computer science, *efficient* problems are the ones whose solutions only require polynomial number of steps, $\mathcal{O}(N^k)$ steps for an input size of N and a given constant k. On the other hand, there are inefficient problems which require exponential large number of steps,

$\mathcal{O}(k^N)$ using the best known classical algorithms. The exponential scaling of these problems makes them computationally hard to solve for a large input size. In the last couple of decades, there have been many small scale experimental demonstrations of quantum simulations on various physical platforms [11]–[17].

In the quantum computing domain, significant progress has been made on both theoretical and experimental fronts. The field has gained momentum after Peter Shor proposed a polynomial-time quantum algorithm for factorizing large integers [18]. Factorizing large integers uses exponential number of steps on a classical computer which makes it intractable for large numbers, which is crucial for the security of RSA based encryption protocols widely used these days. Shor's algorithm is exponentially faster than the best *known* classical algorithm and has been demonstrated for a number of physical systems [19]–[21]. Another quantum algorithm was proposed by Lov Grover that offers the quadratic speedup over any known classical algorithm for finding a particular entry in an unstructured database, i.e., only requires $\mathcal{O}(\sqrt{N})$ number of steps as opposed to $\mathcal{O}(N)$ steps in a classical search algorithm [22], [23].

Recently, Google announced to have achieved a major milestone, the so-called quantum supremacy experiment which consists in solving a computational problem, in particular, sampling instances of a quantum circuit that no classical computer can feasibly solve [24]. With this phenomenal experiment by the Google team, we have officially entered in the quantum computing era.

For a practical realization of the quantum technology, many physical systems have been explored in last couple of decades. The list of potential candidates includes superconducting circuits [25], quantum optics [26], trapped ions [27], quantum dots [28], nuclear spins [19], and neutral atoms [29]. Optical systems have emerged as one of the leading testbeds to explore quantum science and technology.

The very existence of a single light particle, or photon (quanta of energy), confirms the quantum nature of light. Photons are chargeless, massless particles and interact very little with the environment, which allows them to travel long distances easily, making them an excellent candidate for carrying quantum information [30], [31].

Not only photons are crucial sources for quantum communication protocols, they also offer a great promise for quantum computing applications: a single photon makes an excellent room-temperature quantum bit (qubit) by encoding the logical *zeros* and *ones* onto the polarization states of the photon, i.e., $|0\rangle_L = |H\rangle$ and $|1\rangle_L = |V\rangle$, thereby known as a polarization qubit. The other kind of encoding is done by having a single photon in two spatial modes, i.e., $|0\rangle_L = |10\rangle$ and $|1\rangle = |01\rangle$, which is formally known as dual-rail encoding. While photonic qubits are low-noise and their quantum states could be easily manipulated with simple optical tools, the weak optical nonlinearity has been a major obstacle in implementing two-qubit gates such as Controlled-NOT (CNOT), which is necessary for the universal quantum computation. To circumvent the weak nonlinearity, Knill, Laflamme, and Milburn (KLM) proposed an efficient quantum computing scheme using single-photon sources, linear optics (beamsplitters and phaseshifters), photodetectors, and feedback from photodetectors [32]. The key component of the KLM scheme is a nondeterministic implementation of C-NOT gate using ancilla single-photon sources and feedback from the photodetectors, which offers the required nonlinearity, albeit measurement based and has a success probability of 1/4. While the success probability can be improved to near unity, the requirements of large number of ancilla single-photon sources poses significant experimental challenges for scalability [33]–[37].

Thus far we have only considered quantum computing with qubits where information is encoded in the discrete states of physical systems in a finite dimensional Hilbert space. This is also known as quantum computing with discrete-variable (DV) systems. There is another relatively new direction for quantum computation known as continuous-variable quantum computation (CVQC), originally proposed by Llyod and Braunstein in 1998 [38].

CVQC is somewhat similar to the analog model of computing, where information is encoded and processed over the continuous states of physical systems, i.e., the dimension of the Hilbert space is inherently infinite. One such encoding can be achieved by using the continuous position and momentum degrees of freedom of a quantum harmonic oscillator (QHO). One physical platform to implement CVQC protocols is through quantum optics. As we discuss later, the quantization of an electromagnetic field results in quantum harmonic oscillator like formalism, where amplitude and phase quadratures of the field act as position and momentum observables of the QHO respectively [39]. Another physical implementation for CVQC has been proposed using the vibrational modes of an ion as opposed to using discrete energy states of an ion in qubit based QC [40].

The key advantage of optics based CV quantum information lies in its unprecedented scalability and experimental feasibility for generating massively entangled multipartite states known as cluster states, which are experimentally realized using nonlinear optical processes. A cluster state is a universal quantum computing resource for measurement-based quantum computing (MBQC), originally proposed by Raussendorf and Briegel [41] for DV systems and was extened to Gaussian CV systems by Jing Zhang and Samuel L. Braunstein [42], along with a proposal to generate one-dimensional cluster states using only single-mode squeezed vacuum states and linear optics. Later, Menicucci *et al.* proposed a generalized scheme and showed that addition of any non-Gaussian element with Gaussian cluster states is sufficient for universal quantum computation [43]. In MBQC, a cluster state is first prepared, and then the computing proceeds solely by a sequence of adaptive single-qubit (or qumode) measurements and feed-forward operations. While the outcomes of these sequential measurements are random, any quantum algorithm can be *deterministically* implemented [41]. It is worth emphasizing that the 2D-cluster state (in square grid lattice) is a universal resource, i.e., it offers the implementation of a arbitrary quantum algorithm by choosing a sequence of single-qubit measurements designed according to the algorithm [41], [43]. Therefore, a physical realization of CVQC consists in preparing a 2D-cluster states and the ability to perform single-qubit measurements. While we have a detailed discussion on MBQC in Chapter 2, section 2.6, here we briefly summarize the progress in the field on both theoretical and experimental fronts. For qubit systems, a cluster state preparation starts with identically prepared independent qubits each in the superposition state $|+\rangle = (|0\rangle + |1\rangle)/\sqrt{2}$ followed by controlled-phase (C-PHASE) gate applied between adjacent qubit pairs, which generates the essential entanglement for the MBQC. This has been demonstrated for a few qubits on both optical systems (with polarization encoding) and neutral atoms [44]–[46].

For CV systems, an N-mode Gaussian cluster state can be generated using N single-mode squeezed fields emitted by N optical parametric oscillators (OPOs) and a linear interferometer consists of $O(N^2)$ beamsplitters [47]. Using this scheme, Ref. [48] reported a four-mode cluster state utilizing two amplitude-quadrature and two phase-quadrature squeezed states. While this scheme is efficient as it has polynomial scaling in resources, its experimental implementation is challenging for larger cluster states. With this scheme, a larger cluster scale implementation requires indistinguishably of all N single-mode squeezed fields and the phase stabilization of all optical paths in $O(N^2)$ ports interferometer. Therefore, an experimental implementation of a large cluster state using this method is a daunting task.

This major obstacle for scalability was resolved by taking inspiration from the original proposal by Pfister *et al.* to generate multipartite entangled states, in particular Greenberger-Horne-Zeilinger (GHZ) state using only a single nondegenerate OPO [49]. This proposal was extended by Menicucci *et al.* for a two-dimesional (2D) Gaussian CV cluster state, a universal resource for CVQC [50]. This approach exploits the quantum optical frequency comb (QOFC) generated by carefully engineering the phasematching of the nonlinear medium in the OPO and does not necessitate an interferometer, which makes this scheme more experimentally feasible for larger cluster states.

In 2014, a multipartite entangled state consists of 60 *measured* frequency modes in a dual-rail quantum wire, i.e., one dimensional (1D) topology was demonstrated in Professor Olivier Pfister's lab [51][2]. Alternatively, both 1D and 2D CV cluster states have also been proposed and demonstrated by time multiplexing of up to one million optical modes using fiber delays [52]–[56]. Recently, Xuan *et al.* showed that the phase modulation of the QOFC emitted offers an elegant way to increase the topological dimension of the cluster state from 1D linear cluster to 2D square-lattice cluster state [57].

Thus it is clear that quantum optics implementations of cluster states offer a scalable platform for MBQC. As mentioned above, any quantum algorithm can be implemented by performing a sequence of single qumode (or qubits) measurements. While quadrature measurements of optical fields can be performed with near-unit quantum efficiency using balanced homodyne detection technique (discussed in section 2.7.1), these measurements alone do not enable universal QC with 2D Gaussian cluster states. In order to achieve the universality, a non-Gaussian resource (either state or gate or projective measurement) is necessary [38]. This is discussed in detail in Section 2.6. In quantum optics based implementations for cluster states, the Gaussian resources are easily accessible using linear optics, squeezing Hamiltonians, i.e., second order nonlinear optics, and quadrature measurements via homodyne detection. On the other hand, non-Gaussian resources are experimentally demanding due to lack of strong higher order (> 2) nonlinearity such as Kerr nonlinearity. The other avenue for enabling non-Gaussian resources is via photon-number-resolved detection (PNRD), which is now a matured technology up to several tens of photons using superconducting transition-edge sensors (TESs) [58]–[60], and with the spatial- and time-multiplexed detection schemes employing superconducting nanowire single-

[2]While 60 entangled modes were experimentally measured, the OPO gain bandwidth allows for as high as 6700 modes. The measurement was limited by the phase modulation bandwidth of electro-optic modulator (EOM).

photon detectors (SNSPDs) and single-photon avalanche-photodiodes (SPADs) [61]–[68].

Not only does PNRD offers a way to perform non-Gaussian measurements, they also allow us to prepare non-Gaussian states and to implement non-Gaussian gates such as qubic phase gate. Significant progress has been made towards non-Gaussian state engineering using techniques such as photon subtraction [69]–[71] and photon addition [72], photon catalysis [73], [74], and by converting Gaussian states to non-Gaussian states using PNRD [75], [76].

In addition to offering a testbed for quantum science [77]–[79], non-Gaussian resources offer advantages in many other quantum technologies such as quantum communication, bosonic quantum error correction [80], entanglement distillation [81], quantum metrology and sensing [82], and quantum imaging [83], [84]. It is therefore of paramount importance to be able to fully characterize and develop non-Gaussian resources in order to fully exploit the advantages offered by the quantum technology.

Finally, the coming age of PNR detector led to both theoretical and experimental advances in characterizing quantum states via state tomography using PNR measurements [1], [2], [85]–[88].

This thesis has two central themes. The first part focuses on characterizing non-Gaussian states using PNR measurements performed by the TES. The second part focuses on characterizing quantum detectors by Wigner functions, and designing room temperature PNR detectors using click or no-click detectors such as single-photon avalanche-photodiodes. We now provide an outline for this thesis.

Thesis outline

This thesis is organized as follows. Chapter 2 introduces some routinely used tools in quantum optics. In chapter 3, we demonstrate a quantum state tomography method proposed by Wallentowitz and Vogel [1] and Banaszek and Wódkiewicz [2] (WVBW), which allows the *direct* reconstruction of the Wigner function of an unknown quantum state [89] using PNR measurements. In this experiment, we reconstruct the Wigner function of a heralded single-photon Fock state. We observe the negativity of the Wigner function in the raw data without any inferences or corrections for decoherence. At the end of this chapter, we extend the WVBW scheme to reconstruct the Wigner function of a multimode quantum state.

Chapter 4 generalizes the WVBW scheme for point-by-point Wigner function reconstruction with PNR measurements. The generalized scheme reconstructs the density matrix of an arbitrary quantum state by experimentally determining the Wigner function (or quantum state) overlap, between the unknown state and a small set of known coherent states. Each overlap is determined by the parity expectation value obtained from photon-number-resolving measurements on only a single mode of the output field after an interference between each coherent state and the unknown state. We then use computationally efficient semi-definite programming (SDP) to obtain the density matrix of the unknown quantum state in the Fock basis.

Next, we develop computationally efficient and physically reliable techniques to account for experimental imperfections such as losses, noise, and mode-mismatch between the coherent states and the unknown state. We demonstrate the proposed scheme for a weak a coherent state and a single-photon Fock state.
In chapter 5, we investigate the feasibility and performance of PNR detection using a segmented detector, constituted by waveguide-coupled, low-dark current single-photon avalanche photodiodes (SPADs).

The crucial advantage of this design is that the nonideal quantum efficiency of the SPADs does not amount to photon loss, unlike terminally coupled PNR detectors in the temporally or spatially multiplexed schemes where photons get detected by SPADs at the end of the multiplexing setup [62]–[64]. Remarkably, we note that the reasonable levels of losses, dark counts and electrical cross-talk noise do not degrade the PNR performance as much as having a limited number of SPADs does. Therefore, the number of integrated SPADs is the dominant factor toward high-quality PNR detection at the room temperature.

In chapter 6, we propose an experimentally feasible method for characterizing a photodetector by reconstructing the Wigner functions of the detector's POVM elements [90]. The method is shown to be robust against the experimental noise by using numerically efficient quadratic convex optimization techniques. We also show that for phase insensitive detectors the proposed method becomes particularly simple as it only requires $(2m_0 + 1)$ measurements to fully characterize a detector that saturates for photon-number more than m_0.

Chapter 7 discusses a new type of a Heisenberg-limited quantum interferometer with photon-subtracted twin beams. We show that such an interferometer can yield Heisenberg-limited performance and gives a direct fringe reading, unlike for the twin-beam input of the Holland-Burnett interferometer. We then propose a feasible experimental realization, using a degenerate optical parametric oscillator above threshold. The deleterious effects due to experimental losses are also considered. In chapter 8, we conclude and offer an outlook.

Chapter 2

Quantum optics

In this chapter, we introduce the basis mathematical formalism in quantum optics. We start with the quantization of the electromagnetic field followed by a brief discussion on some commonly used quantum states, operators, and measurement techniques. Next, an overview for characterizing quantum states and quantum detectors is provided.

2.1 Quantization of an electromagnetic field

In order to study the quantum mechanical properties of light one needs the quantization of the electromagnetic field. The classical free field is described by the source free Maxwell's equations where the electric (**E**) and magnetic (**B**) fields follow the physical properties mathematically formulated as:

$$\nabla.\mathbf{B} = 0, \tag{2.1}$$

$$\nabla \times \mathbf{E} = -\frac{\partial \mathbf{B}}{\partial t}, \tag{2.2}$$

$$\nabla.\mathbf{D} = 0, \tag{2.3}$$

$$\nabla \times \mathbf{H} = \frac{\partial \mathbf{D}}{\partial t}, \tag{2.4}$$

where ϵ_0 and μ_0 are electric and magnetic permittivity of free space, and $\mathbf{D} = \epsilon_{\mathbf{0}}\mathbf{E}$ and $\mathbf{H} = \frac{\mathbf{B}}{\mu_{\mathbf{0}}}$. Solving Maxwell's equations for the electric field constrained in the certain physical volume leads to [39]

$$\mathbf{E}(\mathbf{r}, \mathbf{t}) = i \sum_k \left(\frac{\hbar\omega_k}{2\epsilon_0}\right)^{1/2} [a_k \boldsymbol{\phi}_k(\mathbf{r}) e^{-i\omega_k t} - a_k^* \boldsymbol{\phi}_k^*(\mathbf{r}) e^{i\omega_k t}], \tag{2.5}$$

where $\hbar$ is the scaled Plank constant and k is the mode index number describing the polarization and the Cartesian components of a field propagation vector $\mathbf{k}$. The set $\{\boldsymbol{\phi_k}\}$ consists of orthonormal mode functions to represent the electric field in a given physical volume. The frequency of the mode function $\boldsymbol{\phi_k}$ is ω_k and a_k and a_k^* are complex Fourier amplitudes in classical electrodynamics. Quantization can then be accomplished by choosing a_k and a_k^* as two mutually adjoint operators $\hat{a}_k$ and $\hat{a}_k^\dagger$ such that they satisfy the bosonic commutation relations defined as

$$[\hat{a}_k, \hat{a}_{k'}] = [\hat{a}_k^\dagger, \hat{a}_{k'}^\dagger] = 0, \;\; [\hat{a}_k, \hat{a}_{k'}^\dagger] = \delta_{k,k'}. \tag{2.6}$$

Since these modes are non-interacting, their dynamical behaviour can be described by treating them as an ensemble of independent fields. As a result, the system Hamiltonian can be determined by adding the individual Hamiltonians as

$$\hat{H} = \frac{1}{2} \int (\epsilon_0 \boldsymbol{E}^2 + \mu_0 \boldsymbol{H}^2) d\mathbf{r} = \sum_k \hbar\omega_k \left(\hat{a}_k^\dagger \hat{a}_k + \frac{1}{2}\right) \tag{2.7}$$

From Eq. (2.7), we can see that the Hamiltonian is equivalent to the Hamiltonian of independent quantum harmonic oscillators, whereby $\hat{a}_k$ and $\hat{a}_k^\dagger$ are the annihilation and creation operators respectively, and $\hat{N}_k = \hat{a}_k^\dagger \hat{a}_k$ is the number operator for k-th harmonic oscillator. In the context of the light, $\hat{N}_k$ is known as photon-number operator for mode k. Therefore, Eq. (2.7) represents the total energy of the field, where $\frac{\hbar\omega_k}{2}$ is the vacuum fluctuations or zero point energy in the mode k. To further develop the mathematical formalism of the quantized electromagnetic field, we restrict ourselves to a single-mode, i.e, $k = 1$ and omit the index k in everything that follows in this chapter. We will specify when we have a multi-mode case. The Hamiltonian of a single-mode electromagnetic field described the annihilation operator $\hat{a}$ is

$$\hat{H} = \hbar\omega\left(\hat{a}^\dagger \hat{a} + \frac{1}{2}\right) = \hbar\omega\left(\hat{N} + \frac{1}{2}\right), \tag{2.8}$$

where $\hat{N}$ the single-mode photon-number operator with eigenvalues, $n \in \mathbb{N} = \{0, 1, 2, \cdots\}$. Since $\hat{a}$ and $\hat{a}^\dagger$ are not Hermitian operators, they do not represent any physical observable experimentally measured in the lab, but one can define Hermitian operators by using linear combinations of $\hat{a}$ and $\hat{a}^\dagger$. These operators are defined as

$$\hat{Q} := \frac{\hat{a} + \hat{a}^\dagger}{\sqrt{2}}, \tag{2.9}$$

$$\hat{P} := -i\frac{\hat{a} - \hat{a}^\dagger}{\sqrt{2}}, \tag{2.10}$$

$$[\hat{Q}, \hat{P}] = i. \tag{2.11}$$

The Heisenberg uncertainty relation is

$$\triangle Q \triangle P \geq \frac{1}{2}. \tag{2.12}$$

In quantum optics community, $\hat{Q}$ and $\hat{P}$ are known as amplitude and phase quadratures of the field. Their eigenstates are

$$\hat{Q}|q\rangle = q|q\rangle, \tag{2.13}$$

$$\hat{P}|p\rangle = p|p\rangle. \tag{2.14}$$

Since $\hat{Q}$ and $\hat{P}$ are Hermitian operators, their eigenstates offer complete orthogonal bases to represent any arbitrary quantum state as

$$|\psi\rangle = \int_{\mathbb{R}} \psi(q)|q\rangle dq \tag{2.15}$$

$$|\psi\rangle = \int_{\mathbb{R}} \tilde{\psi}(p)|p\rangle dp, \tag{2.16}$$

where $\mathbb{R}$ represents the real space. The orthogonality and completeness properties are

$$\langle q|q'\rangle = \delta(q-q'), \qquad \langle p|p'\rangle = \delta(p-p') \tag{2.17}$$

$$\int_{\mathbb{R}} |q\rangle\langle q|dq = \mathbb{I}, \qquad \int_{\mathbb{R}} |p\rangle\langle p|dp = \mathbb{I} \tag{2.18}$$

Moreover, a generalized quadrature operator is defined as

$$\hat{X}(\phi) := \hat{Q}\cos\phi + \hat{P}\sin\phi \tag{2.19}$$

The generalized quadrature is measured using an interferometric technique known as balanced homodyne detection (BHD), detailed in section 2.7. In the next section, we discuss three main pictures of quantum mechanics used for the time evolution of the states and operators.

2.2 Time evolution in quantum mechanics

In quantum mechanics, there are three mathematical formulations known as Schrödinger picture, Heisenberg picture, and the interaction picture due to Dirac. The key is to either evolve wave functions or operators or both according to the mathematical convenience while ensuring the measurement outcomes such as expectation values remain invariant. Let's consider the time evolution of a quantum system with Hamiltonian $\hat{H}$ given as

$$\hat{H} = \hat{H}_0 + \hat{V}, \tag{2.20}$$

where $\hat{H}_0$ is free-field Hamiltonian and $\hat{V}$ is the interaction Hamiltonian.

2.2.1 Schrödinger Picture

In the Schrödinger picture of quantum mechanics, the observables or operators remain constant while the wave functions (or state vector) evolve in time. The evolution is given by Schrödinger picture as

$$\frac{d|\psi\rangle}{dt} = -\frac{i}{\hbar}\hat{H}|\psi\rangle \tag{2.21}$$

If we consider the Hamiltonian invariant during the time evolution of the system from the initial time t_i to final time t_f , the solution of Eq. (2.21) is

$$|\psi(t_f)\rangle = e^{\frac{-i\hat{H}(t_f-t_i)}{\hbar}}|\psi(t_i)\rangle$$

Furthermore, one can define a unitary operator as

$$\hat{U}(t_f, t_i) := e^{-\frac{i}{\hbar}\hat{H}(t_f-t_i)}. \tag{2.22}$$

Note that $\hat{U}(t_f, t_i)$ always exists, for a time-dependent Hamiltonian which commutes with itself at different times, the unitary operator is

$$\hat{U}(t_f, t_i) := e^{-\frac{i}{\hbar}\int_{t_i}^{t_f} \hat{H}(t)dt}. \tag{2.23}$$

As a result, the expectation value of an observable at time t_f is give by

$$\langle \hat{O} \rangle_{t_f} = \langle \psi(t_f) | \hat{O} | \psi(t_f) \rangle \tag{2.24}$$

2.2.2 Heisenberg Picture

In the Heisenberg picture, the operators evolve in time and the wave functions remain invariant. The expectation value of an observable at time t_f can then be formulated as

$$\langle \hat{O} \rangle_{t_f} = \langle \psi(t_i) | \hat{O}(t_f) | \psi(t_i) \rangle, \tag{2.25}$$

where $\hat{O}(t_f)$ is the time evolved operator at t_f given by

$$\hat{O}_{t_f} := \hat{U}^{\dagger}(t_f, t_i)\hat{O}(t_i)\hat{U}(t_f, t_i). \tag{2.26}$$

For brevity, we denote the operator in Heisenberg picture by $\hat{O}_H$ and by $\hat{O}_S$ in the Schrödinger picture. Note that at $t = t_i$, we have $\hat{O}_S(t_i) = \hat{O}_H(t_i)$. These operators are related as

$$\hat{O}_H(t) := \hat{U}^{\dagger}(t_f, t_i)\hat{O}_S\hat{U}(t_f, t_i). \tag{2.27}$$

Time evolution of $\hat{O}_H$ in the Heisenberg can be mathematically formulated as

$$\frac{d\hat{O}_H(t)}{dt} = -\frac{i}{\hbar}[\hat{O}_H(t), \hat{H}_s] \tag{2.28}$$

where $\hat{H}_s$ is the system Hamiltonian in Schrödinger picture. It is worth mentioning that the Heisenberg picture is analogous to Hamilton's equations of motion in classical mechanics, where the commutators are replaced by the Poisson brackets.

2.2.3 Interaction Picture

In the interaction picture (also known as the Dirac Picture) both operators and states evolve in time. We first define an operator in the interaction picture as

$$\hat{O}_I(t) := \hat{U}_0(t)\hat{O}_H\hat{U}_0^\dagger(t), \tag{2.29}$$

where $\hat{U}_0(t) := e^{-\frac{i\hat{H}_0 t}{\hbar}}$ is the evolution under the Hamiltonian operator $\hat{H}_0$ in Eq. (2.20). The time derivative of Eq. (2.29) leads to

$$\frac{d\hat{O}_I(t)}{dt} = \frac{i}{\hbar}[\hat{O}_I, \hat{H}_0] + \hat{U}_0\frac{d\hat{O}_H}{dt}\hat{U}_0^\dagger \tag{2.30}$$

A simple calculation using Eq. (2.28) shows that

$$\hat{U}_0\frac{d\hat{O}_H}{dt}\hat{U}_0^\dagger = -\frac{i}{\hbar}([\hat{O}_I, \hat{H}_0] + [\hat{O}_I, \hat{V}]). \tag{2.31}$$

Using Eqs. [2.30,2.31], one arrives to

$$\frac{d\hat{O}_I(t)}{dt} = -\frac{i}{\hbar}[\hat{O}_I(t), \hat{V}_I(t)]. \tag{2.32}$$

Likewise, the evolution of the system wave function is given as

$$\frac{d|\psi_I(t)\rangle}{dt} = -\frac{i}{\hbar}\hat{H}_0|\psi(t)\rangle \tag{2.33}$$

As a result, we see that in interaction picture operators evolve under the interaction part of the Hamiltonian, $\hat{V}$ and the wave function dynamics is governed by the free-field Hamiltonian $\hat{H}_0$.

2.3 Quantum states, operators, and measurements

In this section, we discuss some routinely used quantum states, operators, and measurements in quantum optics.

2.3.1 Vacuum state

The vacuum state is the ground state of the quantum harmonic oscillator and it satisfies

$$\hat{a}|0\rangle = 0. \tag{2.34}$$

From Eq. (2.8), we see that for $n = 0$. i.e., absence of any photons, the energy has the lowest value of $\hbar\omega/2$. This is truly a quantum mechanical property of the light, which plays an important role in quantum interferometry, discussed in detail in chapter 7. We now calculate the expectation value of the first and second moments of the amplitude and phase quadratures

$$\langle 0|\hat{Q}|0\rangle = \langle 0|\hat{P}|0\rangle = 0, \tag{2.35}$$

$$\langle 0|\hat{Q}^2|0\rangle = \langle 0|\hat{P}^2|0\rangle = \frac{1}{2}. \tag{2.36}$$

The standard deviations in both quadratures are

$$\triangle Q = [\langle\hat{Q}^2\rangle - \langle\hat{Q}\rangle^2]^{\frac{1}{2}}, \tag{2.37}$$

$$\triangle P = [\langle\hat{P}^2\rangle - \langle\hat{P}\rangle^2]^{\frac{1}{2}}. \tag{2.38}$$

For the vacuum state, we have

$$\triangle Q = \triangle P = \frac{1}{\sqrt{2}}. \tag{2.39}$$

Since we have $\triangle Q \triangle P = 1/2$, one can immediately see from Eq. (2.12) that the vacuum state satisfy the Heisenberg minimum-uncertainty relation

$$\triangle Q \triangle P = \frac{1}{2}. \tag{2.40}$$

2.3.2 Fock states

Fock states are eigenstates of the photon number operator. Thus we have

$$\hat{N}|n\rangle = n|n\rangle \tag{2.41}$$

An n-photon Fock state, $|n\rangle$ is prepared by creating n photons in the vacuum field. Mathematically, they are defined by n successive actions of the creation operator to the vacuum field.

$$|n\rangle = \frac{\hat{a}^{\dagger n}}{\sqrt{n!}}|0\rangle. \tag{2.42}$$

Here we utilize the fact that the action of creation operator is defined as

$$\hat{a}^{\dagger}|n\rangle = \sqrt{n+1}|n\rangle. \tag{2.43}$$

Likewise, an annihilation operator acting on an n-photon Fock state leads to

$$\hat{a}|n\rangle = \sqrt{n}|n-1\rangle. \tag{2.44}$$

Using Eq. (2.43) and Eq. (2.44), we can determine the energy of a n-photon Fock state.

$$E_n = \langle n|\hat{H}|n\rangle = \langle n|\hbar\omega\left(\hat{a}^\dagger\hat{a} + \frac{1}{2}\right)|n\rangle = \hbar\omega\left(n + \frac{1}{2}\right) \tag{2.45}$$

We now discuss some properties of the Fock states.

- Orthogonality: Fock states $|n\rangle$ and $|n' \neq n\rangle$ are orthogonal.

$$\langle n|n'\rangle = \delta_{n,n'} \tag{2.46}$$

- Completeness: Fock states offer a complete basis to represent an arbitrary single-mode quantum state in the Hilbert space spanned by $\{|n\rangle, n \in \mathbb{N}\}$.

$$|\psi\rangle = \sum_{n=0}^{\infty} \psi_n|n\rangle, \tag{2.47}$$

$$\rho = \sum_{n,n'=0}^{\infty} \rho_{n,n'}|n\rangle\langle n'|, \tag{2.48}$$

$$\sum_{n=0}^{\infty} |n\rangle\langle n| = \mathbb{I}, \tag{2.49}$$

where the diagonal entries $\rho_{n,n}$ correspond to the probability of having n photons. Note that this can be simply extended to arbitrary multi-mode state as

$$\rho = \sum_{n_1,n_2,\cdots m_1,m_2,\cdots=0}^{\infty} \rho_{n_1,n_2,\cdots m_1,m_2,\cdots}|n_1, n_2, \cdots\rangle\langle m_1, m_2, \cdots| \tag{2.50}$$

In this case, the completeness property leads to

$$\sum_{n_1,n_2,\cdots m_1,m_2,\cdots}^{\infty} |n_1, n_2, \cdots\rangle\langle m_1, m_2, \cdots| = \mathbb{I}. \tag{2.51}$$

Coherent state

A coherent state is an eigenstate of the annihilation operator.

$$\hat{a}|\alpha\rangle = \alpha|\alpha\rangle, \tag{2.52}$$

where $\alpha = (q + ip)/\sqrt{2} \in \mathbb{C}$. Coherent states are classical states in the sense that their dynamics can be fully described by using the classical theory of the electromagnetic field. One can further express coherent state, $||\alpha|e^{i\phi}\rangle$ with $|\alpha|$ being the amplitude and ϕ is the phase, in the photon-number basis as

$$|\alpha\rangle = e^{-\frac{|\alpha|^2}{2}} \sum_{n=0}^{\infty} \frac{\alpha^n}{\sqrt{n!}}|n\rangle. \tag{2.53}$$

The mean photon-number of a coherent state is

$$N = \langle\alpha|\hat{N}|\alpha\rangle = \sum_{n=0}^{\infty} nP(n) = |\alpha|^2, \tag{2.54}$$

where $P(n)$ is the probability of having n photons and it is given by the Poissonian distribution.

$$P(n) = e^{-|\alpha|^2}\frac{|\alpha|^{2n}}{n!} \tag{2.55}$$

Additionally, some interesting properties of the coherent states are:

- Non-orthogonality: For coherent states $|\alpha\rangle$ and $|\beta\rangle$, we get

$$\langle\beta|\alpha\rangle = e^{-\frac{|\beta|^2+|\alpha|^2-2\beta^*\alpha}{2}} \tag{2.56}$$

- Overcompleteness: Coherent states form an overcomplete basis and can be used to represent any quantum state in the basis $\{|\alpha\rangle, \alpha \in \mathbb{C}\}$

$$\frac{1}{\pi}\int |\alpha\rangle\langle\alpha| d^2\alpha = \mathbb{I} \tag{2.57}$$

Coherent states have equal uncertainties in both quadratures, i.e., $\triangle Q = \triangle P = 1/\sqrt{2}$ and hence, also satisfy the minimum uncertainty relation as per Eq. (2.12). As we will see later, coherent states offers a tomographically complete set of probes for quantum detector tomography and have been extensively used for this purpose [90]–[92].

2.3.3 Phase-averaged coherent state

The phase-averaged coherent state is prepared by randomizing the optical phase of a coherent state.

$$\rho = \frac{1}{2\pi}\int_0^{2\pi} |\alpha\rangle\langle\alpha| d\phi = \sum_{n=0}^{\infty} P(n)|n\rangle\langle n|, \tag{2.58}$$

where $P(n)$ is given by Eq. (2.55). We see that phase-averaged coherent state is diagonal in photon-number basis. In the lab, one can use a fast-modulated PZT mirror to randomize the optical phase of a coherent state.

2.3.4 Thermal mixtures

Thermal light sources are the most common ones, any object at a finite temperature emits radiation with statistical properties of a thermal mixture. The density operator of a thermal mixture is also diagonal in photon-number basis.

$$\rho = \sum_{n=0}^{\infty} P(n)|n\rangle\langle n|, \tag{2.59}$$

where $P(n) = \frac{\bar{n}^n}{(1+\bar{n})^{n+1}}$ is the Bose-Einstein photon-number distribution mean photon-number $\bar{n}$. Thermal mixtures could be generated by randomizing the phase and amplitude of a coherent state by using a rotating ground-glass disk in the lab.

2.3.5 Squeezed states

Single-mode squeezed vacuum

The next class of states considered here are squeezed states, which are created by a nonlinear process. A squeezed state has less uncertainty in one quadrature than the vacuum state. To hold the Heisenberg uncertainty relation, the noise in the other quadrature must be higher than that of a vacuum state. The single-mode squeezing operator is given by

$$\hat{S}(\zeta) = e^{\frac{\zeta^*}{2}\hat{a}^2 - \frac{\zeta}{2}\hat{a}^{\dagger 2}}, \tag{2.60}$$

where $\zeta := re^{i\phi}$ is the squeezing parameter with the amplitude $r \geq 0$ and $0 \leq \phi \leq 2\pi$ with $\phi/2$ being the squeezing angle. In the Heisenberg picture, the annihilation and creation operators transform to

$$\hat{S}^\dagger(\zeta)\hat{a}\hat{S}(\zeta) = \hat{a}\mathrm{cosh}r - \hat{a}^\dagger e^{i\phi}\mathrm{sinh}r, \tag{2.61}$$

$$\hat{S}^\dagger(\zeta)\hat{a}^\dagger\hat{S}(\zeta) = \hat{a}^\dagger\mathrm{cosh}r - \hat{a}e^{-i\phi}\mathrm{sinh}r. \tag{2.62}$$

This transformation is known as Bogoliubov transformation. The SMSV state is obtained by applying the squeezing operator to vacuum state.

$$|SMSV\rangle = \hat{S}(\zeta)|0\rangle = \frac{1}{\sqrt{\mathrm{cosh}r}}\sum_{n=0}^{\infty}\frac{\sqrt{2n!}}{2^n n!}(-e^{i\phi}\mathrm{tanh}r)^n|2n\rangle, \tag{2.63}$$

Note that the SMSV state has support only on even number of photons. Next, we calculate the noise of both the quadratures for a particular case of $\phi = \pi$, and find out that

$$\triangle Q = \frac{e^r}{\sqrt{2}}, \tag{2.64}$$

$$\triangle P = \frac{e^{-r}}{\sqrt{2}}. \tag{2.65}$$

From Eq. (2.64) and Eq. (2.65), we see that the noise in amplitude (phase) quadrature is increased (decreased) compare to that of the vacuum state. In chapter 3, we will discuss two-mode squeezed vacuum in depth and see how it can be used to herald a single-photon Fock state.

In Fig. 2.1, we display the noise distributions in the phase space. From the top row, we see that the vacuum and a coherent state have equal noise in both field quadratures. The thermal mixture has larger noise than the vacuum state as per Fig. 2.1c. Finally, we display the noise ellipse of the SMSV in Fig. 2.1d, where the squeezing angle is $\phi/2$, and Q' and P' are rotated quadratures.

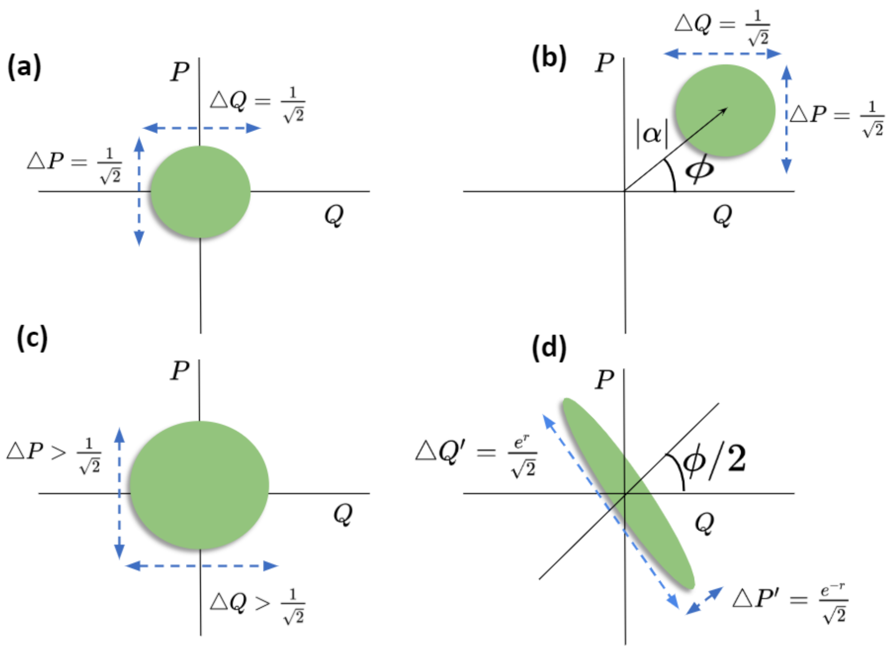

Figure 2.1: Phase space noise distributions of, (a) Vacuum state with equal noise in both field quadratures, (b) Coherent state with equal noise like vacuum, (c) Thermal mixture: it has higher noise than that of a vacuum in both quadratures, (d) Squeezed state has lesser noise than that of a vacuum in one quadrature and higher in the other quadrature. The squeezing angle is $\phi/2$, and Q' and P' are rotated quadratures.

2.4 Quantum operators

We now discuss some commonly used quantum operations and their experimental implementation in the lab.

2.4.1 The Beamsplitter

A beamsplitter (BS) is one the most common, simplest, and yet very fundamental optical element used in the lab. Classically, it is a partially reflecting mirror which splits the incident light into two light beams depending on its reflection (r) and transmission (t) coefficients. The classical picture of the BS ignores the vacuum mode always present in the unused port of the BS. Quantum mechanically, a BS has four ports as per Fig. 2.2, where $\hat{a}$ and $\hat{b}$ are the annihilation operators representing the input modes. The unitary operator for the beamsplitter interaction is

$$\hat{U}_{BS} = e^{\theta(\hat{a}^\dagger \hat{b} - \hat{a}\hat{b}^\dagger)}. \tag{2.66}$$

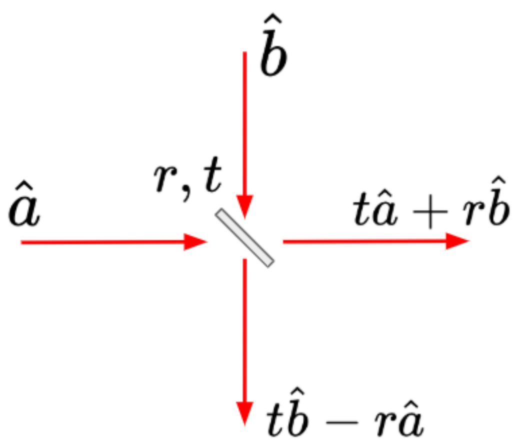

Figure 2.2: Quantum model of a beamsplitter.

Adapting the Heisenberg picture, we can find the output modes after the BS interaction.

$$\hat{a} \rightarrow t\hat{a} + r\hat{b} \tag{2.67}$$

$$\hat{b} \rightarrow t\hat{b} - r\hat{a}, \tag{2.68}$$

where $t = \cos\theta$ and $r = \sin\theta$ are transmission and reflection coefficients respectively. Note that $t^2 + r^2 = 1$, which is a consequence of energy conservation implying that the total photon-number is conserved after BS interaction. The field quadrature operators evolve to

$$\hat{q}_a \rightarrow t\hat{q}_a + r\hat{q}_b \tag{2.69}$$

$$\hat{q}_b \rightarrow t\hat{q}_b - r\hat{q}_a \tag{2.70}$$

$$\hat{p}_a \rightarrow t\hat{p}_a + r\hat{p}_b \tag{2.71}$$

$$\hat{p}_b \rightarrow t\hat{p}_b - r\hat{p}_a \tag{2.72}$$

For a balanced BS we have, $t = r = 1/\sqrt{2}$. In general, the BS operation can be implemented on any physical platform with the following bi-linear Hamiltonian

$$\hat{H} \propto i(\hat{a}^\dagger\hat{b} - \hat{a}\hat{b}^\dagger). \tag{2.73}$$

2.4.2 The displacement operator

The unitary operator for phase space displacement operation is

$$\hat{D}(\alpha) = e^{\alpha\hat{a}^\dagger - \alpha^*\hat{a}}, \tag{2.74}$$

where $\alpha := (q_\alpha + ip_\alpha)/\sqrt{2}$ is the displacement amplitude. Under the action of $\hat{D}(\alpha)$, mode $\hat{a}$ evolves to

$$\hat{D}^\dagger(\alpha)\hat{a}\hat{D}(\alpha) = \hat{a} + \alpha\mathbb{I}. \tag{2.75}$$

Similarly, the evolution of the quadratures is

$$\hat{D}^{\dagger}(\alpha)\hat{q}\hat{D}(\alpha) = \hat{q} + q_{\alpha} \tag{2.76}$$

$$\hat{D}^{\dagger}(\alpha)\hat{p}\hat{D}(\alpha) = \hat{p} + p_{\alpha} \tag{2.77}$$

The experimental implementation of the displacement operator is detailed in chapter 3. An n-mode displacement operator is given by

$$\hat{D}(\alpha_1, \alpha_2, \cdots, \alpha_n) = \otimes_{i=1}^{n} \hat{D}_i(\alpha_i), \tag{2.78}$$

where $\hat{D}_i(\alpha_i)$ is the displacement operator for i^{th} mode.

2.4.3 The phase-shift operator

For a given mode $\hat{a}$, the phase-shift operator is defined as

$$\hat{U}(\phi) = e^{-i\phi\hat{N}}, \tag{2.79}$$

where $\hat{N} = \hat{a}^{\dagger}\hat{a}$ is the number operator. Under the phase-shift operator, mode $\hat{a}$ evolves to

$$\hat{a} \rightarrow \hat{a}e^{-i\phi} \tag{2.80}$$

and quadrature operators transform as

$$\hat{q} \rightarrow \hat{q}\cos\phi + \hat{p}\sin\phi \tag{2.81}$$

$$\hat{p} \rightarrow \hat{p}\cos\phi - \hat{q}\sin\phi \tag{2.82}$$

$$\tag{2.83}$$

In the lab, phase-shift operation can be implemented using piezoelectric actuator mirror (PZT) or simply by adding path delays. This operation is extensively used in quantum state characterization as well as nullifier measurements in squeezing experiments.

2.5 Phase space representation of optical systems

In classical Hamiltonian mechanics, a physical system composed of M particles is represented by a vector $\vec{r} := \{\vec{q}, \vec{p}\}$ in a $6M$ dimensional phase space, where $\vec{q}$ and $\vec{p}$ denote the position and momentum degrees of freedom. For example, the physical state of a simple 1D harmonic oscillator can be associated with the point coordinates (q, p) as shown in the Fig 2.3 (a). In classical physics, one can determine the phase space coordinates (q, p) at a given time with arbitrary precision.

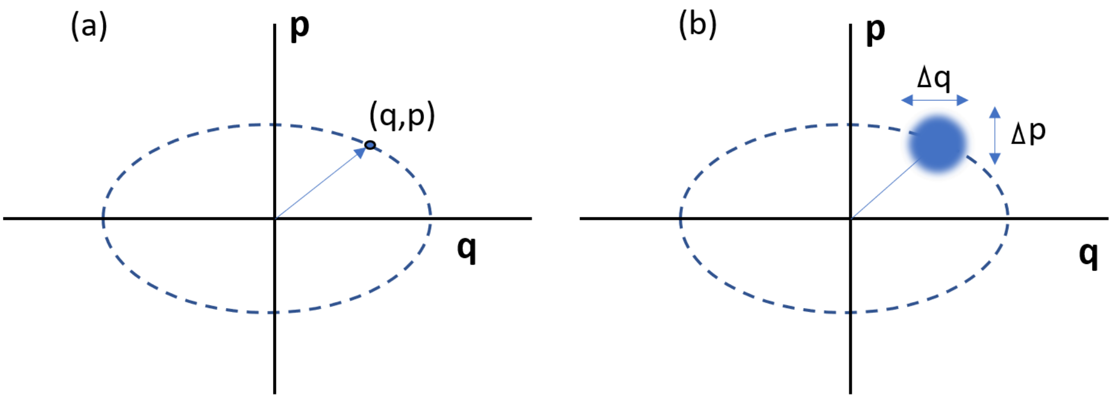

Figure 2.3: (a) Phase space of a simple harmonic oscillator, (b) Phase space of a quantum harmonic oscillator.

A key question then arises—what does it mean to characterize a quantum system? In quantum physics, the Heisenberg uncertainty principle prohibits *simultaneously* knowing the position and momentum with arbitrary precision. Therefore, one defines probability density functions. For example, the probability of the 1D quantum harmonic oscillator being in position range of x_i and x_f is $P_x = \int_{x_i}^{x_f} f(x)dx$, and likewise for the momentum range of p_i and p_f is $P_p = \int_{p_i}^{p_f} g(p)dp$, where $f(x) = |\psi(x)|^2$ and

$g(p) = |\tilde{\psi}(p)|^2$ are the probability densities for position and momentum respectively. A complete knowledge of $f(q)$ and $g(p)$, however, is not sufficient to fully characterize a quantum system. This is due to the informationally incompleteness of these measurements for quantum state characterization, we discuss this in detail in section 2.7. Therefore, one needs to have informationally complete measurements in order to fully characterize a quantum system. In quantum optics, such measurements include generalized quadratures, i.e., their measurement POVM set is $\{|X(\phi)\rangle\langle X(\phi)|, X(\phi) \in \mathbb{R}\}$, measured using homodyne detection and measurements in the coherent state basis with the POVM set $\{|\alpha\rangle\langle\alpha|, \alpha \in \mathbb{C}\}$, performed with heterodyne detection. As we discuss later, these measurements enable us to characterize a quantum system either by reconstructing the phase space distribution function such as Wigner function (discussed next) or by reconstructing the density matrix of the system under investigation.

2.5.1 Wigner Function

Eugene Wigner originally defined the continuous phase-space quasiprobability distribution function to study the quantum corrections in statistical physics [93]. For a quantum state of density operator $\hat{\rho}$, the Wigner function is given by

$$W(q,p) = \frac{1}{\pi}\int_{-\infty}^{\infty} e^{2ipy}\,\langle\, q - y \,|\, \hat{\rho} \,|\, q + y \,\rangle\, dy, \tag{2.84}$$

where q and p are the respective eigenvalues of the position and momentum operators or, in our case, of the amplitude-quadrature, $Q = (\hat{a}+\hat{a}^\dagger)/\sqrt{2}$, and phase-quadrature, $P = i(\hat{a}^\dagger - \hat{a})/\sqrt{2}$, of the quantized electromagnetic field, $\hat{a}$ and $\hat{a}^\dagger$ being the photon annihilation and creation operators, respectively. The Wigner function is uniquely defined and contains all the information about the quantum system. It is normalized over phase space and its marginal distributions correspond to the probability density distributions of the quadratures

$$\int_{-\infty}^{\infty} dp\, W(p,q) = |\psi(q)|^2 \tag{2.85}$$
$$\int_{-\infty}^{\infty} dq\, W(p,q) = |\tilde{\psi(p)}|^2. \tag{2.86}$$

However, unlike classical distributions, the quantum Wigner distribution $W(q,p)$ can't always be interpreted as a joint probability distribution because it can be non-positive (hence non-Gaussian for pure states [94]), e.g. for Fock states with $n > 0$.

Some Properties of the Wigner Functions

- Linearity: For a given linear combinations of density operators, the Wigner function is also the linear combination of individual Wigner functions, as per Eq. (2.87)

$$\rho = \sum_{i=0} \lambda_i \rho_i$$
$$W_\rho(q,p) = \sum_{i=0} \lambda_i W_{\rho_i}(q,p), \tag{2.87}$$

  where $W_{\rho_i}(q,p)$ is the Wigner function of ρ_i.

- State overlap: For given quantum states ρ_1 and ρ_2, the state overlap is

$$O = \mathrm{Tr}[\rho_1\rho_2] = 2\pi \int W_1(q,p)W_2(q,p)dqdp \tag{2.88}$$

  For a given pure state $\rho_1 = |\psi_1\rangle\langle\psi_1|$, the overlap is essentially the fidelity between ρ_1 and ρ_2. In this thesis, we use the fidelity definition given as

$$F = \left[\mathrm{Tr}\big[\sqrt{\sqrt{\rho_1}\rho_2\sqrt{\rho_1}}\big]\right]^2, \tag{2.89}$$

which simplifies to the state overlap for a pure state ρ_1.

$$F = \left[\mathrm{Tr}\left[\sqrt{\rho_1\rho_2\rho_1}\right]\right]^2 = \langle\psi_1|\rho_2|\psi_1\rangle[\mathrm{Tr}|\psi_1\rangle\langle\psi_1|]^2 = \langle\psi_1|\rho_2|\psi_1\rangle = \mathrm{Tr}[\rho_1\rho_2] = O, \tag{2.90}$$

- State purity: For a quantum state described by ρ, the purity of the density operator is

$$\mathrm{Purity}(\rho) = \mathrm{Tr}[\rho^2] = 2\pi\int W^2(q,p)dqdp \leq 1, \tag{2.91}$$

  where the equality holds for pure states.

- Generalization: The Wigner function can be defined for any Hermitian operator, i.e., $A = A^\dagger$. Consequently, the expectation value of an operator $\hat{O}$ is

$$\langle\hat{A}\rangle = \mathrm{Tr}[\rho\hat{A}] = 2\pi\int W_\rho(q,p)W_{\hat{A}}(q,p)dqdp \tag{2.92}$$

We now plot the Wigner functions of some commonly used quantum states. The Wigner function of the vacuum state is displayed in Fig. 2.4.

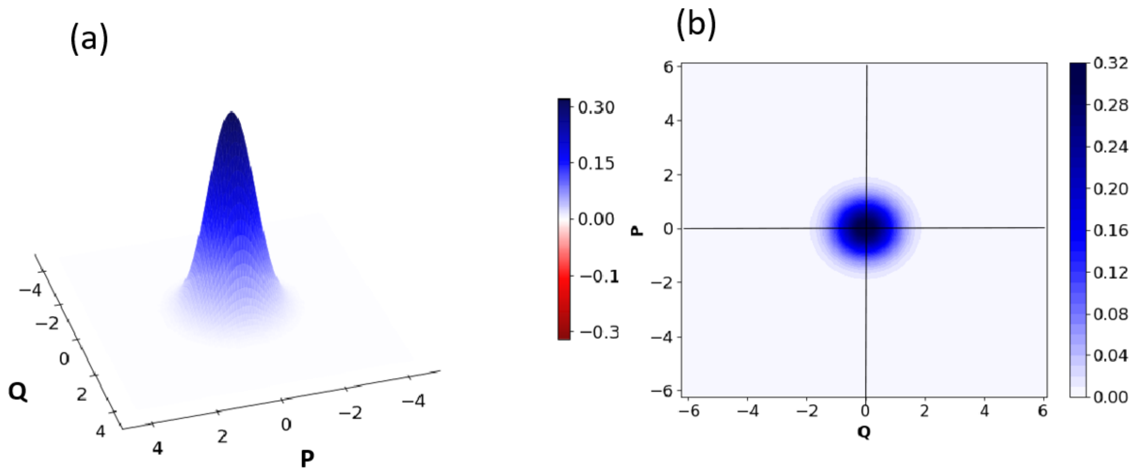

Figure 2.4: Wigner function of the vacuum state

Using Eq. (2.84), one can get the analytical expression of the Wigner function which turned out to be two dimensional Gaussian function having peak at the origin of the phase space.

$$W_{|0\rangle\langle 0|}(q,p) = \frac{1}{\pi}e^{-q^2-p^2} \tag{2.93}$$

In Fig. 2.5, we display the Wigner function of a coherent state which is essentially a displacement of the vacuum Wigner function by the coherent state amplitude.

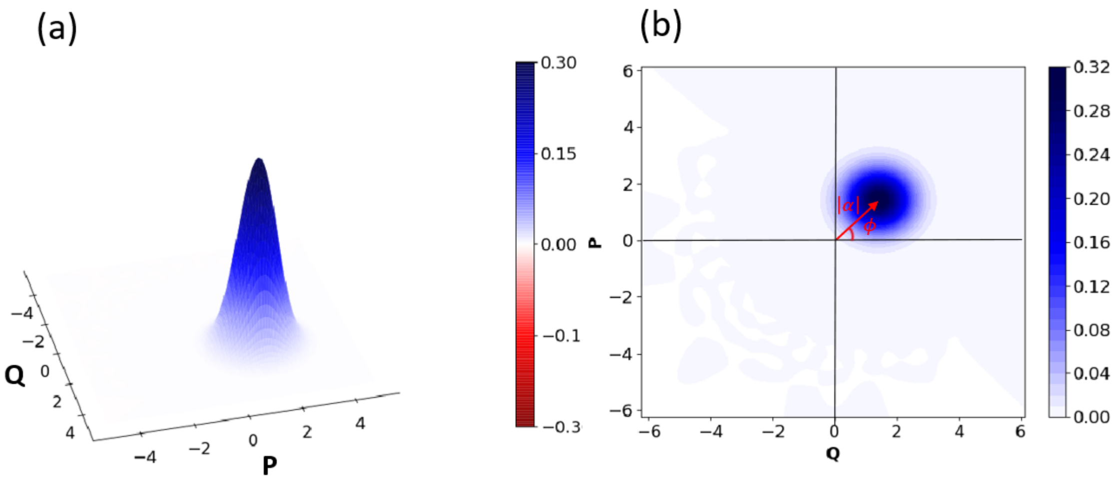

Figure 2.5: Wigner function of a coherent state with amplitude, $\alpha = 1 + 1j$.

Therefore, the Wigner function of a coherent state can be obtained by the coordinate translation of the vacuum Wigner function. As a result, we have

$$W_{|\alpha\rangle\langle\alpha|}(q,p) = \frac{1}{\pi}e^{-(q-\sqrt{2}\mathrm{Re}[\alpha])^2-(p-\sqrt{2}\mathrm{Im}[\alpha])^2} \tag{2.94}$$

Next is the Wigner function of amplitude quadrature single-mode squeezed-vacuum state (SMSV) depicted in Fig. 2.6.

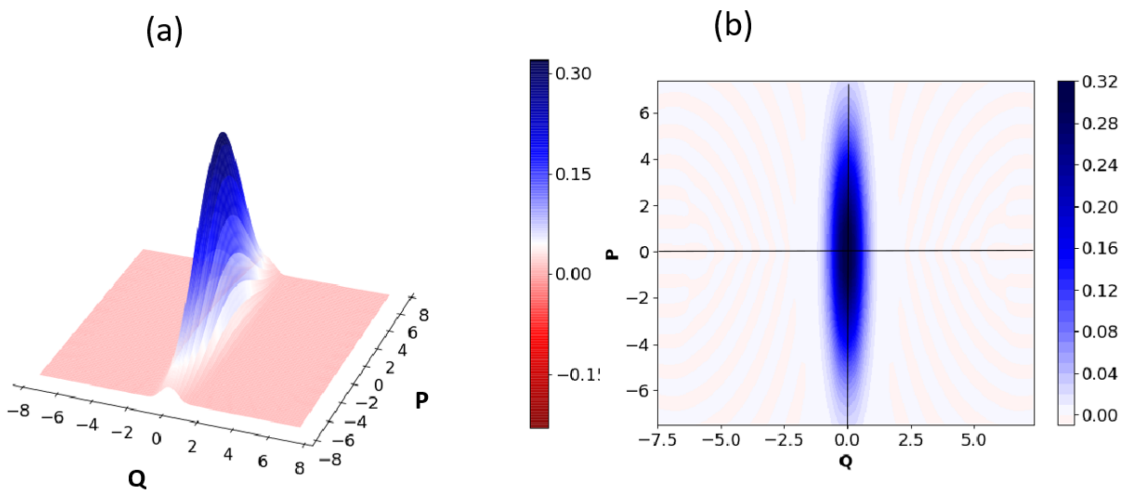

Figure 2.6: Wigner function of squeezed vacuum with $\zeta = 1$.

The Wigner function is thus given by

$$W_{|SMSV\rangle\langle SMSV|}(q,p) = \frac{1}{\pi}\exp(-e^{-\zeta}q^2 - e^{\zeta}p^2), \tag{2.95}$$

So far we have only considered non-negative Wigner functions. We now look at some non-positive Wigner functions and also give analytical expression of the Wigner function for quantum states described in a finite dimensional Hilbert space. In Fig. 2.7, we display the Wigner functions of the Fock states for $n = 1$ and $n = 2$. We see that the Wigner functions are non-Gaussian and have negative values in certain regions of the phase space.

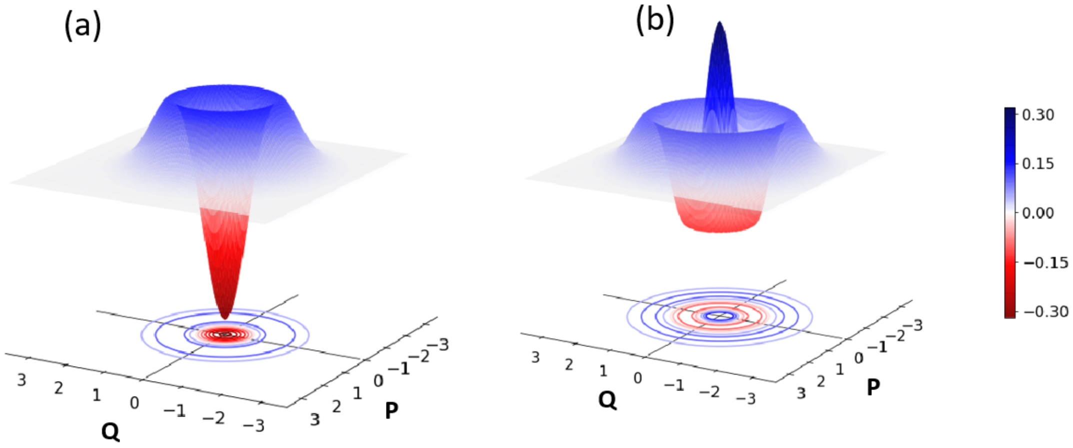

Figure 2.7: The Wigner functions of a single-photon Fock state, (a) and a two-photon Fock state, (b). We can see the negative regions in phase space.

In general, the Wigner function of a quantum state in a finite dimensional Hilbert space can be expressed as a linear combination of the Wigner functions corresponding to each density matrix element, $|\,n\,\rangle\,\langle\,n'\,|$. For a given density matrix

$$\rho = \sum_{n,n'=0}^{N_d} \rho_{n,n'} |n\rangle\langle n'|, \tag{2.96}$$

where $(N_d + 1)$ is the Hilbert space dimension. The Wigner function is

$$W(q,p) = \sum_{n,n'=0}^{N_d} \rho_{n,n'} W_{n,n'}(q,p), \tag{2.97}$$

where $W_{n,n'}(q,p)$ is [95]

$$W_{n,n'}(q,p) = \left\{ \begin{array}{ll} \frac{(-1)^n}{\pi}\sqrt{\frac{2^{n'}n!}{2^n n'!}}(q-ip)^{n'-n}e^{-(q^2+p^2)}L_n^{n'-n}(2(q^2+p^2)) & n \leq n' \\ \frac{(-1)^{n'}}{\pi}\sqrt{\frac{2^n n'!}{2^{n'} n!}}(q+ip)^{n-n'}e^{-(q^2+p^2)}L_{n'}^{n-n'}(2(q^2+p^2)) & n \geq n' \end{array} \right\}, \tag{2.98}$$

where $L_{n'}^{n-n'}$ are the associated Laguerre polynomials. Moreover, the Wigner function of an n-mode Gaussian state can be written as

$$W(\mathbf{x}) = \frac{\exp[(-1/2)[\mathbf{x}-\bar{\mathbf{x}}]^{\mathbf{T}}\mathbf{V}^{-\mathbf{1}}[\mathbf{x}-\bar{\mathbf{x}}]}{(2\pi)^N\sqrt{\det[\mathbf{V}]}}, \tag{2.99}$$

where $\mathbf{x} := [q_1, p_1, q_2, p_2, \cdots, q_N, p_N]$ and $\bar{\mathbf{x}}$ is the mean vector of the quadratures and $\det[\mathbf{V}]$ is the determinant of the covariance matrix [96].

2.5.2 Glauber – Sudarshan P-function

As mentioned earlier, coherent states form overcomplete set of states. The overcompleteness of the coherent states allows us to write arbitrary quantum state in the coherent state basis, which is formally known as Glauber–Sudarshan P representation given as

$$\rho = \int P(\alpha)|\alpha\rangle\langle\alpha| d^2\alpha, \tag{2.100}$$

where $d^2\alpha = d\mathrm{Re}[\alpha]d\mathrm{Im}[\alpha]$ is the integration over the complex space. From Eq. (2.100), one can see that any arbitrary quantum state can be represented in the diagonal form in the Hilbert space spanned by coherent state basis set, $\{|\alpha\rangle, \alpha \in \mathbb{C}\}$. The P function representation is particularly beneficial when one has to determine the expectation values of normally-ordered operators. Mathematically

$$\langle \hat{a}^{\dagger m}\hat{a}^n\rangle_\rho = \int P_\rho(\alpha)\alpha^{*m}\alpha^n d^2\alpha. \tag{2.101}$$

For quantum states such as Fock states, the P functions are highly singular, which makes them undesirable for their experimental reconstructions for characterizing these quantum states.

2.5.3 Husimi Q-function

The Husimi Q-function, originally defined by Kôdi Husimi, is another continuous-variable representation of optical systems. For a single mode quantum state, the Q-function is defined as [97]

$$Q(\alpha) = \frac{1}{\pi}\langle\alpha|\rho|\alpha\rangle = \frac{1}{\pi}\mathrm{Tr}[\rho|\alpha\rangle\langle\alpha|]. \tag{2.102}$$

From Eq. (2.102), we can see that the Q function is essentially the diagonal entries of density matrix operator represented in the coherent state basis. Since ρ is a positive and trace bounded operator, Q-function is always non-negative, normalized, and a regular function. Mathematically

$$0 \leq Q(\alpha) \leq \frac{1}{\pi}. \tag{2.103}$$

The P functions are highly singular for nonclassical states of light, which makes them hard to experimentally reconstruct them. On the other hand, Q functions are regular and several techniques employing six-port and eight-port balanced homodyne schemes have been proposed and experimentally demonstrated for their reconstructions [98], [99]. The Q-function is uniquely defined and contains complete information about the quantum system, i.e., it is equivalent to knowing the density operator of the system. Therefore, it can be used to predict the measurement outcomes by using the P function representation of the positive-valued-operator measures (POVMs) describing a detector[1] . While this formalism works in principle, it's experimental implementations have significant challenges and might result in unphysical results. This is because of highly divergent nature of P functions of the detector POVMs, and using the P functions of the detector POVMs with the state Q functions in the presence of experimental imperfections might result in numerical instabilities. Addi-

[1]Every quantum detector can be completely described by a set of hermitian operators known as positive-valued-operator measures (POVMs). We will discuss this in detail in chapter 5

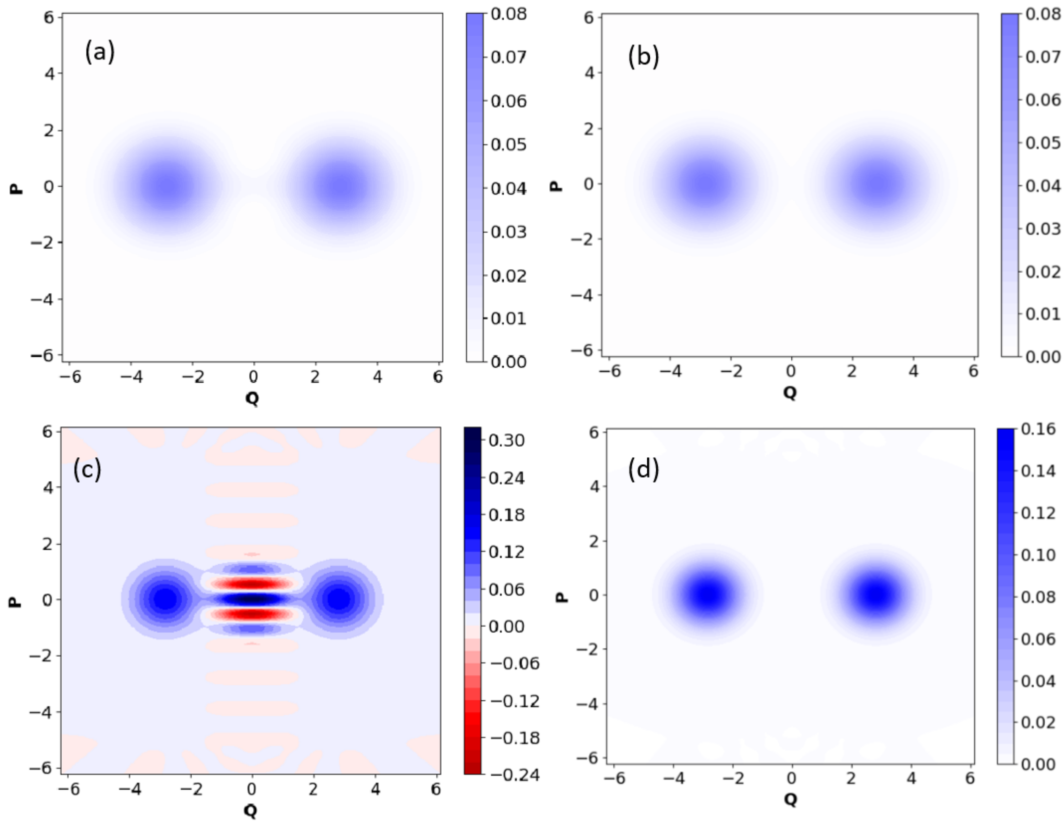

Figure 2.8: Top: (a) Husimi Q-function of a cat state, a quantum superposition of coherent states $|\alpha\rangle$ and $|-\alpha\rangle$, (b) Q function of a statistical mixture of $|\alpha\rangle$ and $|-\alpha\rangle$. Bottom: (c) Wigner function of a cat state, (d) Wigner function of a statistical mixture. All are plotted for $\alpha = 2$ and the Hilbert space is truncated at $N = 40$. The difference in the Q function values in Figs. (a) and (b) is of $\mathbb{O}(10^{-4})$.

tionally, quantum effects such as phase space interference are not pronounced in the Q-function as demonstrated in Fig 2.8, where the top row displays the Q functions of, (a) cat state, a quantum superposition of coherent states, $|\alpha\rangle$ and $|-\alpha\rangle$, (b) statistical mixture of $|\alpha\rangle$ and $|-\alpha\rangle$. The bottom row shows the Wigner functions of, (c) a cat state and (d) a statistical mixture. One can see that it is easier to distinguish the cat state from statistical mixture in the Wigner function representation. Therefore, it is desirable to experimentally reconstruct the Wigner functions of quantum states for quantum state tomography, discussed in section 2.7. This briefly covers some basics of quantum optics.

2.6 Continuous-variable quantum computing

In this section, we cover some basics of continuous-variable quantum computing (CVQC). A detailed discussion can be found in Refs. [100]–[102] and references therein. Table 2.1 shows a correspondence between discrete-variable (DV) and continuous-variable quantum computation. We note that the eigenstates of amplitude and phase quadratures form the computational and conjugate bases respectively. Within the qubit computation, the Hadamard transforms the computational basis, $\{|0\rangle, |1\rangle\}$ to the conjugate basis, $\{|+\rangle, |-\rangle\}$. This is analogous to the quantum Fourier transformation (QFT) in CVQC, i.e., the conjugate basis, $\{|p\rangle, p \in \mathbb{R}\}$ is obtained by applying QFT to $\{|q\rangle, q \in \mathbb{R}\}$. Next, the Pauli group in qubit computing corresponds to Weyl-Heisenberg (WH) group parametrized by two real parameters denoted by ξ and ϖ. While the WH operators offer to implement operations governed by the linear Hamiltonians, they do not allow implementations of higher-order polynomials in the quadrature operators Q and P. This can be understood using Baker-Campbell-Hausdorff (BCH) relation expressed as

$$e^A B e^{-A} = B + [A, B] + \frac{1}{2!}[A, [A, B]] + \cdots \tag{2.104}$$

If both the operators, A and B are linear in quadratures, Q and P, one can immediately see from the BCH relation that any combinations of the WH operators will not give higher-order polynomials because the commutator $[A, B]$ is a constant. For example, an action of $X(\xi)$ on the amplitude eigenstate displaces it by ξ, and simply adds a phase to the phase quadrature eigenstate.

In the pursuit of generating higher-order polynomials, let's consider the following quadratic Hamiltonian

$$H_0 = \frac{Q^2 + P^2}{2} \tag{2.105}$$

In the Heisenberg picture, the evolution of quadrature operators under the quadratic Hamiltonian leads to

$$\dot{Q} = i[H_0, Q] = -P, \tag{2.106}$$

$$\dot{P} = i[H_0, P] = Q. \tag{2.107}$$

A simple algebra shows that

$$Q \to Q\text{cos}t - P\text{sin}t, \qquad P \to P\text{cos}t + Q\text{sin}t. \tag{2.108}$$

It is worth pointing out that the Hamiltonian in Eq. (2.105) is the free-field Hamiltonian and its unitary transformation can be implemented by letting the field evolve for a given time t or by adding a path delay. Thus we see that the quadratic Hamiltonian leads to linear transformations of the canonical amplitude and phase quadratures. This is because the commutator $[Q, P]$ is constant, and $[H_0, Q]$ and $[H_0, P]$ can only create polynomials with the highest order of one in Q and P as per Eq. (2.108).

As discussed in Ref. [38], adding a quadratic Hamiltonian of the form $H \propto (QP+PQ)$ allows the construction of any quadratic Hamiltonian[2]. Since quadratic Hamiltonians do not increase the polynomial order, their repeated actions can not construct

[2] This Hamiltonian corresponds to the squeezing Hamiltonian realized using second order $\chi^{(2)}$ nonlinear process.

the Hamiltonians of arbitrary order. All the unitary transformations corresponding to these Hamiltonians discussed above come under the class of Gaussian unitaries because they preserve the Gaussian nature of a quantum state [101]. While these Gaussian operations can be deterministically implemented, they do not offer any computational advantages with Gaussian states and Gaussian measurements. Bartlett *et al.* showed that any quantum circuit consisting of Gaussian states, Gaussian operations, and Gaussian measurements can be efficiently simulated on a classical computer [103]. This is known as the CV analogue of Gottesman-Knill theorem for qubit systems [104].

Now the question arises – what kinds of physically realizable Hamiltonians do we need in order to construct polynomials of arbitray order? A natural inclination will be to consider higher order optical nonlinearities such as $\chi^{(3)}$, also known as Kerr nonlinearity. The Kerr Hamiltonian is given as

$$H_{\text{Kerr}} \propto (\hat{a}^\dagger \hat{a})^2 = (Q^2 + P^2)^2. \tag{2.109}$$

By making use of the Heisenberg picture, we get [38]

$$[H_{\text{Kerr}}, Q] = \frac{i}{2}(Q^2 P + PQ^2 + 2P^3). \tag{2.110}$$

Likewise, for the phase quadrature

$$[H_{\text{Kerr}}, P] = -\frac{i}{2}(P^2 Q + QP^2 + 2Q^3). \tag{2.111}$$

From Eqs. (2.110) and (2.111), we note that the commutators $[H_{\text{Kerr}}, Q]$ and $[H_{\text{Kerr}}, P]$ increase the order of the polynomial in Q and P. Consequently, repeated commutators allow the construction of any order polynomial in the canonical operators Q and P, and the number of repetitions to construct a polynomial of order n, has a polynomial scaling in n. Moreover, one can in fact use any third order Hamiltonian along with the Hamiltonians Q, P, H_0, and H to generate the Hamiltonians of arbitrary order. For instance, the third order Hamiltonian Q^3 allows the implementation of a cubic phase gate, which is a CV analogue of the non-Clifford gate in DV computation. The addition of the cubic phase gate to the Gaussian toolbox completes the universal gate set for CVQC [38]. Furthermore, we note that the two-qubit gates, C_X and C_Z also have their CV analogues which are used to create entanglement between modes. While weak higher order optical nonlinerities prohibits a deterministic implementation non-Gaussian gates, there are theoretical proposals to implement cubic phase gate or prepare cubic phase state via postselections for PNR measurements [75], [105].

Finally, we see that the measurements in CVQC are homodyne measurements, heterodyne measurements, and photon-number- resolving measurements. More recently, Baragiola *et al.* showed the universality and fault tolerance using only Gaussian resources given a supply of GKP-encoded Pauli eigenstates [106]. This summarizes the common tools in CVQC and how it can be made universal by adding a non-Gaussian element to the relatively easier to implement Gaussian toolbox.

	Discrete variable	**Continuous variable**
Computational Basis	$\{\vert 0\rangle, \vert 1\rangle\}$ $\langle n\vert m\rangle = \delta_{n,m}, n, m \in \{0,1\}$	$\{\vert q\rangle_{q\in\mathbb{R}}\}$ $\langle q\vert q'\rangle = \delta(q-q')$
Conjugate Basis	$\vert\pm\rangle = \frac{1}{\sqrt{2}}(\vert 0\rangle \pm \vert 1\rangle)$	$\{\vert p\rangle_{p\in\mathbb{R}}\}, \vert p\rangle = \frac{1}{\sqrt{2\pi}}\int e^{ipq}\vert q\rangle dq$
Single-qubit/qumode Bipartite state	$\vert\psi\rangle = c_1\vert 0\rangle + c_2\vert 1\rangle$ $\vert\psi\rangle = \frac{1}{\sqrt{2}}(\vert 00\rangle + \vert 11\rangle)$	$\vert\psi\rangle = \int \psi(q)\vert q\rangle dq$ $\vert\psi\rangle = \int \vert q,q\rangle_{a,b} dq$
Qubit/qumode Clifford gates	Pauli group $\langle X, Z\rangle$ $X\vert l\rangle = \vert l \oplus 1\rangle$, $l = 0,1$ $Z\vert l\rangle = e^{il\pi}\vert l\rangle$, $l = 0,1$ $X\vert\pm\rangle = \pm 1\vert\pm\rangle$ $Z\vert\pm\rangle = \vert\mp\rangle$	Weyl-Heisenberg group $\langle\{X(\xi)\}_{\xi\in\mathbb{R}}, \{Z(\varpi)\}_{\varpi\in\mathbb{R}}\rangle$ $X(\xi) = e^{-i\xi P}, Z(\varpi) = e^{i\varpi Q}$ $X(\xi)\vert q\rangle = \vert q+\xi\rangle$ $Z(\varpi)\vert p\rangle = \vert p+\varpi\rangle$ $X(\xi)\vert p\rangle = e^{-i\xi p}\vert p\rangle$ $Z(\varpi)\vert q\rangle = e^{i\varpi q}\vert q\rangle$
Two-qubit/qumode gates	$C_X\vert l,m\rangle = \vert l, l\oplus m\rangle$ $C_Z\vert l,m\rangle = e^{i\pi lm}\vert l,m\rangle$	$e^{-i\alpha Q_1 P_2}\vert q,q'\rangle = \vert q, q'+\alpha q\rangle$ $e^{i\alpha Q_1 Q_2}\vert q,q'\rangle = e^{i\alpha qq'}\vert q,q\rangle$
Non-Clifford gates	$\frac{\pi}{4}$ rotation about z, $R_z(\frac{\pi}{4})$	Cubic phase gate: $e^{i\gamma Q^3}, \gamma\in\mathbb{R}$
Measurement bases	X, Y, and Z	$\vert q\rangle_{q\in\mathbb{R}}$, $\vert\alpha\rangle_{\alpha:=q+ip\in\mathbb{C}}$, $\vert n\rangle_{n\in\mathbb{N}}$, $\hat{N} = \frac{Q^2+P^2-1}{2}$

Table 2.1: Equivalence between discrete and continuous variable quantum computing.

2.7 Characterization of quantum resources

In this section, we provide an overview on characterizing quantum states and quantum detectors. We first focus on the characterization of quantum states, which is

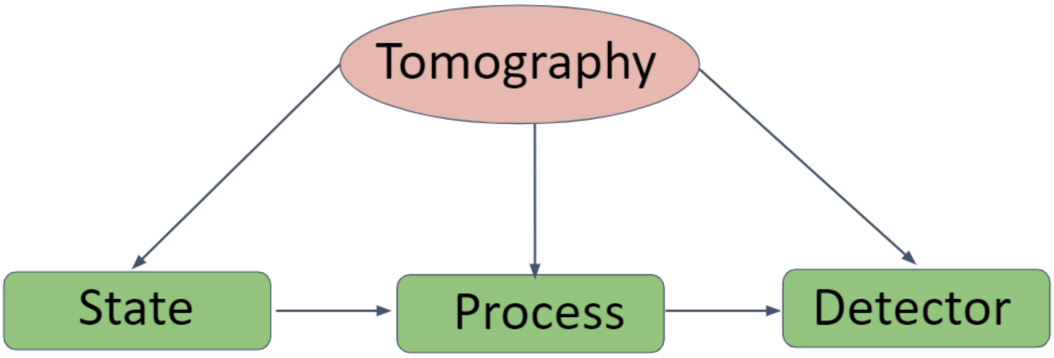

Figure 2.9: Characterization of quantum states, processes, and detectors.

formally known as quantum state tomography (QST), and then we move to characterizing quantum detectors, also known as quantum detector tomography (QDT). Generally speaking, for a given d-dimensional quantum system represented in some basis, QST amounts to experimentally identifying d^2 complex entries of the density matrix, thereby $2d^2$ real parameters. Due to Hermitian nature, i.e., $\rho = \rho^\dagger$ of a physically valid density matrix, all the entries are not independent which reduces the number of real parameters from $2d^2$ to d^2. Furthermore, with the unit trace property (Tr$[\rho] = 1$, the number of required real parameters can be reduced to $d^2 - 1$. Therefore, $\mathcal{O}(d^2)$ real parameters have to be estimated in order to fully characterize the quantum state described by ρ.

Unfortunately, a system of N particles with exponentially large Hilbert space, requires exponentially large $\mathcal{O}(d^{2N})$ number of measurements to fully characterize it, which makes QST computationally hard for systems with many particles. Although there has been significant progress towards reducing the number of required measurements using tools such as compressed sensing [107] and adaptive-state tomography [108] for fairly pure states, QST still remains an irreducibly hard estimation problem in the general setting.

An experimental implementation of QST requires measuring a quantum state such that the positive-operator-valued measurements (POVMs) describing the measurement device are informationally complete[3].

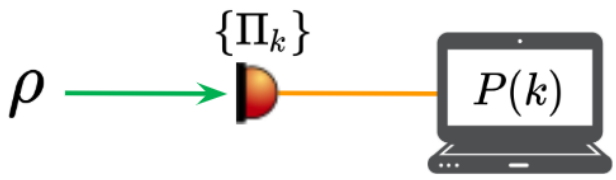

Figure 2.10: A quantum measurement process. The measured state is ρ and POVM element for an outcome, k is Π_k leading to outcome probability of $P(k)$

Since a measurement collapses the quantum state being measured, a complete characterization of the state requires quantum measurements on an ensemble of identically prepared states. One can repeat the measurement process on ensemble in order to build the probability distribution for all measurement outcomes. The probability of an outcome k is given by the Born rule

$$P(k) = \mathrm{Tr}[\rho\Pi_k]. \tag{2.112}$$

A QST protocol requires complete knowledge of the quantum detector used for measurements. Hence, we know the exact form of Π_K in Eq. (2.112). The only unknown in Eq. (2.112) is the density matrix, which could be estimated by inverting it under physicality constraints discussed in chapter 4.

We now discuss quantum detector tomography. Since trace is cyclic, the role of quantum state, ρ and measurement operator, Π_k can be interchanged in Eq. (2.112). Consequently, QDT involves experimental reconstruction of the measurement operators or the POVMs $\{\Pi_k\}$. For optical detectors, a light prepared in a set of *known* tomographically complete states a.k.a probes is sent to the detector. The probabilities of different measurement outcomes are then used to invert Eq. (2.112) to determine Π_k. In this thesis, we dedicate chapter 6 to discuss QDT in great depth. We now look

[3]POVMs are discussed in great depth in chapter 5

into some continuous-variable tomography methods for both quantum states. Since a quantum system can be equivalently represented by using either of the phase space distribution functions discussed in section. 2.5, the CV tomography can be performed by reconstructing these distributions. As discussed in section. 2.5, the Wigner function representation has the advantage of having a clear visualization of phase space interference effects so it is usually preferred for CV tomographic protocols. One such protocol is based on known as balanced homodyne detection (BDH), discussed next.

2.7.1 State tomography with balanced homodyne detection

The most common method to characterize a CV quantum state is to reconstruct its Wigner quasiprobability distribution with field quadrature measurements obtained from BHD technique [109], [110]. In this method, the quantum signal $\hat{a}$ is interfered with a relatively stronger amplitude and phase modulated local oscillator (LO) $\hat{b}$, at a balanced beamsplitter, as shown in Fig 2.11.

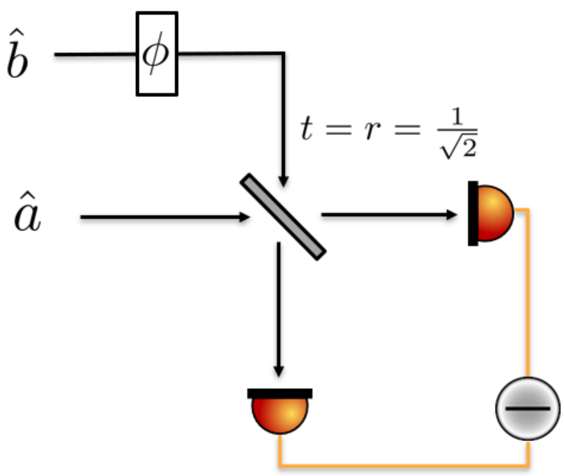

Figure 2.11: Schematic of the balanced homodyne method.The unknown state and the local oscillator are described by annihilation operators $\hat{a}$ and $\hat{b}$ respectively.

The output fields of the beamsplitter are incident to two photodiodes whose photocurrents are sent to an electronic subtractor. The current from a photodetector is proportional to the energy (total photon-number) of the field impinging on it. As a result, we have

$$I_{-} \propto \mathrm{Tr}[\rho^{out}_{a,b}(\hat{N}^{in}_{a} - \hat{N}^{in}_{b})] = \mathrm{Tr}[\rho^{in}_{a,b}(\hat{N}^{out}_{a} - \hat{N}^{out}_{b})], \tag{2.113}$$

where $\rho^{in(out)}_{a,b}$ is joint quantum state before (after) the balanced beamsplitter. $\hat{N}^{out(in)}_{a}$ and $\hat{N}^{out(in)}_{b}$ are the total number of photons detected by the top and bottom photodiode respectively. We solve Eq. (2.113) in the Heisenberg picture. As we discussed in section 2.3, the evolution of signal and LO modes is given as

$$\hat{a} \to \frac{\hat{a} + \hat{b}}{\sqrt{2}} \tag{2.114}$$

$$b \to \frac{\hat{a} - \hat{b}}{\sqrt{2}}. \tag{2.115}$$

Next, we calculate the evolved photon-number difference operator as following

$$\begin{aligned} \hat{N}^{out}_{a} - \hat{N}^{out}_{b} &= \frac{(\hat{a} + \hat{b})^{\dagger}(\hat{a} + \hat{b}) - (\hat{a} - \hat{b})^{\dagger}(\hat{a} - \hat{b})}{2} \\ &= \hat{a}^{\dagger}\hat{b} + \hat{a}\hat{b}^{\dagger} \end{aligned} \tag{2.116}$$

Using Eq. (2.113) and Eq. (2.116) with $\rho^{in}_{ab} = \rho_a \otimes (|\beta_{LO}\rangle\langle\beta_{LO}|)_b$, we get

$$I_{-} \propto |\beta| \langle (\hat{a}e^{i\phi} + \hat{a}^{\dagger}e^{-i\phi}) \rangle_{\rho_a} \propto |\beta| \langle \hat{X}(\phi) \rangle_{\rho_a}, \tag{2.117}$$

where $\hat{X}(\phi) = (\hat{a}e^{-i\phi} + \hat{a}^{\dagger}e^{i\phi})/\sqrt{2}$ is the generalized quadrature of the signal mode. Note that we have used the fact that local oscillator being a coherent state can be described by a complex variable $\beta_{LO} = |\beta_{LO}|e^{i\phi}$, where ϕ is the phase of the LO. As a result from Eq. (2.117), one can see that the expectation value of the signal field quadrature has been amplified by the strong LO field which allows its detection by high quantum efficiency conventional photodiodes and standard electronics[4].

By varying the LO phases and taking enough measurements at different phases (typically order of 10^4), one can obtain the histograms for probability distributions $P(X(\phi))$ at each phase value. $P(X(\phi))$ is related to the quantum state given by density matrix, ρ and its Wigner function as

$$P(X(\phi)) = \mathrm{Tr}[\rho(|X(\phi)\rangle\langle X(\phi)|)] = \langle X(\phi)|\rho|X(\phi)\rangle \tag{2.118}$$

$$= \int W(Q\mathrm{cos}\phi - P\mathrm{sin}\phi, Q\mathrm{sin}\phi + P\mathrm{cos}\phi)dP \tag{2.119}$$

Note that at $\phi = 0$, $\hat{X}(\phi)$ is just the amplitude quadrature and $P(X(\phi = 0)) = \langle X(\phi = 0)|\rho|X(\phi = 0)\rangle = \langle Q|\rho|Q\rangle = |\psi(q)|^2 = \int W(Q, P)dP$, thereby resulting in the probability density of amplitude quadrature. Once $P(X(\phi))$'s are obtained, one can reconstruct the density matrix by using maximum-likelihood algorithms and Wigner function using inverse Radon transforms [110], [111]. Moreover, a simple calculation shows that

$$P(X(\phi)) = \frac{e^{-X(\phi)^2}}{\sqrt{\pi}} \sum_{n=0} \sum_{m=0} \frac{\rho_{n,m}}{\sqrt{2^{n+m}n!m!}} e^{i(n-m)\phi} H_n(X(\phi))H_m(X(\phi)). \tag{2.120}$$

Here, we have used the fock space representation of the generalized quadrature eigenstate given as

$$|X(\phi)\rangle = \frac{e^{-X(\phi)^2}}{\pi^{1/4}} \sum_{n=0} c_{n,\phi}|n\rangle, \tag{2.121}$$

where $c_{n,\phi} = e^{in\phi}H_n(X(\phi))/\sqrt{2^n n!}$ and $H_n(X(\phi))$ is the Hermite polynomial of degree n. From Eq. (2.120), one can obtain the density matrix of the unknown state by simply inverting it. It is worth mentioning that a BHD device implements the generalized measurement operators, $\{|\hat{X}(\phi)\rangle\langle\hat{X}(\phi)|, X(\phi) \in \mathbb{R}\}$ as seen in Eq. (2.118). Note that the probability distributions for Gaussian states are Gaussian distributions,

[4]Here, by conventional photodiodes we mean photodiodes with no single-photon detection capabilities.

which is why quadrature measurements using BHD are known as Gaussian measurements [101].

Recently, there has been significant interest in homodyne-like (HL) schemes, where the actual photon-number difference distribution is measured in place of macroscopic photocurrent differences. It has been proven and experimentally demonstrated that the pattern function technique, originally developed for macroscopic photocurrents [111], can also be applied to a HL scheme where the LO intensity is comparable to the quantum state under investigation [112]. The HL scheme can be tuned to the BHD method as one increases the amplitude of the LO to the regime where it can be treated as a classical field [87]. Although the pattern functions or inverse Radon transforms can be calculated using numerically efficient algorithms [111], they are prone to instabilities leading to nonphysical reconstructions in the presence of noise and low detection efficiencies [113]. To avoid the nonphysical reconstructions, many methods based on maximum-likelihood (MaxLik) algorithms have been proposed [113]. Here, the goal is to find a physical density matrix which maximizes a likelihood function and is consistent with the measured probability distributions. The MaxLik ensures the physicality of the reconstructed density matrix and the non-unity detection efficiencies can be directly incorporated. However, the MaxLik algorithm converges slowly in general and may even fail if the detectors have low quantum efficiency [85]. It is well understood that maximum likelihood (MaxLik) algorithm is optimal only with informationally complete measurements [114]. Therefore, due to the informationally incompleteness of the tomographic measurements for CV systems, there may be many positive density matrices which are all equally likely. In this case, the estimated quantum state might not be the true state. Therefore, it is desired to develop QST methods which require minimal postprocessing of the data and leads to a physical reconstruction of the true state.

2.7.2 State characterization using PNR measurements

A more direct approach to reconstruct the Wigner function without any heavy numerical post-processing was proposed by Wallentowitz and Vogel [1] and by Banaszek and Wódkiewicz [2], which we call WVBW scheme throughout this thesis. The proposed method employs photon-number-resolving (PNR) measurement as opposed to the quadrature measurements in BHD. In chapter 3, we demonstrate the WVBW scheme method for a single-photon Fock state. In chapter 4, we propose a generalization of the WVBW scheme and experimentally demonstrate it for a weak coherent state and a single-photon Fock state.

Chapter 3

Quantum State Tomography by Photon-number-resolving Measurements

> It doesn't matter how beautiful your theory is, it doesn't matter how smart you are. If it doesn't agree with experiment, it's wrong.
>
> Richard P. Feynman

In this work, we directly reconstruct the Wigner quasiprobability distribution of a narrowband single-photon state by quantum state tomography using photon-number-resolving measurements with transition-edge sensors (TES) at system efficiency of 58(2)%. Our method is state-independent as we make no assumptions on the nature of the measured state, although a limitation on photon flux is imposed by the TES' saturation threshold. We observe the negativity of the Wigner function in the raw data without any inference or correction for decoherence. We also include a discussion on characterizing a multi-mode quantum state using this scheme.

This chapter is mostly based on the published paper titled, “State-independent quantum tomography of a single-photon state by photon-number-resolving measurements,” Rajveer Nehra, Aye Win, Miller Eaton, Niranjan Sridhar, Reihaneh Shahrokhshahi, Thomas Gerrits, Adriana Lita, Sae Woo Nam, and Olivier Pfister, Optica, 6(10), pp.1356-1360.

3.1 Introduction

Single and multiphoton sources prepared in Fock states are of fundamental importance: not only do they enable experiments that epitomize the wave-particle “duality” of quantum mechanics, they also can only be described by quantum theory due to the non-positivity of their Wigner quasi-probability distribution [111], [115]. This acquires major significance in the context of quantum information and quantum computing over continuous variables (CVQC) [116], [117] as it is well known that all-Gaussian- (gates and states) CV quantum information suffers from no-go theorems for Bell inequality violation [77], entanglement distillation [81], and quantum error correction [80]. However, none of these no-go theorems apply to CVQC when including non-Gaussian states or gates [118]–[120]. Non-Gaussian resources are therefore essential to CVQC and can be implemented, for example, by Fock-state generation or detection [121]. It is therefore important to be able to characterize Fock states fully and efficiently, possibly in real time. One standard method of state tomography is Wigner function reconstruction. Quantum state tomography in phase space [109] can be performed by reconstructing the Wigner function from the measurement statistics of the generalized quadrature $Q\cos\phi + P\sin\phi$, measured by balanced homodyne detection (BHD) where phase ϕ is the tomographic angle (see section 2.7.1). This was first done for heralded single photon states in 2001 [122] and recently improved [123]. As discussed in chapter 2, an issue with BHD-based tomography is that the reconstruction process is computationally intensive, using the inverse Radon transform, or maximum likelihood algorithms [110]. A more direct approach to reconstruct the Wigner function was proposed by Wallentowitz and Vogel [1] and by Banaszek and Wodkiewicz [2]. It is based on the following expression of the Wigner function [124]

$$W_{\hat{\rho}}(\alpha) = \frac{1}{\pi}\mathrm{Tr}[\hat{\rho}\hat{D}(\alpha)(-1)^{\hat{N}}\hat{D}^{\dagger}(\alpha)], \tag{3.1}$$

where $\alpha = (q+ip)/\sqrt{2}$, $\hat{D}(\alpha) = \exp(\alpha\hat{a}^{\dagger} - \alpha^{*}\hat{a})$ is the displacement operator, and $\hat{N} = \hat{a}^{\dagger}\hat{a}$ is the number operator. Equation (3.1) reveals that the Wigner function at a particular phase space point α is the expectation value of the displaced parity operator $\hat{D}(-1)^{\hat{N}}\hat{D}^{\dagger}$ over $\hat{\rho}$ or, equivalently, the expectation value of the parity operator $(-1)^{N}$ over the displaced density operator $\hat{D}^{\dagger}\hat{\rho}\hat{D}$. This provides a direct measurement method given that one has access to photon-number-resolving (PNR) measurements. In particular, the value of the Wigner function at the origin is the expectation value of the photon number parity operator

$$W(0) = \frac{1}{\pi}\sum_{n}^{\infty}(-1)^{n}\rho_{nn}. \tag{3.2}$$

Hence, the PNR detection statistics of a quantum system of density operator $\hat{\rho}$ yields a direct determination of the Wigner function at the origin. In order to recover the Wigner function at all points, one can simply displace $\hat{\rho}$ by the amplitude α. This can be done by interference at a highly unbalanced beamsplitter [125] of transmission to refelection coefficient ratio $t/r \ll 1$, as depicted in Fig.3.1. This technique is commonplace in quantum optics and was used, for example, to implement Bob's CV unitary in the first unconditional quantum teleportation experiment [126]. In all rigor, the resulting Wigner function is a more general one, the s-ordered Wigner function, $W(s\alpha; s)$, which tends toward $W(\alpha)$ when $s = -t/r \to 0$ [127]. This method

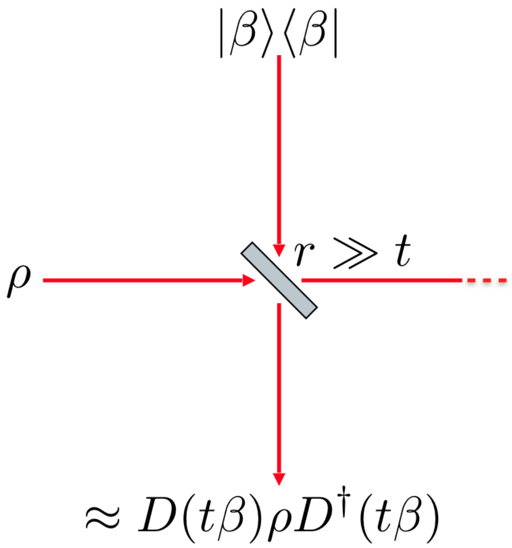

Figure 3.1: Implementation of a displacement by a beamsplitter. The initial coherent state amplitude is β with $|\beta| \gg 1$, so that we can have $t \ll 1$ in order to preserve the purity of the quantum signal $\hat{\rho}$, while still retaining a large enough value of $|\alpha| = t|\beta|$, as needed for the raster scan of the Wigner function in phase space.

was implemented for quantum state tomography of phonon Fock states of a vibrating ion [128], as well as microwave photon states in cavity QED [129], [130]. For quantum states of light, it has been experimentally realized for the positive Wigner functions of vacuum and coherent states, as well as phase-diffused coherent-state mixtures, initially detecting no more than one photon [131] and subsequently detecting several photons [132], [133]. The nonpositive Wigner function of a single-photon state was reconstructed using PNR measurements by time-multiplexing non-PNR, low efficiency avalanche photodiodes, albeit using *a priori* knowledge of the input state in order to deconvolve the effect of losses [66].

This work is the first demonstration of state-independent photon-counting quantum state tomography of a non-positive Wigner function. The only assumption made here is that the initial quantum state consists of low photon numbers to avoid the saturation limit of the detector, which is less than five photons per microseconds for the superconducting Transition-Edge Sensor (TES) used in our experiment. Since no other prior knowledge is assumed about the state to be measured, this technique is equally applicable to any arbitrary quantum state with low photon flux. We directly observe negativity of the Wigner function with no correction for detector inefficiency.

3.2 Experimental setup and methods

3.2.1 Cavity-enhanced narrowband heralded single-photon source

3.2.1.1 General model

Our single photon source is based on type-II spontaneous parametric downconversion (SPDC) in a periodically poled $KTiOPO_4$ (PPKTP) crystal. A pump photon at frequency ω_p is downconverted into a cross-polarized signal-idler photon pair at $\omega_{s,i}$, such that energy $\omega_p = \omega_s + \omega_i$ and momentum $\vec{k}_p = \vec{k}_s + \vec{k}_i$ are conserved as shown in Fig. 3.2, and the presence of the signal photon is heralded by detecting the idler photon [122]. All tomographic measurements were therefore conditioned on the detection of an idler photon. The SPDC Hamiltonian is given by [134], [135]

$$H \propto i\hbar\chi^{(2)} \int d^3\vec{r}\; E_p^{(-)}(\vec{r},t)E_i^{(+)}(\vec{r},t)E_s^{(+)}(\vec{r},t) + H.c. \tag{3.3}$$

where $\chi^{(2)}$ is the crystal's second-order nonlinearity and the fields in the Heisenberg picture take the form,

$$\begin{aligned} E^{(-)}_{j=p,s,i}(\vec{r},t) &= E^{(+)}(\vec{r},t)^\dagger \\ &= \int d\omega_j\; A(\vec{r},\omega_j)\,\hat{a}_j\, e^{i[k_j(\omega_j)r-\omega_j t]}, \end{aligned} \tag{3.4}$$

where $A(\vec{r},\omega_j)$ is an approximately slowly varying amplitude and $\hat{a}_j$ is the annihilation operator for the mode of frequency ω_j. Solving for the state under the evolution of the Hamiltonian in Eq. (3.3) for low parametric gain regime and a non-depleted classical

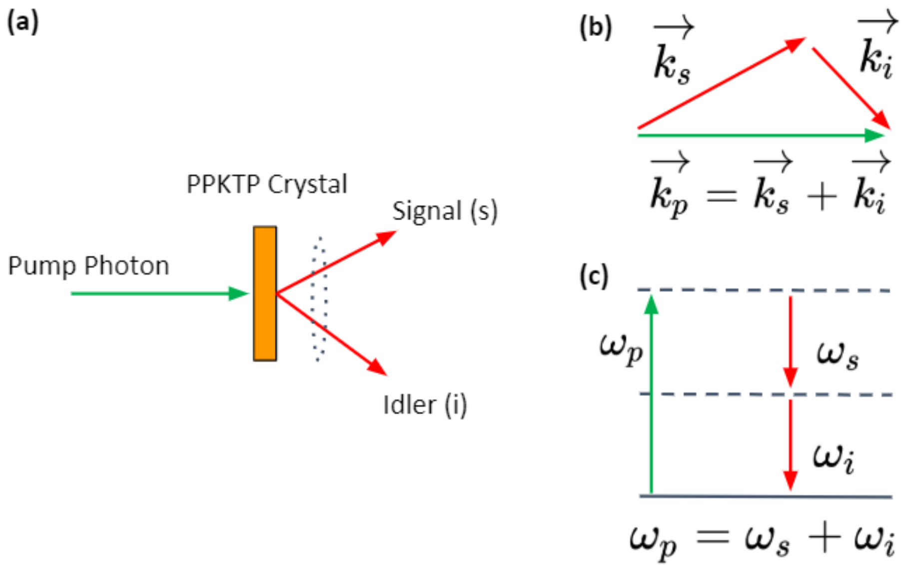

Figure 3.2: (a). Schematic of SPDC process. A higher energy photon interacts with PPKTP crystal and gets downconverted to signal and idler photon pairs. (b) displays the phase matching condition, where $\vec{k}_p(\vec{k}_s, \vec{k}_i)$ are wavevectors for pump (signal, idler) fields. (c) shows energy conservation during the process with ω_p being the pump frequency and $\omega_s(\omega_i)$ are signal (idler) frequencies.

pump yields the output quantum state

$$|\psi\rangle = \int d^3\vec{k}_{s,i}\, d\omega_{s,i}\, \phi(\vec{k}_s, \omega_s, \vec{k}_i, \omega_i)\, \hat{a}_s^\dagger \hat{a}_i^\dagger \,|\,0\,\rangle_s \,|\,0\,\rangle_i \tag{3.5}$$

where $\phi(\vec{k}_s, \omega_s, \vec{k}_i, \omega_i)$ determines the spectral and spatial properties of the SPDC, depending on the pump field and the non-linear crystal (phase matching bandwidth around $\vec{k}_p = \vec{k}_s + \vec{k}_i$). Note that, in a PPKTP crystal, collinear phasematching is used. We can see from Eq. (3.5) that the signal and idler photon pairs are emitted in a multitude of spatial and spectral modes. Therefore, any measurement on a particular idler mode will collapse the quantum state given by Eq. (3.5) to a mixture of signal-mode states. As a result, the heralded signal state will not be a pure quantum state, which limits its applications in quantum information processing [136], [137]. This is because a nonzero vector phase-mismatch can lead to a detected, heralding idler photon with a "twin" signal photon completely out of alignment and therefore undetectable, even in the absence of losses, which greatly diminishes the experimentally accessible quantum correlations. One therefore needs to emit photon pairs in the well defined spatial and spectral modes which are optimally coupled to the detectors. This involves spectral and spatial filtering and has been widely studied both theoretically and experimentally [138]–[143]. Our spectral and spatial filtering steps are discussed in the next section.

3.2.1.2 Spectral and spatial filtering

A detailed discussion on our cavity-enhanced single-photon source can be found in Reihaneh Shahrokhshahi's thesis from Professor Olivier Pfister's group at the University of Virginia, Charlottesville. Here, we summarize all the essential steps. Spectral and spatial filtering was achieved by using optical resonators: both actively, by placing the nonlinear crystal in a resonant cavity — thereby building an optical parametric oscillator (OPO) — and passively, by using a filtering cavity (FC) and an interference filter (IF) after the OPO. The OPO was used in the well-below-threshold optical parametric amplifier (OPA) regime. The OPO cavity enhanced the SPDC at doubly resonant (signal and idler) frequencies by a factor of the square of the cavity finesse [144]. However, this enhancement was still masked by the "sea" of nonresonant SPDC photons until we filtered the idler with a short FC, which selected only one OPO mode, and with an IF, which selected only one of the FC modes. After filtering, we are allowed to consider the simpler OPA Hamiltonian

$$H = i\hbar\kappa\, \hat{a}_s^\dagger \hat{a}_i^\dagger + H.c., \tag{3.6}$$

where κ is the product of the pump amplitude and $\chi^{(2)}$. This yields the well-known two-mode squeezed state

$$|\psi\rangle = (1-\zeta^2)^{\frac{1}{2}} \sum_{n=0}^{\infty} \zeta^n |n\rangle_s |n\rangle_i, \tag{3.7}$$

where $\zeta = \tanh(\kappa t)$. In the weak pump regime, both κt and $\zeta \ll 1$, and Eq. (3.7) can be approximated by

$$|\psi\rangle \simeq |0\rangle_s|0\rangle_i + \zeta|1\rangle_s|1\rangle_i + \mathcal{O}(\zeta^2) \tag{3.8}$$

A detection of a single photon in the idler mode thus projects the signal mode into a single-photon state. Note that, since the heralding process consists in postselection of the idler channel, filtering losses in this channel are unimportant. Indeed, if the pump power is kept low enough that practically no pairs from different modes ever overlap in time, one can then reasonably claim that the detected, the heralded signal photon will be the twin of the filtered, heralding idler photon, as per Eq. (3.8). It is important to also note that the situation will change if one seeks to herald a multi-photon state by using PNR detection for heralding, as per Eq. (3.7). In that case, losses in the heralding channel cannot be tolerated as they will lead to errors. We investigate it next.

3.2.1.3 A generalized model for heralded state generation

We now understand how an imperfect PNR detector used in idler (heralding) path and optical losses in the signal (heralded) path play a role in the heralded state generation. From Equation (3.7), the density matrix of the two-mode squeezed vacuum state is

$$\rho = \sum_{n,n'}^{\infty} c_{n,n} c^*_{n',n'} |n, n\rangle\langle n', n'|, \tag{3.9}$$

where $c_{n,n} = (1 - \zeta^2)^{\frac{1}{2}} \zeta^n$. For a perfect PNR detector in the heralding path and no losses in the heralded path, the probability of heralding a k-photon Fock state can be determined by the Born rule

$$p(k) = \mathrm{Tr}[\rho(\mathbb{I}_s \otimes |k\rangle\langle k|_i)] = |c_{k,k}|^2. \tag{3.10}$$

Let's consider an imperfect heralding PNR detector with detection efficiency, η_i. The POVM element corresponding to k photons detection is given by

$$M_k = \sum_{k=m}^{\infty} p(k|m)|m\rangle\langle m|, \tag{3.11}$$

where $p(k|m) = \binom{m}{k}\eta_i^k(1-\eta_i)^{m-k}$ is the conditional probability of detecting k photons given m photons are incident to the PNR detector. Using Eq. (3.9) and Eq. (3.11), the probability of heralding k-photon Fock state is then

$$p(k) = \mathrm{Tr}[\rho(\mathbb{I}_s \otimes M_{k,i}] = \sum_{l=k}^{\infty} |c_{l,l}|^2 p(k|l) \tag{3.12}$$

The heralded state is

$$\rho_k = \frac{\mathrm{Tr}_i[\rho(\mathbb{I}_s \otimes M_{k,i})]}{\mathrm{Tr}[\rho(\mathbb{I}_s \otimes M_{k,i})]}. \tag{3.13}$$

Further simplification leads to

$$\rho_k = \frac{\sum_{l=k}^{\infty}|c_{l,l}|^2 p(k|l)|l\rangle\langle l|}{\sum_{l=k}^{\infty}|c_{l,l}|^2 p(k|l)}. \tag{3.14}$$

From Eq. (3.14), we see that an imperfect PNR detector projects the TMSV on to a statistical mixture. Therefore, it is crucial to have a PNR detector with high quantum efficiency in heralding experiments for state preparation. It is worth mentioning that for a perfect PNR detector, i.e., $\eta_i = 1$, the POVM element is a pure projective measurement as in Eq. (3.11). Consequently, the heralded state in Eq. (3.14) has zero conditional probabilities, $p(k|l)$ for all $l \neq k$, thereby leading to a heralded pure state, $\rho_k = |k\rangle\langle k|$.

Next, we consider the losses in the heralded path modeled by adding a fictitious beamsplitter of transmission η_s and reflection $1-\eta_s$. The heralded state is described by $\hat{a}$ and the other unused port of beamsplitter has vacuum mode represented by

$\hat{b}$. We adopt the Heisenberg picture to find out the two-mode output state after the fictitious beamsplitter. Mathematically,

$$\rho_{\text{out}}^{a,b} = \hat{U}_{BS}(\rho_k \otimes |0_b\rangle\langle 0_b|)\hat{U}_{BS}^{\dagger}. \tag{3.15}$$

By employing the Heisenberg picture evolution of operators $\hat{a}$ and $\hat{b}$, we have

$$\rho_{\text{out}}^{a,b} = \frac{1}{\mathcal{N}}\sum_{l=k}^{\infty}|c_{l,l}|^2 p(k|l)(\sqrt{\eta_s}\hat{a}^{\dagger} + \sqrt{1-\eta_s}\hat{b}^{\dagger})^l|0_a, 0_b\rangle\langle 0_a, 0_b|(\sqrt{\eta_s}\hat{a} + \sqrt{1-\eta_s}\hat{b})^l, \tag{3.16}$$

where $\mathcal{N} = \sum_{l=k}^{\infty}|c_{l,l}|^2 p(k|l)$. We are interested in finding the quantum state in mode $\hat{a}$. A further simplification of Eq. (3.16) after tracing out mode $\hat{b}$ leads to

$$\rho_{\text{heralded}} = \frac{1}{\mathcal{N}}\sum_{l=k}^{\infty}|c_{l,l}|^2 p(k|l)\sum_{m=0}^{l}\binom{l}{m}^2 \eta_s^{l-m}(1-\eta_s)^m m!(l-m)!|l-m\rangle\langle l-m|, \tag{3.17}$$

Thus Eq. (3.17) describes the heralded state in the most general case[1]. For a heralded single-photon Fock state, i.e., $k = 1$, and in the weak pump regime when $l = k = 1$ mostly contributes to the sum in Eq. (3.17), we get

$$\rho_{\text{heralded}} = (1-\eta_s)|0\rangle\langle 0| + \eta_s|1\rangle\langle 1|. \tag{3.18}$$

As a result, the heralded state is a statistical mixture of vacuum and a single-photon Fock state. It is worth pointing out that as long as the pump power is kept low such that Eq. (3.8) holds true, the detector efficiency or losses in the heralding (idler) path do not matter for heralding a single-photon Fock state. Note that this would not hold true for heralding a multiphoton Fock state, for instance two-photon Fock state, as we can see that from the presence of η_i dependence in $p(k|l)$, as per Eq. (3.17).

[1]Note that we have not considered the effect due to detector dark-count noise on heralded state preparation, only non-ideal quantum efficiency is considered. This assumption is reasonable when heralding is done using superconducting transition-edge sensor because these detectors have negligible dark-count noise.

Although, one can suppress the effects of an imperfect heralding PNR detector by setting up the pump power in such a way that the contribution due to $n > 2$ in Eq. (3.7) is negligible but it then reduces the two-photon emission. Therefore, it is desirable to have to high efficiency PNR detector in order to generate a two-photon Fock state at high rate.

Additionally, as the pump power increases the summand in Eq. (3.17) would have contribution from $l > k$ terms, i.e., a heralded single-photon state results in a statistical mixture of higher Fock components. Therefore, it is desired to keep the pump power way-below OPO threshold.

In the experiment, a significant contribution to photon loss in the heralding path is due to the mode mismatch between the OPO and the filter cavity (FC), which must also be locked on resonance simultaneously, as detailed in the next section. By careful modematching of a seed OPO beam to the FC, we were able to achieve 83% transmission of the OPO mode through the FC. This was achieved by using the setup displayed in Fig 3.3. We seed the OPO through the highly reflective (99.995%) mirror and its transmission through the OPO output coupler was divided into two parts using a PBS. The first part (dashed line) was used to lock the OPO using PDH locking loop and the second part was guided to the FC. We further carefully aligned the optics in order to optimize the FC transmission for pure TEM_{00} mode. To quantify the modematching of the OPO and FC, we first measured the power before the FC and then the power after the FC was measured while keeping the FC locked by manually tuning the Servo fine gain.

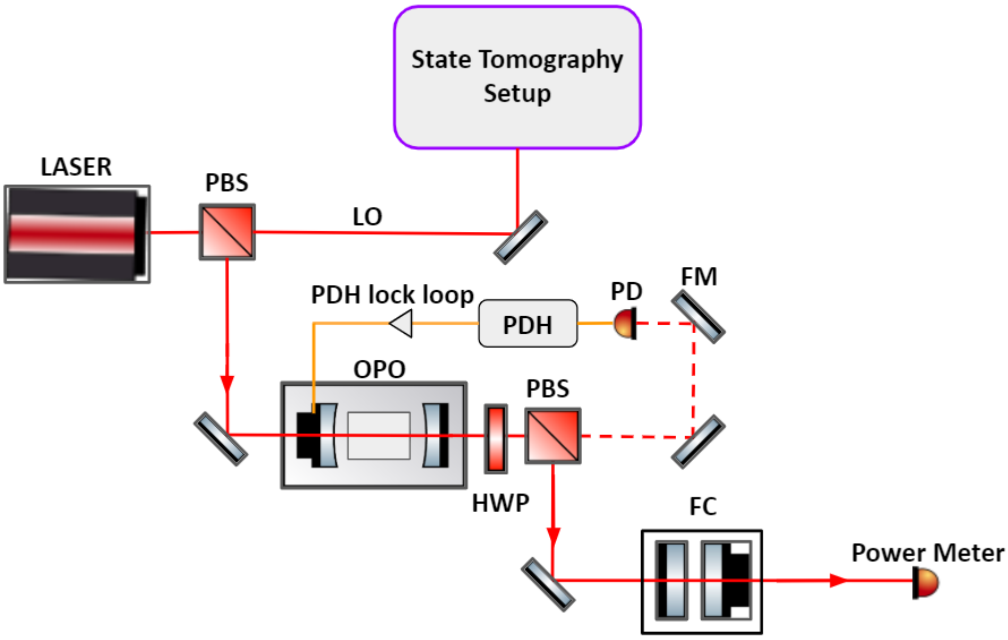

Figure 3.3: Experimental setup for optimizing the modematching of OPO beam to the FC.

3.2.2 Experimental setup for quantum tomography

3.2.2.1 Setup description

The experiment, depicted in Fig.3.4, built upon our previous demonstration of coherent-state tomography [133] with the addition of the heralded single-photon source. The OPO was pumped by a stable frequency-doubled 532 nm Nd:YAG nonplanar ring oscillator laser (1 kHz FWHM). A type-II (YZY) quasi-phasematched PPKTP crystal, of period 450 μm, was used in the doubly resonant OPO. The two-mirror OPO cavity, as mentioned above, was one-ended, with a finesse of F $\simeq$ 300, an FSR of 1.5 GHz and a FWHM of 5 MHz. One mirror's inside facet was 99.995% reflective for the signal and idler fields near 1064 nm and 98% transmissive for the pump field at 532 nm (the outside mirror facet was uncoated); the other mirror's inside facet was 98% reflective at 1064 nm and 99.95% reflective at 532 nm (its outside facet was antireflection

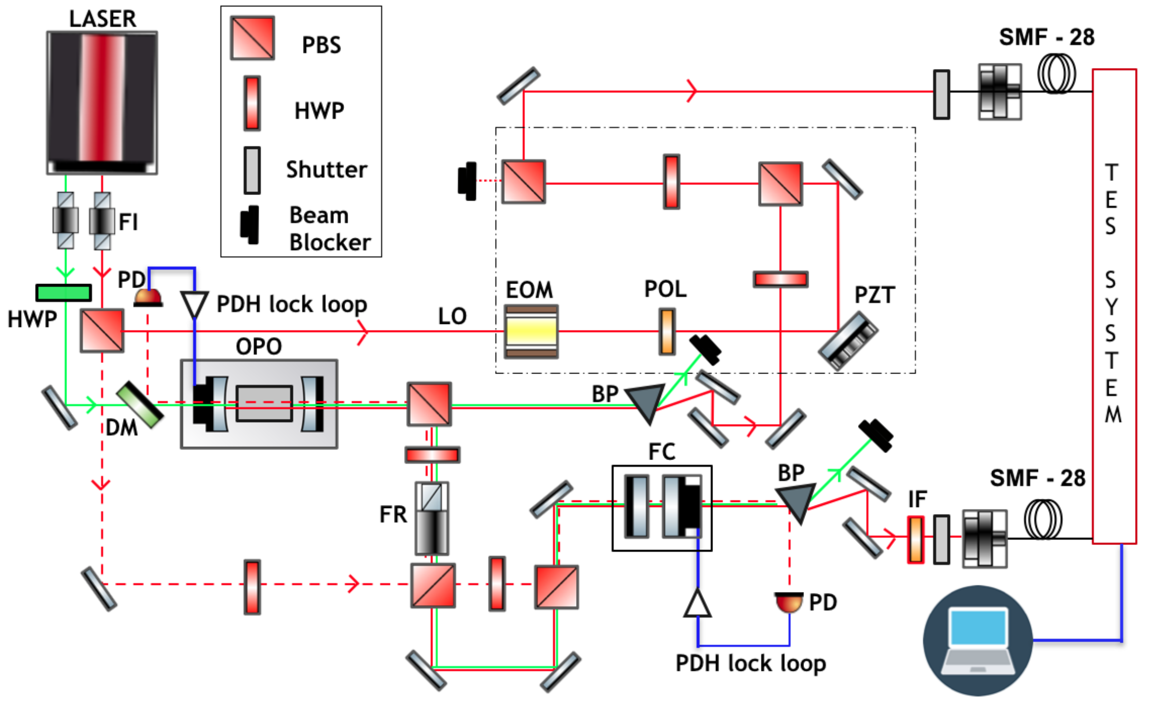

Figure 3.4: Experimental setup. The red dotted lines denote the locking beam paths for the on/off Pound-Drever-Hall (PDH) servo loops of the OPO and the FC. The displacement operation is contained in the black dash-dotted box at the top. BP: Brewster prism. DM: Dichroic Mirror. EOM: Electro-optic modulator. FI : Faraday Isolator. FR: Faraday Rotator. HWP: Half-wave plate. IF : Interference Filter. LO: Local Oscillator input to the displacement field. PBS: Polarizing Beamsplitter. PD: Photodiode. POL: Polarizer. PZT: Piezoelectric transducer.

coated at 1064 nm). The cavity was near-concentric with a super-Invar structure, the mirrors' radius of curvature being 5 cm and the mirrors $\simeq$10 cm apart. The FC was made of two 5 cm-curvature, 99% reflective mirrors placed $\simeq$0.5 mm apart. The OPO mode was aligned and mode-matched to all parts of the experiment (FC, TES fibers) by using a seed beam which was injected into the OPO through its highly (99.995%) reflecting mirror and exited through its output coupler. The seed beam was carefully mode-matched to the OPO so as to be a pure TEM_{00} mode before being sent to the rest of the setup. The seed beam set up is displayed in Fig 3.5. We guide a part of OPO seed transmission (dashed-line) to the FC PDH locking photodiode which provides the error signal used to lock the OPO to a pure TEM_{00} mode. Note that the OPO is still being PDH locked by its own Vescent Servos, a key difference here is

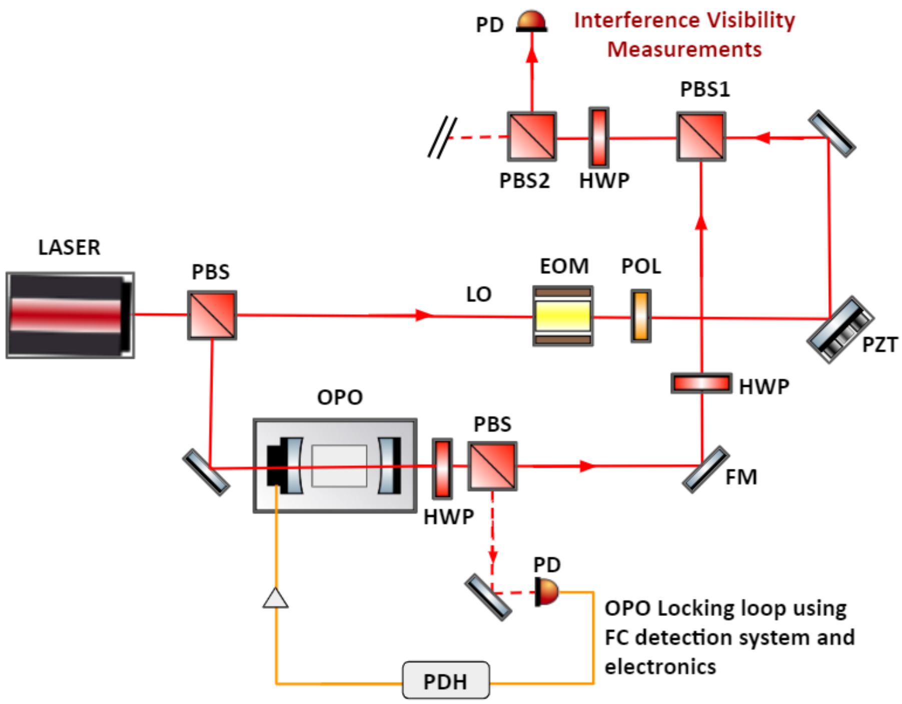

Figure 3.5: Experimental setup for optimizing the modematching the LO field to single-photon field.

that the locking signal is being provided by the photodiode which is originally used for the FC PDH locking. Once the OPO is locked, we guide the other bright part of the seed beam to interfere with the LO. Both the LO and the OPO seed beam transmission are matched spatially at the first PBS1, and then their polarization are mixed using the HWP. We then optimize the free-space visibility of their interference at one of the ports of the PBS2 before coupling it to SMF-28. Further, it was also used for optimizing the fiber coupling.

3.2.2.2 Stabilization procedure

Both the OPO and the FC cavities were Pound-Drever-Hall (PDH) locked [145] to a reference laser beam provided by the undoubled output of the pump laser.

3.2.2.3 PDH locking

This was achieved by an "on/off" locking system, effected by a system of computer-controlled diaphragm shutters. In the "on" locking phase, the input to the single-photon sensitive PNR detectors was closed and the reference laser was unblocked and sent into both the OPO and the FC (dotted lines in Fig.3.4) whose PDH lock loops were closed for a few seconds. Because of its super-Invar structure, the OPO drift was low and the PDH loops could then be open, in the "off" phase, with their correction signals held constant. The shutter of the reference laser was closed and the paths between the OPO and the PNR detectors were open for data acquisition, for as long as 3 seconds, see Fig.3.6. This procedure allowed us to lock the OPO to its doubly

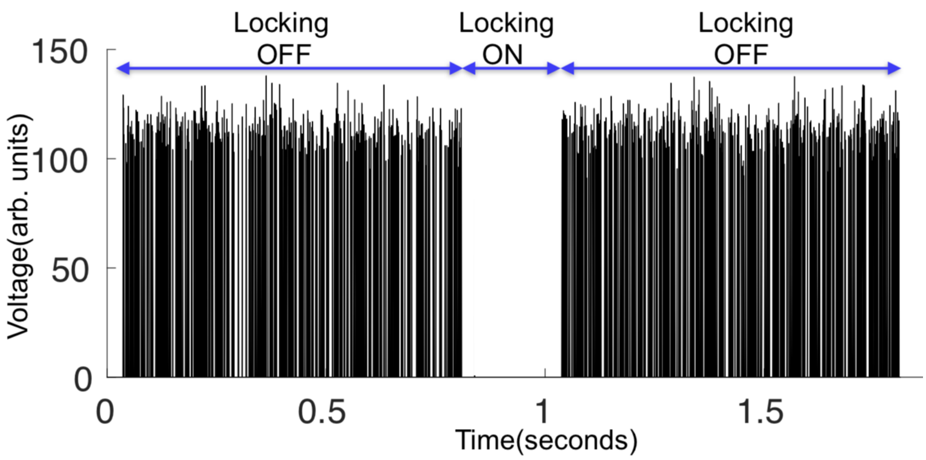

Figure 3.6: On/off cycles of alternated active locking and data acquisition. Data collection begins for a period of 800ms while the auxiliary locking beam is blocked, followed by a period of 200ms where the auxiliary locking (broken red line in the experiment schematic) is enabled for active locking and the signal channel is blocked. This process occurs cyclically during data collection to prevent excess photon flux from damaging the TES while ensuring a stable OPO cavity mode.

resonant, frequency degenerate mode at $\omega_s = \omega_i = \omega_p/2$. This was essential as the displacement field, also provided by the undoubled output of the pump laser, had to be at the same frequency as the OPO's quantum signal beam and phase-coherent with it. Note that finding this frequency degenerate, doubly resonant OPO mode is nontrivial since the double resonance condition

$$\omega_s = \omega_i \tag{3.19}$$
$$\Leftrightarrow \frac{m_s}{L + n_s(T)\ell} = \frac{m_i}{L + n_i(T)\ell} \tag{3.20}$$

features two different indices of refraction $n_s \neq n_i$ (L is the cavity length in air only, ℓ the crystal length and $m_{s,i} \in \mathbb{N}$ are the mode numbers). It is, however, possible to temperature-tune the OPO crystal to achieve stable frequency degeneracy [146]–[148]. This required active temperature control of the PPKTP crystal to the level a few millidegrees, around 27.810° C, using a commercial wavelength electronics temperature controller.

3.2.2.4 PNR detection

Our PNR detection system is comprised of two transistion-edge sensors (TESs), consisting of tungsten chips in a cryostat, coupled through standard telecom fiber. A detailed description of the TES system can be found in Refs. [133], [149]. The TESs are cooled using an adiabatic demagnetization fridge at a stable temperature of 100 mK, at the bottom edge of the steep superconducting transition slope (resistance versus temperature) in Fig. 3.7(b). As seen in Fig. 3.7, when a photon is incident to the sensor, its energy is absorbed by the tungsten chip, yielding a sharp increase in its resistance which is detected as a pulse in the TES current by an inductively coupled SQUID amplifier over a rise time on the order of 100 ns. Due to linear behaviour of the resistance versus temperature a two-photon absorption causes a larger temperature change which produces a larger signal than a single-photon absorption, thereby allowing photon-number resolution measurements in the superconducting regime.

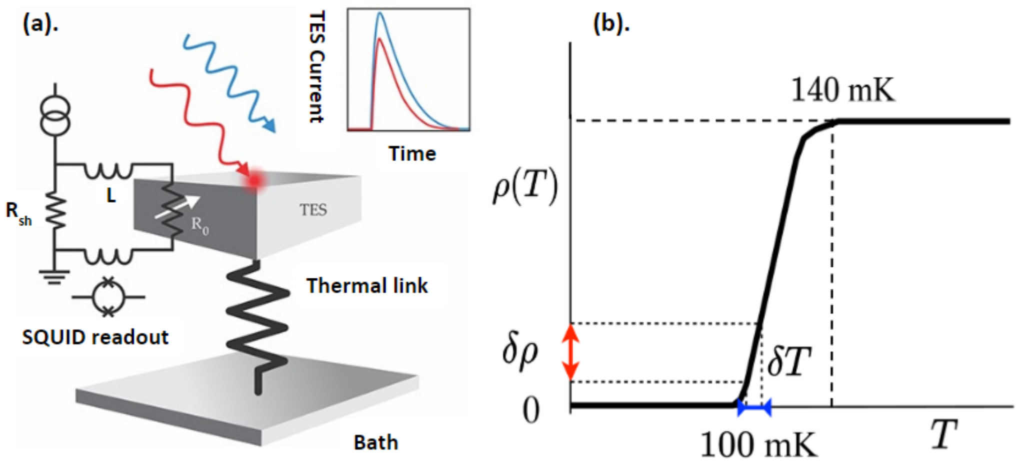

Figure 3.7: (a) Taken from Ref. [3], when a photon is detected, its heat is then dissipated to the bath through a weak thermal link. The absorbed heat causes a sharp increase in its resistance which is detected as a pulse in the TES current by an inductively coupled SQUID amplifier. (b) Working principle of a transition-edge sensor consists of a tungsten thin film. The sensor operates in the superconducting temperature range of 100 mK –140 mK. In this regime, any small variation in temperature causes a large change in resistance.

The heat is then dissipated through a weak thermal link, over a time on the order of 1 μs. During this time, the TES is still active (as opposed to, say, of nanowire detectors or avalanche photodiodes). Due to the finiteness of its superconducting transition slope, the TES can resolve up to 5 photons. The absolute maximum photon flux sustainable by the TES without the tungsten driven into the normal conductive regime is therefore 5 photons/μs in the continuous-wave regime, i.e., a power of 1 pW. The OPO's average power was kept at 100 fW by setting the pump power to 200 μW (the OPO threshold was 200 mW). Once the lab lights were turned off and fiber couplers were covered by a black foil, we observed that the background counts were negligible when the TES signal was suppressed by rotating the pump's linear polarization by 90°, thereby completely phase-mismatching the nonlinear interaction in PPKTP.

3.2.2.5 Displacement calibration

Since we are probing the Wigner function point-by-point defined by the amplitude of the displacement field α, it is essential to know α. The displacement operator was implemented by interfering the OPO signal mode with a phase- and amplitude-modulated coherent-state displacement field at a highly unbalanced beamsplitter with a reflectivity $r^2 = 0.97$. The interference visibility between the seed OPO beam and the displacement field was 90%, which ensured a good mode overlap between the displacement field and single-photon field. The amplitude shift $|\alpha|$ was effected by a homemade, temperature-stabilized electro-optic modulator consisting in an X-cut, 20 mm-long rubidium titanyl arsenate ($RbTiOAsO_4$) crystal; the phase shift $\arg(\alpha)$ was effected by a piezoelectric transducer- (PZT) actuated mirror. Both the EOM and the PZT mirror were driven by homemade, low-noise, high voltage drivers, fed by computer-controlled Stanford Research Systems lock-in amplifiers. The amplitude displacement was varied in 20 steps from $|\alpha| = 0$ to $|\alpha_{\max}| = 0.796(7)$, fixed by the TES' photon flux limit of 5 photons/μs. The phase displacement was varied in 10 steps from 0 to 2π. The amplitude steps $|\alpha| = \sqrt{\eta}|\beta|$, where η is the overall detection efficiency, were directly calibrated by comparing the TES photon statistics to that of a Poisson distribution

$$P(n) = e^{-|\alpha|^2} \frac{|\alpha|^{2n}}{n!}, \tag{3.21}$$

with the OPO beam blocked. This allowed us to determine the displacement amplitude

$$|\alpha| = \left[\frac{2P(2)}{P(1)} \right]^{\frac{1}{2}}. \tag{3.22}$$

Note that this method requires the presence of 2-photon detection events, i.e., $|\alpha_{\min}| \simeq 0.15$ for the very first displacement amplitude, besides the zero displacement for which we blocked the displacement beam. Photon number statistics were averaged over 2 seconds to ensure an average calibration accuracy

$$\triangle|\alpha| = 3 \times 10^{-3} \tag{3.23}$$

of the displacement amplitude. However, the error on the maximum displacement was somewhat larger

$$\triangle|\alpha_{\text{max}}| = 7 \times 10^{-3}, \tag{3.24}$$

due to the photon pileups occurring at higher flux which make the continuous-wave TES signals harder to analyze. We observed the long-term power stability of the laser to be on the order of 1% over an hour. The laser's short-term intensity noise was much lower as ensured by a built-in "noise eater" intensity servo. Moreover, the temperature stability of the EOM was on the order of 1 mK. Because of all this, we consider the error $\triangle|\alpha|$ on the displacement calibration to be valid over the course of our data acquisition time of several minutes.

The phase steps were calibrated by scanning the interference fringe between the OPO seed beam and the displacement field, which provided a set of 10 voltage values for the PZT mirror. Experimental data runs were conducted by scanning the amplitude at fixed phases, with the phase PZT voltage being refreshed at every amplitude EOM voltage step. For each point of the quantum phase space, a continuous stream of data was acquired at 5 MS/s, digitized using an PCI board, and stored for subsequent photon statistical analysis. A detailed discussion of our data analysis of continuous-wave photon counting can be found in our previous paper and in Niranjan Sridhar's PhD thesis on coherent state tomography using PNR measurements [133]. Here, we detail the main steps of the TES data processing for continuous-wave (CW) fields. We first identified each detection event by finding rising edges in the TES signal using numerical differentiation. A rising edge is characterized as a detection event if it rises at least X% (typically 40-50%) of the average height of a single-photon detection event above the mean noise level. Note that this threshold depend on the

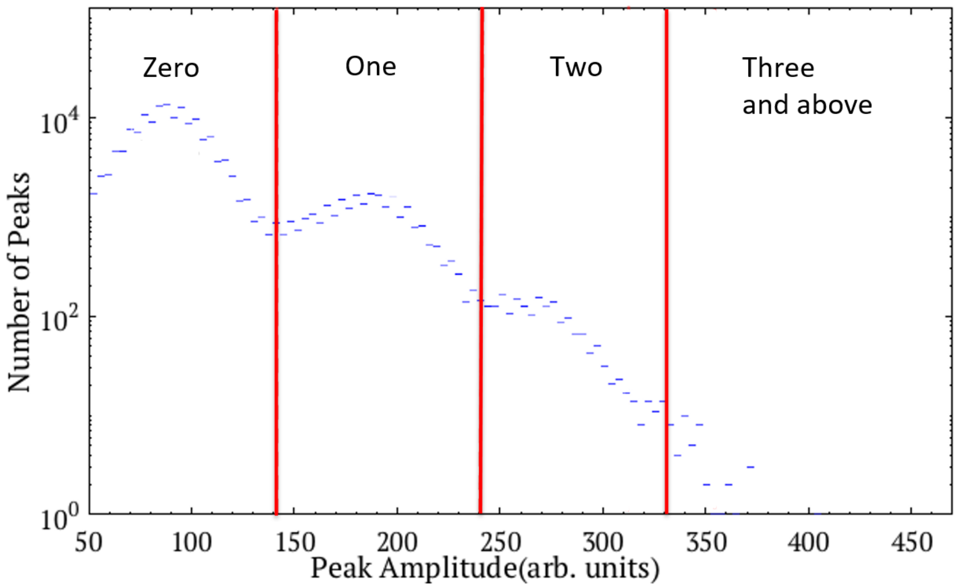

Figure 3.8: TES photon-number histogram when a weak monochromatic coherent state at 1064 nm is sent to the sensor. Each '-' represents a small bin.

TES temperature and SQUID biases and should be set in the calibration process. We then store the maximum signal in the $\approx 2\mu$s following each starting time and this maximum value is stored as well. As a result, the rising edge is comprised of about 10 sampling points each sampled at every 200 ns since the sampling speed is 5 MS/s. Although this method is general but the analysis here is dependent on the sampling speed. For instance, if the sampling was done at 10 MS/s, then each sampled point would be after every 100 ns. We then construct the histogram from the recorded maximum signal heights which is displayed in Fig. 3.8 where we can see a clear distinction for different photon-number events. Using the histogram, we can then define the photon-number quantization thresholds which are further used to characterize the photon-number events of the TES signal. It is worth mentioning that sometimes TES signal might be noisy due to bias not being set at the right value. In this case, smoothing the data might be beneficial using carefully designed Savitzky-Golay filter implemented in MATLAB in order to ensure that it does not distort the peak characteristics.

3.3 Experimental results

In this section, we characterize the quality of our single-photon source by measuring the heralding ratio, cross-correlation of signal and idler channels, and quantum mechanical second order coherence $g^{(2)}(0)$.

3.3.1 Heralding ratio

The heralding ratio is the probability of seeing one photon in the OPO signal (heralded) beam with no displacement field, provided one photon was detected in the filtered idler (heralding) beam. To measure the heralding ratio, we first identify the single-photon events in the TES trace for idler (heralding) channel and store the time stamps corresponding to detection events. We then look for single-photon events in the immediate vicinity of these time stamps in the signal (heralded channel) data to determine the coincidences. As a result, the ratio of coincidences and single-photon events in the idler channel gives the heralding ratio or heralding efficiency. Measured results are displayed in Table 3.1.

	N_s	N_i	N_c
Single-photon events	54320 ± 90	1556 ± 30	903 ± 17

Table 3.1: Experimentally measured number of single-photon counts on both channels. N_s: number of photons in the (heralded) signal channel, N_i: number of photons on the (heralding) idler channel, N_c: number of coincident counts.

The pump power was kept low enough to suppress two-photon events in the OPO signal in the absence of a displacement field. In Fig 3.9, we plot a small portion of the raw TES data traces for both heralded and heralding channel. Black dashed-ellipse correspond to degenerate single-photon pair events. We can see that the heralded channel has a lot more counts than the heralding channel, as expected since the latter is filtered by the FC and the IF.

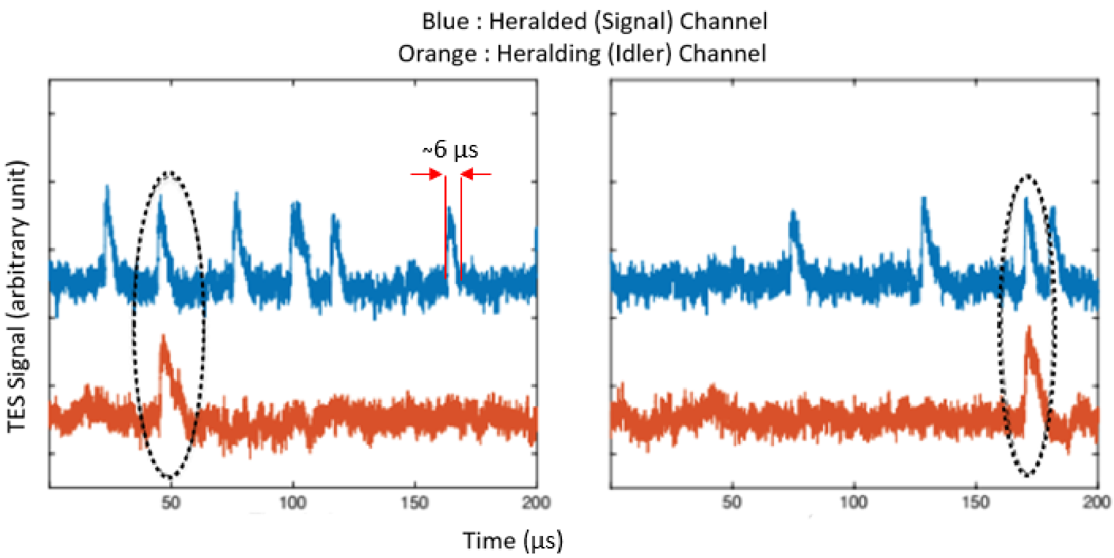

Figure 3.9: TES data traces for both heralded (blue) and heralding channel (organge). Dashed-ellipse contains the single-photon coincidences.

We then calculate the heralding efficiency defined as

$$\eta_s = \frac{N_c}{N_i} \tag{3.25}$$

$$= 0.58 \pm 0.02 \tag{3.26}$$

and can also be considered the overall detection efficiency, η_s of the heralded channel, i.e., of the quantum signal. Next, we determine the cross-correlation function between signal (heralded) and idler (heralding) channels, displayed in Fig. 3.10 [2] As one can see that correlation decays after a time delay of $\approx 6\mu s$, which is equivalent to the total length of a single-photon spike from the TES. This ensures that the correlation is absolutely due to the single-photon coincidences. Asymmetry and slight offset from zero time delay in the correlation function (C) might be attributed to the systematic delay between TES' channels and their inherent jitter of $\approx$ 100 ns.

[2]The MATLAB cross-correlation is: $C(s,i)[m] = \sum_{n=0}^{N-m-1} f_s(n+m)g_i(n)$.

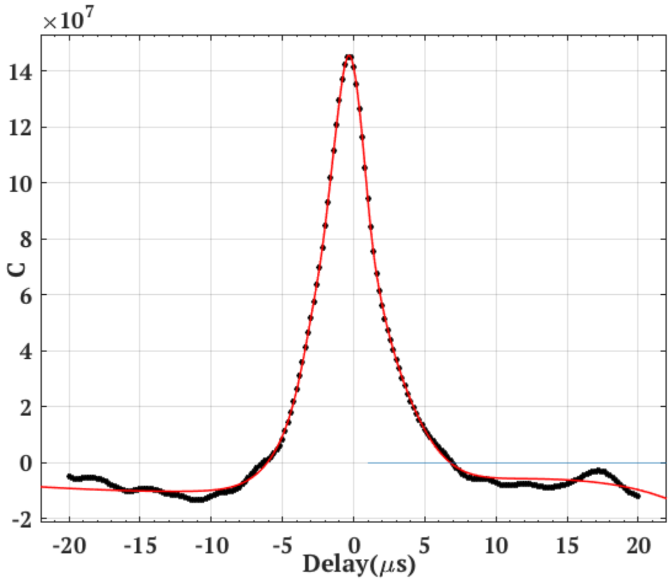

Figure 3.10: Correlation function between signal and idler channel. Black data points are at every 200 ns delay and red curve is a Gaussian fit.

We then calculate the quantum mechanical second order coherence of the heralded single-photon state, which is defined as

$$g^{(2)}(0) = \frac{\langle : \hat{n}^2 : \rangle}{\langle \hat{n} \rangle^2}, \tag{3.27}$$

where $:\hat{n}^2 := \hat{a}^{\dagger 2}\hat{a}^2$ is the normal ordering of the creation and annihilation operators. For a pure n-photon Fock state, $g^2(0)$ turned out to be

$$g^{(2)}(0) = \frac{\mathrm{Tr}[|n\rangle\langle n| : \hat{n}^2 :]}{\mathrm{Tr}[|n\rangle\langle n|\hat{n}]^2} = \frac{n(n-1)}{n^2} \tag{3.28}$$

From Eq. (3.28), one can see that for an ideal single-photon Fock state $|n = 1\rangle$, $g^{(2)}(0) = 0$. In general, nonclassical states of light have $0 \leq g^{(2)}(0) \leq 1$ which leads to photon antibunching effect [39]. On the other hand, classical states of light must have $g^{(2)}(0) \geq 1$ which is formally known as photon bunching. With finite heralding efficiency and optical losses present in the heralded path, the single-photon state in the low pump power regime can be approximated by using Eq. (3.17) as

$$\rho = p_0|0\rangle\langle 0| + p_1|1\rangle\langle 1| + p_2|2\rangle\langle 2| + \mathcal{O}(\zeta^4). \tag{3.29}$$

Using Eq. (3.28) and Eq. (3.29), $g^{(2)}(0)$ can be formulated as

$$g^{(2)}(0) = \frac{2p_2}{(p_1 + 2p_2)^2} \tag{3.30}$$

From Fig. 3.11, we see that the two-photon counts are extremely low, which results in a very low second-order coherence $g^{(2)}(0) = 0.07(5)$ determined using Eq. (3.30) .

3.3.2 Photon probability distributions versus displacement amplitude

Figure 3.11 displays the measured photon number distributions for a heralded single-photon input when $|\alpha| = 0$ (left) and 0.25 (right). For no displacement, the histogram reflects the exact same measurement as in Table 3.1 and Eq. (3.25), and the result yields a compatible value of 0.58(2). For $|\alpha| = 0.25$, the two-photon peak grows from the presence of the displacement field. In both cases, the observations agree with the theoretical distribution, calculated with $\eta = 0.58$. As expected, the single-photon component decreased while the vacuum and higher photon components increased. It can be thought of as follows: If we displace a pure single-photon state, then we obtain

$$\begin{aligned} D(\alpha)|1\rangle &= D(\alpha)a^\dagger D^\dagger(\alpha)|\alpha\rangle \\ &= a^\dagger|\alpha\rangle - \alpha^*|\alpha\rangle. \end{aligned}$$

Clearly, the first term has no vacuum component, as does the initial state $|1\rangle$, but the second term does have a vacuum component. Therefore, the displacement of a

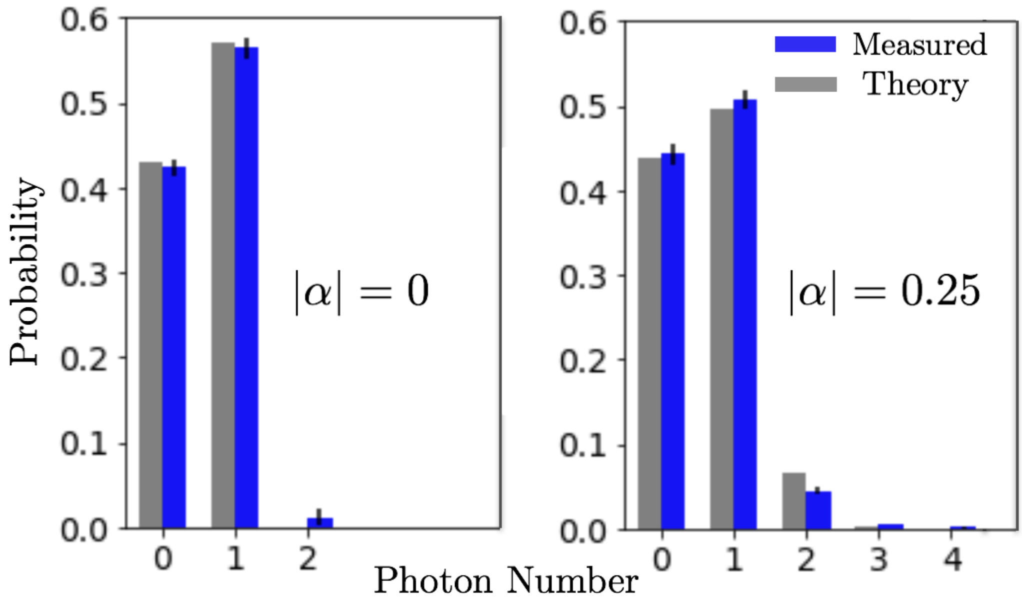

Figure 3.11: Measured photon-number distributions, left: $\alpha = 0$ and right : $|\alpha| = 0.25$. Error bars (1σ) are calculated from the statistics of the measurements.

single-photon state increases its vacuum component probability amplitude, somewhat unintuitively. In the case where our initial state is a mixture of vacuum and single-photon, then it can be seen that for low enough displacement amplitudes, the vacuum component still increases from its previous value. As the displacement becomes large, the vacuum component will eventually decrease. In Fig. 3.12, we display the TES data traces for both signal and idler channels in the presence of the displacement field of amplitude of $|\alpha| \approx 0.4$. We can see that in the weak-pump regime the single-photon (1γ) events in idler channel are most likely due to true single-photon detection, not because of a multiphoton state being detected as a single-photon due to losses in the idler path or non-ideal detection efficiency of the TES. The corresponding single-photon (1γ) and two-photon (2γ) events in the signal channel are then due to either displaced vacuum when the twin photon is lost or due to the displaced single-photon field.

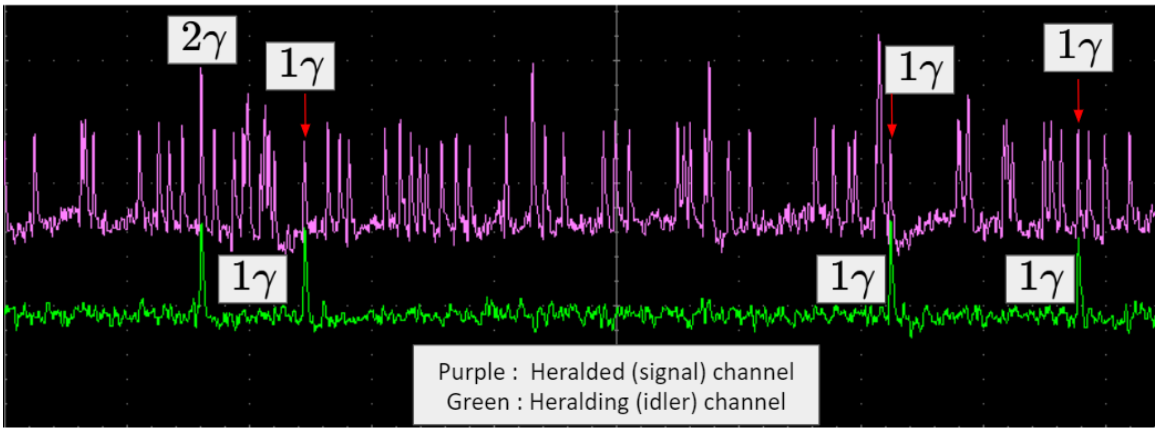

Figure 3.12: TES data traces for both heralded (purple) and heralding channel when displacement field was turned on. 1γ and 2γ are single-photon and two-photon events respectively.

3.3.3 Model Wigner function and loss analysis

Before we turn to the tomography results, we outline the Wigner function model that accounts for the aforementioned nonideal system detection efficiency. There are several sources of losses in our experiment: photon absorption and general scattering out of the mode due to mismatch. As mentioned above, losses in the heralding channel can be factored out in the generation of a heralded single-photon state provided that the OPO output never contains more than one photon per mode during the detection window, which was the case in this work.

It is also important to note that the TES fiber is single-mode at telecom wavelengths but not at our operating wavelength of 1064 nm. Hence we need to address the possibility of multimode coupling into the TES fiber. To quantify the multimode coupling, we introduce a parameter called normalized optical frequency or V-number of an optical fiber, which is defined at a given wavelength, λ and fiber core radius, a as following

$$V = \frac{2\pi a}{\lambda}\mathrm{NA}, \tag{3.31}$$

where NA is the numerical aperture which is related with the acceptable incident angle of θ_0 of the fiber as [150]

$$\mathrm{NA} = \sin\theta_0 = \sqrt{n_{\mathrm{core}}^2 - n_{\mathrm{clad}}^2}\ , \tag{3.32}$$

where n_{core} and n_{clad} are the refractive indexes of the fiber core and cladding respectively. The SMF-28e+ Corning fiber has NA = 0.14 and core radius a = 4.1 μm. Using these parameters in Eq. (3.31) at the optical telecommunication wavelength $\lambda = 1550$ nm, we get $V = 2.327$ which is below the cutoff V-number of $V_{\text{cut-off}} = 2.405$ for any fiber to be a single-mode fiber. In our experiment, the working wavelength for optical fibers is 1064 nm at which V-number turned out to be 3.389 which leads to a multimode coupling into the SMF-28e+. In order to further determine the approximate number of modes supported in an optical fiber, we use

$$N_{\mathrm{modes}} \approx \frac{V^2}{2} = 5.7426 \tag{3.33}$$

As a result, we see that SMF-28e+ roughly supports five modes. To minimize the coupling to higher modes, we optimized our fiber coupling to as high as 90% with the seed beam (discussed in the "spectral and spatial filtering" section above) and we also measured the intensity variations of about 1% at the output of the fiber. This ensures that most of the fiber coupling was to the fundamental mode of the fiber. Furthermore, a simple reasoning shows that this is not a matter of concern if there are no losses in the fiber. Indeed, the coupling of the input field into each of the different, orthogonal propagation modes of the fiber can be accurately described by as many beamsplitting operations into distinguishable outputs. While each of these beamsplitting operations does bring in vacuum fluctuations, all beamsplitter outputs are still detected and the final TES detection is simply that of the total photon number of all the fiber modes. In the absence of losses, the multimode fiber is a passive optical element which conserves the total photon number and the final total photon number measurement must therefore give the same exact result as the initial one, before the quantum light is coupled into the fiber. An argument could be made that fiber losses could be mode dependent, with higher-order modes being more likely to leak out of the fiber; we assume that this is negligible in our case because the operating wavelength was close enough to the specified single-mode wavelength that the mode order should not be that high.

We measured the coupling efficiency, η_{OFC}, into the TES fiber on the optical table by cleaving the fiber to insert a power meter and re-fusing it to the TES thereafter. However, we didn't measure the overall fiber transmission into the TES cryostat. This was bundled with the TES quantum efficiency in η_{TES}, which was inferred from all other measured efficiencies, as summarized in Table 3.2. We modeled losses by considering

η_{TES}	η_{OT}	η_{BS}	η_{OFC}	η_s
0.71(3)	0.93(1)	0.97(1)	0.90(2)	0.58(2)

Table 3.2: η_{TES}: TES quantum efficiency (including fiber transmissivity); η_{OT} : optical transmission of single-photon signal field from the OPO to the displacement operation; η_{OFC}: optical fiber coupling. The overall efficiency of the signal channel is $\eta_s = \eta_{\mathrm{TES}} \times \eta_{\mathrm{OT}} \times \eta_{\mathrm{BS}} \times \eta_{\mathrm{OFC}}$.

a fictitious beamsplitter of transmissivity η_s and reflectivity $(1-\eta_s)$, placed between the displacement and a detector of unity efficiency as shown in Fig.3.13. The input state of this system is

$$\hat{\rho}_{\mathrm{in}} = |1\rangle_{a\,a}\langle 1| \otimes |0\rangle_{b\,b}\langle 0|. \tag{3.34}$$

After applying the displacement $\hat{D}_a(\beta)$ and beamsplitter $\hat{U}_{ab}$ operators we obtain the reduced, detected density operator by tracing out the vacuum mode

$$\hat{\rho}_{\mathrm{out}} = \mathrm{Tr}_b\left[\hat{U}_{ab}\hat{D}(\beta)|1\rangle_{a\,a}\langle 1| \otimes |0\rangle_{b\,b}\langle 0|\hat{D}^\dagger(\beta)\hat{U}^\dagger_{ab}\right] \tag{3.35}$$

$$= \hat{D}(\sqrt{\eta_s}\beta)\left[\eta_s|1\rangle_{a\,a}\langle 1| + (1-\eta_s)|0\rangle_{a\,a}\langle 0|\right]\hat{D}(\sqrt{\eta_s}\beta)^\dagger. \tag{3.36}$$

From Eq. (3.36) we can see that displacement by β followed by losses η_s is essentially the same as introducing losses first by mixing the pure single-photon state

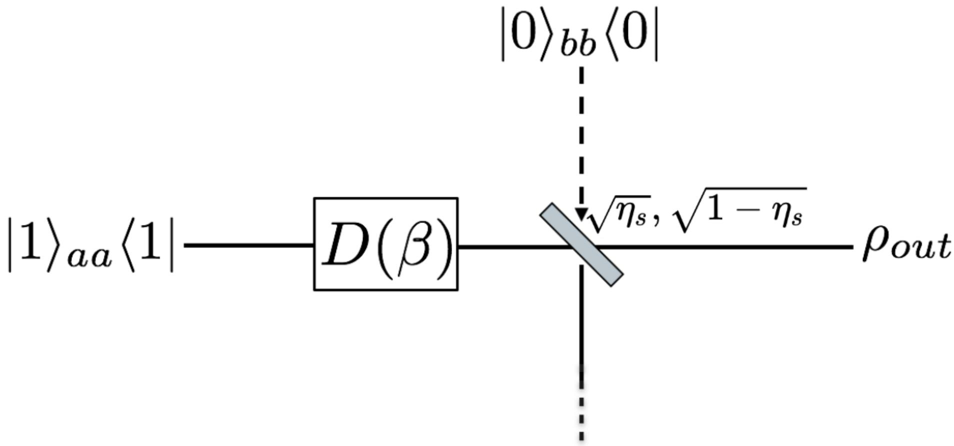

Figure 3.13: Loss model. The beamsplitter transmission and reflection coefficients are $\sqrt{\eta_s}$ and $\sqrt{1-\eta_s}$ respectively.

with vacuum, and then applying a displacement by the reduced amount $\sqrt{\eta_s}\beta$. Due to the linearity of the Wigner function, Eq. (3.36) shows that the experimentally reconstructed Wigner function will in fact be

$$W(p,q) = \eta_s W_{|1\rangle\langle 1|}(p,q) + (1-\eta_s) W_{|0\rangle\langle 0|}(p,q). \tag{3.37}$$

As expected, losses (1-η_s) add a Gaussian vacuum function to the original nonpositive Wigner function of the single-photon state. In particular, the undisplaced photon-number distribution will yield the overall transmissivity of the whole experiment η_s, as in Fig.3.11, left.

3.3.4 Quantum tomography of a single-photon state

We now turn to the state tomography results. Figure 3.14 shows the reconstructed Wigner function along with a fit with Wigner function Eq. (3.37), of free parameter η_s. The Wigner function is plotted for experimentally measured values of $|\alpha|$ where phase space coordinates are $(q,p) = (\sqrt{2}|\alpha|\cos\phi, \sqrt{2}|\alpha|\sin\phi)$, where ϕ is the tomographic

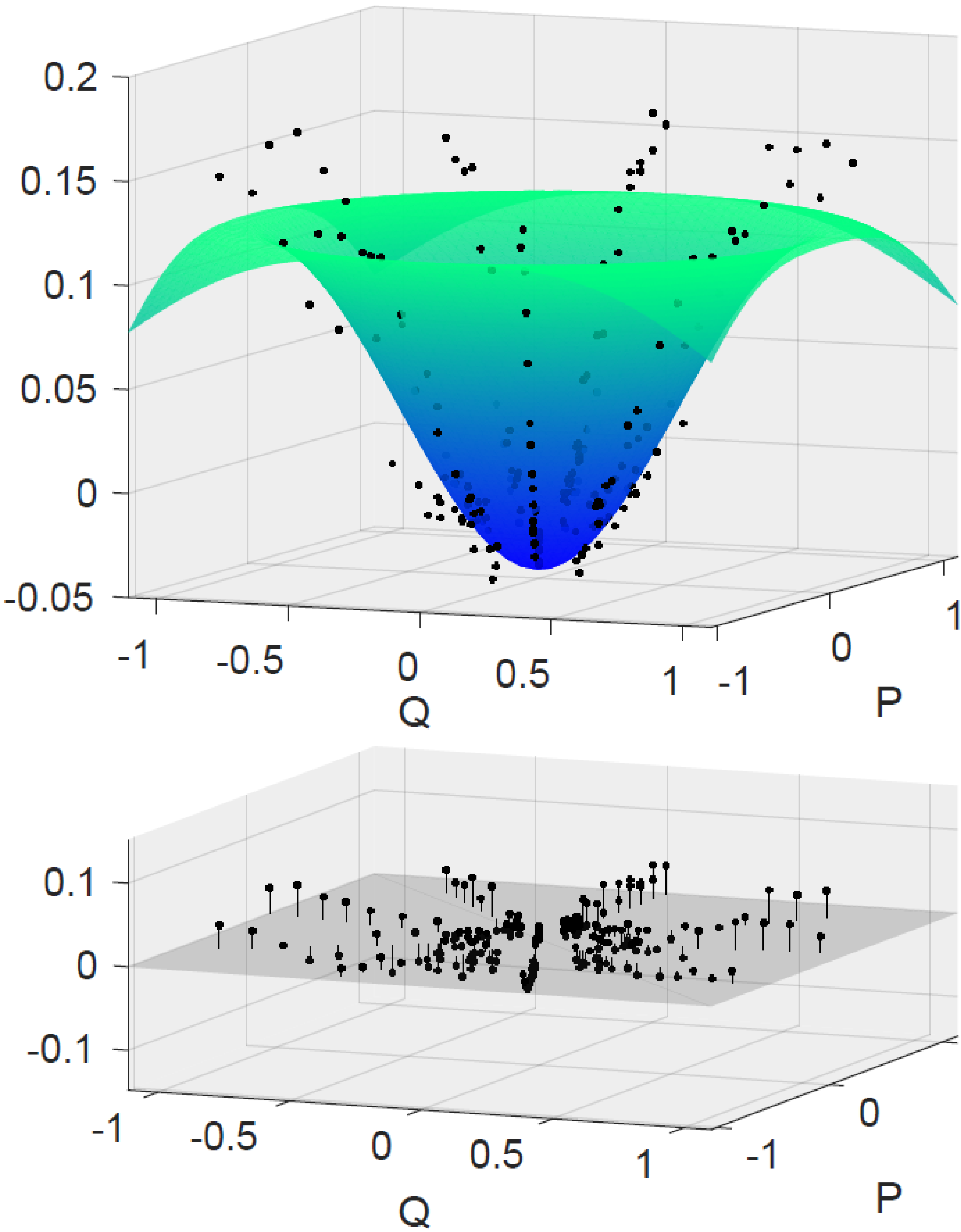

Figure 3.14: Top, reconstructed Wigner function. Black points: reconstructed values from raw data. Solid surface: least-square Wigner-function fit, Eq. (3.37). Bottom, fit residuals.

angle. We can clearly see the negativity around the origin of the phase space,

$$W(0,0) = -0.035 \pm 0.005. \tag{3.38}$$

Errors in the displacement amplitudes were considered to be negligible due to the long-term amplitude stability of the laser producing the displacement field and the high-accuracy of the calibration as mentioned in the "displacement calibration" section. The Wigner function error bars (1σ) at zero-displacement were obtained from the statistics of multiple data sets with the displacement field blocked. At non-zero displacement, in order to speed up the measurement process and minimize experimental drifts, we decided to use the statistics of the measurement results at 10 different phases for the same displacement amplitude. This procedure yields a conservative estimate of the Wigner function error bars (1σ), in the particular case of a single-photon Fock state, because it assumes that the measured Wigner function has the required cylindrical symmetry about the origin of phase space. The results are plotted on Fig.3.15.

Note that the fact that Wigner function isn't significantly altered by this averaging — in fact, both the 2D fit in Fig.3.14 and the 1D fit in Fig.3.15 yield $\eta_s = 0.57(3)$ — speaks to the high quality of the phase-space rotational symmetry of our data. One can notice that the fit residuals are reasonably small around the origin of phase space but grow larger in the outskirts of the function, near our maximum displacement values. Additionally, we were not able to probe the Wigner function at many phase space points around the origin because we needed a minimum amplitude of $|\alpha| \approx 0.15$ for the coherent state in order to see a two-photon event required for displacement calibration. This is not going to be a matter of concern if one uses TESs in the pulsed regime, where one can simply use only zero-photon detection events to calibrate the amplitude of the displacement field. These correspond to larger detected photon numbers on the TES, for which photon pileups during the TES' cooling time make data analysis more arduous [133].

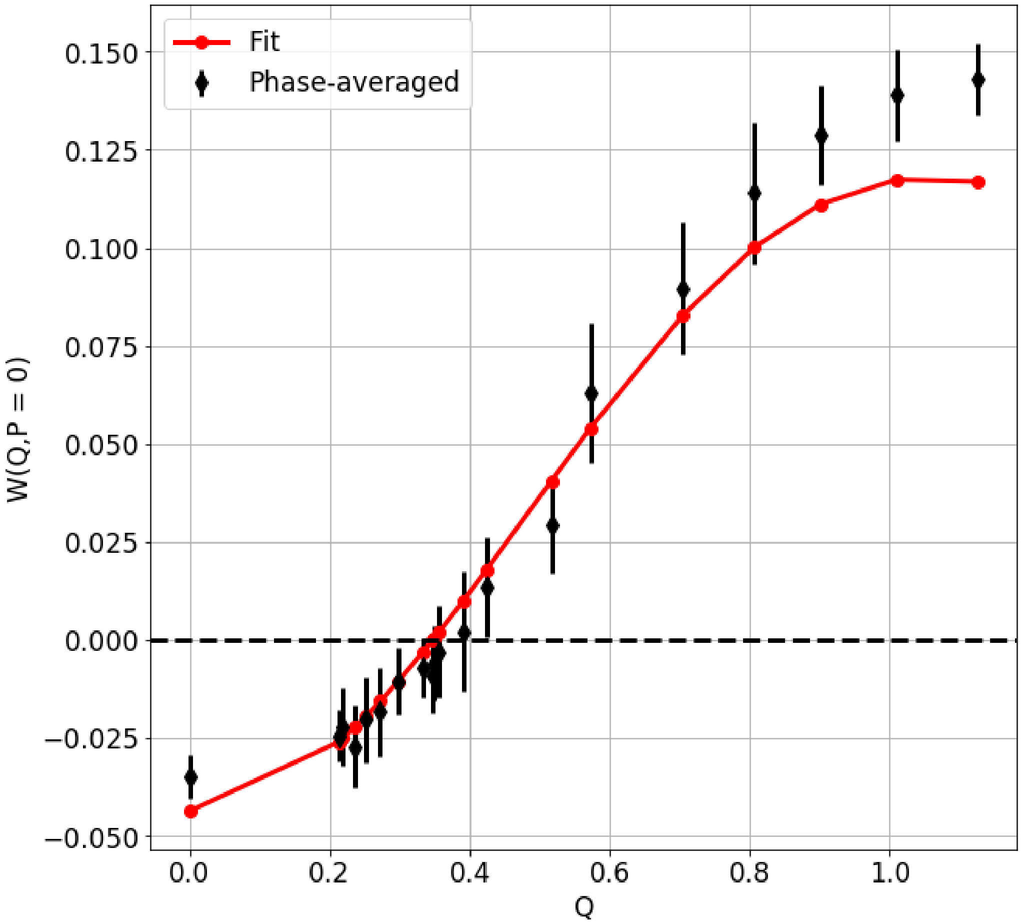

Figure 3.15: Phase-averaged Wigner function. The Wigner function fit yielded $\eta_s = 0.57(3)$, which is consistent with the heralding efficiency 0.58(2). Error bars are discussed in the text.

We also plot reconstructed Wigner function corresponding to each phase of the displacement field, as depicted in Fig. 3.16.

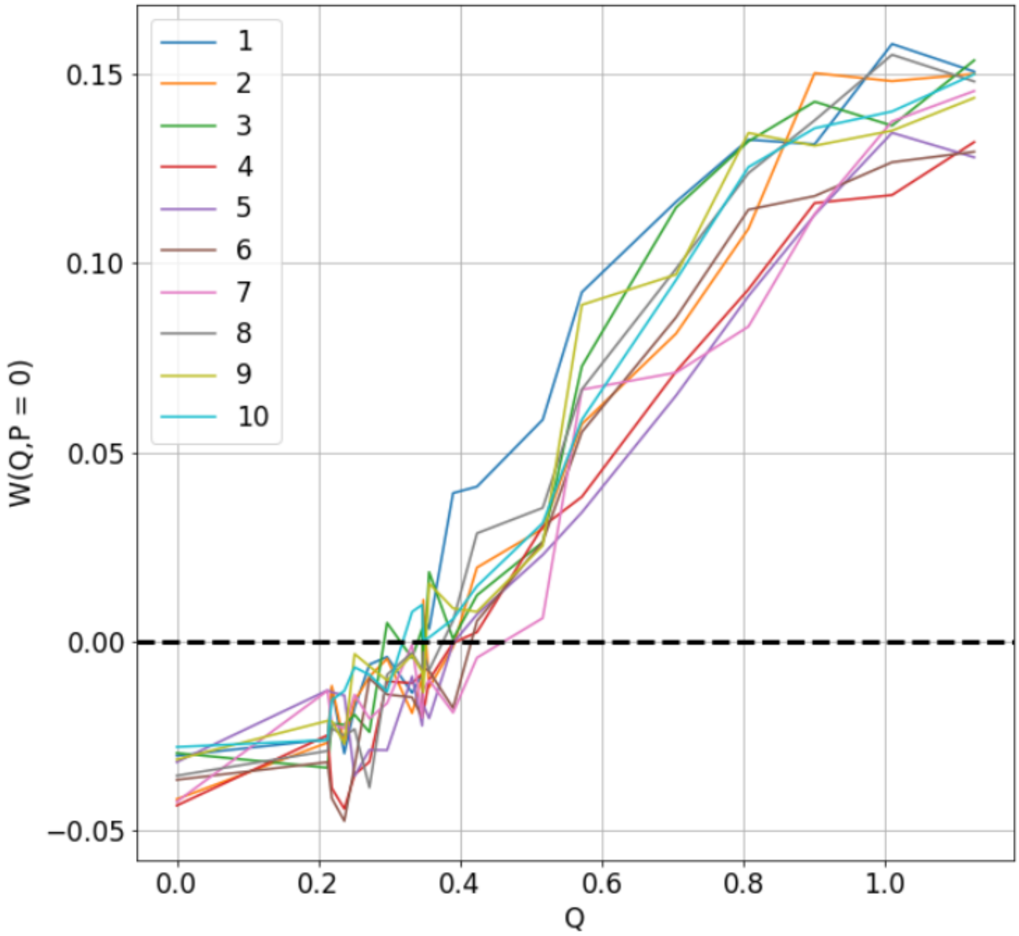

Figure 3.16: Experimentally reconstructed Wigner function slices for 10 phases of the displacement field.

While the overall trend remains as expected and the phase-averaged Wigner function has a strong agreement with the expected Wigner function when all the losses and detection efficiency are taken in account, there are some fluctuations in the Wigner functions at different phases. These fluctuations might be attributed to the long-term drifts in the laser intensity as the entire data run took a few hours including the sampling and streaming the data to computer memory. Therefore, it is advantageous to calibrate the amplitude of displacement field right after acquiring the data each phase space coordinate. This was not the case in our data acquisition process, we calibrated all the amplitudes after entire tomography data was acquired. It seems plausible to do so, but it might lead to some random vibrations or bumps on the optical table because it would be required to lift the plexiglass at each time in order to block the OPO signal. Although a programmable shutter could be used in the future to avoid lifting. Additionally, the multimode coupling into the optical fiber makes it overly sensitive to random variations and bumps as it slightly changes the internal structure of the fiber, thereby changing the total internal reflection conditions. Consequently, the fundamental mode might get coupled to higher-order modes that might leak out from the fiber. This concludes the tomography results. We now discuss how to characterize a multimode quantum state using this technique.

3.4 Direct characterization of a multimode quantum state

In this section, we extend direct state characterization for a multimode quantum state. We start with the two-mode state written in the photon-number basis as

$$\rho_{1,2} = \sum_{n_1,n_2,n_1',n_2'}^{\infty} c_{n_1,n_2,n_1',n_2'} |n_1, n_2\rangle\langle n_1', n_2'|. \tag{3.39}$$

The two-mode Wigner function can be written as

$$W(\alpha,\beta) = \frac{1}{\pi^2}\mathrm{Tr}[\hat{D}(\alpha)\otimes\hat{D}(\beta)\rho_{1,2}\hat{D}(\beta)^{\dagger}\hat{D}(\alpha)^{\dagger}(-1)^{\hat{N}_1+\hat{N}_2}], \tag{3.40}$$

where $\hat{D}(\alpha)\otimes\hat{D}(\beta)$ is the two-mode displacement operator, and the two-mode joint parity is

$$P_{1,2} = (-1)^{\hat{N}}, \tag{3.41}$$

where $\hat{N} = \hat{N}_1 + \hat{N}_2$ is total photon-number operator with $\hat{N}_1$ being number operator for mode 1 with eigenvalue n_1 and $\hat{N}_2$ is the number operator for mode 2 with eigenvalue n_2. Analogous to the single-mode Wigner function, the value at the origin ($\alpha = 0, \beta = 0$) of two-mode Wigner function is the expectation value of joint parity operator. As a result, we have

$$W(\alpha, \beta = 0) = \frac{1}{\pi^2}\mathrm{Tr}\big[(-1)^{\hat{N}_1+\hat{N}_2} \sum_{n_1,n_2,n_1',n_2'=0}^{\infty} c_{n_1,n_2,n_1',n_2'}|n_1, n_2\rangle\langle n_1', n_2'|\big] \tag{3.42}$$

Further simplification leads to

$$W(\alpha, \beta = 0) = \frac{1}{\pi^2} \sum_{n_1,n_2=0}^{\infty} (-1)^{n_1+n_2} c_{n_1,n_2,n_1,n_2}, \tag{3.43}$$

where c_{n_1,n_2,n_1,n_2} are the diagonal elements of two-mode density matrix. This shows that a measurement of joint parity allows to determine the Wigner function at the origin of the four-dimensional phase space. In order to find the Wigner function over the entire phase space, one needs to displace both modes as shown in Fig 3.17 over the entire 4-dimensional phase space, and then the measurement of the overall parity allows to reconstruct the two-mode Wigner function at the amplitudes of the displacement field. As a result, the two-mode Wigner function can be *directly* reconstructed by displacing each mode followed by two-mode parity measurements. This method can be further generalized to an arbitrary multimode-state.

3.5 Conclusions

In this chapter, we demonstrated state-independent photon-counting quantum state tomography with PNR measurements using a superconducting TES system and evidenced clear negativity in the single-photon Fock Wigner function with no correction for photon loss. This work has been limited by two factors: when working with continuous-wave detection, photon fluxes become overwhelming to the TES when $|\alpha| \to 1$. Moreover, photon pileups, in particular during the TES cooling time,

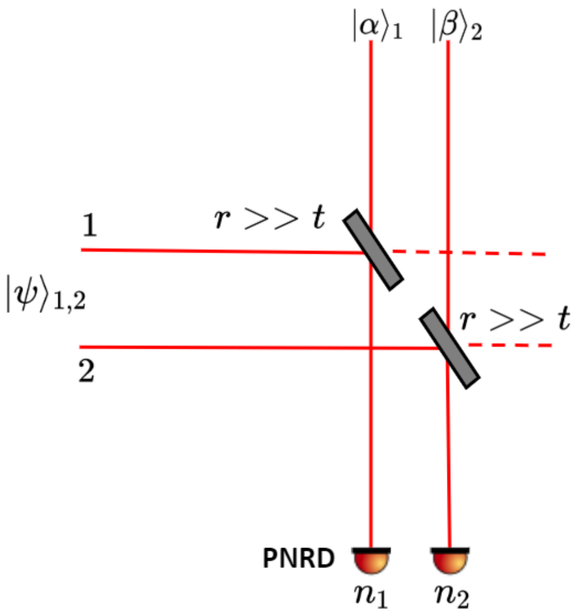

Figure 3.17: Schematic of two-mode Wigner tomography using PNR measurement.

greatly complicate data analysis [133]. In the future, we will multiplex several TES channels in order to access larger displacement amplitudes, i.e., larger regions of phase space. This will also reduce the photon pileup effect. Finally, owing to the intrinsic simplicity of photon-counting quantum tomography, we believe it is possible to herald and visualize Fock state Wigner functions in real time for quantum information applications.

Chapter 4

Generalized Overlap Quantum State Tomography

> A good idea has a way of becoming simpler and solving problems other than that for which it was intended.
>
> Robert E. Tarjan

This chapter is primarily based on the paper titled, "Generalized Overlap Quantum State Tomography," Rajveer Nehra, Miller Eaton, Carlos González-Arciniegas, M. S. Kim, and Olivier Pfister, arXiv:1911.00173v2 [quant-ph] (Submitted). In this work, we propose and experimentally demonstrate a quantum state tomography protocol that generalizes and improves upon the Wallentowitz-Vogel [1] and Banaszek-Wódkiewicz [2] (WVBW) point-by-point Wigner function reconstruction discussed in chapter 3. The full density operator of an arbitrary quantum state is reconstructed in the Fock basis, using numerically efficient semidefinite programming, after interference with a small set of calibrated coherent states. This new protocol is resource- and computationally efficient, is robust against noise, does not rely on approximate state displacements, and ensures the physicality of results. The proposed scheme is demonstrated for a weak coherent state and a single-photon Fock state. We also disuss

4.1 Motivation for this work

Since a quantum system is fully characterized by its density operator [151], the experimental implementation, and investigation, of quantum state tomography [152] plays a crucial role in quantum information (QI). While the dimension 2^N of a N-qubit Hilbert space prohibits full quantum state tomography for large values of N due to exponential growth, except in the particular case of sparse density operators [153], full state tomography of small scale quantum systems can still be realized and is essential to characterizing important resource states, e.g. quantum error correcting codes. As we discussed in chapter 3, the Wigner function [93], [154] plays a central role as a quantum state descriptor strictly equivalent to the density operator ρ:

$$W(q,p) = \frac{1}{\pi}\int_{-\infty}^{\infty} e^{2ipy}\langle q-y|\hat{\rho}|q+y\rangle dy, \tag{4.1}$$

where quantum phase space variables q and p are the eigenvalues of the position-like amplitude quadrature, $\hat{Q} = (\hat{a}+\hat{a}^\dagger)/\sqrt{2}$, and momentum-like phase quadrature, $\hat{P} = i(\hat{a}^\dagger - \hat{a})/\sqrt{2}$, of the electromagnetic field, and where $\hat{a}$ is the bosonic annihilation operator for a given qumode, typically specified by its wave vector, frequency and polarization. The experimental determination of the Wigner function, first proposed and realized by interferometric, homodyne quadrature measurements [109], thus constitutes another approach to quantum state tomography. A technical difficulty of the aforementioned optical homodyne tomography approach resides in the need for computationally intensive reconstruction procedures, using either the inverse Radon transform (whence the “tomography” moniker) or maximum likelihood algorithms [110]. Recently E. S. Tiunov *et al.* proposed a scheme using machine learning, restricted Boltzmann machine (RBM), which has significant advantages over MaxLik based OHD [155], yet is not provably efficient for arbitrary quantum states [156]. Such difficulties can be alleviated by replacing field measurements with photon-number ones, using the fact that the Wigner function at the origin of phase space coincides with the expectation value of the photon-number parity operator [124]. This yields an expression of the Wigner function in the Fock basis which is easy to reconstruct, as was first proposed by Wallentowitz-Vogel [1] and Banaszek-Wodkiewicz [2]. As detailed in chapter 3, the WVBW includes a simple phase space translations, i.e., displacements, of the quantum state to be characterized, followed by parity measurements accessed using photon-number-resolving (PNR) detection, allows easy determination of the Wigner function. More recently, the coming of age of photon-number-resolving (PNR) detection [149] has opened the door to using the full WVBW method on traveling optical fields with no prior knowledge of the measured quantum state [89], [133].

While the WVBW method presents clear advantages in terms of the numerical demands on reconstruction, it requires a phase space raster scan involving a large number of optical displacements, and the pitch of the raster scan is determined by the specific features of the—unknown—Wigner function to be resolved. Moreover, the best experimental implementation of phase space displacements is intrinsically lossy due to an approximate implementation of optical displacements [125]. Finally, the method does require, like homodyne tomography, a very high system detection efficiency in order to prevent the quantum decoherence caused by vacuum fluctuation contamination. Additionally, the WVBW protocol mandates a matrix inversion for each experimental data point in order to infer the true photon-number distribution from the measured loss-degraded distribution which could be experimentally demanding for probing the Wigner functions of complicated structure, such as cat states or

Gottesman-Kitaev-Preskill (GKP) states [66]. Moreover, as we will see later that this inversion becomes very sensitive to errors for larger increasing photon numbers.

In this chapter, we present a generalization of the WVBW approach which uses a Wigner function overlap measurement to reconstruct the density operator, rather than the Wigner function, using computationally efficient semidefinite programming. This general method requires considerably less data acquisition, and ensures physical results which are robust against measurement noise. The effect of known system losses (such as optical losses or detection losses) can also be entirely deconvoluted from the measured density operator. We present the mathematical formalism of this generalized overlap quantum state tomography and present experimental results for a single-photon Fock state and a weak coherent state with performance that far exceeds that of the WVBW demonstration in chapter 3 for a single-photon Fock state. Furthermore, we can perform loss-compensation in a single-shot for the entire density matrix ρ, unlike at each experimental data point in WVBW method. The proposed scheme requires significantly fewer measurements as compared with MaxLik and RBM tomography methods and achieves higher fidelity for all the states considered in Ref. [155].

4.2 Principle of generalized overlap tomography

In this section, we discuss the general framework of quantum tomography with the state overlap. We consider the situation depicted in Fig. 4.1(a): a field with unknown density operator ρ and Wigner function $W_1(q_1, p_1)$ interferes with a reference field in a coherent state $|\,\alpha\,\rangle\,\langle\,\alpha\,|$ of Wigner function $W_2(q_2, p_2)$. We then adopt the Heisenberg picture and determine the evolved output quadratures under the beamsplitter interaction to be $q_1' = tq_1 - rq_2$ and $p_1' = tp_1 - rp_2$. Likewise, $q_2' = rq_1 + tq_2$ and $p_2' = rp_1 + tp_2$. Before the beamsplitter interaction, the two-mode input state is

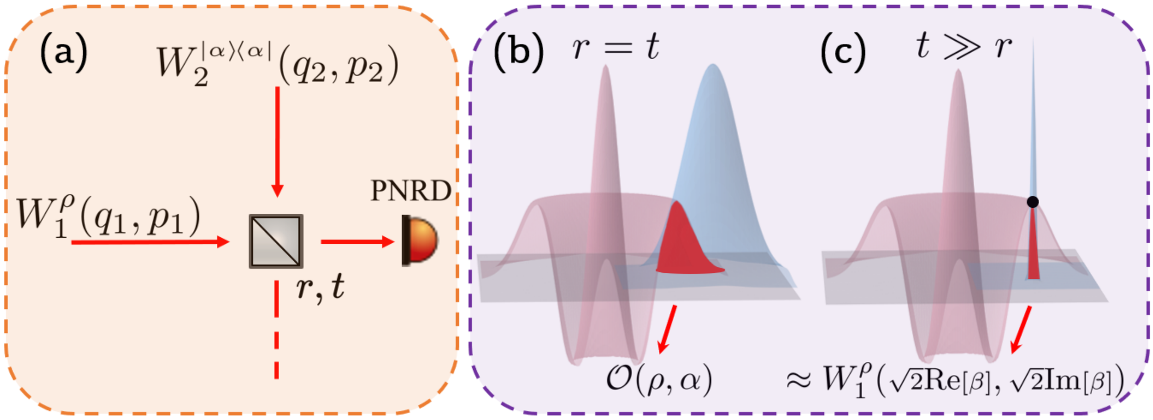

Figure 4.1: (a), Schematic of the experiment: the field to be measured, of density operator ρ, interferes with a calibrated field in coherent state α at a beamsplitter of field reflectance $r \in \mathbb{R}$ and transmittance $t = (1 - r^2)^{1/2}$. PNRD: photon-number-resolving detector. (b), Principle of generalized overlap tomography exemplied with a two-photon Fock state.(c), Limit case of (b), where a highly unbalanced beamsplitter merely implements a displacement of ρ by $-\beta$.

written in the Wigner function representation as

$$W_{1,2}(\mathbf{x}) = W_1(q_1, p_1)W_2(q_2, p_2). \tag{4.2}$$

Next, by using the evolved quadratures, one can write the Wigner function of the beamsplitter output as

$$W'_{1,2}(\mathbf{x}') = W_1(tq'_1 + rq'_2, tp'_1 + rp'_2)W_2(-rq'_1 + tq'_2, -rp'_1 + tp'_2), \tag{4.3}$$

where $\mathbf{x}$ and $\mathbf{x}'$ are column vectors consisting of quadratures corresponding to the input and output modes, respectively. The value of the Wigner function of output mode 1 at the origin can be obtained by setting $q'_1 = p'_1 = 0$ and tracing out over mode 2 leads to

$$W'_1(0, 0; r, t) = \iint W'_{1,2}(\mathbf{x}')dq'_2 dp'_2|_{q'_1, p'_1 = 0}. \tag{4.4}$$

A simple algebra shows that

$$W_1'(0,0;r,t) = \iint W_1(rq_2', rp_2')W_2(tq_2', tp_2')dq_2'dp_2'$$
$$= \frac{1}{r^2}\iint W_1(q,p)W_2(\tfrac{t}{r}q, \tfrac{t}{r}p)dqdp. \tag{4.5}$$

By setting $r = t = \frac{1}{\sqrt{2}}$, we see that Eq. (4.4) gives the Wigner function overlap between ρ and $|\alpha^j\rangle\langle\alpha^j|$. From the Wigner function overlap theorem [111], the overlap $\mathcal{O}$ of the unknown ρ with $|\alpha_j\rangle\langle\alpha_j|$:

$$\mathcal{O}_j = \mathrm{Tr}[\rho|\alpha_j\rangle\langle\alpha_j|] = \pi W_1'(0,0;\tfrac{1}{\sqrt{2}},\tfrac{1}{\sqrt{2}}). \tag{4.6}$$

As a result, we see that measuring the Wigner of the output mode 1 at the origin allows us to measure the state overlap of the unknown quantum state and coherent state. As discussed in chapter 3, we can simply measure photon statistics at only one beamsplitter output to evaluate the expectation value of the photon-number parity operator, which determines the value of Wigner function of this output mode [124], [157] at the origin of phase space.

Before we proceed further, let's note that, in the limiting case of $t \gg r$, the function $W_2(\frac{t}{r}q, \frac{t}{r}p)$ in Eq. (A.1) is a contracted Gaussian that tends toward a Dirac delta function $\delta(\sqrt{2}\mathrm{Re}[\beta], \sqrt{2}\mathrm{Im}[\beta])$, where $\beta = r\alpha/t$, thereby yielding $W_1(\sqrt{2}\mathrm{Re}[\beta], \sqrt{2}\mathrm{Im}[\beta])$, i.e., precisely the WVBW tomography protocol, as illustrated in Fig. 4.1(c). The validity of this limit case is equivalent to the validity of implementing a displacement with an unbalanced beamsplitter. The state overlap approach is free of such considerations and general for any beamsplitter parameters as we show that in the appendix A. For simplicity, from here on, we set $r = t$. Even though this would appear to cause an irremediable loss of information, we show that ρ can nonetheless be accurately and efficiently retrieved by measuring $\mathcal{O}_j$ for a series of distinct coherent states $|\alpha_j\rangle$. The role of the other output port of the BS is also examined in the appendix A.

For a given single-mode quantum state, one can write the density matrix in the photon-number basis as

$$\rho = \sum_{n,n'=0}^{\infty} \rho_{n,n'} |n\rangle\langle n'|. \tag{4.7}$$

Complete characterization of ρ requires determining $\rho_{n,n'}$. To do that, we choose a set of distinct coherent states, $|\alpha_j\rangle$ and experimentally determine the overlap with the unknown state ρ. For a given coherent state represented in the photon-number basis, $|\alpha_j\rangle = \sum_{m=0}^{\infty} c_{jm}|m\rangle$, the overlap can be determined using Eq. (4.6)

$$\mathcal{O}_j = \sum_{m'=0}^{\infty} c^*_{jm'}\langle m'| \sum_{n,n'=0}^{\infty} \rho_{n,n'}|n\rangle\langle n'| \sum_{m=0}^{\infty} c_{jm}|m\rangle. \tag{4.8}$$

A further simplification leads to

$$\mathcal{O}_j = \sum_{n=0}^{\infty}\sum_{m=0}^{\infty} c_{jm}c^*_{jn}\rho_{n,m}, \tag{4.9}$$

where c_{jm}=$\exp(-|\alpha_j|^2/2)\alpha_j^m/\sqrt{m!}$. Ideally, the sum in Eq. (4.9) over n and m goes to infinity but for practical purposes one needs to truncate it at a certain number n_0 such that any terms $n, m > n_0$ do not significantly contribute to the sum. In the physical sense, the truncation can be thought as the finite size of the Hilbert with dimension $n_0 + 1$. As a result, we have

$$\mathcal{O}_j = \sum_{n=0}^{n_0}\sum_{m=0}^{n_0} c_{jm}c^*_{jn}\rho_{n,m}. \tag{4.10}$$

For $N_p = (n_0 + 1)^2$ measurements, we can write Eq. (4.10) in the matrix form as

$$\begin{pmatrix} \mathcal{O}_{(0)} \\ \mathcal{O}_{(1)} \\ \vdots \\ \mathcal{O}_{N_p} \end{pmatrix} = \begin{pmatrix} c_{00}c^*_{00} & c_{00}c^*_{01} & \dots & c_{0n_0}c^*_{0n_0} \\ c_{10}c^*_{10} & c_{10}c^*_{11} & \dots & c_{1n_0}c^*_{1n_0} \\ \vdots & \vdots & \ddots & \vdots \\ c_{N_p0}c^*_{N_p0} & c_{N_p0}c^*_{N_p1} & \dots & c_{N_pn_0}c^*_{N_pn_0} \end{pmatrix} \begin{pmatrix} \rho_{0,0} \\ \rho_{0,1} \\ \vdots \\ \rho_{n_0,n_0} \end{pmatrix}. \tag{4.11}$$

We can rewrite Eq. (4.11) in compact form as

$$\mathbf{O} = \mathbf{CP}, \tag{4.12}$$

where $\mathbf{O} \in \mathbb{R}^{(n_0+1)^2}$, $\mathbf{P} \in \mathbb{C}^{(n_0+1)^2}$ and $\mathbf{C} \in \mathbb{C}^{(n_0+1)^2 \times (n_0+1)^2}$. Note that $\mathbf{P}$ is the unknown density matrix written in the Liouville vector form, i.e, stacking all the rows of density matrix in a column vector of dimension $(n_0 + 1)^2$. Next, we can invert Eq. (4.12) to reconstruct $\mathbf{P}$. To do this, we employ semidefinite programming (SDP) to run a convex quadratic optimization algorithm that minimizes the ℓ^2-norm, $||\mathbf{O} - \mathbf{CP}||_2$, subject to physicality constraints in order to extract $\mathbf{P}$. The procedure is computationally efficient and yields a unique solution. Note that $\mathbf{C}$ does not have to be a square matrix, so that the number of measured overlaps (the dimension of $\mathbf{O}$) can be increased for better data statistics. Thus the semidefinite program is mathematically defined as

$$\begin{aligned} \underset{\rho}{\text{Minimize}} \quad & ||\mathbf{O} - \mathbf{CP}||_\mathbf{2} \\ \text{Subject to} \quad & \rho \geq 0, \quad \text{Tr}[\rho] = 1, \end{aligned} \tag{4.13}$$

where $||.||_2$ is the ℓ^2-norm defined as $||V||_2 = \sqrt{\sum_i |v_i|^2}$. We now turn to numerical simulations performed using open source Python modules QuTip and CVXPY [158], [159] where the Hilbert space for each optical mode was constructed in the Fock basis with a high enough dimensionality to ensure state probability amplitudes decayed to less than 10^{-7} before truncation. Under these parameters, the numerically efficient SDP algorithms converged in order of 10^{-2} seconds on a 3GHz Intel i5 quad core processor with 16 GB RAM. We perform numerical simulations for both real- and complex-valued density matrices. First, the method is demonstrated in Fig. 4.2 for the example cases of the cat state, $|\psi\rangle \propto |\alpha\rangle + |-\alpha\rangle$ where $\alpha = \sqrt{3}$, and a Gottesman-Kitaev-Preskill (GKP) state of mean photon number 5. These states were reconstructed using 400 different coherent states of 20 equidistant amplitude increments from $\beta = 0$ to $\beta = \sqrt{6}$ and 20 phase increments from 0 to 2π, to achieve fidelities with the target states greater than 0.999 for the cat state, and a fidelity of 0.985 for the GKP state. The reduced fidelity for GKP state is due to the fact that the Wigner function has complicated features compare to cat state which necessitates the number of coherent probes (or overlap measurements) to be higher than that of a cat states.

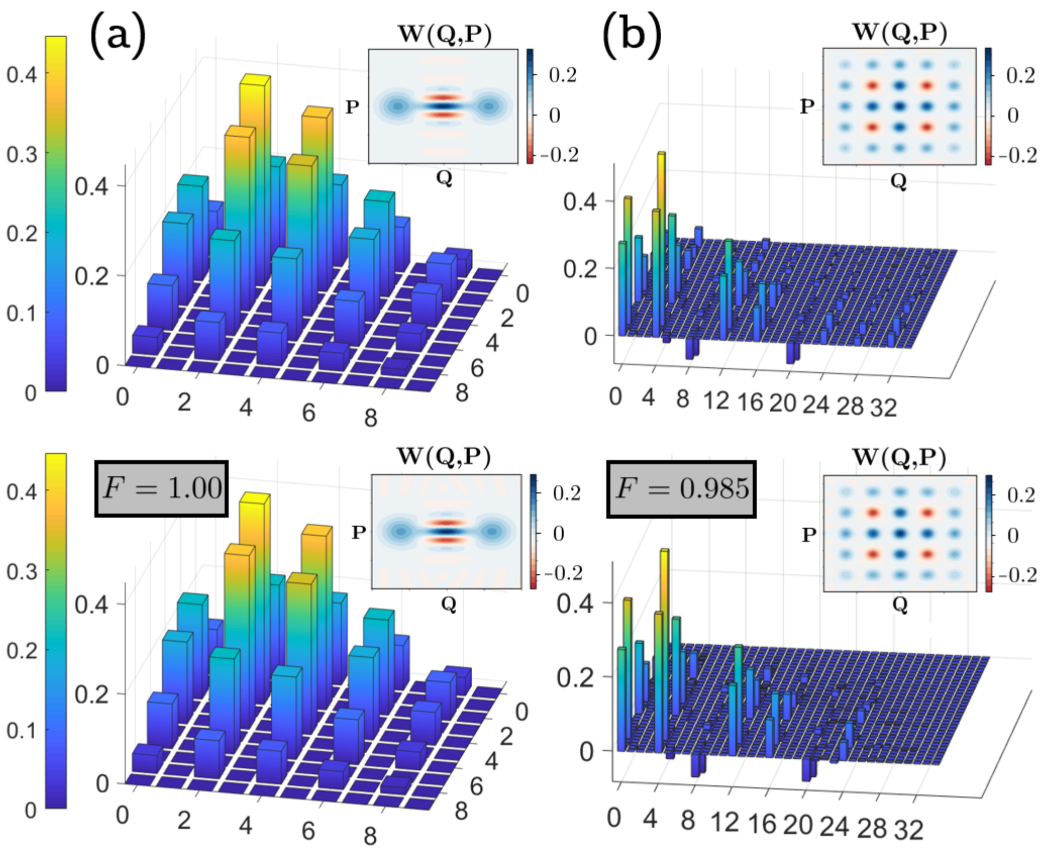

Figure 4.2: Tomographic reconstruction using 400 coherent state probes for **(a)** a cat state of amplitude $\sqrt{3}$, and **(b)** a GKP state with a mean photon number of 5. The top row displays the density matrix for the ideal theoretical state, and the bottom shows the numerical reconstructions. Insets display the plotted Wigner function of each state.

In general, the state tomographer is assumed to have no prior knowledge of the state to be characterized. Thus it is important to scan the entirety of phase space in question with different coherent states so as to have sufficient overlap measurements to capture all features of the state under characterization process. If some prior knowledge of the state is obtained, then the coherent state probes can be restricted to a localized region of phase space near the unknown quantum state which might help in reducing the number of overlap measurements.

Second, we demonstrate the tomography protocol for complex-valued density matrices displayed in Fig. 4.3. We perform the tomography with coherent state probes that range in amplitude in 20 equidistant steps from $|\beta| \in [0, \sqrt{3}]$ and 20 phases $\phi \in [0, 2\pi]$, for a coherent state denoted by complex variable, $\alpha = \sqrt{2}(i+1)$ and a superposition of photon-number states with the complex probability amplitude. The Wigner functions are shown along with separate plots for the real and imaginary elements of the respective reconstructed density matrices, including an inset fidelity with the ideal states.

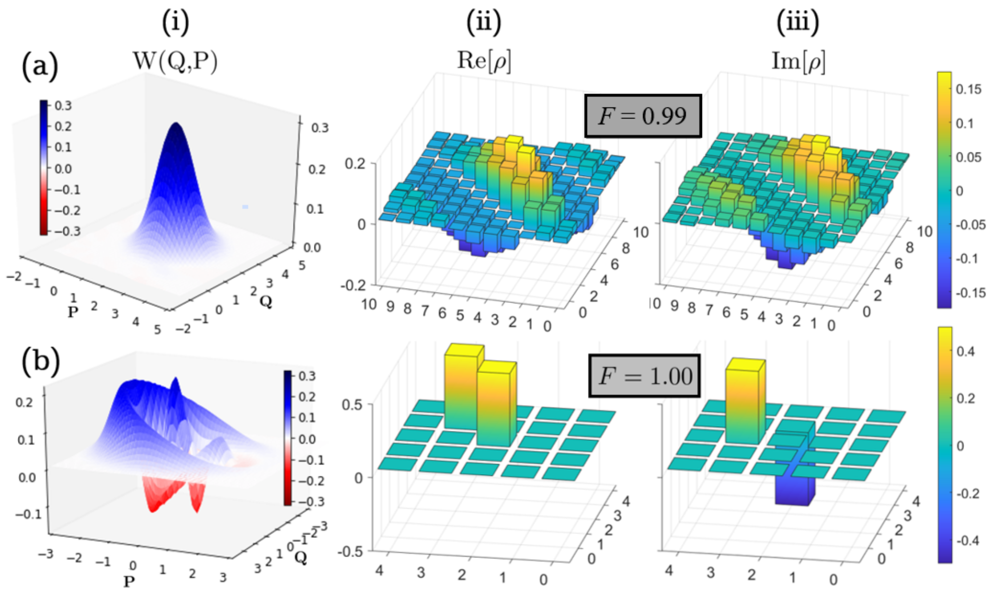

Figure 4.3: Reconstruction of states with complex-valued density matrices for (a) the coherent state, $|\alpha\rangle$, with $\alpha = \sqrt{2}(i+1)$ and (b) the superposition $\frac{1}{\sqrt{2}}(|2\rangle - i|3\rangle)$. The inset fidelity is calculated between the reconstructed state and the ideal target state. (i) Reconstructed Wigner functions. (ii) Real elements of the density matrices. (iii) Imaginary elements of the density matrices. Note that the viewing perspective for the coherent state is changed in (a) for a better visualization.

4.3 Imperfections: losses, experimental noise, and mode mismatch

Thus far we have only considered an ideal experiment with no noise, losses, and a perfect mode matching between the fields of coherent state probes (or local oscillators (LOs)) and unknown state. We now deal with all these imperfections and devise methods to compensate for the losses and mode mismatch while suppressing the effects of experimental noise in the reconstruction.

4.3.1 Loss Compensation

Photon loss is the primary source of imperfections in the state tomography. Since our method solely requires photon-number distributions to perform the complete state tomography, we are interested in inferring the true photon-number distribution from the loss-degraded experimentally measured photon-number distribution. Methods to correct for loss-degraded photon number distributions when counting photons are known [66], [160], [161], but this requires performing a matrix inversion for each experimental measurement as discussed in detail next.

4.3.2 Photon-number distribution correction

In this section, we deal with the optical losses to the state before and after interference with the coherent states $|\alpha_j\rangle$'s. All these optical losses and non-ideal detector efficiency can be modeled by inserting a single fictitious beamsplitter of transmittivity η in front of a perfect detector. Our goal here is then to infer the true photon-number distribution from the loss-degraded measured photon-number distribution denoted by P_n and P'_n respectively. For a detector of overall detection efficiency (including optical losses), η and no darkcount noise, the POVM element corresponding to n-photon detection event is given by

$$\Pi_n = \sum_{m=n}^{m_0} P(n|m)|m\rangle\langle m|, \tag{4.14}$$

where $P(n|m) = \binom{m}{n}\eta^n(1-\eta)^{m-n}$ is the conditional probability of detecting n photons if m photons are incident to the detector and m_0 is the photon-number at which the detector saturates. For an input state given by density matrix $\rho = \sum_{n,n'=0}^{\infty} \rho_{nn'}|n\rangle\langle n'|$, the probability of detecting n photons is

$$P'_n = \mathrm{Tr}[\rho\Pi_n]. \tag{4.15}$$

Using Eq. (6.1) and Eq. (4.15), we get

$$P'_n = \sum_{m=n}^{m_0} P(n|m)\rho_{mm} = \sum_{m=n}^{m_0} P(n|m)P_m, \tag{4.16}$$

where $\rho_{mm} = P_m$ is the probability of having m photons in the input state ρ before losses. From Eq. (4.16), one can see that the measured photon-number distribution, P'_n is linearly related to true photon-number distribution, P_m. Furthermore, Eq. (4.16) can be rewritten for all detector outcomes in the matrix form as

$$\mathbf{P}' = \mathbf{\Pi}\mathbf{P}, \tag{4.17}$$

where $\mathbf{P}'$ and $\mathbf{P}$ are column vectors of length $m_0 + 1$ representing loss-degraded experimentally measured and ideal (without losses) photon-number distribution respectively. $\mathbf{\Pi}$ is an upper triangular matrix of dimension $(m_0+1)\times(m_0+1)$ characterizing the photon-number resolving detector. Thus by simply inverting Eq. (4.17), one can obtain the true photon-number statistics from the experimental data, which allows to perform the complete state tomography using the method discussed above. It is worth noting that for a perfect detector, i.e., $\eta = 1$, $\mathbf{\Pi}$ is an identity matrix which means the measured photon-number distribution is essentially the true distribution. This has been experimentally demonstrated for state characterization [161], [162] and the WVBW protocol, but requires a matrix inversion for each experimental data point [66]. Additionally, the linear inversion in the presence of any small deviations in $\mathbf{P}'$ can lead numerical instabilities causing unphysically large or negative entries in $\mathbf{P}$. We now propose an inversion scheme which allows to compensate for losses in one fell swoop for the whole density matrix ρ, in lieu of point-by-point as in WVBW method. The proposed inversion scheme guarantees the physicality of the reconstruction as we see next.

4.3.3 Complete density matrix correction

We now aim to correct an arbitrary density matrix given a known loss. In this case, we have experimentally measured loss-degraded ρ', but our goal is then to compensate the losses in order to reconstruct the density matrix before the loss, ρ. As shown in Fig. 4.4, this can be modeled by sending ρ through a fictitious loss beamsplitter with reflection and transmission coefficients of $r = \sqrt{1-\eta}$ and $t = \sqrt{\eta}$, where η is the overall detection efficiency in the experiment. The general single-mode quantum

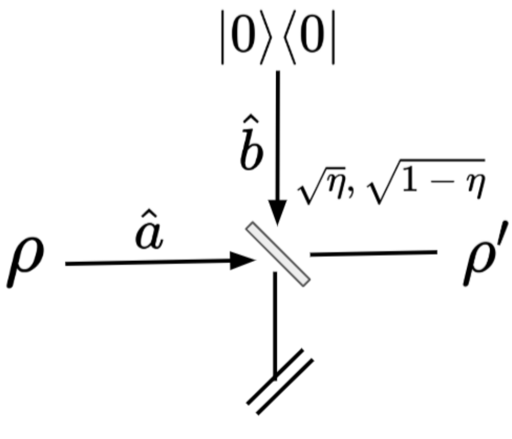

Figure 4.4: Lossy channel.

state density matrix before the loss is

$$\rho = \sum_{n,n'=0}^{\infty} \rho_{n,n'} |n\rangle\langle n'|. \tag{4.18}$$

If this state enters into the loss beamsplitter in mode $\hat{a}$ with vacuum in mode $\hat{b}$, then the mode operators transform in the Heisenberg picture according to $\hat{a} \to t\hat{a} + r\hat{b}$ and $\hat{b} \to -r\hat{a} + t\hat{b}$ to yield an output density matrix

$$\rho_{out} = \sum_{n,n'=0}^{\infty} \rho_{n,n'} \frac{(t\hat{a}^\dagger + r\hat{b}^\dagger)^n}{\sqrt{n!}} |0\rangle_a |0\rangle_b \langle 0|_b \langle 0|_a \frac{(t\hat{a} + r\hat{b})^{n'}}{\sqrt{n'!}}. \tag{4.19}$$

Tracing out over mode $\hat{b}$ yields the final state after loss, which is given by

$$\rho' = \mathrm{Tr}_b[\rho_{out}] = \sum_{n,n'=0}^{\infty} \rho_{n,n'} \sum_{k=0}^{n} \sum_{k'=0}^{n'} A_{n,n',k,k'} |n-k\rangle\langle n'-k'| \langle k|k'\rangle \delta_{k,k'}, \tag{4.20}$$

where we have

$$A(n, n', k, k') = \sqrt{\binom{n}{k}\binom{n'}{k'}} r^{k+k'} t^{n+n'-k-k'}. \tag{4.21}$$

Substituting $n-k$ and $n'-k$ with m and m' allows us to rearrange the expression and rewrite a sum over the Fock components in order as

$$\rho' = \sum_{m,m',k=0}^{\infty} \rho_{(m+k),(m'+k)} A(m+k, m'+k, k, k) |m\rangle\langle m'|, \tag{4.22}$$

where it is easy to see that each element of the density matrix after loss is related to the original state by

$$\begin{aligned} \rho'_{m,m'} &= \sum_{k=0}^{\infty} \rho_{m+k,m'+k} \tbinom{m+k}{k}^{\frac{1}{2}} \tbinom{m'+k}{k}^{\frac{1}{2}} r^{2k} t^{m+m'} \\ &= \sum_{k=0}^{\infty} \rho_{m+k,m'+k} \tbinom{m+k}{k}^{\frac{1}{2}} \tbinom{m'+k}{k}^{\frac{1}{2}} (1-\eta)^k \eta^{\frac{m+m'}{2}} \end{aligned} \tag{4.23}$$

It is worth emphasizing that for $m = m'$, Eq. (4.23) essentially transforms to Eq. (4.16) only for photon-number distribution, i.e, the diagonal entries of the density matrix ρ'. As a result, Eq. (4.23) can be viewed as a generalized Bernoulli distribution [163] which can be inverted to read

$$\rho_{m,m'} = \sum_{k=0}^{\infty} (-1)^k \rho'_{m+k,m'+k} \binom{m+k}{k}^{\frac{1}{2}} \binom{m'+k}{k}^{\frac{1}{2}} \left(\frac{r}{t}\right)^{2k} t^{-m-m'}. \tag{4.24}$$

In practice, the sum over k can be truncated to some value, N_{max}, beyond which the entries in the initial density matrix are negligible. We can then reformulate Eq. (4.23) as a series of N_{max} linear maps from the i^{th} diagonal of ρ' to the i^{th} diagonal of ρ, where the main diagonal corresponds to $i = 0$. Each of these linear maps, $\mathbf{M}^{(i)}$, is an upper triangular matrix of dimension $N_{max} - i \times N_{max} - i$ with elements

$$\mathbf{M}^{(i)}_{jk}(\eta) = \left\{ \begin{array}{cc} 0 & j > k \\ \sqrt{\binom{k}{k-j}\binom{i+k}{k-j}}(1-\eta)^{(k-j)}\eta^{\frac{i}{2}+j} & \text{otherwise} \end{array} \right\} \tag{4.25}$$

Since each $\mathbf{M}^{(i)}(\eta)$ is triangular with nonzero diagonal elements, the inverse mappings can be found by inverting the generalized Bernoulli transformation and are given by [163]

$$\mathrm{Inv}[\mathbf{M}^{(i)}(\eta)] = \mathbf{M}^{(i)}(\eta^{-1}). \tag{4.26}$$

It is somewhat counter-intuitive that we are able to recover the complete information about the quantum state which has undergone through irreversible photon losses to the vacuum field $\hat{b}$ coming from the unused port of the beamsplitter in Fig. 4.4. The existence of this inversion is due to the known well-defined statistical nature of the loss channel, which makes it possible to perfectly reconstruct any ρ within a finite-dimensional Hilbert space when η and ρ' are *precisely* known [163]. However, the presence of any small deviations in an experimentally measured ρ' can lead to unphysically large or negative diagonal density matrix elements in the reconstruction of ρ, even while ρ remains normalized. This is similar to the possible numerical instabilities that arise when using pattern-functions [113]. Here, we solve this issue by inverting each $\mathbf{M}^{(i)}(\eta)$ using semidefinite programming where the optimization problem is defined as

$$\begin{aligned} &\underset{\rho}{\text{Minimize}} \quad \sum_{i=0}^{N_{max}} ||\rho'^{(i)} - \mathbf{M}^{(i)}\rho^{(i)}||_2 \\ &\text{Subject to} \quad \rho \geq 0, \ \ \text{Tr}[\rho] = 1, \ \text{and} \ \ \rho_{m,m} \leq \eta^{-m}\rho'_{m,m}, \end{aligned} \tag{4.27}$$

where $\rho^{(i)}$ denotes the i^{th} diagonal of ρ where $i = 0$ is the main diagonal and $\mathbf{M}^{(i)}(\eta)$ is the linear map describing the binomial-law loss degradation along each diagonal of ρ. The third constraint stems from the fact that Eq. (4.23) yields $\rho'_{mm} = \eta^n \rho_{mm} + \epsilon$, where ϵ is positive. Additionally, it is only necessary to sum over the upper diagonals of ρ in the minimization (hence the sum starting at $i = 0$), due to the enforced positivity of ρ. If the value of the loss parameter η is known, this loss deconvolution method is numerically efficient by the virtue of being a convex optimization and physically reliable due to enforced physicality constraints in Eq. (4.27).

In Fig. 4.5, we display the numerical simulations for a four-photon Fock state and a cat state. In each instance, the state is sent through a 50% lossy channel followed by the generalized tomographic procedure with coherent state probes having 40 amplitude and 40 phase increments as opposed to 20 amplitudes and 20 phases used in the ideal numerical simulation above. The high number of coherent state measurements was chosen to ensure highly accurate tomographic reconstructions for the lossy state. Fig. 4.5 (a) displays the actual numerical reconstructions where the fidelities are determined with the ideal four-photon Fock state and a cat state. We notice that due to 50% losses negative regions or phase space fringes of the Wigner function are erased out.

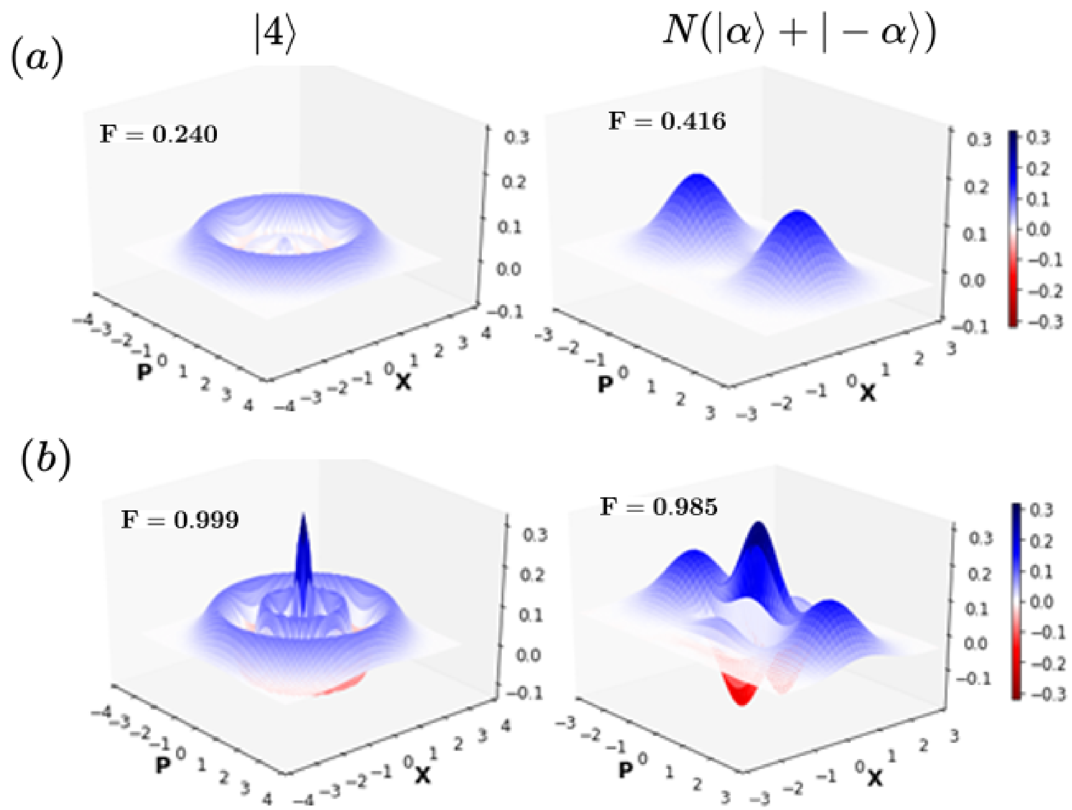

Figure 4.5: (a) Reconstruction of a four-photon Fock state and a cat state with $\alpha = \sqrt{3}$ in the presence of 50% losses. (b) Loss compensation using SDP. All fidelities are determined with the ideal states.

We then plot the loss compensated reconstruction using SDP in Fig. 4.5 (b). Remarkably, we find that the loss compensation leads to near-unity fidelity reconstruction and the negative regions of the Wigner function are retrieved.

Next we compare the proposed loss compensation scheme with the analytical generalized Bernoulli transformation from Eq. (4.24). The effects of numerical instabilities are demonstrated with a reconstruction of a cat state with 30% loss. Numerical simulations are displayed in Fig. 4.6. On the left, we have the photon-number distribution of a loss-compensated cat state and its Wigner function. First the loss-degraded cat state was tomographed and then we use the generalized Bernoulli transformation defined in Eq. (4.24) to obtain the loss-compensated density matrix and plot its Wigner function.

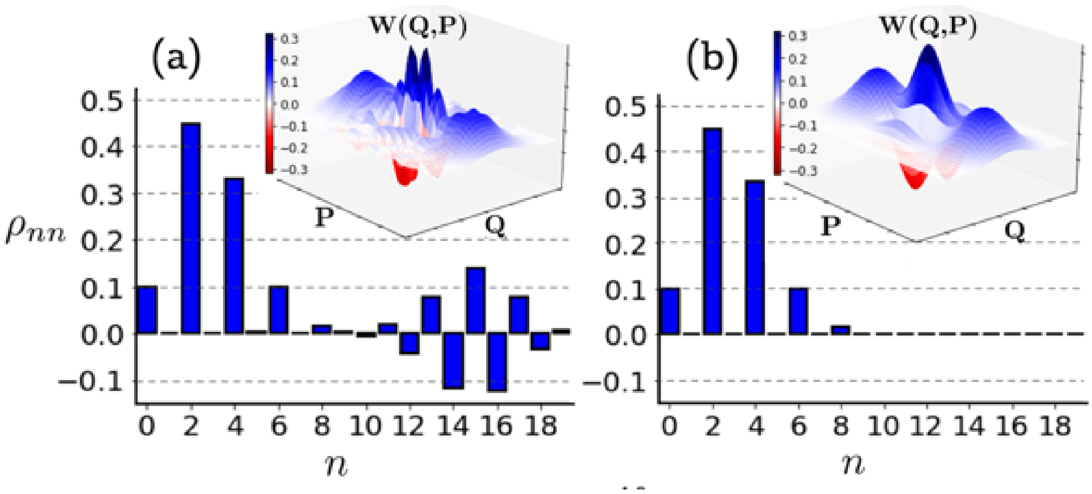

Figure 4.6: Loss-compensation for tomographed cat state of amplitude $\sqrt{3}$ after 30% loss and Hilbert space cut-off of $d = 20$, with (a) inversion using the generalized Bernoulli transformation and (b) inversion using SDP. The figure insets show the Wigner function for each state. We notice the negative diagonal entries for photon-numbers greater than 10 on the left pane

From the Fig. 4.6(a), we can see that inversion with generalized Bernoulli transformation fails to reliably reconstruct the state as confirmed by negative entries in diagonal (or negative probabilities). These errors become pronounced for low detector efficiencies at high photon-numbers as seen Fig. 4.6 (a) for the specific case of a loss-compensated cat state. Therefore, it becomes extremely crucial to have *a priori* information about the energy of the quantum state in order truncate the Hilbert space precisely to avoid numerical instabilities at high photon numbers. On the right in Fig. 4.6, we show the loss-compensated reconstruction using the proposed SDP in Eq. (4.27). One can clearly see that the inversion using SDPs successfully reconstructs the state after loss-compensation as evident from the absence of negative diagonal entries or smoothness and well-bounded nature of the reconstructed Wigner function. We emphasize that all the errors, i.e., $|\rho'_{i,j} - \rho_{i,j}|$, in the loss-degraded reconstructed density matrix elements are on the order of 10^{-3}, where ρ' is the loss-degraded experimentally reconstructed density matrix using 400 coherent probes and ρ is an ideal cat state that has undergone 30% losses. Thus we note that how small errors on density matrix elements from performing the tomographic procedure on a loss-degraded cat state give rise to an unphysical loss-compensated state using the analytical matrix inversion from Ref. [163], whereas inversion using SDPs guarantees the physicality of the loss-compensated state.

To further quantify the quality of the reconstruction using SDP inversion, we define a new parameter Q as

$$Q := \log[1 + \mathrm{T}(\rho, \sigma)], \tag{4.28}$$

where where $\mathrm{T}[\rho, \sigma]$ is the trace distance defined as

$$T(\rho, \sigma) := \frac{1}{2}||\rho - \sigma||_1 = \frac{1}{2}\mathrm{Tr}\left[\sqrt{(\rho - \sigma)^\dagger(\rho - \sigma)}\right], \tag{4.29}$$

where ρ and σ are the density matrices describing the reconstructed state and ideal state, respectively and $||.||_1$ is the ℓ^1-norm defined as $||M||_1 = \sum_i |\lambda_i|$ with λ_1 being the eigen values of the hermitian matrix $M = \rho - \sigma$. We note that $0 \leq T(\rho, \sigma) \leq 1$, where the equality from the left is satisfied for $\rho = \sigma$ and the right equality holds for orthogonal states. As a result, we get $Q = 0$ when the reconstruction is perfect and any increment in Q from zero quantifies the errors in the reconstruction. We now calculate the Q parameter using both Bernoulli transformation and the proposed SDP method for a cat state and a single-photon Fock state. Results are displayed in Fig. 4.6. The trace distance is calculated between the reconstructed state, ρ and the ideal state, σ which is then used to determine Q parameter.

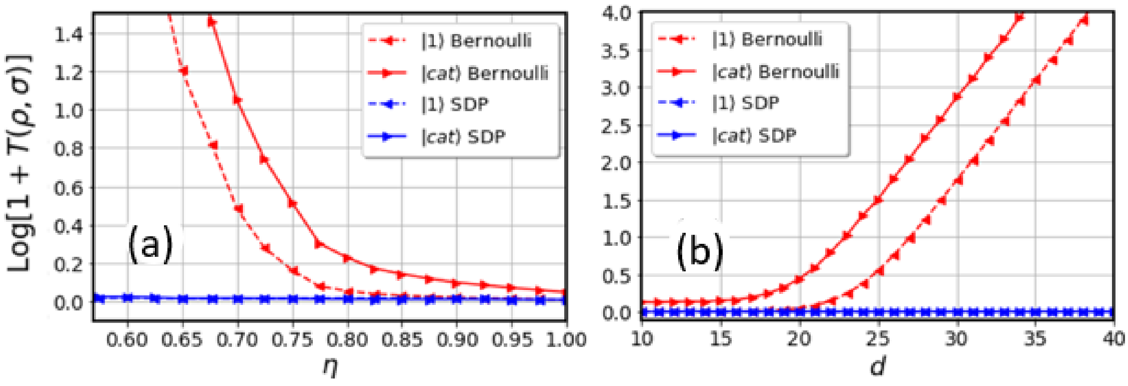

Figure 4.7: (a) The logarithm of the trace-distance between the reconstructed state and the ideal target state is plotted against η for the Hilber space cut-off of $d = 20$. (b) The logarithm of the trace-distance is plotted against the Hilbert space truncation d for given $\eta = 0.70$. Both of these simulations are done for a cat state and a single-photon Fock state. We note that $T(\rho, \sigma) > 1$ occurs due to the unphysical reconstruction of ρ and large non-positive diagonal elements.

In Fig. 4.7 (a), we plot the Q versus overall loss η for a given Hilbert space truncation of $d = 20$. One can clearly see that the validity of the loss-compensation can heavily depend on the overall loss parameter η if the loss-compensation was done using the generalized Bernoulli transformation. On the other hand, loss-compensation with SDP does not show any dependence on η and it works much better than Bernoulli transformation for a typical range of overall losses in an experiment as seen from $Q \approx 0$, the blue curves in the Fig. 4.7.

In Fig. 4.7 (b), we see the effects of Hibert space truncation for a given detection efficiency $\eta = 0.70$. We note that the deviation (or Q parameter) grows quickly as d increases in the case of inversion with Bernoulli transformation. However, Q remains both small and relatively independent of d when using SDP. As a result, the proposed loss-compensation method is significantly improves on loss-compensation in state tomography.

Furthermore, we can use this technique to our advantage in mitigating detector saturation threshold for PNR measurements. By introducing a well-calibrated loss right before the PNR detector, we can decrease the energy of the interfered state to be measured which allows us to use a lower maximum amplitude for $|\alpha_{\max}\rangle$ and also reduces the energy of the unknown state. In the next section, we show that adding the well-calibrated losses prior to the interference in the path of unknown state as well as coherent state probes has the same effect of having losses after the interference as shown in Fig. 4.8, left.

4.3.4 Equivalence of photon-number distributions

Here, we show that both networks in Fig. 4.8 leads to same photon-number distribution. The left configuration has a well-calibrated beamsplitter of transmission η right before a perfect PNR detector. The right configuration has beamsplitters with transmission η in both paths right before the balanced BS. The interfered signal is then detected by a perfect PNR detector.

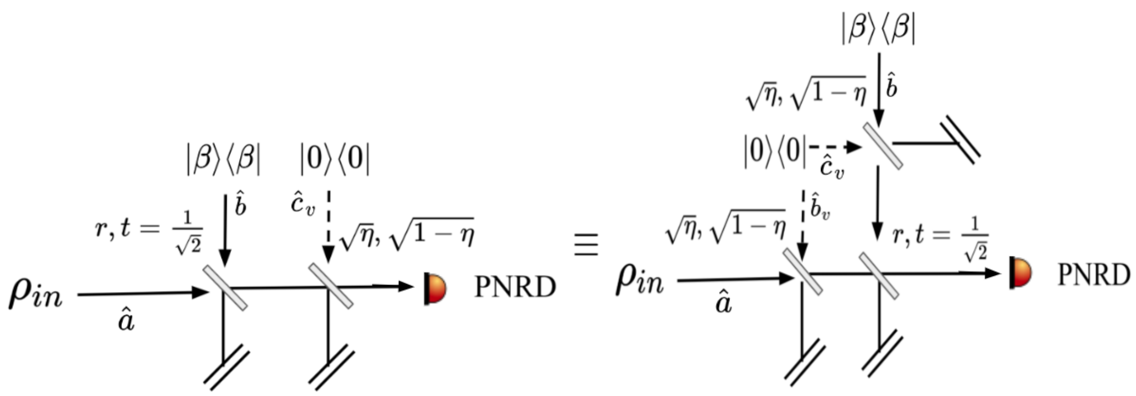

Figure 4.8: Schematic of the loss model. Left and right networks produce the same photon-number distribution.

To show the equivalence of the photon-number distributions measured in each configuration, we adapt the approach originally introduced in Ref. [1]. The signal and coherent states are described by annihilation operators $\hat{a}$ and $\hat{b}$ respectively, and $\hat{c}_v$ and $\hat{d}_v$ are vacuum modes coming from the unused port of the beamsplitters. For a perfect PNR detector, the probability of measuring n photons is given by [164]

$$P(N = n) = \left\langle : \frac{\hat{N}^n}{n!} e^{-\hat{N}} : \right\rangle_{\rho_{in}}, \tag{4.30}$$

where $\hat{N} = \hat{d}^\dagger \hat{d}$ is the photon-number operator of the detection mode and the expectation value is calculated over the initial states, and :: is the normal ordering of the creation and annihilation operators. By employing the Heisenberg picture, we first determine the detection mode in terms of input modes for the network on the left of Fig. 4.8. The input mode denoted by annihilation operator, $\hat{a}$ evolves to

$$\text{After first BS:} \;\; \hat{a} \rightarrow \frac{\hat{a} + \hat{b}}{\sqrt{2}} \tag{4.31}$$

$$\text{After second BS:} \;\; \sqrt{\eta}\left(\frac{\hat{a} + \hat{b}}{\sqrt{2}}\right) + \sqrt{1-\eta}\,\hat{c}_v \tag{4.32}$$

Since the input states for mode $\hat{b}$ and $\hat{c}_v$ are coherent and vacuum states respectively, the normal ordering allows to treat them as complex numbers. As a result, the effective photon-number operator is given by

$$\hat{N}^L_{\text{eff.}} = \hat{d}^{\dagger L} \hat{d}^L, \tag{4.33}$$

where the detection mode is

$$\hat{d}^L = \sqrt{\eta}\left(\frac{\hat{a} + \beta}{\sqrt{2}}\right). \tag{4.34}$$

Likewise, for the right network, we have

$$\text{After first BS:}\quad \hat{a} \rightarrow \sqrt{\eta}\hat{a} + \sqrt{1-\eta}\hat{b}_v \tag{4.35}$$

$$\text{After top BS:}\quad \hat{b} \rightarrow \sqrt{\eta}\hat{b} + \sqrt{1-\eta}\hat{c}_v \tag{4.36}$$

$$\text{After balanced BS:}\quad \hat{d} = \frac{1}{\sqrt{2}}(\sqrt{\eta}\hat{a} + \sqrt{1-\eta}\hat{b}_v + \sqrt{\eta}\hat{b} + \sqrt{1-\eta}\hat{c}_v),$$

where $\hat{c}_v$, $\hat{b}_v$ are vacuum modes and $\hat{b}$ is a coherent state. We again utilize the fact that normal ordering allows coherent states to be represented by a complex number and the vacuum state can also be considered as a coherent state with zero amplitude. Thus, the detection mode can be further simplified as

$$\hat{d}^R = \sqrt{\eta}\left(\frac{\hat{a}+\beta}{\sqrt{2}}\right). \tag{4.37}$$

From Eq. (4.34) and Eq. (4.37), one can see that both networks have the same detection mode, therefore would produce the same photon-number distribution for a given quantum state, ρ_{in} under investigation. This shows that by adding the well-calibrated losses, one can alleviate the detector threshold by a considerable amount. This plays a crucial role when one needs to characterize a highly energetic state with the state-of-the-art PNR technology that only allows to resolve photons in the order of tens.

4.4 Mode mismatch correction

We now consider the effects of mode mismatch between the fields of the unknown state and coherent states (or local oscillators (LOs)) on the measured photon-number distributions. In contrast to balanced homodyne detection (BHD), the imperfect modematching between the coherent state and the signal fields cannot simply be treated as losses in the proposed scheme. This can be understood as follows: In

BHD, the measured photocurrent difference is proportional to only the interference term, i.e, $I_- \propto \hat{a}^\dagger \alpha_{LO} + \hat{a}\alpha^*_{LO}$, which implies that only the overlapping portion of the signal field gets amplified by the strong local oscillator (LO) and the non-overlapping portion is considered as losses. We now show that this will no longer be the case with the proposed method.

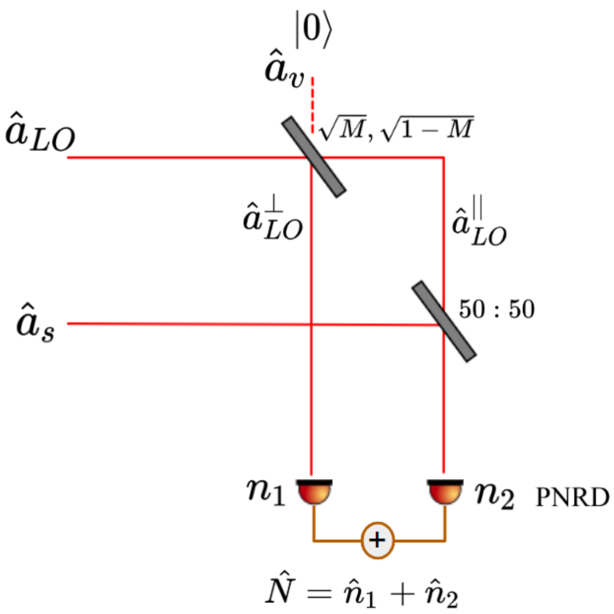

Figure 4.9: Model for mode mismatch analysis.

As displayed in Fig 4.9, the interference between the local oscillator and signal mode, denoted by $\hat{a}_{LO}$ and $\hat{a}_s$ respectively, can be decomposed into two orthogonal modes that each reach the PNR detector. The LO can be seen as interfering with vacuum mode $\hat{a}_v$ to be split into a component that overlaps (interferes) entirely with the signal field, $\hat{a}^{||}_{LO}$, and an orthogonal component, $\hat{a}^{\perp}_{LO}$, that proceeds to the detector without interacting with the signal. Defining the mode-mismatch parameter M, as the transmission of the fictitious beamsplitter decomposing the components of the LO and making use of the Heisenberg picture, we get

$$\hat{a}_{LO}^{\perp} = \sqrt{1-M}\hat{a}_{LO} + \sqrt{M}\hat{a}_v. \tag{4.38}$$

$$\hat{a}_{LO}^{||} = -\sqrt{M}\hat{a}_{LO} + \sqrt{1-M}\hat{a}_v. \tag{4.39}$$

Likewise, the signal mode after interfering with $\hat{a}_{LO}^{||}$ at the balanced BS evolves to

$$\hat{a}_s \to \hat{U}_{BS}\hat{a}_s\hat{U}_{BS}^{\dagger} = \frac{\hat{a}_s + \hat{a}_{LO}^{||}}{\sqrt{2}}, \tag{4.40}$$

where $\hat{U}_{BS}$ is the unitary operator of the balanced beamsplitter. We then find the photon-number operators corresponding to both the fields reaching to the PNR detectors. Thus, we get

$$\hat{n}_1 = (\hat{a}_{LO}^{\perp})^{\dagger}\hat{a}_{LO}^{\perp} \tag{4.41}$$

$$\hat{n}_2 = \left(\frac{\hat{a}_s + \hat{a}_{LO}^{||}}{\sqrt{2}}\right)^{\dagger}\left(\frac{\hat{a}_s + \hat{a}_{LO}^{||}}{\sqrt{2}}\right) = \hat{U}_{BS}\hat{a}_s^{\dagger}\hat{a}_s\hat{U}_{BS}^{\dagger} \tag{4.42}$$

As a result, the total number operator is

$$\hat{N} = \hat{n}_1 + \hat{n}_2 = (\hat{a}_{LO}^{\perp})^{\dagger}\hat{a}_{LO}^{\perp} + \hat{U}_{BS}\hat{a}_s^{\dagger}\hat{a}_s\hat{U}_{BS}^{\dagger}. \tag{4.43}$$

By employing Eq. 4.30, one can further determine the probability of detecting total $n = n_1 + n_2$ photons by both the detectors in Fig. 4.9 as

$$P(n = n_1 + n_2) = \left\langle : \frac{\hat{N}^n}{n!} e^{-\hat{N}} : \right\rangle_{\rho_{in}}, \tag{4.44}$$

where $\hat{N} = \hat{n}_1 + \hat{n}_2$ is the two-mode photon-number operator. We then use the fact that in the normal ordering formulation, the annihilation operators denoting coherent states can be simply treated as complex variables, $\alpha_{LO}^{\perp}$ and $\alpha_{LO}^{||}$. Therefore, we have

$$\hat{N} = (1-M)|\alpha_{LO}|^2 + \hat{U}_{BS}\hat{a}_s^{\dagger}\hat{a}_s\hat{U}_{BS}^{\dagger}. \tag{4.45}$$

Using Eq. (4.44) and Eq. (4.45) results in

$$P(n) = \left\langle : e^{-\left[(1-M)|\alpha_{LO}|^2 + \hat{U}_{BS}\hat{a}_s^{\dagger}\hat{a}_s\hat{U}_{BS}^{\dagger}\right]} \frac{\left[(1-M)|\alpha_{LO}|^2 + \hat{U}_{BS}\hat{a}_s^{\dagger}\hat{a}_s\hat{U}_{BS}^{\dagger}\right]^n}{n!} : \right\rangle_{\rho_{in}} \tag{4.46}$$

After further simplification, we get

$$\begin{aligned} P(n) &= \left\langle : e^{-\left[(1-M)|\alpha_{LO}|^2 + \hat{U}_{BS}\hat{a}_s^{\dagger}\hat{a}_s\hat{U}_{BS}^{\dagger}\right]} \sum_{l=0}^{n} \binom{n}{l} \frac{\left(\hat{U}_{BS}\hat{a}_s^{\dagger}\hat{a}_s\hat{U}_{BS}^{\dagger}\right)^l [(1-M)|\alpha_{LO}|^2]^{n-l}}{n!} : \right\rangle_{\rho_{in}} \\ &= \sum_{l=0}^{n} \left\langle : \frac{e^{\hat{U}_{BS}\hat{a}_s^{\dagger}\hat{a}_s\hat{U}_{BS}^{\dagger}} \left(\hat{U}_{BS}\hat{a}_s^{\dagger}\hat{a}_s\hat{U}_{BS}^{\dagger}\right)^l}{l!} : \right\rangle_{\rho_{in}} \frac{e^{-[(1-M)|\alpha_{LO}|^2]}[(1-M)|\alpha_{LO}|^2]^{n-l}}{(n-l)!} \end{aligned} \tag{4.47}$$

From Eq. (4.47), one can see that the probability of detecting n photons is the convolution of two probability distributions. The first term in the normal ordering form corresponds to detecting l photons in the signal mode after the interference with $\hat{a}_{LO}^{||}$ while the second Poissonian distribution term is the probability of $(n-l)$ photons being detected in the orthogonal LO mode, $\hat{a}_{LO}^{\perp}$. We can further rewrite Eq. (4.47) in a compact way as

$$P(n) = \sum_{l=0}^{n} P^{||}(l)P^{\perp}(n-l). \tag{4.48}$$

Note that $P^{\perp}(n-l)$ can be determined by knowing the overlap parameter, M, which is experimentally measured from a bright-field visibility measurement [165]. The overlap parameter is defined as

$$M = \frac{\mathcal{V}}{2-\mathcal{V}}. \tag{4.49}$$

Once M is determined, we have the information about the amplitude of the non-overlapping LO field, i.e, $\sqrt{1-M}\alpha_{LO}$, which allows us to determine $P^{\perp}(n-l)$. Next, we can simply invert Eq. (4.48) in order to reconstruct the true photon-number distribution for the interfered field of unknown state and the mode matched part of LO field $|\alpha_{LO}^{||}\rangle = |\sqrt{M}\alpha_{LO}\rangle$. Note that for classical visibility nearing unity (as in our experiment), $\mathcal{V} \approx \sqrt{M}$.

4.4.1 Experimental noise

A crucial point is the impact of inevitable experimental fluctuations on the numerical stability of the solution in Eq. (4.12). The linear equation for the overlap measurements is

$$\mathbf{O} = \mathbf{C}\mathbf{P}. \tag{4.50}$$

In the ideal case, the solution of this linear equation is then

$$\mathbf{P} = \mathbf{C}^{-1}\mathbf{O}. \tag{4.51}$$

If we have some noise or experimental fluctuations in the experiment which leads to measuring $\mathbf{O}'$ instead of the true overlap measurements $\mathbf{O}$. Thus we have

$$\mathbf{O}' = \mathbf{C}\mathbf{P}. \tag{4.52}$$

In this case, the new solution is

$$\mathbf{P}' = \mathbf{C}^{-1}\mathbf{O}' = \mathbf{C}^{-1}\mathbf{O} + \mathbf{C}^{-1}\delta\mathbf{O}, \tag{4.53}$$

where $\delta\mathbf{O}$ is the deviation from the true overlap measurements, i.e., $\delta\mathbf{O} = \mathbf{O}' - \mathbf{O}$. One can see from Eq. (4.53) that the new solution $\mathbf{P}'$ has an additional noise term $\mathbf{C}^{-1}\delta\mathbf{O}$ to the original solution $\mathbf{P} = \mathbf{C}^{-1}\mathbf{O}$. The errors, $\delta\mathbf{O}$ in the overlap measurements gets amplified by $\mathbf{C}^{-1}$ and can potentially lead to unphysical results. Thus the invertible nature of the matrix $\mathbf{C}$ determines the numerical stability of Eq. (4.50). To further quantify the sensitivity of the inversion against experimental noise, a parameter known as the condition number of matrix $\mathbf{C}$ is formally defined as

$$\text{Condition}(\mathbf{C}) = \frac{\frac{||\mathbf{C^{-1}}\delta\mathbf{O}'||}{||\mathbf{C^{-1}O}||}}{\frac{|\delta\mathbf{O}||}{||\mathbf{O}||}}, \tag{4.54}$$

where $||.||$ is the ℓ^2- norm. The condition number is essentially the ratio of relative changes in $\mathbf{P}$ to relative changes in $\mathbf{O}$. If the condition number is not too much larger than one, then the linear equation governed by the matrix $\mathbf{C}$ is well-conditioned, thereby its inverse can be approximated with high accuracy even in the presence of reasonable experimental noise. If the condition number is much larger than 1, then the linear equation will be considered as ill-conditioned and any errors in the overlap measurements would substantially alter the solution for $\mathbf{P}$. A detailed discussion on the nature of $\mathbf{C}$ and how it changes the reconstruction can be found in Ref. [166]. In our case, by the nature of its slowly-decaying Poissonian coefficients, matrix $\mathbf{C}$ necessarily contains both large and small entries and, therefore, both large and small singular values, which makes it ill conditioned [167], and therefore its inversion extremely sensitive to experimental fluctuations in the measured photon statistics or the inversion is numerical unstable. In order to suppress these instabilities, we choose to use a Tikhonov regularization procedure [168], formulated as the SDP problem

$$\begin{aligned} &\underset{\rho}{\text{Minimize}} \quad && ||\mathbf{O} - \mathbf{CP}||_2 + \gamma||\mathbf{P}||_\mathbf{2} \\ &\text{Subject to} && \rho \geq 0, \quad \text{Tr}[\rho] = 1, \end{aligned} \tag{4.55}$$

where γ is a small regularization parameter set according to the noise level [169]. The optimization still remains quadratic convex which can be solved efficiently. We now perform some numerical simulations in the presence of amplitude and phase noise in the coherent state probes. We model our noise in the same spirit as [91], [92] by introducing artificial fluctuations in the amplitude and phase of the coherent states, $|\alpha^j\rangle$. The amplitude noise is sampled using a Gaussian distribution of zero mean and standard deviation of $\sigma = 2\%|\alpha^j|^2$, and likewise the phase noise is sampled from $\sigma \in [-1, 1]$ degrees using a Gaussian distribution with zero mean.

To demonstrate the effect of experimental fluctuations on the reconstruction, we numerically performed the state tomography of an ideal 4-photon Fock state and the statistical mixture desribed by $\rho_{\text{mix}} = 0.8|5\rangle\langle 5| + 0.2|\beta\rangle\langle\beta|$ in the presence of 50% detection losses, where the varying coherent state probes now have both phase and amplitude noise. Numerical results are displayed in Fig. 4.10 with 40 amplitudes and 40 phases of coherent states. Evidently, we are able to identify the Wigner functions; however, we now see the appearance of noise-induced ripples as shown in Fig. 4.10a, which obfuscate the differences between the pure Fock state and the mixture. In order to suppress the noise effects, we repeat the experiment $N = 30$ times in order to obtain smooth Wigner functions by averaging the overlap measurements. From Fig. 4.10b, we can clearly see the ripples become diminished, which demonstrates the rather intuitive result that performing multiple measurements in the presence of noise can improve resolution. We note that the added noise in these numerical simulations is larger than the typical noise present in the well stabilized lasers with built-in noise eater servos.

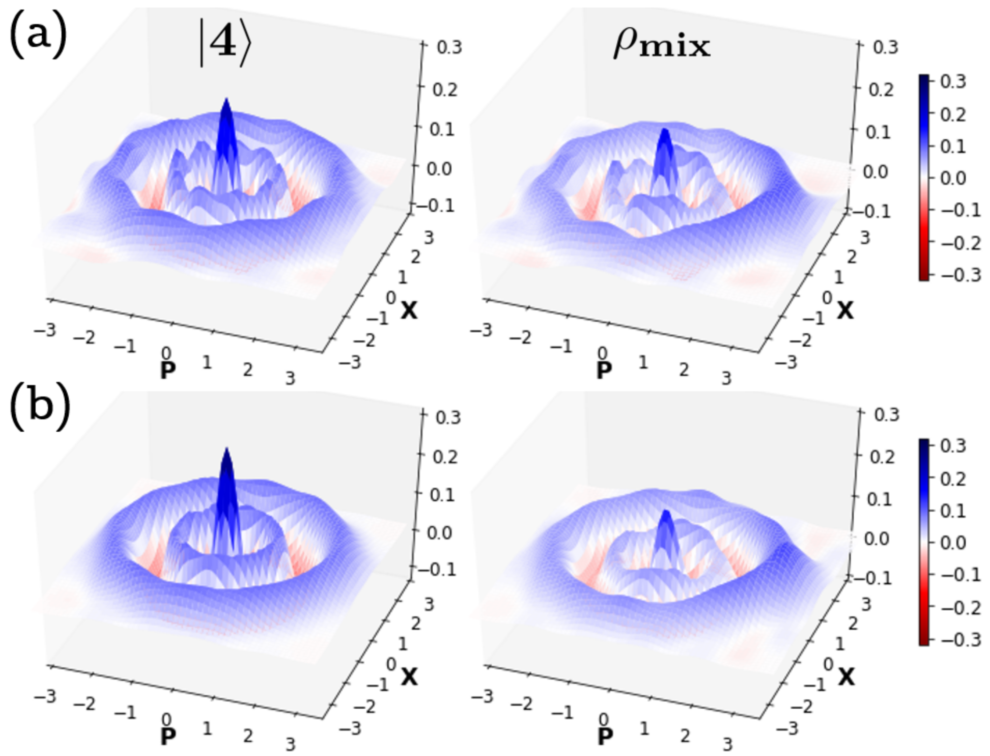

Figure 4.10: Reconstructions of an ideal 4-photon Fock state and statistical mixture following a 50% loss in the presence of noise. (a) The coherent state probes have noisy fluctuations of 2% intensity and 1 degree in phase. (b) Averaging noisy measurement outcomes produces a smoothing effect on the reconstructed states.

Furthermore, we note that this procedure remains robust and state-independent in the sense that allowing γ to vary by an order of magnitude (from 0.001 to 0.01) negligibly impacts the state reconstruction in each case considered, as measured by the change in fidelity with the appropriate target state. Several other kinds of regularization techniques have been explored for state tomography, process tomography, and detector tomography [90]–[92], [170]–[172].

4.4.2 High-loss compensation

In this section, we show that quantum states with losses greater than 50% can also be accurately tomographed and compensated for loss even in the presence of noise. However, increasing loss requires greater accuracy in the measured loss-degraded density matrix for the reconstruction to be valid. This is not prohibitive to the success and simply requires increasing the number of overlap measurements until the desired accuracy in the tomographic procedure is reached.

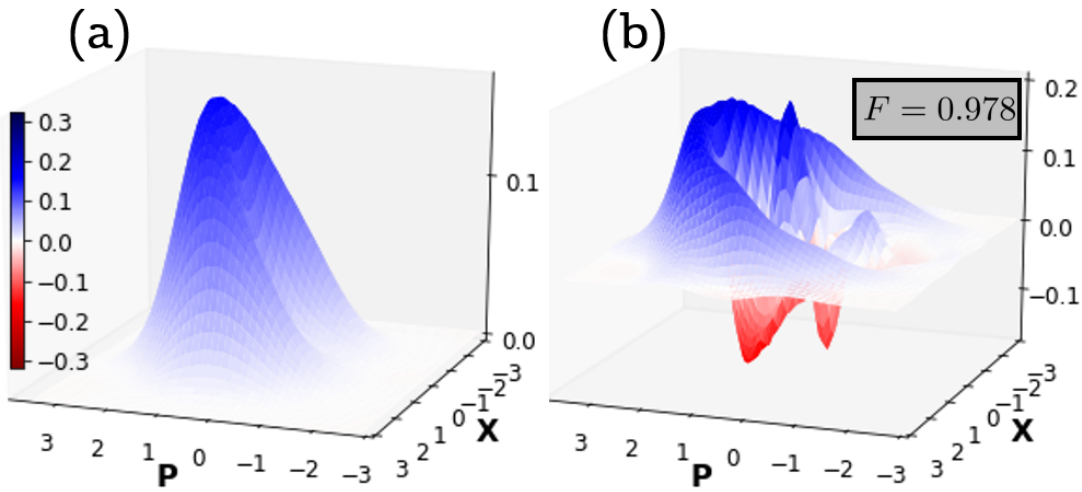

Figure 4.11: (a) Reconstruction for the superposition $\frac{1}{\sqrt{2}}(|2\rangle + |3\rangle)$ after 70% loss in the presence of noise on the tomographic probes. (b) loss-compensated reconstruction using SDP. We notice that the negativity of the Wigner function is recovered.

Nonetheless, we demonstrate that the process is successful for high losses in the presence of noise without an undue requirement on the number of measurements to be made. For the state $|\psi\rangle = \frac{1}{\sqrt{2}}(|2\rangle + |3\rangle)$, the reconstruction is displayed in Fig. 4.11 in the presence of a known 70% loss with phase and amplitude fluctuations on the coherent state probes. The tomography is performed with coherent states at 40 amplitudes and 40 phases with 0.5% intensity 0.5 degree phase noise sampled using Gaussian distributions. The overall fidelity of the loss-compensated state with the target is $F = 0.978$. The state reconstruction can be further improved by increasing the number of measurements and by averaging many experimental runs as discussed above.

This concludes the theoretical framework for the proposed generalized overlap state tomography method. We now turn to experimental implementations for a weak coherent state of amplitude and a heralded single-photon Fock state.

4.5 Experimental implementation

The experimental setup displayed in Fig. 4.12 is identical to our previous implementation of WVBW tomography detailed in chapter 3. It is based on a very stable CW Nd:YAG laser whose undoubled output provided all coherent states (or LO) upon phase and amplitude modulations by a computer controlled piezoelectric-actuated mirror and a home-made $RbTiOAsO_4$ electro-optic modulator, respectively. The calibrated coherent-state amplitude range was $|\alpha| = 0.138(2)$ to $0.339(3)$, in six steps, calibrated by our PNR detector, a superconducting transition edge sensor (TES) [133], [149]. The calibration was done by comparing the TES photon statistics to that of a Poisson distribution with the signal beam blocked as detailed in our previous implementation [89]. The phase steps were calibrated by scanning the interference fringe between the OPO seed beam and the coherent state beam, which provided a set of 10 voltage values for the PZT mirror corresponding to 10 discrete steps of 0.58(5) radians.

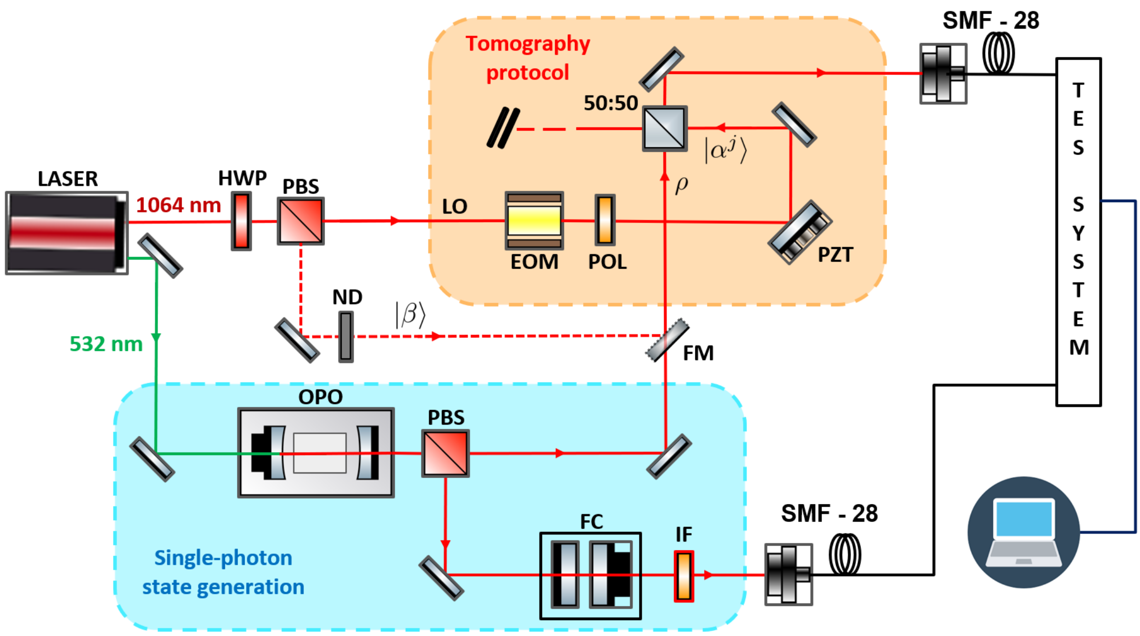

Figure 4.12: Experimental setup. The tomography protocol is contained in the orange box where the mode-matched LO is interfered with the state ρ. When the FM is in position, tomography for the coherent state, β, is performed; otherwise, ρ is the single-photon state generated in the aqua colored box. EOM, electro-optic modulator; FC, filter cavity; FM, flip mirror; HWP, half-wave plate; IF, interference filter; LO, local oscillator; ND, neutral-density filter; OPO, optical parametric oscillator; PBS, polarizing beamsplitter; POL, polarizer; PZT, piezoelectric transducer.

The tomography of a quantum states is performed by interfering a mode-matched local oscillator (LO) with the signal state, ρ, at a balanced beamsplitter followed by detection of one output mode using a photon-number resolving transition-edge sensor (TES) as shown in Fig. 4.12. A portion of the LO is split and strongly attenuated by neutral density (ND) filters to be used as a coherent state, $|\beta\rangle$, for the signal when the flip mirror is engaged. When the flip mirror is not in place, the signal is a single-photon source based on heralded, cavity-enhanced type-II spontaneous-parametric downconversion from a periodically-poled $KTiOPO_4$ crystal. As discussed in chapter 3, the spectral and spatial filtering was achieved by the optical parametric oscillator created by placing the crystal in a resonant cavity and an additional Fabry-Perot filter cavity on the heralding arm as shown in Fig. 4.12. The cavities were Pound-Drever-Hall-locked [145] using a portion of the LO in an "on/off" configuration as described in

Ref. [89]. The coherent-state probes derived from the LO were amplitude modulated with a combination of polarizer and electro-optic modulator (EOM) and were phase controlled with a mirror-mounted piezoelectric actuator (PZT). Extensive details on the single-photon source, mode filtering, and the LO amplitude calibration using the TES can also be found in chapter 3.

4.5.1 Coherent state tomography

First, we implemented the generalized overlap tomography protocol for a weak coherent state. The rationale for measuring a coherent state was to display a phase-dependent, i.e. non-cylindrically symmetric structure in phase space. The coherent state $|\beta\rangle$ was chosen $|\beta| = 0.191(3)$, as calibrated by the TES Poissonian photon statistics. For each of the 60 coherent-state probes $|\alpha_j\rangle$, data was acquired for approximately 3 seconds to obtain $\sim 10^5$ events from which to construct the photon-number probability distributions. We then deconvolve the effects of mode-mismatch on the measured PNR distribution as discussed in Section 4.4. We measured the mode overlap parameter of $M = 0.83(2)$ of the signal coherent state $|\beta\rangle$ with the coherent state probes (LO in the Fig. 4.12) and deconvolve the Poissonian distribution of the mode-mismatched $|\sqrt{1-M}\alpha^j\rangle^{\perp}$ from our measured PNR statistics as per Eq. 4.48. It is very important to note that the overlap measurements obtained from the expectation of parity are now between $\rho = |\beta\rangle\langle\beta|$ and $|\sqrt{M}\alpha^j\rangle^{||}$ for each coherent state probe, and therefore the coefficient matrix $\mathbf{C}$ must be modified accordingly. This is achieved by simply multiplying the measured coherent state amplitudes $|\alpha_j|$'s by the factor $\sqrt{M}$.

The SDP tomography results after correcting for mode mismatch are displayed on Fig. 4.13. Examining the magnitude of the density matrix elements, we clearly see that the diagonal and off-diagonal terms of ρ were both successfully reconstructed. The phase and amplitude accuracy is more evident when comparing the associated

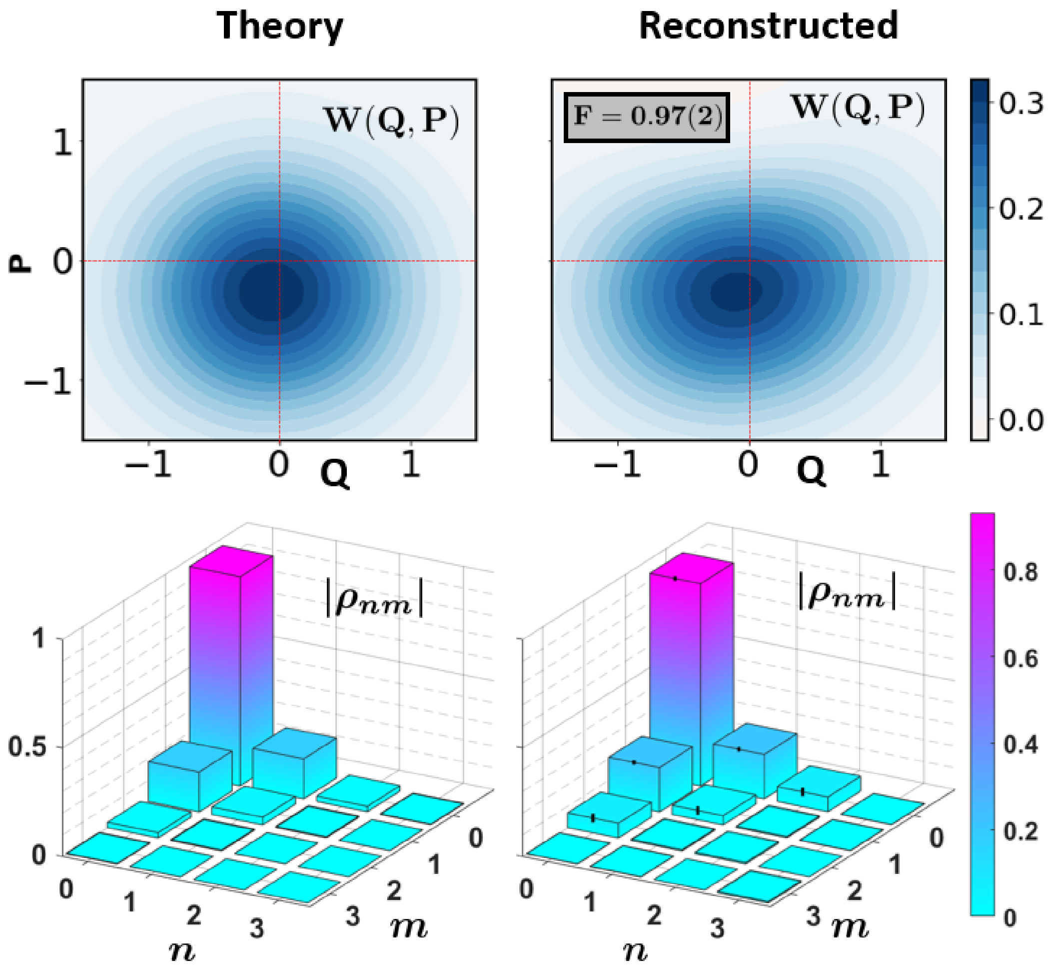

Figure 4.13: Tomography of a weak coherent state. Bottom Left, absolute value of the target (theory) density matrix elements and its Wigner function, top left. Right, reconstructed density matrix and associated Wigner function. The black error bars are obtained from the measurement statistics.

Wigner functions plotted in Fig. 4.13, right, where the red dashed lines delineate the zero axis values. We achieve a fidelity of $F = 0.97(2)$ between the reconstructed state, ρ, and the target pure state, $|\beta\rangle$ calibrated by the TES. The slight asymmetry of the Wigner function is imputable to residual phase noise in our measurements as we only use passive noise cancellation techniques for the optical paths. Imperfections in phase control and stability resulted in approximately 0.05 radians of phase-error on probe calibrations that contribute to the slight asymmetry in the experimentally constructed Wigner functions of the coherent state.

4.5.2 Single-photon Fock state tomography

We then performed the tomography of a heralded single-photon Fock state. The reconstructed density matrices and constructed Wigner functions are shown in Fig.4.14. On the top left, we have the mode-mismatch corrected reconstruction for a single-

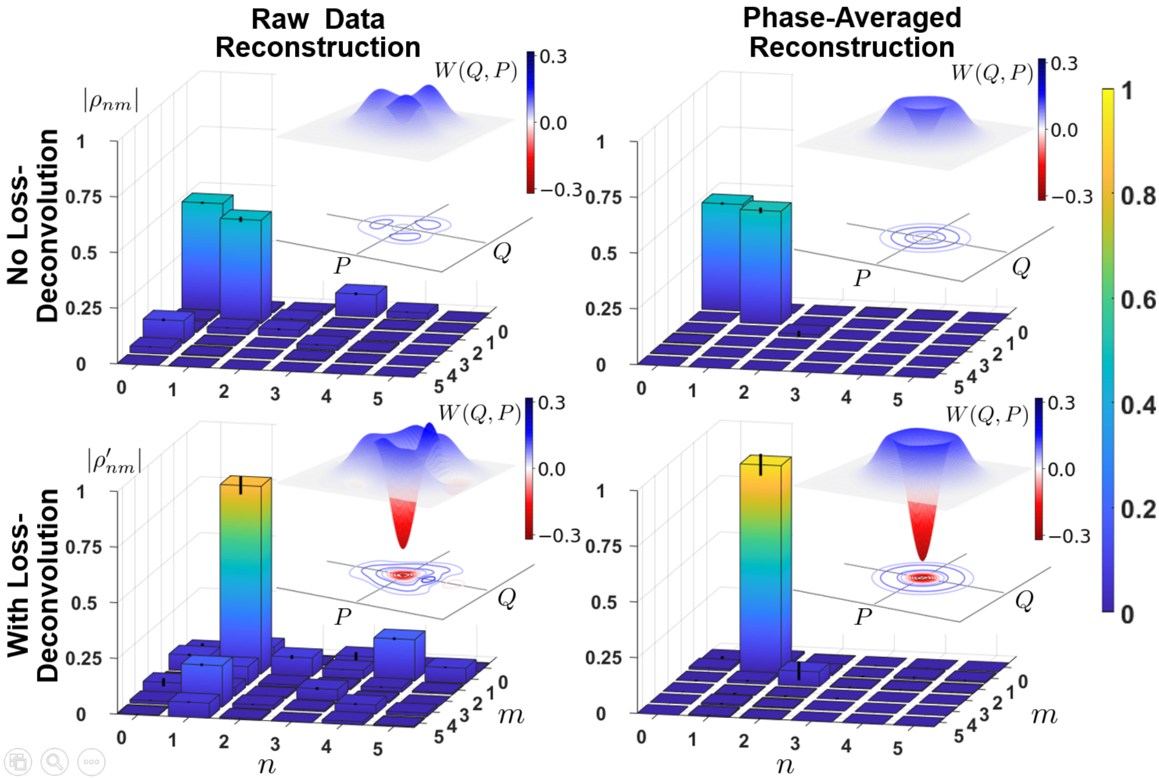

Figure 4.14: Generalized overlap tomography of a single-photon Fock state. Top row, SDP with mode mismatch corrected but no correction for losses. Bottom row, loss-deconvoluting SDP reconstruction. Left column, direct reconstructions. Right column, reconstructions using phase-averaged measurements. Reconstruction fidelities are 0.85(8) and for the bottom left panel and 0.94(6) for the bottom right panel. Inset: Wigner functions calculated from reconstructed density matrices.

photon Fock state and the bottom left displays the loss-compensated reconstruction where losses were calibrated by measuring the heralding ratio as discussed in chapter 3. The mode overlap parameter, $M = 0.86(2)$ was measured using the bright field visibility of the interference between OPO seed transmission and the LO field.

Due to the nature of our heralded source undergoing an overall loss, η, we expect to measure a statistical mixture of the one-photon and vacuum states which has a

rotationally symmetric Wigner function [89], [122] by the virtue of the density matrix being diagonal in the photon-number basis. Under this assumption, an average over the optical phases of the coherent probes can be performed, yielding the results on the right column of Fig. 4.14. It is, of course, also interesting to examine the unaveraged measurements, left column of Fig. 4.14, in order to assess the quality of our tomographic reconstruction. Despite the effects of experimental noise, visible in the off-diagonal terms, the reconstruction has a fidelity of $\mathcal{F} = 0.94(2)$ with the expected mixture where $\eta = 0.50(1)$, as measured by the heralding ratio as in chapter 3.
The performance of the noise deconvolution by SDP is displayed on the bottom row of Fig. 4.14. The overall loss was determined to be $\eta = 0.50(1)$ by measuring the heralding ratio, as was done in chapter 3. Assuming no prior knowledge about the state other than this calibrated measurement loss, the reconstructed loss-compensated state is depicted in the bottom left of Fig. 4.14, where we achieved a fidelity of $F = 0.85(8)$ with a single-photon Fock state. While the phase noise of the LO does not contribute to the overlap measurements with a phase-insensitive state such as heralded single-photon Fock state, the amplitude noise and other experimental fluctuations might be attributed to the ripples seen in the reconstructed Wigner function.

Adding the assumption of a phase-invariant state and averaging measurements as in Refs. [122], [123], [173] for each of the ten phases before compensating for loss yielded the nearly perfect reconstruction shown in the bottom right panel, where we achieved $F = 0.94(6)$. It is worth emphasizing that the negativity of the single-photon Wigner function was fully recovered after compensating for loss and measured mode-mismatch of $M = 0.86(2)$ (Fig. 4.14, bottom row), even though the 50% loss level suppressed negativity when no loss deconvolution was performed (Fig. 4.14, top row).
Finally, it is important to note that the maximum amplitude probe was $|\alpha_{\max}| \simeq 0.34$, which led to a mean photon number detection of $\langle N \rangle \simeq 0.56$, yet our overlap tomography accurately reconstructed the Wigner function at quadrature coordinates beyond q or $p = 3$ (consistent with our truncation of the Hilbert space to n_o=5).

This is in stark contrast to the WVBW case of chapter 3, in which the maximum of the Wigner function, at q or $p = 1$, could not be reached using displacements with $|\alpha_{\max}| \simeq 0.80$ and $\langle N \rangle \simeq 1.64$. Therefore, generalized overlap tomography necessitates PNR detection of significantly lower photon flux while still requiring the detection of only a single field mode.

4.6 Conclusions

In this chapter, we proposed and experimentally demonstrated the generalized overlap quantum state tomography using PNR measurements on a single field-mode. Our approach, *(i)*, makes no prior assumption on the initial state *(ii)*, exploits numerically efficient, noise-robust SDP that enforces physicality, *(iii)*, uses fewer, lower-amplitude probes that point-by-point WVBW tomography (which might outperform WVBW for complex states where fine resolution of the Wigner function is required), *(iv)*, implements no approximated displacement operations, *(v)*, requires only a *single* PNR detector and necessitates fewer measurements than densely probing the Wigner function [166], *(vi)*, compensates for known losses with fewer numerical instabilities.

Our approach is equally valid for other physical systems and can be readily applied in circuit quantum electrodynamics [174]. It could also be used to directly measure the purity of a quantum state by measuring the overlap between two copies of the same system, which allows access to the second order Rényi entropy extensively used to quantify the entanglement of many-body physical systems [175].

Finally, the proposed scheme can be simply extended to characterize a multi-mode quantum system by interfering with a multi-mode set of coherent states followed by measuring the overall parity of the state after the interference.

The work was supported by NSF grants PHY-1708023 and PHY-1820882 and it was carried jointly with Miller Eaton.

Chapter 5

Room Temperature Photon-number-resolving Segmented Detectors

> A measurement always causes the system to jump into an eigenstate of the dynamical variable that is being measured, the eigenvalue this eigenstate belongs to being equal to the result of the measurement.
>
> — P. A. M. Dirac (1958) in The Principles of Quantum Mechanics, p. 36

This chapter is adapted from the published paper titled, "Photon-number-resolving segmented detectors based on single-photon avalanche-photodiodes," Rajveer Nehra, Chun-Hung Chang, Qianhuan Yu, Andreas Beling, and Olivier Pfister, Opt. Express, 28, 3660-3675 (2020). Here, we investigate the feasibility and performance of photon-number-resolved photodetection employing single-photon avalanche photodiodes (SPADs) with low dark counts. While the main idea is to split n photons into m detection modes with a vanishing probability of more than one photon per mode, we investigate here a important variant of this situation where SPADs are side-coupled to the same waveguide rather than terminally coupled to a propagation tree. This prevents the nonideal SPAD quantum efficiency from contributing to photon loss.

We propose a concrete SPAD segmented waveguide detector based on a vertical directional coupler design, and characterize its performance by evaluating the purities of Positive-Operator-Valued Measures (POVMs) in terms of number of SPADs, photon loss, dark counts, and electrical cross-talk.

5.1 Introduction

Quantum measurements are essential to quantum information science and technology. Photon-Number-Resolving (PNR) detection, in particular, fully exploiting the corpuscular nature of classically undulatory light, is key in quantum metrology and sensing [84] and quantum technologies [83]. A PNR detector produces a signal that has a linear dependence with the number of incident photons, which allows it to resolve an n-photon state from $(n+1)$-photon state. Photon-number-resolving detectors have been realized with superconducting transition-edge sensors (TES) [58], [176], silicon photomultipliers [177], superconducting nanowires [65], [178]–[180], linear mode avalanche photodiodes (SPADs), and quantum-dot field-effect transistors [181], [182]. Moreover, methods based on spatial- and time-multiplexing of non-PNR detectors have been proposed for PNR measurements using SPADs [61]–[65]. Such proposals have been thoroughly modeled mathematically [183]–[186].

This chapter is organized as follows. In Section 5.2, we provide the mathematical formulation of quantum measurements. Section 5.3 details two models for splitting n photons over m modes, and we then conclude in Section 5.4.

5.2 Quantum measurements: collapse of a wavefunction

Quantum measurements are described by a set of hermitian operators acting on the Hilbert space of the system. An ideal quantum measurement originally postulated by John von Neumann says that a measurement performed on a quantum system instantaneously collapses the quantum state onto one of the eigenstates of measured observable [187]. Let us consider a spin-$\frac{1}{2}$ particle described by wavefunction $|\psi\rangle$ in two-dimensional Hilbert space spanned by $\hat{S}_z$ eigenstates $\{|\uparrow\rangle := [1 \;\; 0]^{\mathrm{T}}, |\downarrow\rangle := [0 \;\; 1]^{\mathrm{T}}\}$ as shown in Fig. (5.1).

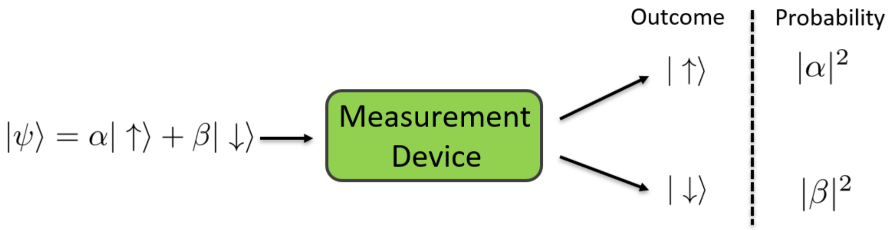

Figure 5.1: Visualization of a von Neumann measurement device.

An ensemble of these identically prepared particles is sent to a $\hat{S}_z$ measurement device which either registers $|\uparrow\rangle$ or $|\downarrow\rangle$ with probability $|\alpha|^2$ for $|\uparrow\rangle$ and $|\beta|^2$ for $|\downarrow\rangle$. This process can be completely described by the action of two projective operators, namely

$$\begin{aligned} \Pi_{|\uparrow\rangle} &= |\uparrow\rangle\langle\uparrow|, \\ \Pi_{|\downarrow\rangle} &= |\downarrow\rangle\langle\downarrow|. \end{aligned} \tag{5.1}$$

Furthermore, the probability of obtaining an outcome is given by the Born rule

$$P_{i=|\uparrow\rangle,|\downarrow\rangle} = \mathrm{Tr}[|\psi\rangle\langle\psi|(|i\rangle\langle i|)] = \langle\psi|i\rangle\langle i|\psi\rangle = |\langle i|\psi\rangle|^2. \tag{5.2}$$

Since these are the only two possible outcomes, the probabilities must add up to unity. Thus, we have

$$P_{|\uparrow\rangle} + P_{|\downarrow\rangle} = \mathrm{Tr}[|\psi\rangle\langle\psi|(|\uparrow\rangle\langle\uparrow|)] + \mathrm{Tr}[|\psi\rangle\langle\psi|(|\uparrow\rangle\langle\uparrow|)] = \langle\uparrow|\psi\rangle|^2 + |\langle\downarrow|\psi\rangle|^2 \tag{5.3}$$

$$= \mathrm{Tr}[|\psi\rangle\langle\psi|(|\uparrow\rangle\langle\uparrow| + |\downarrow\rangle\langle\downarrow|)] = |\alpha|^2 + |\beta|^2 = 1 \tag{5.4}$$

As a result, we see that Eq. (5.4) holds only if we have

$$|\uparrow\rangle\langle\uparrow| + |\downarrow\rangle\langle\downarrow| = \mathbb{I} \tag{5.5}$$

We now understand measuring light in the von Neumann measurement formalism. Consider a light prepared in an arbitrary quantum state written in photon-number basis as

$$|\psi\rangle = \sum_{n=0}^{\infty} \psi_n |n\rangle. \tag{5.6}$$

If this light is incident to an ideal photon-number-resolving device, the probability of measuring n photons is

$$P(n) = \mathrm{Tr}[|\psi\rangle\langle\psi|(|n\rangle\langle n|)] = |\psi_n|^2. \tag{5.7}$$

Since Fock states provide a complete basis. By the definition of their completeness property, we have

$$\sum_{n=0}^{\infty} |n\rangle\langle n| = \mathbb{I}. \tag{5.8}$$

As a result, the set of projectors $\{|n\rangle\langle n|; n \in \mathbb{N}\}$ completely describes an ideal photon-number-resolving detector. However, in a realistic case measurement devices do not necessarily implement projective measurements but more a general measurement known as Positive-Operator-Valued Measures (POVMs) which have been widely used to model photodetection [188], [189].

The POVMs are a set of Hermitian operators $\{\Pi_k\}$ with some properties discussed below. The probability of an outcome k is again given using the Born rule

$$p(k) = \mathrm{Tr}[\rho \Pi_k]. \tag{5.9}$$

- Completeness: Analogous to projective measurements, POVM measurements are also complete. For a measurement device sensitive to only K outcomes, we have
$$\sum_{k=0}^{K-1} \Pi_k = \mathbb{I}.$$
One can immediately see that this property is a restatement of the probabilities of all possible outcomes adding up to one.
$$\sum_{k=0}^{K-1} p(k) = \sum_{k=0}^{K-1} \mathrm{Tr}[\rho \Pi_k] = \mathrm{Tr}\left[\rho \sum_{k=0}^{K-1} \Pi_k\right] = 1$$
Therefore, characterizing a measurement device involves identifying the POVM elements corresponding to all possible measurement outcomes. This is formally known as quantum detector tomography discussed in detail in chapter 6. Experimental quantum-detector tomography has been achieved in a number of different situations [64], [91], [190].

- Orthogonality: Unlike projective measurements, POVMs are not necessarily orthogonal to each other, which implies that repeated POVM measurements might not result in the same outcome.

$$\Pi_k \Pi_l \neq \delta_{k,l} \Pi_k \tag{5.10}$$

We now consider the POVMs for a PNR detector with quantum efficiency η and no dark-count noise [1]. To model the detection losses, one can consider a physical case where a beamsplitter with transmission η and reflection $1-\eta$ is placed in front of an ideal PNR detector as depicted in Fig. 5.2.

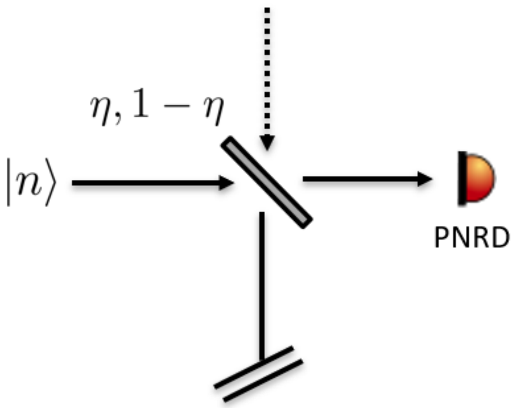

Figure 5.2: Model for a PNR detector with efficiency η, where η is the beamsplitter transmission.

For a given n-photon Fock state $|n\rangle$, the probability of k photons arriving to the detector is essentially the probability of k photons getting detected. With the BS transmission η, the conditional probability of k photons getting transmitted out of n input photons is given by the binomial probability defined as

$$P(k|n) = \binom{n}{k} \eta^k (1-\eta)^{n-k}. \tag{5.11}$$

One can further determine the probability of detecting k photons in the general case as

$$P_k = \sum_{n-k}^{\infty} P(k|n) P_n, \tag{5.12}$$

where $P(k|n)$ is the conditional probability of detecting k photons given n photons are incident to the detector, and $P(n)$ is the of having n photons in the given state

[1] For simplicity, we neglect the dark-count noise for now. We take it into account in Section 5.3.5.3

of light. In the operator formalism, the POVM operator for k-photon detection event can be defined as

$$\Pi_k = \sum_{n=k}^{\infty} P(k|n)|n\rangle\langle n|. \tag{5.13}$$

For example, we consider a coherent state of amplitude α with mean photon-number $\lambda = |\alpha^2|$, which is measured by an imperfect PNR detector. The photon-number distribution of the coherent state is

$$P_k = e^{-\lambda}\frac{\lambda^k}{k!}. \tag{5.14}$$

The loss-degraded (or measured) photon-number distribution is can be determined using Eq. (5.12), Eq. (5.11), and Eq. (5.14). Thus, we have

$$P_k = \sum_{n-k}^{\infty} \binom{n}{k} \eta^k (1-\eta)^{n-k} e^{-\lambda}\frac{\lambda^n}{n!}. \tag{5.15}$$

Note that Eq. (5.15) can also be obtained using the Born rule. Mathematically,

$$P_k = \mathrm{Tr}[\Pi_k|\alpha\rangle\langle\alpha|] \tag{5.16}$$

Using the photon-number basis representation of the coherent state and the POVM element from Eq. 5.13, we get

$$P_k = e^{-\eta\lambda}\frac{(\eta\lambda)^k}{k!}. \tag{5.17}$$

From Eq. (5.17), we see that the amplitude of the measured coherent state is attenuated by the detection efficiency η of an imperfect PNR detector.

We now define the purity of a POVM element to characterize the PNR performance of a detector. From Eq. (5.13), we can see that Π_k is a statistical mixture of pure measurement operators or projectors, and it becomes a pure measurement for $\eta = 1$. Since POVMs are not necessarily pure measurements, to quantify their purity one can define the purity in the similar fashion as quantum states. The purity of a POVM element for an outcome k is defined

$$\mathrm{Purity}(\Pi_k) = \frac{\mathrm{Tr}[\Pi_k^2]}{\mathrm{Tr}[\Pi_k]^2}. \tag{5.18}$$

The purity is a positive quantity. It also satisfies

$$\frac{1}{D} \leq \mathrm{Purity}(\Pi_k) \leq 1, \tag{5.19}$$

where D is the dimension of the Hilbert space of the POVM element Π_k, i.e., the number of projectors with nonzero probabilities in the sum of Eq. (5.13)[2]. Clearly, a POVM element giving a completely random outcome will yield $D \to \infty$ and a purity of zero. Therefore, the reciprocal of the purity $\mathrm{Purity}(\Pi_k)^{-1}$ can be seen intuitively as a loose estimator of the number of input states that result in a certain outcome k. As a result, the $\mathrm{Purity}(\Pi_k)$ could be used to characterize the PNR performance of the detector, as in a perfect PNR detector has $\mathrm{Purity}(\Pi_k) = 1$ for all the POVMs. We have discussed mathematical tools essential for this chapter and now move on to modeling the photon splitting employing two models.

5.3 Models

In this section, we consider two models of splitting n photons over m detection modes with a vanishing probability of more than one photon per mode. First, we consider beamsplitter tree (BST) consisting of balanced beamsplitters and single-photon avalanche-photodiodes (SPADs) are used for detection at the terminal of the tree. Second, we investigate a new design where SPADs are side-coupled to the a waveguide rather than terminally coupled as in BST.

[2]Note that the sum in Eq. (5.13) goes to infinity but for practical limitations, it can be truncated at some finite value, say n_0 such that the terms beyond n_0 do not contribute to the sum significantly.

5.3.1 Beamsplitter Tree

We first consider the splitting using beamsplitter tree (BST) where each beam splitter is balanced, i.e., $r = t$ where r and r are reflections and transmission coefficients respectively. The input n-photon Fock state is described by annihilation operator $\hat{a}_1$ and the unused $m-1$ ports of the BST are vacuum modes described by $\hat{a}_2$, $\hat{a}_3$, ..., $\hat{a}_m$. The annihilation operators corresponding to detection modes at the terminal of the BST are $\hat{a}^l_1$, $\hat{a}^l_2$, ...,$\hat{a}^l_{m-1}$, $\hat{a}^l_m$, which are detected by single-photon avalanche-photodiodes (SPADs). We model photon splitting using BST depicted in Fig. (5.3) in the Heisenberg picture.

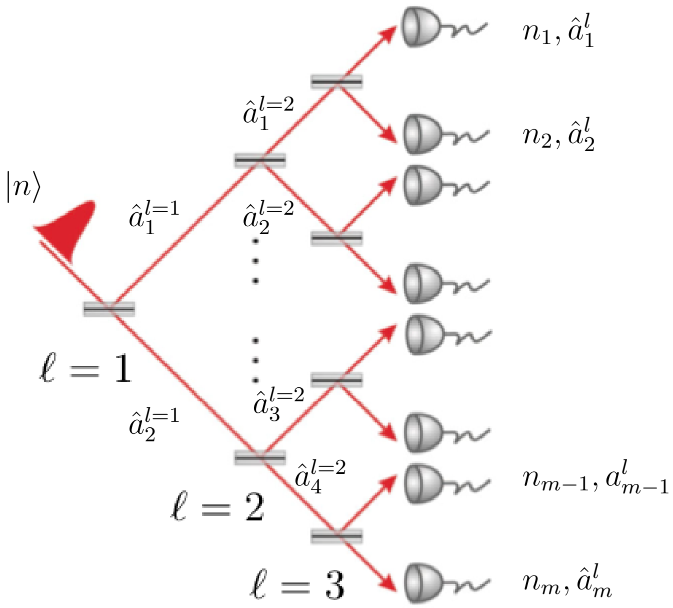

Figure 5.3: Beam-splitter tree: the level index l goes from $l = 1$ to l and m denotes the number of output modes or the number of SPADs. The input mode is represented by $\hat{a}_1$ and the detection modes are $\hat{a}^l_1$, $\hat{a}^l_2$, ...,$\hat{a}^l_{m-1}$, and $\hat{a}^l_m$.

To determine the output quantum state after the BST linear network, it is convenient to write the input quantum state in the basis spanned by the detection modes. We do this by back-propagating the detection modes. We start with the simplest case of $l = 1$ and $m = 2$, i.e., the BST has only one beamsplitter. The input mode is described by annihilation operator $\hat{a}_1$ and the two detection modes are $\hat{a}_1^{l=1}$ and $\hat{a}_2^{l=1}$. In this case, the input mode can be written in terms of output modes as

$$\hat{a}_1 = \frac{\hat{a}_1^{l=1} + \hat{a}_1^{l=1}}{\sqrt{2}} \tag{5.20}$$

Next, we consider $l = 2$ and $m = 4$ where the detection modes are $\hat{a}_1^{l=2}$, $\hat{a}_2^{l=2}$, $\hat{a}_3^{l=2}$ and $\hat{a}_4^{l=2}$. Similar to $m = 2$ case, one can simply backpropagate the detection modes to write the input mode in terms of detection modes. Mathematically,

$$\hat{a}_1 = \frac{\frac{\hat{a}_1^{l=2}+\hat{a}_1^{l=2}}{\sqrt{2}} + \frac{\hat{a}_3^{l=2}+\hat{a}_4^{l=2}}{\sqrt{2}}}{\sqrt{2}} = \frac{\hat{a}_1^{l=2} + \hat{a}_2^{l=2} + \hat{a}_3^{l=2} + \hat{a}_4^{l=2}}{2}. \tag{5.21}$$

One can further extend it to a BST of length l and $m = 2^l$ as

$$\hat{a}_1 = \frac{1}{\sqrt{2^l}} \sum_{i=1}^{m=2^l} \hat{a}_i^l. \tag{5.22}$$

As a result, the output quantum state is

$$|\psi\rangle_{\text{out}} = \frac{1}{\sqrt{n!}} \left(\frac{1}{\sqrt{m}}\right)^n \left(\sum_{i=1}^{m} a^{\dagger l}_{i}\right)^n |0\rangle^{\otimes m}. \tag{5.23}$$

Using multinomial expansion we can simply it to

$$|\psi\rangle_{out} = \left(\frac{1}{\sqrt{m}}\right)^n \underbrace{\sum_{n_1=0}^{n} \cdots \sum_{n_m=0}^{n}}_{\sum_{j=1}^{m} n_j = n} \left\{ \frac{\sqrt{n!}}{n_1! n_2! \ldots n_m!} \prod_{i=1}^{m} ((\hat{a}^l)_i^\dagger)^{n_i} \right\} |0\rangle^{\otimes m}. \tag{5.24}$$

Using Eq. (5.24), we can further determine the probability of obtaining a certain configuration $\vec{n} = [n_1 \; n_2 \; \cdots \; n_m]^{\mathrm{T}}$, which is given by

$$P(|n_1, n_2, \cdots n_m\rangle) = \left(\frac{1}{m^n}\right) \frac{n!}{n_1! n_2! \cdots n_m!}. \tag{5.25}$$

It is easy to verify that the total probabilities corresponding to all possible configurations add to unity.

$$P(n,m) = \left(\frac{1}{m^n}\right) \underbrace{\sum_{n_1=0}^{n} \cdots \sum_{n_m=0}^{n}}_{\sum_{j=1}^{m} n_j = n} \frac{n!}{n_1! n_2! ... n_m!} = \left(\frac{1}{m^n}\right) \underbrace{(1+1+\cdots+1)^n}_{m^n} = 1 \quad (5.26)$$

We are interested in finding the probability of getting k clicks given a n-photon Fock state, $|n\rangle$ is incident to the BST. Considering lossless case where no photons are lost during the propagation through the BST and all the SPADs have unity quantum efficiency, i.e., $\eta = 1$, the conditional probability of registering k clicks is

$$P_m(k|n) = \frac{n!}{m^n} \binom{m}{k} \underbrace{\sum_{n_1=1}^{n} \cdots \sum_{n_m=1}^{n}}_{\sum_{j=1}^{k} n_j = n} \frac{1}{\prod_{i=1}^{k} n_i!}. \quad (5.27)$$

Eq. (5.27) can be understood as following. Since it is the probability of getting k clicks out of n input photons incident to the lossless BST, it means that k detectors receive all n photons and $m-k$ receive no photons. There are in total $\binom{m}{k}$ ways for registering k clicks out of m detectors. The number of detected photons in each detectors may be different that determines the probability of getting k clicks for an input state with n photons. Therefore, one needs to consider all possible solutions of the following linear equation.

$$n_1 + n_2 + ... + n_k = n, \quad (5.28)$$

where each $n_i \in [1, n]$. Consequently, the overall probability would be the sum of probabilities corresponding to each splitting configuration (or the solution of linear equation) of photon splitting over m modes. Once we have found the splitting configurations, we are further interested in finding the probability of getting n clicks for a n-photon state is incident to the BST, which means each clicked detector has only one photon, i.e., $n_i = 1, \forall \ i \in [1, k]$. Thus, for $k = n$, Eq. (5.27) simplifies to

$$P_m(n|n) = \binom{m}{n} \frac{n!}{m^n}. \tag{5.29}$$

We plot Eq. (5.29) in Fig. (5.4) for $m = 100$ and $n \in [2, 6]$. For a given n photons as input, one can see that as the number of detectors, m increases the probability of having $k = n$ clicks increases.

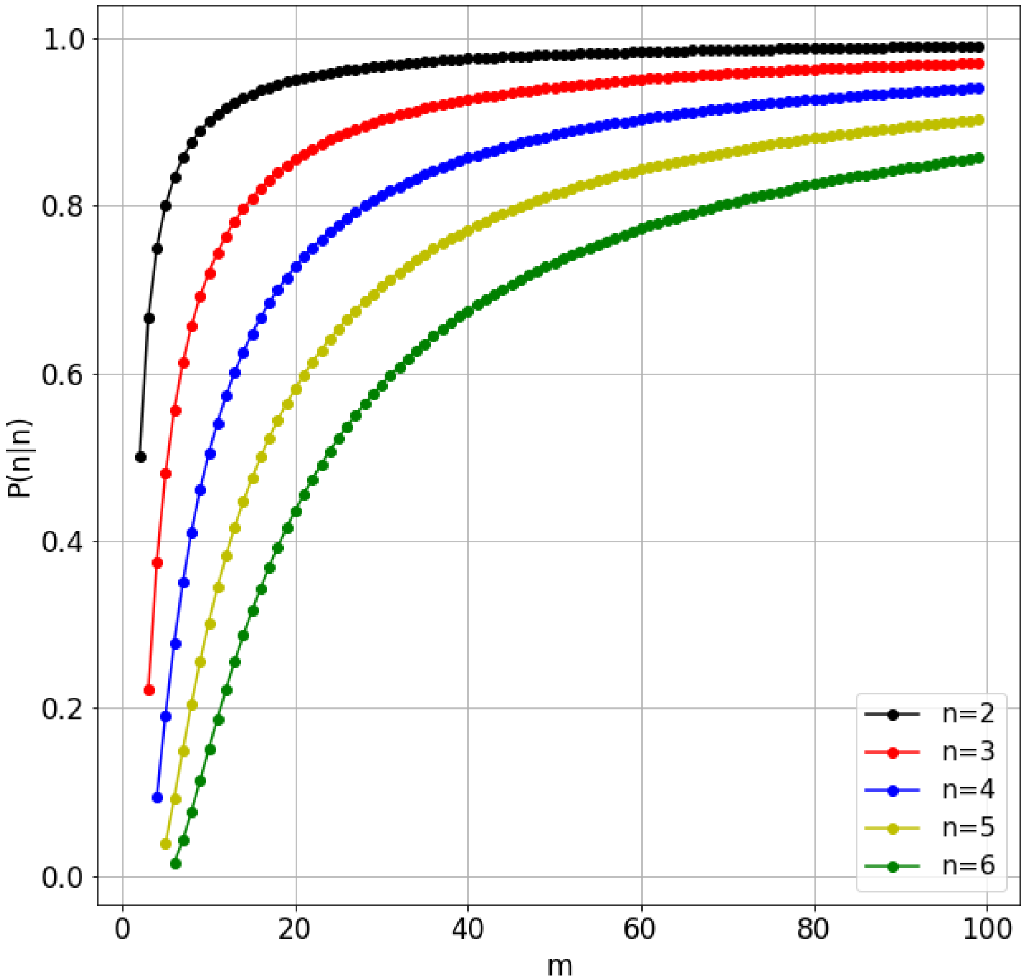

Figure 5.4: Conditional probabilities $P_m(n|n)$ versus m, and $\eta = 1$.

We further simplify Eq. (5.29) as

$$P_m(n|n) = \frac{m(m-1)(m-2)\cdots(m-n+1)}{m^n} = 1\left(1-\frac{1}{m}\right)\left(1-\frac{2}{m}\right)\cdots\left(1-\frac{n}{m}+\frac{1}{m}\right). \tag{5.30}$$

From Eq. (5.30), we can see that $P_m(n|n)$ approaches to unity as $m \to \infty$. Therefore, it is beneficial to increase the length of the BST in order to have a good PNR performance, but it then increases the chances of photons being lost during the propagation through the BST. Additionally, the imperfect quantum efficiency of SPADs will contribute to the photon loss in the realistic case. In the next section, we propose a new design in order to avoid the losses caused by nonideal SPADs.

5.3.2 Segmented Detector

We now investigate the possibility of PNR detection using a segmented detector, constituted by waveguide-coupled, low dark-current SPADs, as per Fig. (5.5).

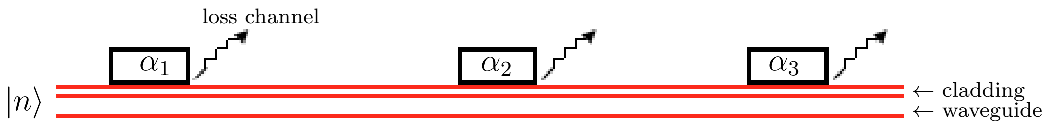

Figure 5.5: Principle sketch of a segmented detector. Guided photons are detected alongside propagation by SPADs which frustrate total internal reflection. The quantum efficiency (QE) of SPAD #j is α_j^2. The design goal is to eschew detection losses, which are distinct from the nonunity of α_j^2, and keep all undetected photons in the waveguide for further detection.

This linear array is essentially a long detector divided into m detector segments, each with an individual read-out. The gist of this design is that photons that are not absorbed in the first SPAD must not be lost and be coupled back into the waveguide to be absorbed later. The crucial advantage of this configuration is that nonideal quantum efficiency of the SPADs does not amount to photon loss, unlike terminally coupled PNR detectors in which temporally or spatially split photons impinge on

SPADs on the end of their path [62]–[64] as in BST. Moreover, the SPAD coupling should follow a gradient down the waveguide so as to ensure no more than one photon is detected at a time (since SPADs are not PNR) while still ensuring efficient detection. The design goal is therefore to whittle down an initial n photons, one by one. We envision that such a segmented photodetector will become feasible in large-scale integrated photonic platforms using either monolithic or heterogeneous integration of SPADs on low-loss waveguides, as has already been hinted at by the integration on waveguides of PIN photodiodes [191], [192] and of transition edge sensors [193], [194]. The essential physics of the SPAD coupling can be captured by a simplified model, pictured in Fig. (5.6), which assumes that the SPAD length is exactly equal to the period of the mode beat between the main waveguide and the SPAD.

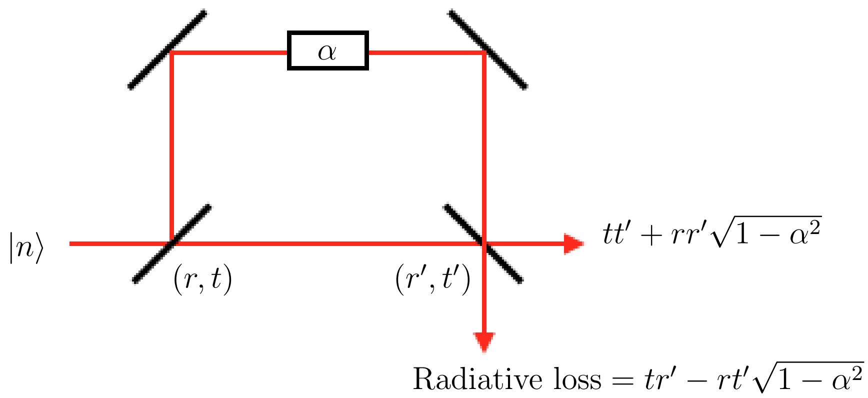

Figure 5.6: Model for detection alongside propagation.

In Section 5.3.3, we give concrete and detailed waveguide modeling results for this configuration, which has already been experimentally realized for PIN photodiodes [4]. The simplified model will be enough, without loss of generality, for the quantum analysis of the PNR behavior in Section 5.3.4. We take the SPAD quantum efficiency to be α^2, accounting for both coupling efficiency and intrinsic absorption, such that its field transmissivity is $1-\alpha^2$. Note that it is desirable for α not be too large, so that the probability for any SPAD to see more than one photon during the same detection window can be vanishing, since SPADs are not PNR detectors; this translates into the condition $\alpha^2 \ll 1/n$, for n incident photons. In some cases, the mere click statistics from a click/no-click detector system suffice to certify the non-classicality of a state [183], [195]. In such cases, the proposed design is particularly beneficial as it increases the overall detection efficiency by recycling the photons which are not absorbed at the first time but are detected as they propagate in the waveguide.

We require that the bottom output of the exit beamsplitter in Fig. (5.6), which is effectively the radiative loss channel of the waveguide, be nulled by destructive interference. The condition can be achieved in the presence of SPAD absorption by choosing parameters (r, t, r', t') of the beamsplitters, and absorption coefficient α, such that

$$tr' - rt'\sqrt{1-\alpha^2} = 0. \tag{5.31}$$

If this is the case, then the detection process truly takes place alongside propagation and finite quantum efficiency — necessary here to attain PNR performance with SPADs, by detecting no more than one photon at a time — does not contribute to photon loss. This kind of optical coupling from the waveguide into the SPAD absorber and back into the waveguide can be accomplished by using a vertical directional coupler design discussed in detail in Section 5.3.3.

In order to further simplify the model for Section 5.3.4, at no cost to its generality, we can recast our segmented detector as the SPAD sequence depicted in Fig. (5.7).

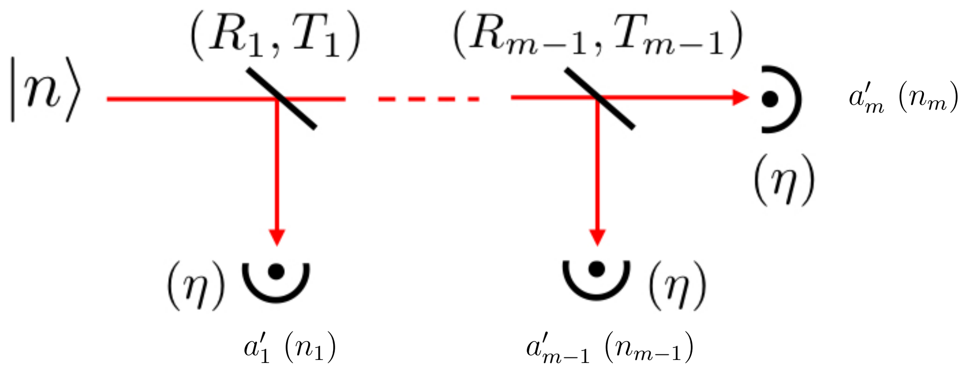

Figure 5.7: Model of a PNR segmented photodetector with $R_j + T_j \equiv r_j^2 + t_j^2 = 1, \forall j \in [1, m]$. For j$^{\text{th}}$ SPAD, we have $t_j = tt' + rr'\sqrt{1-\alpha^2}$, where $t_j = T_j^{1/2}$, determined from Fig. (5.6).

In that case, the loss channel corresponding to deviations to Eq. (5.31) becomes equivalent to $\sqrt{1-\eta}$, where η is the quantum efficiency of the terminally coupled SPADs in Fig. (5.7). While there is no fundamental difference between radiative losses in Fig. (5.5) and Fig. (5.6) and $\eta < 1$ in Fig. (5.7), there is, again, a conceptual difference between $\alpha^2 < 1$, which doesn't lead to photon loss since the photon can re-enter the waveguide, and $\eta < 1$, which does constitute photon loss. In addition, $\eta < 1$ also accounts for the mechanism by which the photon can be absorbed in a SPAD without causing an avalanche. Our theoretical model in Section 5.3.4 will also account for dark counts and electrical cross-talk.

5.3.3 Segmented waveguide detector design

To verify the optical design of the segmented detector, a monolithically integrated InP-based p-i-n waveguide photodetector consisting of 6 PIN photodiodes (PDs), coupled to one waveguide [4], Fig. (5.8)(a) was previously reported. These simulations were performed by Qianhuan Yu from Professor Andreas Beling's group at UVa, a detailed discussion can be found in Qianhuan Yu's thesis. Optical coupling from the waveguide into the PD absorber and back into the waveguide was accomplished by using a vertical directional coupler design as shown in Fig. (5.8)(b).

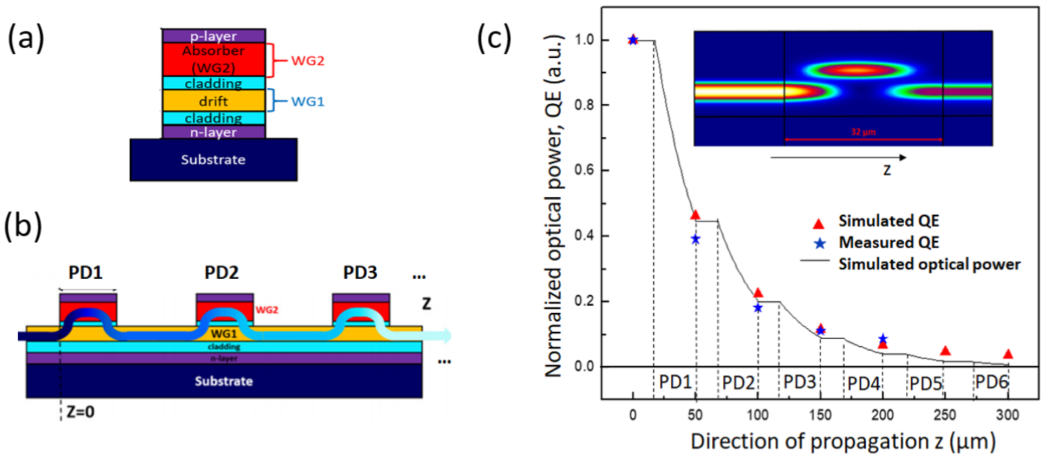

Figure 5.8: (a) Cross-section of waveguide photodiode [4]; (b) Side view schematic of light propagating in the segmented waveguide photodetector. (c) Normalized optical power and QE of PD1 to PD6 in the segmented photodetector. The inset shows the optical intensity in PD1 with a PD length of 32μm.

Input light propagates in the passive waveguide WG1 and couples into the absorption waveguide (WG2) of the PD where electron-hole pairs are generated. Residual light in the WG2 couples back into WG1 at the end surface of each PD.

By using a segmented photodetector with six elements, an overall quantum efficiency (QE) of 90% was experimentally demonstrated. Fig. (5.8)(c) shows the simulated optical power along the segmented photodetector for the design in [4] along with the QE of each PD. Each period in the photodetector was 50 μm long with a 32 μm-long PD and a 18 μm-long passive waveguide. The solid line shows how the optical power decreases while propagating in direction z. We simulated a total optical loss of 1% at the front and rear side of each PD. WG1 was assumed to be lossless. The red and blue symbols show the simulated and measured QE for each individual PD in the photodetector. Here, the optical power was referred to the input power in the waveguide at z = 0. The simulated total QE was 96.5% which was close to the measured value of (90±5)% [4]. The error originated from uncertainty in determining the fiber-chip coupling loss; the difference between simulation and measurement can be explained by fabrication tolerances and non-zero waveguide loss. To reduce the latter, the waveguide length can be reduced to $< 10\mu$m. To further reduce the radiation loss and enable segmented detectors with larger PD count we designed a new structure and made two changes compared to [4]: (i) we added an additional cladding layer on top of the passive waveguide WG1, and (ii), we also reduced the thickness of the absorption layer from 30 nm in [4] to only 6 nm as seen in Fig. (5.9).

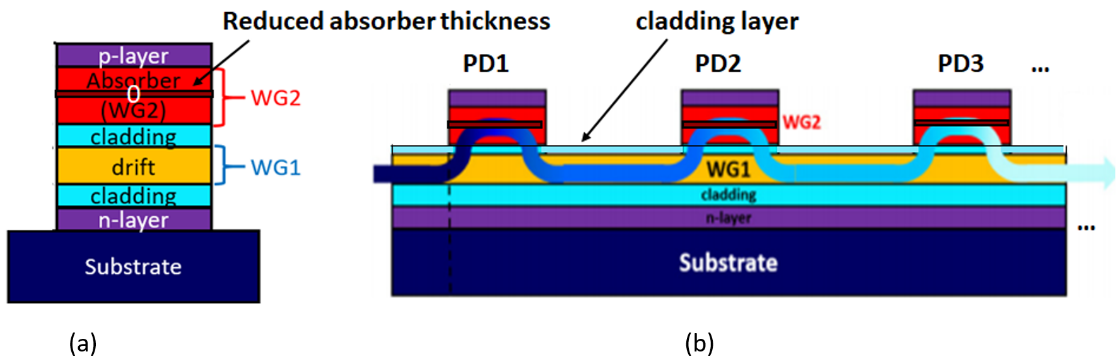

Figure 5.9: (a) Cross-section of of new waveguide photodiode design with thin absorber; (b) Side view schematic of light propagating in the segmented waveguide photodetector with cladding layer.

A small active volume is beneficial since it helps reducing the dark current, jitter, and increases the PD's count rate. Given the fact that the PD length can only be an integral multiple of the mode beat length L [191], we designed a 50-element segmented detector with 20 PDs with PD length L, followed by 15 PDs with PD length 2L, 6 PDs with 4L, 3 PDs with 6L, and 6 PDs with 10L as demonstrated in Fig. (5.10)(a). This ensures complete absorption and a similar number of photogenerated electron-hole pairs in each of the 50 PDs. Fig. (5.10)(b) shows the stepwise decay of the simulated optical power in the segmented detector with uniform PD QE of 2.5% in each PD. We estimated the overall radiation loss to be as low as 7% by simulating the same structure without including any imaginary indices, Fig. (5.10)(b). It should be mentioned that additional loss originating from WG1 can be as low as 1% or 4% assuming either a low-loss Si_3N_4 waveguide (0.1 dB/cm [196]) or an InGaAsP waveguide (0.4 dB/cm [197]).

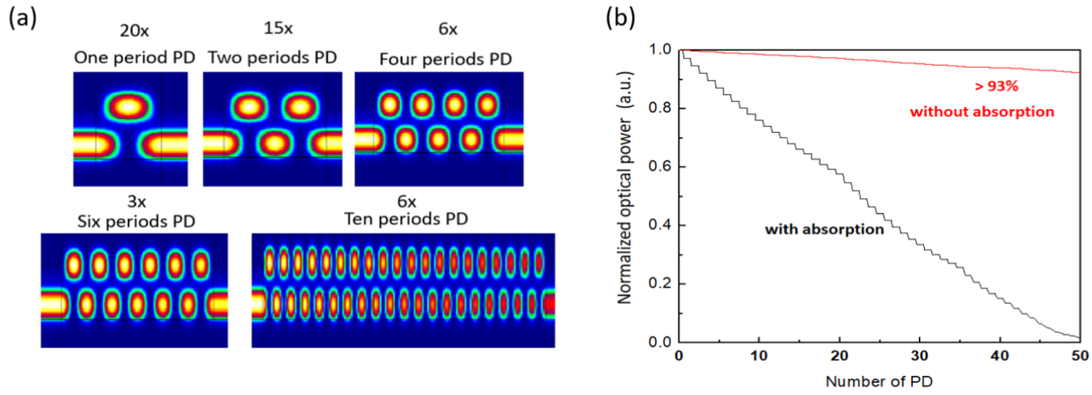

Figure 5.10: (a) Simulated optical intensity in PDs with various lengths; (b) Normalized optical power with (black) and without (red) absorption in the 50-element segmented detector with 8 mm total length.

5.3.4 Quantum modeling of a segmented detector

We now provide a complete POVM analysis of a segmented detector. As discussed in Section 5.2, the POVM element in the most general case for k independent SPAD pulses, or "clicks," is given by

$$\Pi_k = \sum_{n=0}^{\infty} P(k|n)|n\rangle\langle n|, \tag{5.32}$$

where $P(k|n)$ is the conditional probability of getting k clicks given an n-photon input. Note that the sum over n starts from zero because k clicks might entirely get registered from the dark-noise. Further, the purity of the POVM element for outcome k is given as

$$\text{Purity}(\Pi_k) = \frac{\text{Tr}(\Pi_k^2)}{\text{Tr}(\Pi_k)^2} = \frac{\sum_{n=0}^{\infty} P(k|n)^2}{\left[\sum_{n=0}^{\infty} P(k|n)\right]^2}. \tag{5.33}$$

As discussed in Section 5.2, Purity(Π_k) = 1 corresponds to pure PNR measurements, i.e., projective measurements, and a POVM measurement with Purity(Π_k) = 0 will yield a completely random outcome. Hence, Purity(Π_k) can be utilized to quantify the PNR capabilities of the detector. Here we study the theoretical purity of the POVM elements of Eq. (5.33) versus the input photon number, in the presence of nonidealities such as loss channels, which make $k < n$ due to radiative losses and detector absorption without avalanche. We also study how electrical cross-talk and dark counts, which make $k > n$ due to non-photon-triggered avalanches, absorption-triggered parasitic flashes on the detector surface, and afterpulsing affect the POVM purities. Note that afterpulsing, i.e., dark counts caused by charges from previous avalanches trapped in impurity levels, is also conditioned on the number of clicks on a given SPAD but we'll treat this effect as a second order one and neglect it, effectively treating afterpulsing as dark counts.

We again model Fig. (5.7) by using the Heisenberg picture approach. The quantum input mode is described by annihilation operator a_1 and input Fock state $|n\rangle$, the other $m-1$ input modes a_2, a_3, ..., a_m are vacuum modes, and the detection modes are a'_1, a'_2, ..., a'_m. We consider $m-1$ beamsplitters (T_j, R_j) and $\eta = 1$ (no losses) for all modes. The input quantum state is

$$|n\rangle = \frac{{a_1^\dagger}^n}{\sqrt{n!}}|0\rangle^{\otimes m}. \tag{5.34}$$

In order to find the probability of an outcome it is convenient to write the output quantum state in terms of detection modes. Using backpropagation of the detection modes, a_i's we get

$$a_1^\dagger = r_1 a_1'^\dagger + \sum_{k=2}^{m-1} [\prod_{l=1}^{m-1} t_l] r_{k-1} a_k'^\dagger + \prod_{l=1}^{m-1} t_l a_m'^\dagger, \tag{5.35}$$

and the output quantum state is

$$|\psi\rangle_{out} = \frac{1}{\sqrt{n!}}\left(r_1 a_1'^{\dagger} + \sum_{k=2}^{m-1}\prod_{l=1}^{m-1} t_l\, r_{k-1}\, a_k'^{\dagger} + \prod_{l=1}^{m-1} t_l\, a_m'^{\dagger}\right)^n |0\rangle^{\otimes m} \tag{5.36}$$

and the multinomial expansion yields

$$|\psi\rangle_{out} = \underbrace{\sum_{n_1=0}^{n}\cdots\sum_{n_m=0}^{n}}_{\sum_{j=1}^{m} n_j = n} \frac{\sqrt{n!}}{n_1!n_2!...n_m!} r_1^{n_1} \prod_{k=2}^{m-1} \tau_{1,k-1}^{n_k} r_k^{n_k}\, \tau_{m-1,1}^{n_m} \prod_{i=1}^{m} a_i'^{\dagger n_i} |0\rangle^{\otimes m}, \tag{5.37}$$

where each n_i can take any value from 0 to n and $\tau_{i,j} = t_i \dots t_j$.

Given n input photons, the probability $P_m(k|n)$ of getting k clicks from m SPADs — where each click may result from one or several simultaneous photons, since single SPADs aren't PNR — is, in the lossless case,

$$P_m(k|n) = \underbrace{\sum_{n_1=0}^{n}\cdots\sum_{n_m=0}^{n}}_{(*)\sum_{i=1}^{k} n_i = n} \frac{n!}{\prod_{i=1}^{m} n_i!}\, X, \tag{5.38}$$

$$\text{where } X = \left(r_1^{n_1} \prod_{k=2}^{m-1} \tau_{1,k-1}^{n_k} r_k^{n_k}\, \tau_{m-1,1}^{n_m}\right)^2 \tag{5.39}$$

$$= R_1^{n_1} T_1^{n-n_1} \times R_2^{n_2} T_2^{n-n_1-n_2} \times \cdots \times R_{m-1}^{n_{m-1}} T_{m-1}^{n-\sum_{j=1}^{m-1} n_j}. \tag{5.40}$$

The asterisk in Eq. (5.38) symbolizes the following constraint: in this lossless case, k clicks will be obtained if and only if k different SPADs out of m receive *at least* one photon, and the other $m-k$ SPADs receive zero photons. An explicit formula will be given for the symmetrized detector in the next section. Further, we see that X is essentially the multiplication of probabilities for detection events at each photodiode. For instance, the probability for reflection of n_1 photons and transmission of $n-n_1$ is $R_1^{n_1} T_1^{n-n_1}$ at the first beam-splitter, which happens to be the first factor in Eq. (5.40) and same follows for rest of the factors.

We can obtain the probability of getting a particular configuration of n_i's such that $\sum_{j=1}^{m} n_i = n$ holds true is

$$P(|n_1, n_2, \cdots n_m\rangle) = \frac{n!}{n_1!n_2!\cdots n_m!}X. \tag{5.41}$$

Note that our goal is to actually split the n input photons among $m \gg n$ modes with never more than 1 photon per mode. The first beamsplitter's reflectivity must then be much less than n^{-1}. Taking all beamsplitters identical is clearly not optimal since the subsequent modes will gradually see fewer photons and can therefore afford larger reflectivities without running the to risk of detecting more than one photon. Also, at the end of the segmented device, the last beam splitter should clearly be balanced since the constraint has to be symmetric for both its output ports. Bearing all this in mind, a symmetrized device appears to be the optimal choice. We investigate it next.

5.3.5 Symmetrized segmented detector

5.3.5.1 Lossless case

We take $\eta = 1$ and the beamsplitters' reflectivities to be $R_j = \frac{1}{m-j+1}$, where $j \in [1, m-1]$, yields the simplification

$$\begin{aligned} X =&[R_1^{n_1}T_1^{n-n_1}][R_2^{n_2}T_2^{n-n_1-n_2}]\cdots[R_{m-1}^{n_{m-1}}T_{m-1}^{n-\sum_{j=1}^{m-1}n_j}] \\ =&\left[\left(\frac{1}{m}\right)^{n_1}\left(\frac{m-1}{m}\right)^{n-n_1}\right]\left[\left(\frac{1}{m-1}\right)^{n_2}\left(\frac{m-2}{m-1}\right)^{n-n_1-n_2}\right]\cdots\left[\left(\frac{1}{2}\right)^{n_{m-1}}\left(\frac{1}{2}\right)^{n-\sum_{i=1}^{m-1}n_i}\right] \\ =&\frac{1}{m^n}. \end{aligned} \tag{5.42}$$

and makes the symmetrized segemented detector equivalent to a symmetric beamsplitter tree, to the notable difference that SPADs are not terminally coupled here and so their nonideal QE does not contribute to detection losses. Eq. (5.38) thus

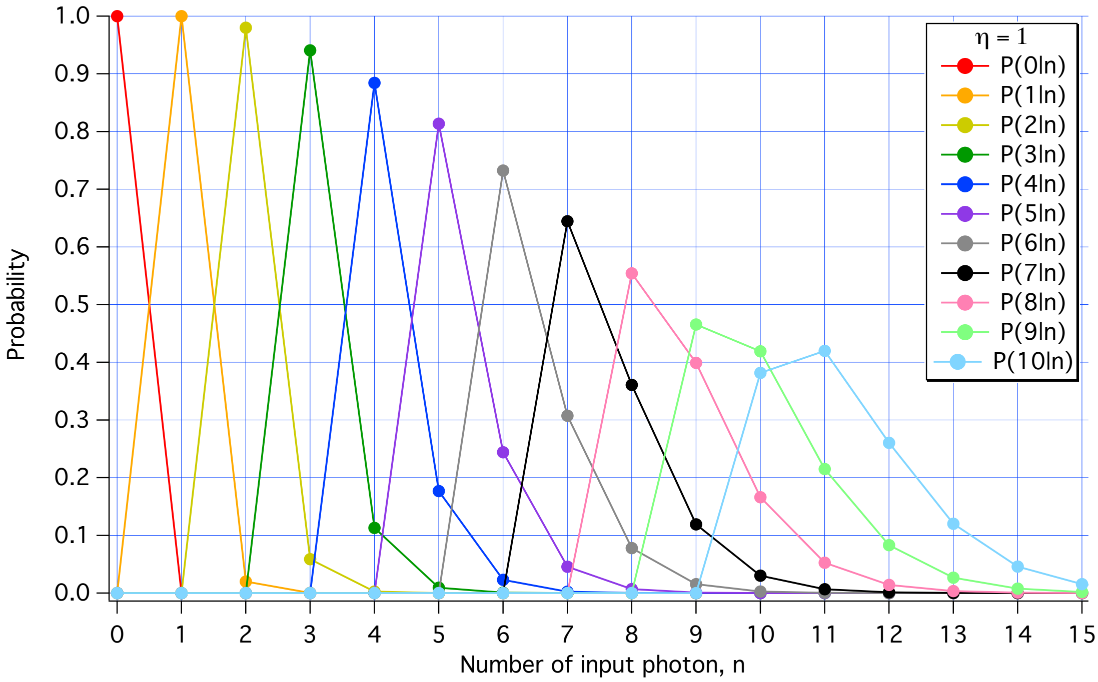

Figure 5.11: Conditional probabilities $P_{50}(k|n)$ versus n, for $\eta = 1$.

simplifies to

$$P_m(k|n) = \frac{n!}{m^n}\binom{m}{k}\underbrace{\sum_{n_1=1}^{n}\cdots\sum_{n_k=1}^{n}}_{\sum_{j=1}^{k} n_j = n}\frac{1}{\prod_{i=1}^{k} n_i!}. \tag{5.43}$$

These conditional probabilities are plotted in for $m = 50, 100, 1000, 2000$ and $\eta = 1$. From Fig. 5.11, Fig. 5.12, Fig. 5.13, and Fig. 5.14, it is evident that $P(k|n)$ increases as number of detectors m increases. It is also worth mentioning that as the SPAD number m increases, the peak width reduces for higher clicks, which implies that POVM purity increases for a given click-number k. As can be seen in Fig. (5.15), reasonably good PNR performance (POVM purity of at least 90%) is reached for $n \sim 10$ with $m \sim 1000$.

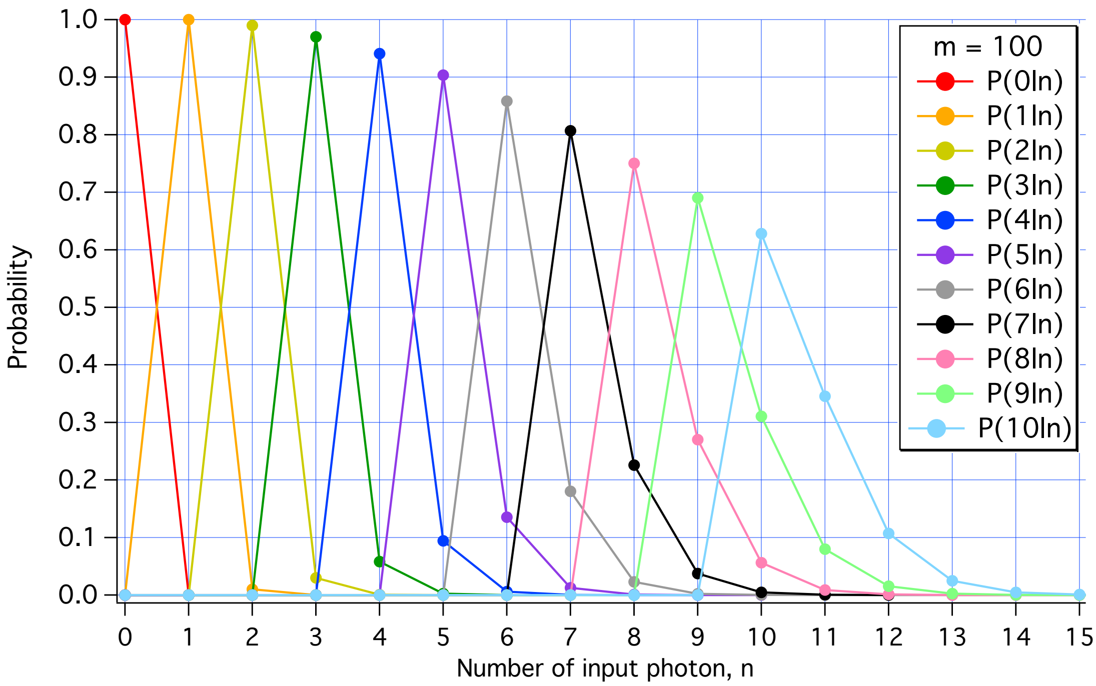

Figure 5.12: Conditional probabilities $P_{100}(k|n)$ versus n, for $\eta = 1$.

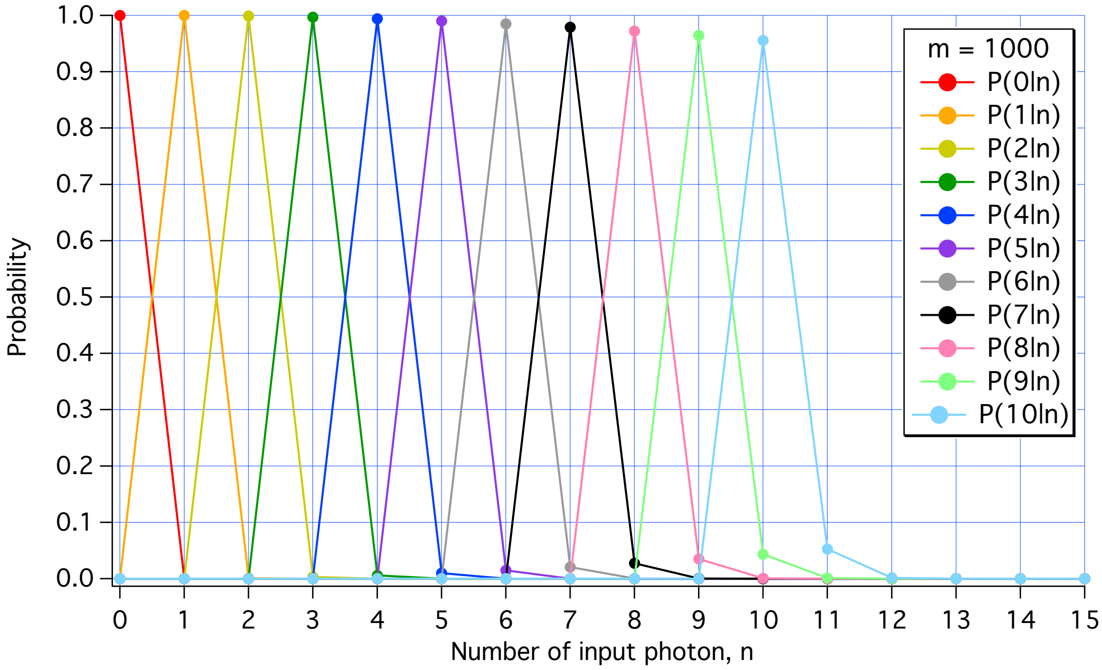

Figure 5.13: Conditional probabilities $P_{1000}(k|n)$ versus n, for $\eta = 1$.

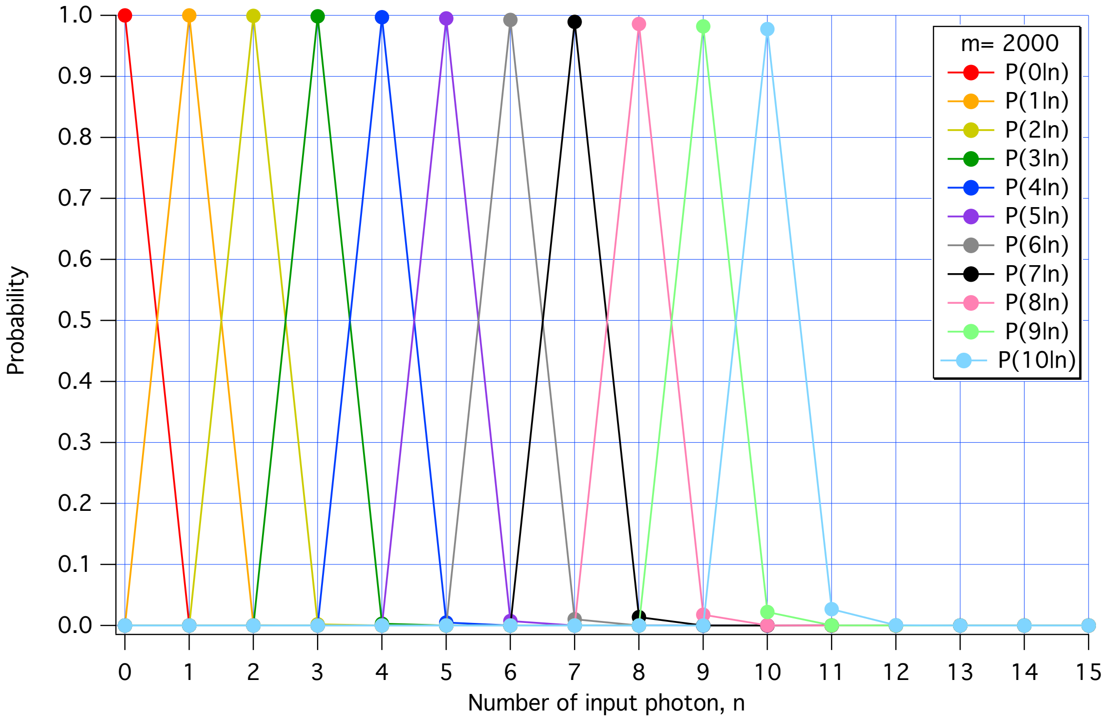

Figure 5.14: Conditional probabilities $P_{2000}(k|n)$ versus n, for $\eta = 1$.

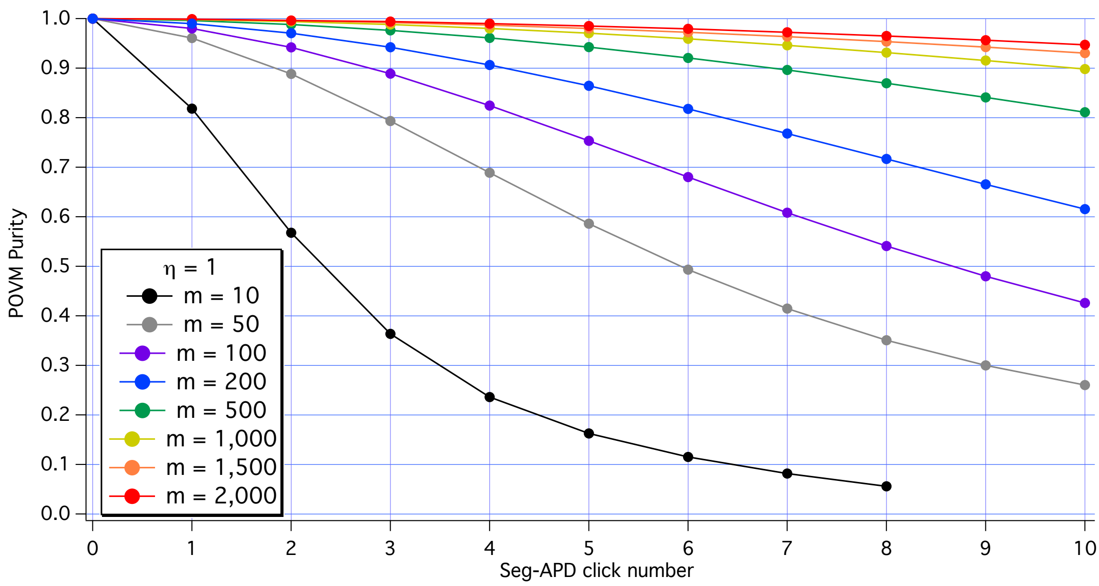

Figure 5.15: POVM element Purity($\prod_k$) versus click number k, for different m.

5.3.5.2 Lossy case

We now consider the effect of photon losses in each detection mode, i.e., $\eta < 1$. Again, η should not be misconstrued as the SPAD absorption efficiency because the latter plays no role in photon losses, as unabsorbed photons can enter back into the waveguide and get detected by subsequent SPADs. Further more, the quantity $1-\eta$ is the probability of a photon exiting the waveguide undetected or a photon was absorbed without causing an avalanche, losing its chance for further detection. We assume that the parameter η is independent of the photon number. The probability to get zero clicks in one mode is

$$P_1(0|n,\eta) = (1-\eta)^n. \tag{5.44}$$

Likewise, the probability to get one click in one mode is [198]

$$P_1(1|n,\eta) = \sum_{k=1}^{n} \binom{n}{k} \eta^k (1-\eta)^{n-k} = 1-(1-\eta)^n. \tag{5.45}$$

It is important to note that in the sum over k starts with 1 here because we neglected dark counts. Therefore, Eq. (5.43) can be generalized to the lossy case as

$$P_m(k|n,\eta) = n! \left(\frac{1-\eta}{m}\right)^n \binom{m}{k} \underbrace{\sum_{n_1=0}^{n} \cdots \sum_{n_m=0}^{n}}_{\sum_{j=1}^{m} n_j = n} \frac{1}{\prod_{j=1}^{m} n_j!} \prod_{l=n_1}^{n_k} \left[\left(\frac{1}{1-\eta}\right)^l - 1\right], \tag{5.46}$$

In Eq. (5.46), in addition to multinomial coefficient for probability we also have the product term due to non-unity quantum efficiency. It is worth noting that the probability of getting zero clicks is still the same as the case of one detector, i.e., Eq. (5.44), and for $\eta = 1$, Eq. (5.46) turns out to be same as Eq. (5.43) for $n_i \geq 1$ where $i \in [1,k]$ for k clicks. For $\eta < 1$ the computer simulations run extremely slowly for higher values of m (reminiscent of the boson sampling problem), therefore we were limited to $m = 50$ for the calculation of conditional probabilities at $\eta = 0.9, 0.99, 0.999$. A closed analytical expression can be found in Ref. [199], it allows to compute multinomial probabilities more efficiently. The results at $\eta = 0.9$ are displayed, for illustrative purposes, in Fig. (5.16).

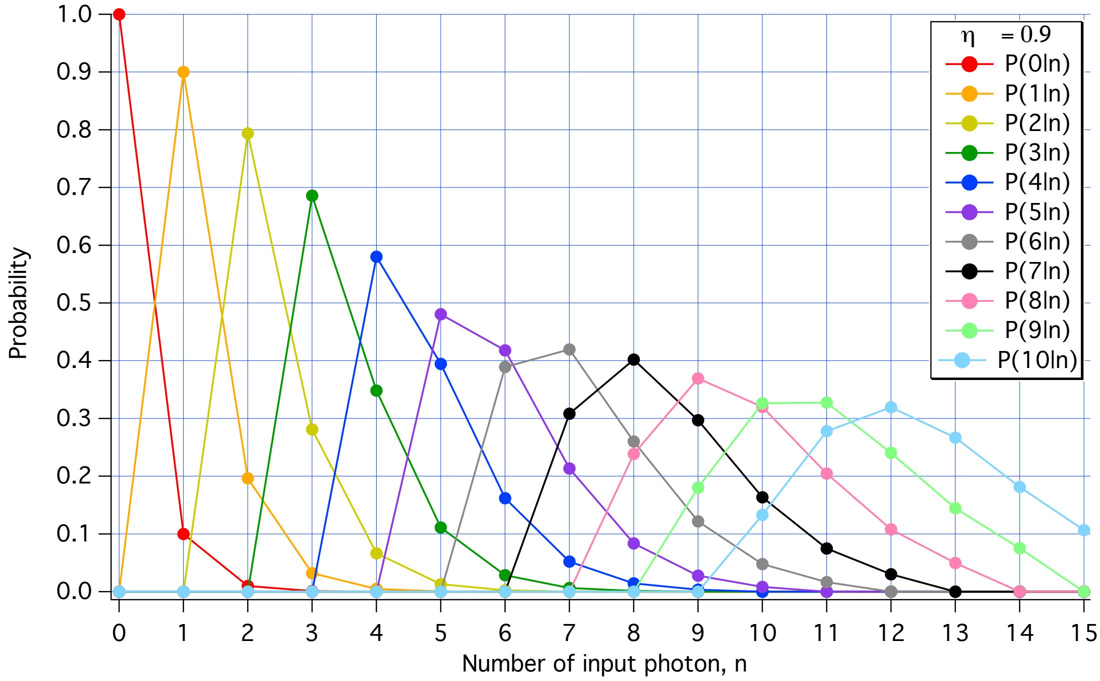

Figure 5.16: Conditional probabilities $P_{50}(k|n)$ versus n, for $\eta = 0.9$.

The degradation of the count probability with photon loss is evident, compared to Fig. (5.14). Also recall that $\eta = 0.9$ means 10% loss per detection mode which is a very poor performance as previous experimental work on low loss waveguides shows one can do much better [200].

The purity calculation, displayed in Fig. (5.17), is particularly illuminating.

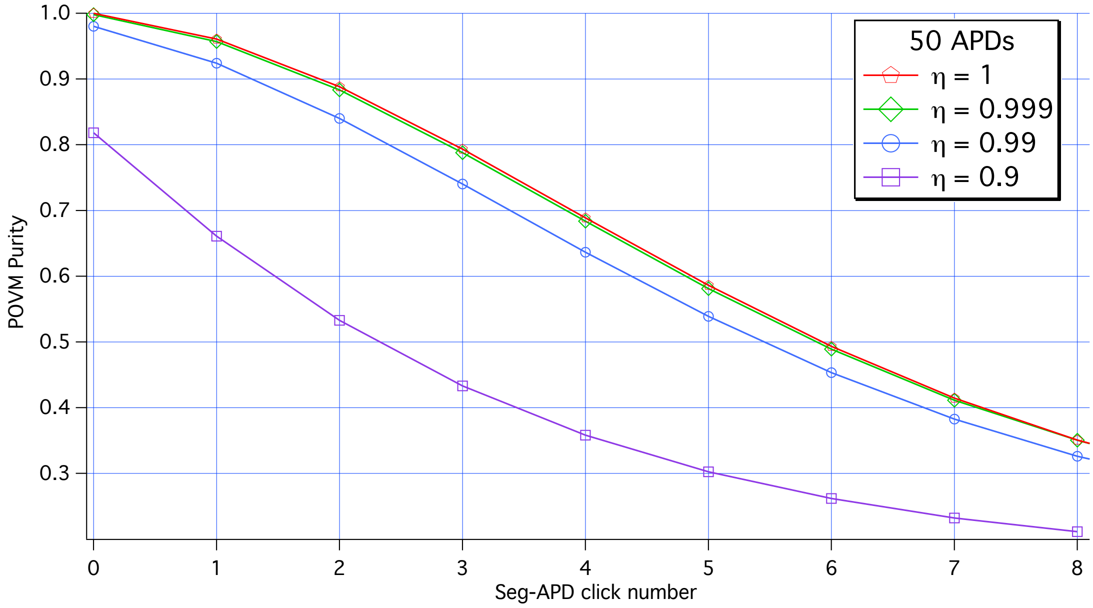

Figure 5.17: POVM element Purity($\prod_k$) versus click number k, for several values of η at $m = 50$

Indeed, it is clear that, as η increases beyond the low $\eta = 0.9$ level, the photon losses have a decreasing to negligible ($\eta = 0.999$, i.e., 0.1% loss per detector) effect on purity, which is essentially limited by m, as per Fig. (5.15). This is an interesting result. It is likely that the same level of photon loss may have a more detrimental effect as m increases, however, the exact scaling of this effect is not yet known, due to the long computation times for the nonideal case. Figures (5.17) and (5.16) can be related by the aforementioned intuitive meaning of the POVM purity: consider, for example, $k = 5$ in Fig. (5.17), for which the POVM purity $\simeq 0.3$. This implies that the number of input states leading to clicks with significant probabilities is about 3 to 4, which corresponds to the number of points making up most of the purple $P(5|n)$ peak in Fig. (5.16). Also, one can clearly see that, as the purity decreases with k in Fig. (5.17), the conditional probabilities have broader and broader supports with larger k in Fig. (5.16).

5.3.5.3 Dark count noise modeling

We now model dark counts for the segmented detector. We start with a fixed dark count probability, δ, independent of the input photon-number. Recall that a non-PNR detector has 2 POVM elements Π_1^d and Π_0^d corresponding to 2 detection events, click and no-click respectively. In the presence of dark counts, the probability of having no click becomes, from Eq. (5.44),

$$P_0^d = (1-\delta)(1-\eta)^n, \tag{5.47}$$

which can be interpreted as the joint probability of Eq. (5.44) (no photon detected from the incident light, with probability $(1-\eta)^n$) and no click from dark counts, with probability of $(1-\delta)$. Since both of those events are independent, the overall probability of them occurring simultaneously is the multiplication of individual probabilities. Thus, the probability of registering a click is

$$P_1^d = 1 - P_0^d = 1 - (1-\delta)(1-\eta)^n, \tag{5.48}$$

and the 1-click POVM for a phase insensitive detector is

$$\Pi_1^d = \sum_{n=0}^{n=\infty} \left[1 - (1-\delta)(1-\eta)^n\right] |n\rangle\langle n|. \tag{5.49}$$

Note that the sum in Eq. (5.49) is now starting from zero which accounts for the possibility of dark counts, of probability δ, with no light incident on the detector. We now consider two identical click detectors as shown in Fig. 5.18.

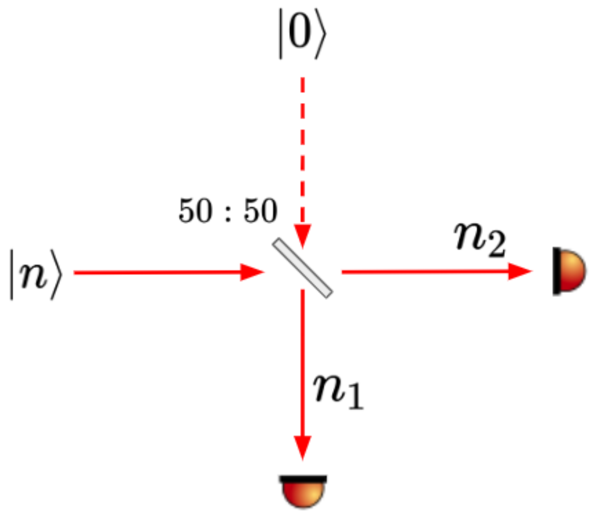

Figure 5.18: Multiplexing set up for 2 click detectors.

Detection event space has 3 elements which are zero-, single- and two-click events. Hence, there will be three POVM elements, $\{\Pi_0, \Pi_1, \Pi_2\}$ such that $\Pi_0 + \Pi_1 + \Pi_2 = \mathbb{I}$. The probability of getting zero-click outcome

$$P_0 = \left(\frac{1}{2}\right)^n \underbrace{\sum_{n_1=0}^{n}\sum_{n_2=0}^{n}}_{\sum_{j=1}^{2} n_j = n} \frac{n!}{n_1! n_2} \underbrace{(1-\delta)^2}_{\text{No dark counts}} \underbrace{(1-\eta)^{n_1}(1-\eta)^{n_2}}_{\text{No photons detected}} \tag{5.50}$$

$$= \left(\frac{1}{2}\right)^n \underbrace{\sum_{n_1=0}^{n}\sum_{n_2=0}^{n}}_{\sum_{j=1}^{2} n_j = n} \frac{n!}{n_1! n_2} (1-\delta)^2 (1-\eta)^n \tag{5.51}$$

Likewise, the probabilities of one- and two-click detection events are

$$P_1 = \left(\frac{1}{2}\right)^n \underbrace{\sum_{n_1=0}^{n}\sum_{n_2=0}^{n}}_{\sum_{j=1}^{2} n_j = n} \frac{n!}{n_1! n_2} [\{\underbrace{(1-(1-\delta)(1-\eta)^{n_1})}_{\text{Bottom detector clicked}} \underbrace{(1-\delta)(1-\eta)^{n_2}\}}_{\text{No click from top detector}} \tag{5.52}$$

$$+ \underbrace{\{(1-(1-\delta)(1-\eta)^{n_2})(1-\delta)(1-\eta)^{n_1}\}}_{\text{Other way around}}] \tag{5.53}$$

$$P_2 = \left(\frac{1}{2}\right)^n \underbrace{\sum_{n_1=0}^{n}\sum_{n_2=0}^{n}}_{\sum_{j=1}^{2} n_j = n} \frac{n!}{n_1! n_2} [\{\underbrace{(1-(1-\delta)(1-\eta)^{n_1})}_{\text{Bottom detector clicked}} \underbrace{(1-(1-\delta)(1-\eta)^{n_2}\}}_{\text{Top detector clicked}} \tag{5.54}$$

$$\tag{5.55}$$

We can simply check that $\sum_{j=0}^{3} P_j = 1$. One can further extend it to m detectors and k clicks. The k-click POVM is then

$$P_m(k|n,\eta) = n!(1-\delta)^m \left(\frac{1-\eta}{m}\right)^n \binom{m}{k} \underbrace{\sum_{n_1=0}^{n} \cdots \sum_{n_m=0}^{n}}_{\sum_{j=1}^{m} n_j = n} \frac{1}{\prod_{j=1}^{m} n_j!} \prod_{l=n_1}^{n_k} \left[\frac{1}{1-\delta}\left(\frac{1}{1-\eta}\right)^l - 1\right]. \tag{5.56}$$

Fig. (5.19) displays the simulated POVM purities for $m = 16$, $k \leqslant 5$, $\eta = 0.90$, and dark count probabilities $\delta = 0$, 0.001, 0.01, and 0.1. (Due to the heavy numerical load, we could not compute for larger SPAD numbers m.) We see that the POVM purities decrease as dark count probability increases, unsurprisingly. However, the key point is that $\delta = 0.1\%$ is practically indistinguishable from zero dark counts in this case, where the scalability of the segmented detector and efficiency η are the main limitation to PNR operation.

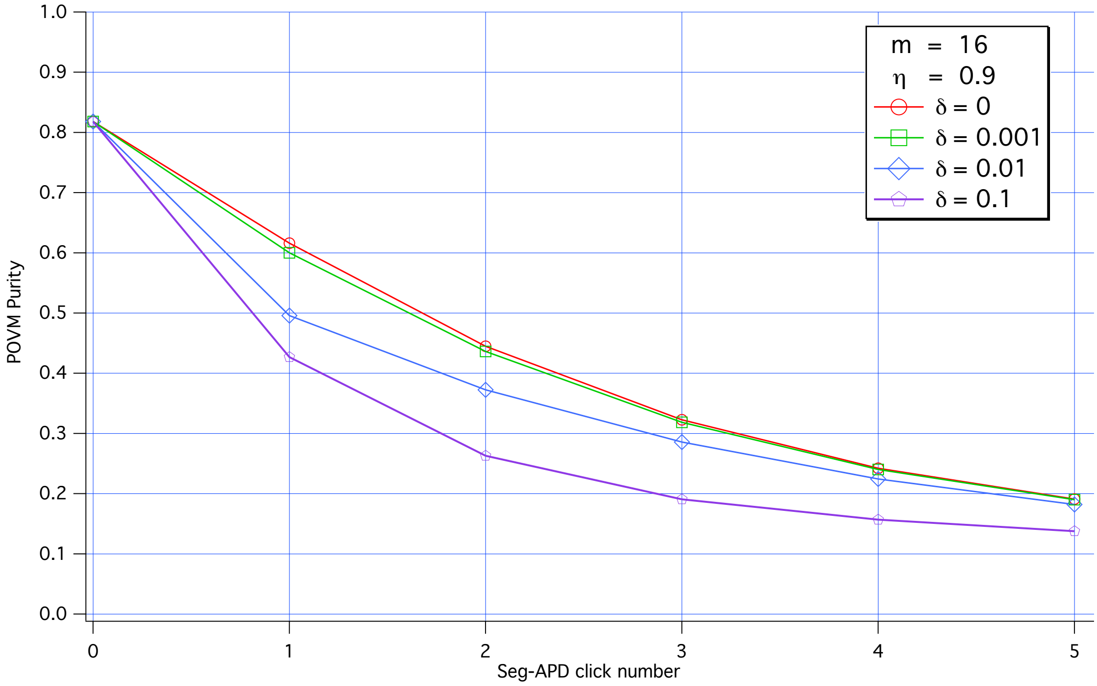

Figure 5.19: POVM element Purity(Π_k) versus click number k, for several values of dark count probabilities, δ at $m = 16$

5.3.5.4 Cross-talk noise modeling

A cross-talk event is registered when an avalanche in a particular SPAD causes an avalanche in the neighboring SPADs [201]. Since the dark-count rate can be extremely low in our design, we only consider the cross-talk events due to the incident light. The effect of cross-talk can be reduced by increasing the distance between consecutive SPADs but this will increase the propagation losses in the waveguide. Thus, it becomes critical to account for registered clicks caused due to cross-talk. To model the cross-talk, we first consider the simplest case of two SPADs on the waveguide. In this case, the POVM set has 3 elements corresponding to zero-, one-, and two-click detection outcomes. If n photons are coupled to the waveguide, n_1 photons are coupled to first SPAD and n_2 are coupled to the second SPAD. We define a new parameter ϵ, which is the probability cross-talk event caused by an avalanche in neighboring

SPADs. In the two-SPAD case, the probability of a cross-talk event registered by the first SPAD is $(1-\epsilon)^{n_2}$, where $n_2 = n - n_1$ is the number of photons passed to second SPAD. Thus, the probability of getting zero-click outcome is

$$P_0^{d,\epsilon} = \left(\frac{1}{2}\right)^n \underbrace{\sum_{n_1=0}^{n}\sum_{n_2=0}^{n}}_{\sum_{j=1}^{2} n_j = n} \frac{n!}{n_1! n_2!} \underbrace{(1-\delta)(1-\eta)^{n_1}(1-\epsilon)^{n_2}}_{*} \underbrace{(1-\delta)(1-\eta)^{n_2}(1-\epsilon)^{n_1}}_{\#} \tag{5.57}$$

$$= (1-\delta)^2(1-\eta)^n(1-\epsilon)^n, \tag{5.58}$$

where '$*$' and '#' are the probabilities of having no click from the first and second SPAD respectively. Likewise, for one- and two-click detection events we have

$$P_1^{d,\epsilon} = \left(\frac{1}{2}\right)^n \underbrace{\sum_{n_1=0}^{n}\sum_{n_2=0}^{n}}_{\sum_{j=1}^{2} n_j = n} \frac{n!}{n_1! n_2!} \{ \underbrace{[1-(1-\delta)(1-\eta)^{n_1}(1-\epsilon)^{n_2}]}_{\text{First SPAD clicked}} \underbrace{[(1-\delta)(1-\eta)^{n_2}(1-\epsilon)^{n_1}]}_{\text{No click from second SPAD}}$$
$$+ \underbrace{[1-(1-\delta)(1-\eta)^{n_2}(1-\epsilon)^{n_1}][(1-\delta)(1-\eta)^{n_1}(1-\epsilon)_2^n]}_{\text{The other way around}} \}, \tag{5.59}$$

$$P_2^{d,\epsilon} = \left(\frac{1}{2}\right)^n \underbrace{\sum_{n_1=0}^{n}\sum_{n_2=0}^{n}}_{\sum_{j=1}^{2} n_j = n} \frac{n!}{n_1! n_2!} [1-(1-\delta)(1-\eta)^{n_1}(1-\epsilon)^{n_2}][(1-(1-\delta)(1-\eta)^{n_2}(1-\epsilon)^{n_1}]. \tag{5.60}$$

We can generalize to m detectors and k clicks as

$$P_m(k|n,\eta,\delta,\epsilon) = Cn! \left(\frac{1-\eta}{m}\right)^n \binom{m}{k} \underbrace{\sum_{n_1=0}^{n} \cdots \sum_{n_m=0}^{n}}_{\sum_{j=1}^{m} n_j = n} \left\{ \frac{1}{\prod_{j=1}^{m} n_j!} \prod_{l=n_1}^{n_k} \left[\frac{1}{(1-\delta)(1-\epsilon)^n} \left(\frac{1-\epsilon}{1-\eta}\right)^l - 1 \right] \right\}, \tag{5.61}$$

where $C = (1-\delta)^m(1-\epsilon)^{(m-1)n}$ is a constant depending on dark count and cross-talk rates. In Fig. (5.20), we plot these conditional probabilities for $m = 16$ with the dark-count probability $\delta = 0.9$ and cross-talk $\epsilon = 0.01$. It can be clearly seen that in the presence of dark-count and cross-talk events, the peaks are broadened and shifted to the left in comparison to Fig. (5.16). This implies that a k click event could happen even if less than $n = k$ photons are incident to the detector, which is caused by registered avalanches due to dark-count and cross-talk. In addition, the probability of getting zero click reduces substantially as seen in red curve in Fig. (5.20).

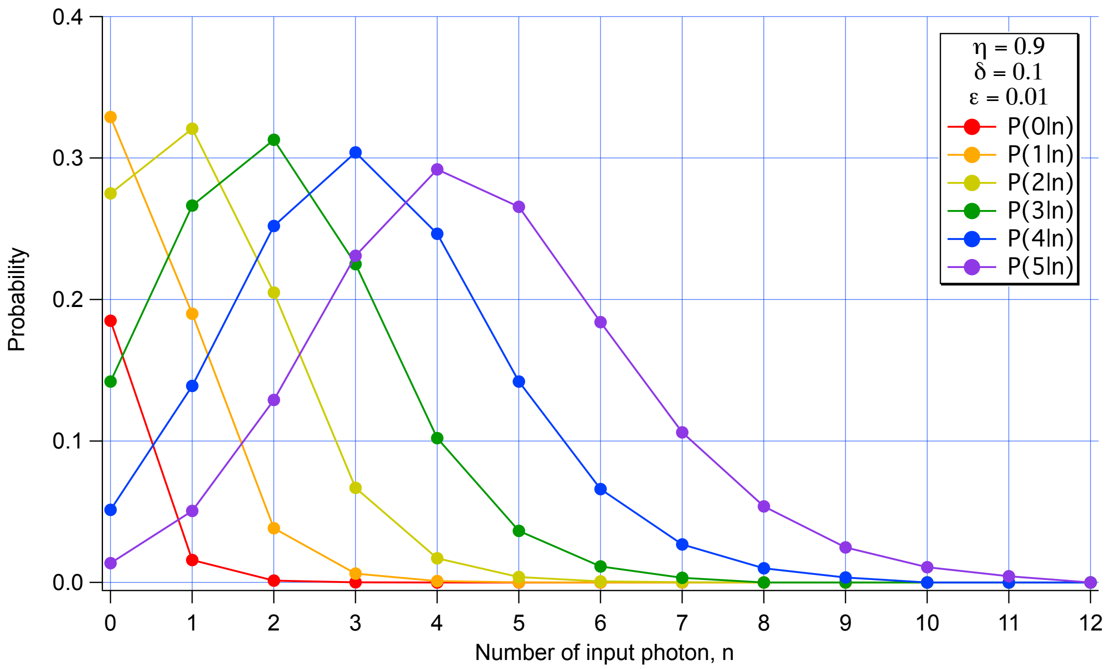

Figure 5.20: Conditional probabilities $P_{16}(k|n)$ versus n, for $\eta = 0.9$, $\delta = 0.1$, and $\epsilon = 0.01$.

In Fig. (5.21), we plot in the POVM purity for $\eta = 0.9$ and $m = 16$ for $\delta = 0, 0.01, 0.1$ and $\epsilon = 0, 0.1, 0.01$. The general trend shows that the POVM purity decreases as dark-count and cross-talk rates increase, unsurprisingly. Note the slight increase in the POVM purity for $\delta = 0.01$ and $\epsilon = 0.01$ for $k = 1$, a consequence of dark-count and cross-talk events compensating for photon loss in the waveguide, as per green curve in Fig. (5.21). Furthermore, we find that for a given rate, say 0.1, dark counts are more detrimental to POVM purity than the cross-talk events as evident from black curve ($\delta = 0.1$, $\epsilon = 0$) and blue curve ($\delta = 0$, $\epsilon = 0.1$) in Fig. (5.21). In general,

$k - k_{\delta,\epsilon}$ clicks can be mistaken as k clicks, where $k_{\delta,\epsilon}$ are the effective registered clicks due to dark count and cross talk. Thus, it becomes crucial to have a PNR detector with negligible δ and ϵ for applications in conditional quantum state preparation and state engineering as well as state characterization with PNR measurements [1], [2], [73], [89]

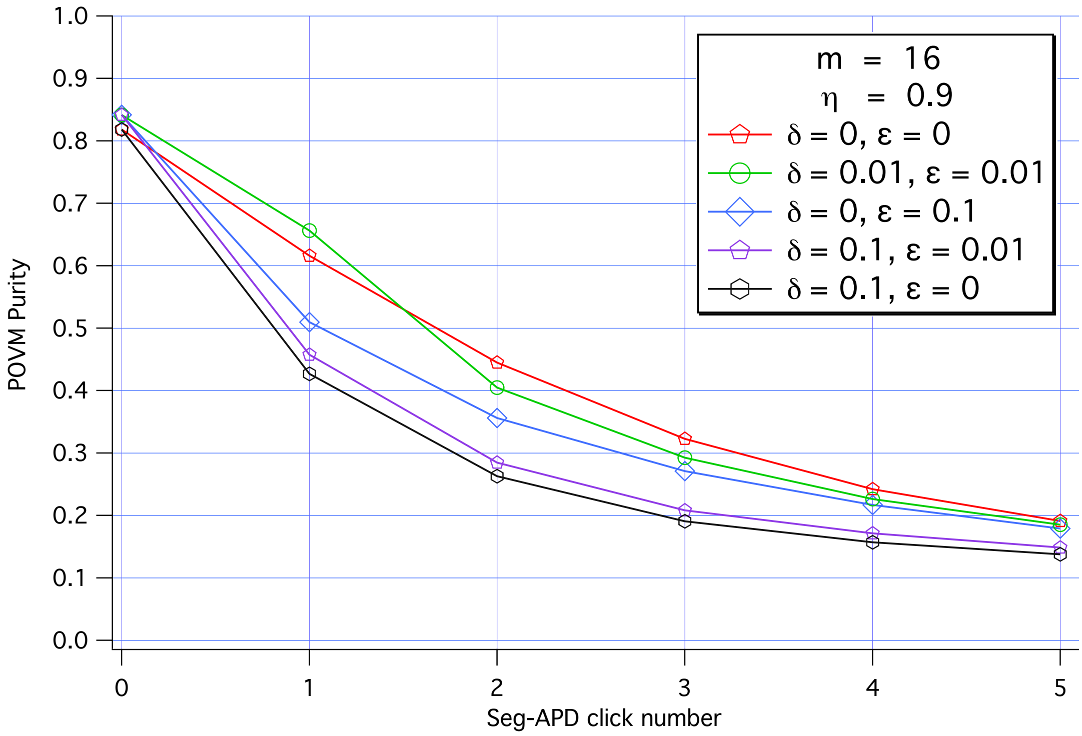

Figure 5.21: POVM element Purity(Π_k) versus click number k, for several values of δ and ϵ at $m = 16$.

In practice, extremely low dark count rates have been achieved, which supports our decision to neglect them: silicon SPADs achieved dark count rates per active area below 1 Hz/μm^2 [202], [203]; InGaAs/InP SPADs tend to have larger dark count rates and 25 μ-diameter devices with a dark count rate of 60 kHz (120 Hz/μm^2) have been demonstrated [204]. In the particular case of the detection of optical field pulses over much shorter times, it is clear that dark count rates several order of magnitude lower than photon detection rated could be achieved. Moreover, detection of sufficiently short optical pulses will ensure that the dead time due to SPAD quenching can also be ignored.

5.4 Conclusion

In this work, we carried out the theoretical evaluation of the photon-count POVM for a segmented detector such as the one designed in Section 5.3.3. Results show that PNR detection in the ideal case of no losses and no dark counts requires on the order of 10^3 SPADs to resolve 10 photons, using an efficient gradient coupling scheme. This level of scaling appears to be worthwhile of an integrated optics effort as it would yield a high quality room-temperature PNR detector. While photon losses were taken into account, it is important to note that they did not include the nonideal quantum efficiency of the SPADs, by design of the segmented detector. The reduction of photon losses will therefore only involve passive optical design considerations, a notable difference with terminally coupled tree-splitting detectors in which the quantum efficiency of the SPADs must be unity. Note also that a tree architecture can still be used to initially split the initial photon number among smaller-sized segmented photodetectors.

It is remarkable that reasonable levels of losses (1% per detector mode), and dark counts and cross-talk noise do not degrade performance as much as having a limited number of SPADs does, the number of integrated SPADs being then the dominant factor toward high-quality PNR detection. This means that investing into such a scalable integrated structure, manufacturable with available integrated photonic technology, can yield the benefit of room-temperature high-quality PNR operation.

Chapter 6

Characterizing Quantum Detectors by Wigner Functions

In this chapter, we propose a method for characterizing a photodetector by directly reconstructing the Wigner functions of the detector's Positive-Operator-Value-Measure (POVM) elements. This method extends the works of S. Wallentowitz and Vogel [Phys. Rev. A 53, 4528 (1996)] and Banaszek and Wòdkiewicz [Phys. Rev. Lett. 76, 4344 (1996)] for quantum state tomography via weak-field unbalanced homodyne technique, discussed in chapter 3, to characterize quantum detectors. The proposed scheme uses displaced thermal mixtures as probes to the detector and reconstructs the Wigner function of the photodetector POVM elements from its outcome statistics. Furthermore, we employ techniques from numerically efficient quadratic convex optimizations to make the reconstruction robust to the inevitable experimental noise.

We also discuss required resources to fully characterize a phase-insensitive detector. This work is adapted from the paper titled, "Characterizing quantum detectors by Wigner functions," Rajveer Nehra and Kevin Valson Jacob, arXiv:1909.10628 [quant-ph] (Submitted).

Motivation for this work

Photodetection has been making consistent progress with rapidly developing optical quantum technology [65], [176], [177], [191], [205], [206]. Not only do detectors provide us with deeper insights on the quantum behaviour of light by allowing us to perform precise measurements, they also are an integral part of quantum technology such as quantum computing, quantum enhanced metrology, and quantum communication [116], [207]–[211].

As discussed in chapter 5, for every quantum detector, one can associate a set of measurement operators $\{M_k\}$ called as Positive Operator Valued Measures (POVMs). When such a device measures a quantum state ρ, the probability of observing an outcome 'k' is

$$p(k)_\rho = \mathrm{Tr}[\rho M_k]. \tag{6.1}$$

Since probabilities are non-negative and sum to one, POVM elements are positive semi-definite and satisfy the completeness property $\sum_{k=0}^{K-1} M_k = \mathbb{I}$. This implies that a set of POVM elements completely describes the measurement device [212], [213]. Therefore, in order to characterize a detector, we have to determine its POVM set.

In order to identify the POVM elements of a detector, one can invert Eq. (6.1) which is known as Quantum Detector Tomography (QDT) [91], [206]. In optical QDT, light prepared in a set of known tomographically complete states a.k.a probes is incident on the detector to be characterized. The probabilities of different measurement outcomes is then used to characterize the detector.

One such possible set of probes is composed of coherent states $\{|\alpha\rangle\langle\alpha|, \alpha \in \mathbb{C}\}$. With a coherent state $|\alpha\rangle$ as the probe, the probability of outcome k is given as

$$p(k)_{|\alpha\rangle} = \mathrm{Tr}[|\alpha\rangle\langle\alpha| M_k] = \pi Q_{M_k}(\alpha), \tag{6.2}$$

where $Q_{M_k}(\alpha)$ is the Husimi Q quasi-probability distribution corresponding to the detector POVM element M_k. Therefore, one can simply reconstruct the Q functions for POVM elements directly from the measurement statistics. Since $Q_{M_k}(\alpha)$ has complete information about the POVM element M_k, ideally it could be used to predict the measurement outcomes for an arbitrary quantum state as follows: consider a quantum state ρ represented in Glauber-Sudarshan P representation as

$$\rho = \int P_\rho(\alpha)|\alpha\rangle\langle\alpha| d^2\alpha, \tag{6.3}$$

where $d^2\alpha := d\mathrm{Re}(\alpha)d\mathrm{Im}(\alpha)$. The probability of outcome k can then be obtained using the Born rule as

$$p(k)_\rho = \mathrm{Tr}[\rho M_k] = \pi \int P_\rho(\alpha) Q_{M_k}(\alpha) d^2\alpha. \tag{6.4}$$

Therefore, by using the Q representation for detector POVM elements and P representation for the input quantum state, one can, in principle determine the outcome probabilities corresponding to detector outcomes.

But this approach suffers from an inherent shortcoming due to the divergent nature of P functions for nonclassical states of the optical field [127]. In addition, as discussed in [91], experimental errors and statistical noise during the experiments may distort Q functions resulting in nonphysical POVM elements. In order to alleviate this shortcoming, it is beneficial to determine the POVM elements in some basis as opposed to the constructing Q-function, for instance photon-number basis, from the measurement outcome statistics. Several techniques have been proposed and demonstrated to reconstruct the POVM elements in the photon-number basis [59], [64], [91], [92], [214], [215]. One can further represent the POVMs in the phase space using Wigner quasiprobability distribution functions as discussed in Section 6.1.

As we discussed in chapter 2, Wigner functions provide a useful method to visualize quantum states and detectors in the phase space [216], [217]. The Wigner function corresponding to a quantum state of light has been experimentally obtained using the balanced homodyne method as well as photon number resolving measurements [89], [122], [123], [131], [133], [218].

It is insightful to note that there exists a symmetry between quantum states and measurement operators. We can see this from Eq. (6.1) wherein, due to the cyclicity of trace, the roles of the state and the operator can be swapped. This is the underlying relation which we exploit in order to identify the Wigner functions of the measurement operators (POVM elements). By obtaining the Wigner functions of the detector, any experimental probability can be found in terms of the Wigner functions of the state as well as of the detector, which are well-behaved unlike highly divergent P functions. Thus, Eq. (6.4) can be written as

$$p(k)_\rho = \mathrm{Tr}[\rho M_k] = 2\pi \int W_\rho(\alpha) W_{M_k}(\alpha) d^2\alpha, \tag{6.5}$$

where $W_\rho(\alpha)$ and $W_{M_k}(\alpha)$ are the Wigner functions of quantum state ρ and POVM element M_k respectively.

In this chapter, we propose an alternative method for quantum detector tomography by directly reconstructing the Wigner quasiprobability functions corresponding to detector POVM elements: it alleviates the need of finding the POVMs in the photon-number basis. Apart from the fundamental interest in obtaining Wigner functions of a detector, the proposed scheme is particularly beneficial to study the decoherence of a quantum detector by observing the behaviour of the POVM Wigner functions in certain regions of the phase space [219].

This chapter is organized as follows. In section 6.1, we detail the method for characterizing photodetectors using displaced thermal mixtures. In section 6.3, we then apply this method to photon-number-resolving detectors. Section 6.4 discusses the resources required for characterizing a phase-insensitive detector. We discuss the number of phase space points where Wigner function should be experimentally measured in order to have a good confidence in reconstruction. In section 6.5, we use convex optimization techniques to make our reconstruction robust to noise. Finally, we note our conclusions in section 6.6.

6.1 Method

We use the well known result that the Wigner function operator can be represented in Fock space as

$$\hat{W}(\alpha) = \frac{2}{\pi}\sum_{n=0}^{\infty}(-1)^n \hat{D}(\alpha)|n\rangle\langle n|\hat{D}^{\dagger}(\alpha), \tag{6.6}$$

where $\hat{D}(\alpha) = \exp(\alpha\hat{a}^{\dagger} - \alpha^{*}\hat{a})$ is the displacement operator with $\alpha \in \mathbb{C}$ [124]. For a detector, our aim is to experimentally reconstruct the Wigner functions corresponding to its POVM elements. Since POVMs are self-adjoint positive semi-definite operators, one can write the Wigner function of a POVM element M_k as

$$W_{M_k}(\alpha) = \frac{2}{\pi}\sum_{n=0}^{\infty}(-1)^n \mathrm{Tr}\left[M_k\hat{D}(\alpha)|n\rangle\langle n|\hat{D}^{\dagger}(\alpha)\right], \tag{6.7}$$

where, for simplicity, we define

$$Q_{M_k}^{(n)}(\alpha) := \mathrm{Tr}\left[M_k\hat{D}(\alpha)|n\rangle\langle n|\hat{D}^{\dagger}(\alpha)\right]. \tag{6.8}$$

It is worth pointing out that the $Q_{M_k}^{(n)}(\alpha)$ is essentially the probability of getting outcome k when a displaced n-photon Fock state is incident to the detector. Although the sum in Eq. (6.7) has infinite terms, in practice one can truncate it to n_0 as further terms do not significantly contribute to the sum. This can be tested by choosing a certain n_0 first and then increase it slightly to, say (n_0+l) see if it changes reconstruction significantly. And if it does not, then n_0 can be chosen to truncate the sums, otherwise one should increase the value of n_0. As a result, we have

$$W_{M_k}(\alpha) \approx \frac{2}{\pi} \sum_{n=0}^{n_0} (-1)^n Q_{M_k}^{(n)}(\alpha). \tag{6.9}$$

From Eq. (6.9) we can see that finding the Wigner function corresponding to 'M_k' amounts to finding out all these summands.

Here, we restrict ourselves to phase-insensitive detectors for simplicity. The phase-insensitive detectors such as photon-number-resolving detector only allow to measure the number of photons in electromagnetic field, but do not provide any information about its phase. On the other hand, the phase-sensitive detectors such as balance homodyne detector allow to measure both the amplitude and phase of the field.
The phase-insensitive detectors have the Wigner functions of their POVM elements rotationally symmetric around the origin, and hence can be characterized on the real axis, i.e., α can be chosen real for numerical simulations. However, we note that this scheme is also applicable to phase-sensitive detectors; and for such detectors, we have to choose α in the complex plane.

6.2 Proposed experimental setup

We now propose an experimental scheme to perform the QDT using this scheme. Fig. 6.1 shows a schematic for our proposed experiment. A laser beam is split into two beams at the first beamsplitter (BS). One beam is used to generate thermal mixtures. Thermal mixtures can be generated by randomzing the phase and amplitude of the laser beam (coherent state). To achieve that, we use a Variable Neutral Density Filter (VNDF) along with a Rotating Ground-Glass Disk (RGGD). VNDF allows to produce coherent states of variable amplitudes, which are further fed to RGGD for the phase and amplitude randomization in order to produce thermal mixtures [220]. The other beam is used as a Local Oscillator (LO) whose amplitude and phase are modulated to reconstruct the Wigner functions over the entire phase space. Amplitude and phase modulation is achieved using Local Oscillator Modulator (LOMD). For phase space displacement implementation, we interfere thermal mixtures with the LO at a highly unbalanced beamsplitter denoted as DBS in the experiment schematic.

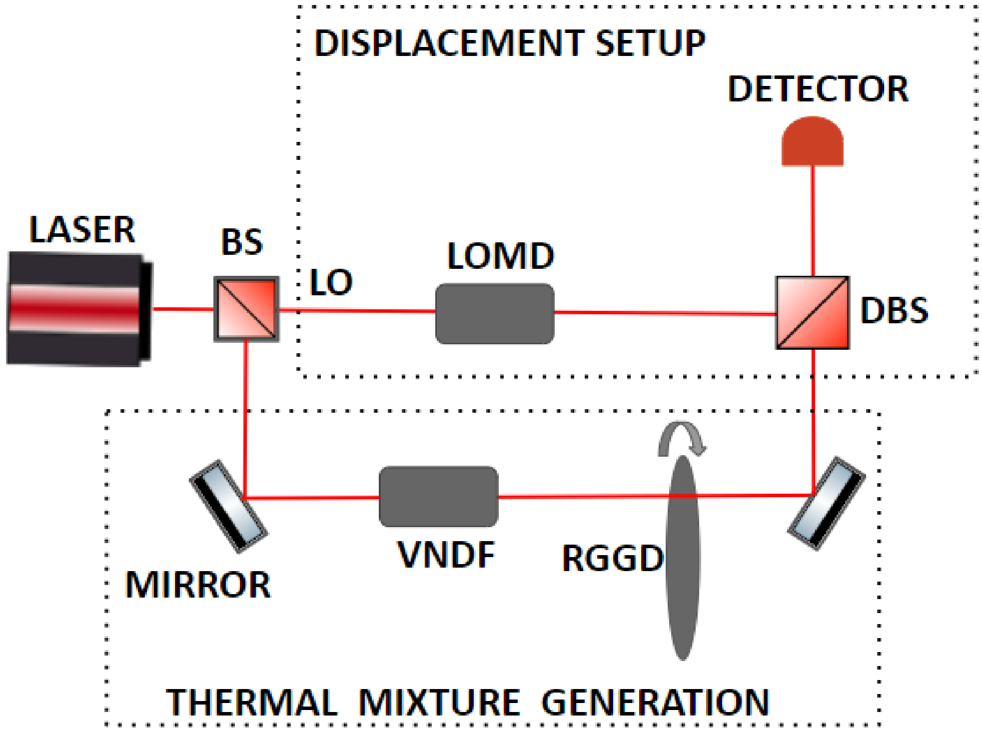

Figure 6.1: Schematic of the experimental setup. BS: beamsplitter. LO: Local Oscillator. VNDF: Variable Neutral Density Filter. RGGD: Rotating Ground-Glass Disk. DBS: Displacement beamsplitter. LOMD: Local oscillator modulator.

In order to do this, we consider $(n_0 + 1)$ distinct thermal mixtures given as

$$\rho^{(j)} = \sum_{n=0}^{\infty} p_n^{(j)} |n\rangle\langle n| \tag{6.10}$$

where $j = 0, \ldots, n_0$ labels the thermal states, and $p_n^{(j)} = \frac{\bar{n}_j^n}{(1+\bar{n}_j)^{n+1}}$ is the Bose-Einstein photon-number distribution of a thermal mixture $\rho^{(j)}$ with mean photon-number $\bar{n}_j$. We then displace these thermal mixtures by amplitude α which is, in general, a complex number. The probability of obtaining 'k' outcome with the displaced thermal input as input is given by

$$Q_k^{(j)}(\alpha) \approx \sum_{n=0}^{n_0} p_n^{(j)} P_{M_k}^{(n)}(\alpha), \tag{6.11}$$

where we choose the thermal state such that the contribution to the RHS from the omitted terms is negligible. This is possible because the thermal state has an exponentially decreasing photon number distribution. In matrix form, we can write Eq. (6.11) as

$$\begin{pmatrix} P_k^{(0)}(\alpha) \\ P_k^{(1)}(\alpha) \\ \vdots \\ P_k^{(n_0)}(\alpha) \end{pmatrix} = \begin{pmatrix} p_0^{(0)} & p_1^{(0)} & \dots & p_{n_0}^{(0)} \\ p_0^{(1)} & p_1^{(1)} & \dots & p_{n_0}^{(1)} \\ \vdots & & & \\ p_0^{(n_0)} & p_1^{(n_0)} & \dots & p_{n_0}^{(n_0)} \end{pmatrix} \begin{pmatrix} Q_{M_k}^{(0)}(\alpha) \\ Q_{M_k}^{(1)}(\alpha) \\ \vdots \\ Q_{M_k}^{(n_0)}(\alpha) \end{pmatrix}. \tag{6.12}$$

We can further write Eq. (6.12) compactly as

$$\mathbf{P} = \mathbf{\Pi} \mathbf{Q}_{\mathbf{M_k}}(\alpha), \tag{6.13}$$

where $\mathbf{P}$ and $\mathbf{Q}_{\mathbf{M_k}}(\alpha)$ are vectors of length (n_0+1), and $\mathbf{\Pi}$ is the probability distribution square matrix of dimension $(n_0+1)\times(n_0+1)$. Thus by solving Eq. (6.13), we can determine $\mathbf{Q}_{\mathbf{M_k}}(\alpha)$, which allows us to calculate the summation in Eq. (6.7). To solve for $\mathbf{Q}_{\mathbf{M_k}}(\alpha)$, one can solve the following convex quadratic optimization problem:

$$\begin{aligned} &\text{Minimize } \ ||\mathbf{P} - \mathbf{\Pi} \mathbf{Q}_{\mathbf{M_k}}(\alpha)||_2, \\ &\text{Subject to } \ 0 \le \mathbf{Q}_{\mathbf{M_k}}(\alpha) \le 1, \\ &\qquad\qquad -1 \le \sum_{n=0}^{n_0} (-1)^n Q_{M_k}^{(n)}(\alpha) \le 1, \end{aligned} \tag{6.14}$$

where $||.||$ is the l_2 norm defined as $||V||_2 = \left(\sum_i |V_i|^2\right)^{1/2}$ for a vector V. The optimization constraints in Eq. (6.14) can be understood as follows. First, the n^{th} element $Q^{(n)}_{M_k}(\alpha)$ of $\mathbf{Q_{M_k}}(\alpha)$ is essentially the probability of getting k-click if a displaced n-photon Fock state is incident to the detector. Therefore, we have $1 \geq Q^{(n)}_{M_k}(\alpha) \geq 0$. Second, Wigner functions are well-defined and bounded between $[-2/\pi, 2/\pi]$ for a POVM element corresponding to a phase-insensitive detector. This is because the POVM element in such a case is a statistical mixture of projectors and the number of projectors, i.e., $|n\rangle\langle n|$ is truncated due to the finite saturation threshold of the detector. In this case we can use the second constraint in Eq. (6.14). Thus solving this optimization allows us to determine the Wigner function at a given phase space point α. Further, we can repeat the process with different displacement amplitudes to reconstruct the Wigner function over the entire phase space.

In practice, the Wigner functions of various detectors with a finite saturation threshold are localized around the origin and vanishes to zero for large α due to decaying Gaussian modulation, so it is unnecessary to displace the thermal states with arbitrarily large α. This can be easily predetermined by knowing the detector threshold and identifying the tail of the Wigner function. In the following section we numerically simulate this method for a phase-insensitive detector. We hasten to add that this method is applicable to any type of detector.

6.3 Modelling a photon-number-resolving detector

In this section, we reconstruct the Wigner functions of a perfect and an imperfect photon-number-resolving (PNR) detector. In general, a POVM element corresponding to 'k' outcome can be written in the photon-number basis as

$$M_k = \sum_{m,n=0}^{\infty} \langle m|M_k|n\rangle |m\rangle\langle n|, \tag{6.15}$$

where $\langle m|M_k|n\rangle$ are the matrix elements of the POVM operator. One can further simplify Eq. (6.15) for a PNR detector with no dark counts as

$$M_k = \sum_{m=k}^{m_0} \langle m|M_k|m\rangle |m\rangle\langle m|. \tag{6.16}$$

Note that Eq. (6.16) differs from Eq. (6.15) in three ways. First, the POVM is diagonal with entries $\langle m|M_k|m\rangle$, which are essentially the probabilities of detecting 'k' photons given 'm' photons are incident to the detector. Thus for a detector with detection efficiency η, we have

$$p(k|m) = \langle m|M_k|m\rangle = \binom{m}{k}\eta^k(1-\eta)^{m-k}. \tag{6.17}$$

Second, we have truncated the sum to 'm_0' such that it exceeds the photon-number at which saturates the detector. Third, the sum is starting from 'k' because with no dark counts noise, one would expect 'k' clicks only if there are $m \geq k$ photons are incident on the detector.

Eq. (6.16) and Eq. (6.17) can be interpreted as follows: The POVM elements of a perfect PNR detector are projectors $\Pi_m = |m\rangle\langle m|$. However, for an imperfect detector, its efficiency $\eta < 1$. If m photons impinge on such a detector, due to its non-unity detection efficiency, $k < m$ photons results in a detection event contributing a factor of η^k to the probability of the event; while $(m-k)$ photons remain undetected contributing a factor of $(1-\eta)^{m-k}$ to the probability of the event. Thus, such POVMs are statistical mixtures of projective measurements.

In numerical simulations, we considered equidistant 51 displacement amplitudes in $\alpha \in [-3.6, 3.6]$, which allowed us to probe the Wigner function uniformly over the entire region of phase space where the Wigner function is non-vanishing. We used 50 equally spaced thermal states of mean photon-number in $\bar{n} \in [0, 4]$. For all of our simulations in open source Python module QuTip [221], we generally limited the dimension of the Hilbert space to 50, and the sum in Eq. (6.16) was truncated with $m_0 = 50$ at which point $P(k|m_0)$ was of the order of 10^{-10} for $\eta = 0.90$.

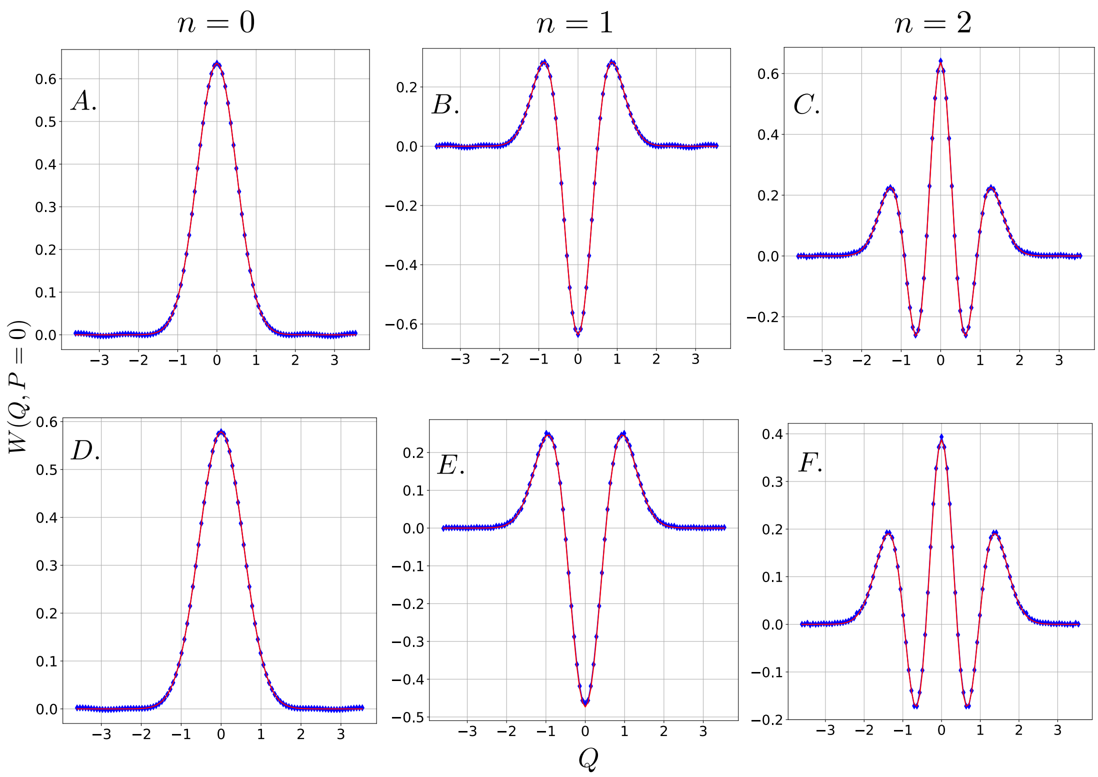

Figure 6.2: Wigner functions for POVM elements corresponding to zero-, one- and two-photon detection events. Red curves are theoretically expected Wigner functions and blue ones the reconstructed one using the proposed method. In the top row, A, B, and C are for a perfect PNR detector; and in the bottom row D, E, and F are for a PNR detector with detection efficiency $\eta = 0.90$.

In Fig. 6.2, we plot the Wigner functions of one, two, and three photon detections for a perfect detector and an imperfect detector with imperfections as modelled in Eq. (6.16). From Fig. 6.2, we notice that the extrema of the Wigner functions of imperfect detectors are closer to the origin than those of perfect detectors. This is due to the contribution of higher order projectors in the Wigner functions of imperfect detectors. In particular for the imperfect single-photon detection event, we see a reduced negativity in the Wigner function around the origin. This is due to the contribution of the Wigner function of the two-photon detection event which is strongly positive around origin. Similar arguments can be made for the the reduced positivity of the Wigner function for zero- and two-photon detection event POVMs.

In our reconstruction, we have uniformly sampled the phase space. A natural question that now arises is whether the number of points that needs to be probed in the phase space can be reduced. We investigate this question in the following section.

6.4 Characterizing a PNR detector with polynomial resources

Although the method outline earlier is general, it had substantial resource requirements as we had to uniformly sample over the phase space. However, this requirement can be drastically reduced if we have the prior knowledge that the detector is phase-insensitive, i.e., the representations of its POVM elements are diagonal in the Fock basis. Note that the phase sensitivity of a detector can easily be checked by varying the phase of the LO while keeping the amplitude fixed. In this case, unlike a PNR detector, a phase sensitive detector outputs different measurement statistics for different phases and fixed amplitudes of the LO. We recall that the Wigner functions of Fock states are Gaussian modulated Laguerre polynomials [111]. This allows us to write the Wigner function the POVM elememt 'M_k' of a PNR detector as

$$W_{M_k}(\alpha) = \frac{2e^{-2|\alpha|^2}}{\pi} \sum_{m=0}^{m_0} (-1)^m p(k|m) \; \mathcal{L}_m(4|\alpha|^2), \tag{6.18}$$

where $\mathcal{L}_m(x)$ represents the Laguerre polynomial of m^{th} degree in $|\alpha|^2$. As the Wigner function is a function of $|\alpha|^2$, it is symmetric around the origin, and can be fully characterized on the real axis. Since the Wigner function is a Gaussian modulated polynomial, the problem of reconstruction is reduced to finding out a polynomial of degree $2m_0$ in α which requires us to find the Wigner function only at $2m_0+1$ points.

As an example, we considered the POVM element corresponding to a single-photon detection event for both perfect and imperfect PNR detectors. In Fig. 6.3, the red curves show the POVM determined by the naive summation up to 15 terms of Eq. (6.7); and the blue curves the reconstructed Wigner functions with black points being the phase space coordinates where the Wigner function was probed.

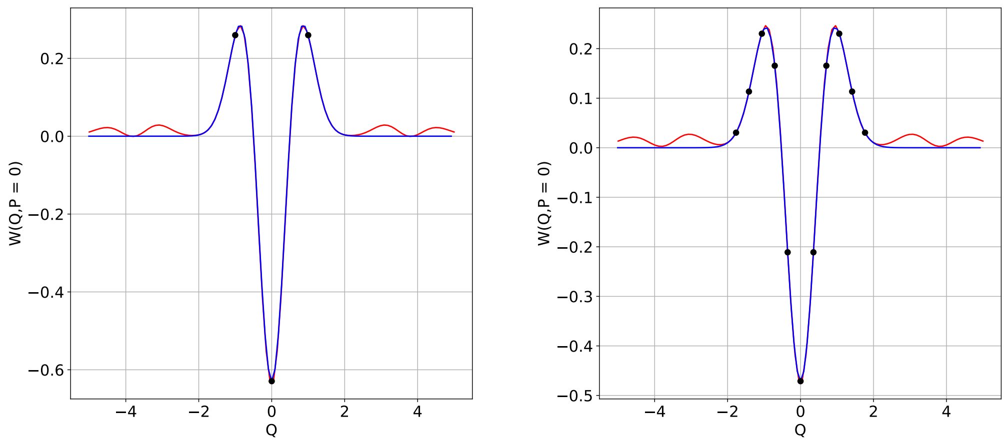

Figure 6.3: Left : Wigner function corresponding to a perfect single-photon detection POVM determined by naive summation up to 15 terms of Eq. (6.7) (Red), and using an Gaussian modulated quadratic fit near the origin (Blue). Black points represent the phase space points where the Wigner function was probed by the proposed method here. The latter approximates well the actual Wigner function. Right : Wigner function corresponding to an imperfect single-photon detection POVM with $\eta = 0.90$.

We see that one needs to probe the Wigner function only at three points for a perfect detector because the Laguerre polynomial $\mathcal{L}_{m=1}(4|\alpha|^2)$ is quadratic in α, and therefore can be fully characterized using three distinct points. Likewise, the Wigner function for an imperfect single-photon POVM can be reconstructed using only 11 distinct points (black points in Fig. 6.3) if we truncate the sum in Eq. (6.16) at $m_0 = 5$ where $p(k|m)$ is of the order of 10^{-6}. In this case, we will have to reconstruct an Gaussian modulated polynomials of degree 10 because the last term in the Eq. (6.16) would be a projector, $|5\rangle\langle 5|$ with Wigner function given by Gaussian modulation of

$\mathcal{L}_{m=5}(4|\alpha|^2)$.

Note that finding the Gaussian modulated polynomial also works for a general detector given by Eq. (6.15). However, instead of reconstructing the Wigner function on the real line, we will have to reconstruct it in the complex plane for which appropriate polynomial interpolation schemes have to be used [222].

6.5 Robustness against experimental noise

In this section, we discuss the robustness of this method against experimental noise. In general, inverting Eq. (6.13) is ill-conditioned as seen by the large ratio of the largest and smallest singular values of the matrix $\mathbf{P}$. This makes the reconstructed POVM elements extremely sensitive to small fluctuations in the measurement statistics, and can lead to nonphysical POVMs.

However, the effects of ill-conditioning can be remarkably suppressed by adding a regularization to the optimization problem. Several types of regularization techniques are discussed in detail in [91], and for this work we use Tikhonov regularization [223]. Using this technique, inverting Eq. (6.13) can be mathematically formulated as the following optimization problem:

$$\begin{aligned}
&\text{Minimize } \; ||\mathbf{P} - \mathbf{\Pi}\mathbf{Q}_{\mathbf{M_k}}(\alpha)||_2 + \gamma||\mathbf{Q}_{\mathbf{M_k}}(\alpha)||_2, \\
&\text{Subject to } \; 0 \leq \mathbf{Q}_{\mathbf{M_k}}(\alpha)) \leq 1, \\
&\qquad\qquad -1 \leq \sum_{n=0}^{n_0} (-1)^n Q_{M_k}^{(n)}(\alpha) \leq 1,
\end{aligned} \tag{6.19}$$

where γ is the regularization parameter. Solving this problem translates to a convex quadratic optimization which can be efficiently solved using any of the widely used convex solvers, for instance, the Python package CVXOPT [159].

In order to simulate the presence of noise in our reconstruction, we introduce noise in the LO's amplitude $|\alpha|$. We model this noise as a Gaussian distribution of mean zero and standard deviation $\sigma = 1\%|\alpha|^2$, i.e., $\sigma = 0.01|\alpha|^2$. Note that this level of noise is much higher than the stabilized lasers available these days at $1064nm$. Therefore, the displacement amplitudes are $(\alpha_1 + \delta d_1, \alpha_2 + \delta d_2 \ldots, \alpha_{max} + \delta d_{max})$, where each δd_i is a random variable sampled from the Gaussian distribution.

To further reduce the effects of the fluctuations, we average the Wigner functions obtained over $N = 40$ iterations of the optimization. As a result, we get

$$\overline{W}_{M_k}(\alpha) = \frac{\sum_{j=1}^{N} W^j_{M_k}(\alpha + \delta\alpha_j)}{N}. \tag{6.20}$$

Having obtained $\overline{W}_{M_k}(\alpha)$, we then we utilize robust nonlinear regression methods to further suppress the fluctuations. We recall that for a phase insensitive detector, the POVMs are Gaussian modulated polynomials of degree $2m_0$ in α, where m_0 is the saturation limit given in Eq. (6.18). Therefore, once we have experimentally probed the Wigner function at $2m_0 + 1$ distinct points of the phase space, we could simply fit a Gaussian modulated polynomial of degree $2m_0$ in α to reconstruct the Wigner function over the entire phase space. Keeping that in mind, we set an optimization problem as:

$$\text{Minimize:} \quad \left\{ \frac{1}{2} \sum_{i=1} L \left[\left(e^{-2|\alpha_i|^2} \text{Poly}(2m_0, \alpha_i) - \overline{W}_{M_k}(\alpha_i) \right)^2 \right] \right\}, \tag{6.21}$$

where L is defined as

$$L(y) = 2(\sqrt{1+y} - 1), \tag{6.22}$$

and $\text{Poly}(2m_0, \alpha_i)$ is a polynomial of degree $2m_0$. Note that this approach of finding the Gaussian modulated polynomial has an advantage of not being biased unlike the simple least-square fitting method which tends to significantly bias in order to avoid high residuals in the data [224].

We further evaluate the quality of reconstruction method by using the relative error defined with l_2 norm as:

$$\triangle := \frac{||W_{M_k}^{\text{theory}}(\alpha) - W_{M_k}^{\text{reconstruted}}(\alpha)||_2}{||W_{M_k}^{\text{theory}}(\alpha)||_2}. \tag{6.23}$$

The result of our reconstruction is shown in Fig. 6.4. Since the fluctuations grow with increasing local oscillator amplitude, the reconstruction of the Wigner function around the origin of phase space is the least disturbed, but with higher displacements the fluctuations grow stronger as seen in Fig. 6.4.
Therefore, it may be beneficial to probe the Wigner function around the origin densely, and sparsely at the higher displacements, in particular $|\alpha| > 1$. Note that probing near the origin doesn't undermine the quality of reconstruction as long as we probe the Wigner function at $2m_0+1$ distinct points because we need only $2m_0+1$ distinct points to reconstruct a polynomial of degree $2m_0$ as seen in Fig. 6.3. In fact, we can further exploit the rotational symmetry of the POVMs corresponding to phase insensitive detector, which means the Wigner function at α has the same value at $-\alpha$. This allows us to only probe the Wigner function at $m_0 + 1$ distinct points to fully characterize a quantum detector that saturates at the photon-number m_0. However, in this work we numerically probe the phase space at equidistant displacement amplitudes.

We now investigate how sensitive our reconstruction is to the choice of γ. To evaluate that, we calculate the relative error defined in Eq. (6.23) for several values of $\gamma \in [10^{-4}, 0.012]$. The result is illustrated on the bottom right in Fig. 6.4 for the POVM element corresponding to $n = 1$ and $\eta = 0.90$. We can clearly see that even if we vary γ by an order of magnitude (from 10^{-3} to 10^{-2}), the relative error only changes by less than one percent. This shows that there is sufficient freedom in the choice of γ.

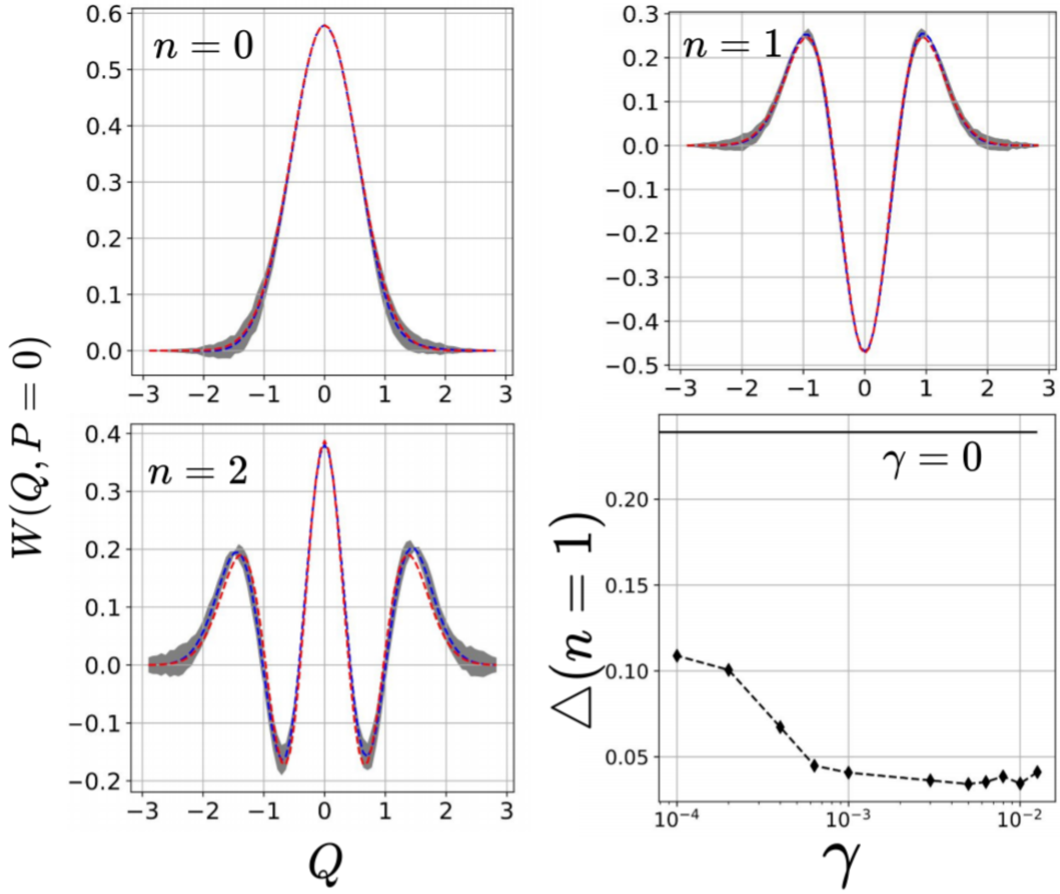

Figure 6.4: Blue: Reconstructed Wigner functions using regularization for zero-,one- and two-photon detection event of a detector with $\eta = 0.90$. Red curves are theoretically expected Wigner functions. Gray areas are error (1σ) obtained using $N = 40$ iterations. Bottom right: Dashed-diamond curve illustrates the robustness of the reconstruction against regularization parameter γ and black solid line is without regularization, i.e, $\gamma = 0$.

6.6 Conclusions

We have developed a method for characterizing photodetectors by experimentally obtaining the Wigner functions corresponding to the POVMs describing the detector measurements. The proposed experimental scheme is simple and easily accessible, in particular, for a phase insensitive detector. Augmented with quadratic convex optimization and robust nonlinear fitting techniques, we demonstrated its robustness to the experimental fluctuations. Future work on this method may involve an account for mode mismatch between the local oscillator and the optical mode of thermal mixtures. This direction of research is motivated by the fact that unlike in the balanced homodyne technique, mode mismatch cannot simply be treated as losses in this method. Another direction is to employ phase-averaged coherent states (PACSs), which are also diagonal in photon-number basis, instead of thermal mixtures. The PACS can be easily prepared in the lab by only randomizing the optical phase of a coherent state. This work was jointly done with Kevin Valson Jacob at Louisiana State University during my visit in 2018.

Chapter 7

Heisenberg-limited quantum interferometry with photon-subtracted twin beams

In this chapter, we propose a new type of a Heisenberg-limited quantum interferometer, whose input is indistinguishably photon-subtracted twin beams. This type of interferometer can yield Heisenberg-limited performance while at the same time giving a direct fringe reading, unlike for the twin-beam input of the Holland-Burnett interferometer. We show that with intensity difference measurements the quantum Cramér-Rao bound for the phase measurement can be achieved. We propose a feasible experimental realization.

This chapter is based on the paper titled, "Heisenberg-limited quantum interferometry with photon-subtracted twin beams", Rajveer Nehra, Aye Win, and Olivier Pfister, arXiv:1707.07641 [quant-ph].

7.1 Introduction

A general interferometer, typified by the Mach-Zehnder interferometer (MZI) of Fig.7.1, measures the phase difference between two propagation paths by probing them with mutually coherent waves. From a purely undulatory standpoint, a sure way of ensuring such mutual coherence is to split an initial wave into two waves, for example by use of a beam splitter. However, the unitarity of quantum evolution mandates that any two-wave-output unitary have a two-mode input as well — rather than a classical, single-mode input. Thus, the quantum description of a "classical" interferometer must feature an "idle" vacuum field in addition to the initial wave as we discuss in chapter 2, and the quantum fundamental limit of interferometric measurements is

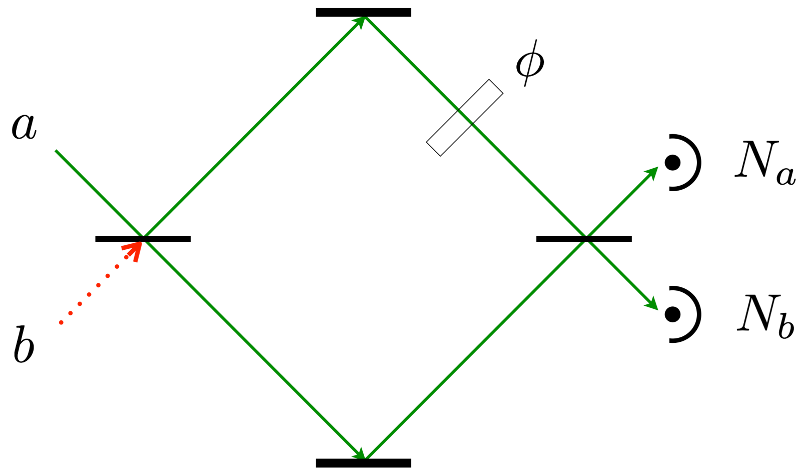

Figure 7.1: A Mach-Zehnder interferometer with phase difference ϕ between two optical paths. Both beam splitters are balanced. Quantum splitting of input field a implies interference with the vacuum field b.

then dictated by the corpuscular statistics of the interference between the two inputs of the beam splitter (Fig.7.1).

We now derive the phase noise for a coherent state, $|\alpha\rangle$ in mode a and vacuum, $|0\rangle$ in mode b as an input to the MZI interferometer in Fig.7.1. In a typical interferometry experiment, one measures the intensity difference at both outputs of the interferometer for a given input [1]. Thus, we need to calculate

$$I_a - I_a = \langle \hat{N}_a - \hat{N}_b \rangle_{|\psi\rangle_{a,b}^{out}}, \tag{7.1}$$

where $N_a = a^\dagger a$ and $N_b = b^\dagger b$ are the photon-number operators and $|\psi\rangle_{a,b}^{out}$ is the two-mode output state. The state after the first 50:50 beamsplitter (BS)

$$|\alpha\rangle_a |0\rangle_b \xrightarrow{\text{After first BS}} \left|\frac{\alpha}{\sqrt{2}}\right\rangle_a \left|\frac{\alpha}{\sqrt{2}}\right\rangle_b \tag{7.2}$$

Likewise, the phase shifted state inside the interferometer

$$\left|\frac{\alpha}{\sqrt{2}}\right\rangle_a \left|\frac{\alpha}{\sqrt{2}}\right\rangle_b \xrightarrow{\text{After phase shifter}} = e^{-i\phi\hat{N}_a} \left|\frac{\alpha}{\sqrt{2}}\right\rangle_a \left|\frac{\alpha}{\sqrt{2}}\right\rangle_b = \left|\frac{\alpha e^{-i\phi}}{\sqrt{2}}\right\rangle_a \left|\frac{\alpha}{\sqrt{2}}\right\rangle_b \tag{7.3}$$

Finally, the output state after the second 50:50 BS

$$\left|\frac{\alpha e^{-i\phi}}{\sqrt{2}}\right\rangle_a \left|\frac{\alpha}{\sqrt{2}}\right\rangle_b \xrightarrow{\text{After second BS}} |\psi\rangle_{a,b}^{out} = \left|\frac{\alpha e^{-i\phi} + \alpha}{2}\right\rangle_a \left|\frac{\alpha e^{-i\phi} - \alpha}{2}\right\rangle_b \tag{7.4}$$

We then determine the intensity difference using Eqs. 7.1 and 7.4, which yields

$$\langle \hat{N}_a - \hat{N}_b \rangle_{|\psi\rangle_{a,b}^{out}} = \mathrm{Tr}[|\psi\rangle_{a,b}^{out} \langle\psi|_{a,b}^{out} (\hat{N}_a - \hat{N}_b)] = |\alpha|^2 \mathrm{cos}\phi \tag{7.5}$$

The measurement uncertainty in the intensity difference is

$$\triangle \langle \hat{N}_a - \hat{N}_b \rangle_{|\psi\rangle_{a,b}^{out}} = \sqrt{\langle (\hat{N}_a - \hat{N}_b)^2 \rangle_{|\psi\rangle_{a,b}^{out}} - \langle \hat{N}_a - \hat{N}_b \rangle^2_{|\psi\rangle_{a,b}^{out}}}, \tag{7.6}$$

$$= |\alpha|^2 \tag{7.7}$$

[1]Quantum interferometry can be thought as an estimation problem where our goal is to estimate the phase difference by measuring some physical observable, a.k.a, the estimator. In this chapter, we will be using the intensity difference at the output ports of MZI to estimate the phase measurement noise.

where we have used

$$\langle(\hat{N}_a - \hat{N}_b)^2\rangle_{|\psi\rangle_{a,b}^{out}} = |\alpha|^2(1 + |\alpha|^2\cos^2\phi) \tag{7.8}$$

Using the error propagation, one can get the phase noise given as

$$\triangle\phi = \frac{\triangle\langle\hat{N}_a - \hat{N}_b\rangle_{|\psi\rangle_{a,b}^{out}}}{\left|\frac{d\langle\hat{N}_a - \hat{N}_b\rangle_{|\psi\rangle_{a,b}^{out}}}{d\phi}\right|}. \tag{7.9}$$

Using Eqs. 7.5, 7.7, and 7.9

$$\triangle\phi = \frac{1}{|\alpha|\sin\phi} = \frac{1}{\sqrt{N}|\sin\phi|}\bigg|_{\phi\to\frac{\pi}{2}} \approx \frac{1}{\sqrt{N}} \tag{7.10}$$

As a result, we note that in a classical interferometer, the vacuum fluctuations at the idle input port limit the phase difference sensitivity between the two interferometer arms to the quantum limit of classical interferometry [225], the input beamsplitter's shot-noise limit (SNL)[2]

$$\Delta\phi_{SNL} \sim \langle N\rangle^{-\frac{1}{2}}\,, \tag{7.11}$$

where ϕ is the phase difference to be measured and $N = N_a + N_b$ is the total photon number operator. This limit is that of phase noise *inside the interferometer* and has nothing to do with, say, the single-mode properties of a coherent state (e.g., laser) input $|\,\alpha\,\rangle$ of photon-number deviation $\Delta N = |\alpha| = \langle N\rangle^{1/2}$ and phase deviation [3] $\Delta\phi \sim \langle N\rangle^{-1/2}$ *before the interferometer.* In fact, Caves showed that a Fock-state input $|\,n\,\rangle$, for which $\Delta N = 0$ and hence $\Delta\phi \to \infty$, still yields the SNL of Eq. (7.11) [225].

When both input modes of the interferometer are properly "quantum engineered,"

[2] The SNL is often called "standard quantum limit." However, the latter was initially defined with a different meaning, in order to address the optimum error of quantum measurements in the presence of back action, such as radiation pressure on interferometer mirrors. [226], [227].

[3] From the number-phase Heisenberg inequality $\Delta N\Delta\phi \geqslant 1/2$, easily derived from the energy-time inequality [228].

one can, in principle, reach the ultimate limit, called the Heisenberg limit (HL),

$$\Delta\phi_H \sim \langle N\rangle^{-1}, \tag{7.12}$$

which can clearly be many orders of magnitude lower than the SNL when $\langle N\rangle \gg 1$. A recent comprehensive review of quantum interferometry can be found in Ref. [229]. The first quantum engineering proposal to break through the SNL was Caves' idea to replace the vacuum state input with a squeezed vacuum [230], which has since been shown to optimize the quantum Cramér-Rao bound when the input field is a coherent state [231]. This was demonstrated experimentally [232], [233] and is now the approach adopted for high-frequency signals (above the standard quantum limit) in gravitational-wave detectors [234], [235]. Many other approaches have been investigated [236], [237], such as twin beams [82], [147], [238]–[241], "noon" states [242]–[246], or two-mode squeezed states. These different schemes were recently compared in terms of their quantum Cramér-Rao bound [247].

It is important to recall here the essential result of Escher, de Matos Filho, and Davidovich: operating a realistic, i.e., lossy, interferometer at the Heisenberg limit requires losses to be no greater than $\langle N\rangle^{-1}$ [248], i.e., the grand total of the loss can never exceed one photon, on average. This result had been obtained earlier by Pooser and Pfister in the particular case of Holland-Burnett interferometry [249]: using Monte Carlo simulations for up to $n = 10\,000$ photons, it was shown that the phase error of a nonideal Holland-Burnett interferometer scales with the Heisenberg limit if the losses are of the order of n^{-1}, and that larger losses degrade the scaling to a limit proportional to the SNL $N^{-1/2}$, staying sub-SNL as long as photon correlations are present in the twin Fock input. This is consistent with the general result of Escher, de Matos Filho, and Davidovich for phase estimation [248].

A direct consequence is that, if the total photon number is too large, ultimate-sensitivity interferometry cannot be Heisenberg-limited in the current state of technology: the most sensitive interferometer to date, the Laser Interferometer Gravitational-wave Observatory (LIGO) boasts $\Delta\phi_{SN} \sim 10^{-11}$ rad and is shot-noise-limited in some spectral regions, therefore featuring $\langle N \rangle \sim 10^{22}$ photons. While a Heisenberg-limited version of LIGO would only require $\langle N \rangle \sim 10^{11}$ photons to reach the same sensitivity, it would also require an unrealistic loss level of 10^{-11}, the optical coatings on LIGO's mirrors "only" reaching already remarkable sub-ppm loss levels [250].

However, the maximally efficient use of photons by Heisenberg-limited interferometry can still be interesting provided we take into account this constraint of an ultimate loss level of 10^{-6}. At this level, a 1064 nm interferometer with (arbitrarily chosen) 10 ms measurements would be allowed to reach the 10^6-photon HL of 1 μrad with only 200 pW, whereas a classical interferometer would need 10^{12} photons, i.e., 200 μW, to have its SNL at 1 μrad. This can be of interest in situations where low light levels are beneficial, such as phase imaging of living biological tissue.

In order to motivate the approach of this chapter, we review and compare and contrast some different HL proposals in Table 7.1. The key points we examine here are:
(i), whether the input state enables HL performance;
(ii), whether a direct interference fringe is observable;
(iii), whether the $\langle N \rangle \gg 1$ regime is experimentally accessible.
As we'll see, the new input state we propose in this chapter is the only one that fulfills all three criteria.

The first two cases are classical interferometer ones. The third one is Caves' squeezed input [230]. These benefit from mature, high-level laser and quantum optics technology, with large average photon numbers from well stabilized lasers [145]. Case 3 benefits from the recent 15 dB squeezing record [251], but it does require that the phase difference between the squeezed state and the coherent state be controlled [252]. Gravitational-wave observatory LIGO is described by case 2, and soon case 3 [235], whereas GEO-600 is now operating with squeezing [234].

Table 7.1: Characteristics and performance of different input states — except the "noon" state* which is a state specified *inside* the interferometer. Also the fringe signal for the "noon" state requires n-photon detection$^{(\ddagger)}$. The phase error $\Delta\phi$ is the quantum Cramer-Rao bound [247]. The state whose use we propose in this chapter is the last one.

	Input* state	*(i)* $\Delta\phi$		*(ii)* $\langle N_a - N_b \rangle$	*(iii)* $\langle N \rangle \gg 1$?
1.	$\vert\, n \,\rangle_a \vert\, 0 \,\rangle_b$ 1001[225]	$\frac{1}{\sqrt{n}}$	SNL	$n \cos\phi$	yes
2.	$\vert\, \alpha \,\rangle_a \vert\, 0 \,\rangle_b$ [225]	$\frac{1}{\sqrt{\langle N \rangle}}$	SNL	$\vert\alpha\vert^2 \cos\phi$	yes
3.	$\vert\, \alpha \,\rangle_a \vert\, 0, r \,\rangle_b$ [230]	$\frac{e^{-r}}{\vert\alpha\vert}$	sub-SNL	$\vert\alpha\vert^2 \cos\phi$	yes
4.	$\vert\, n \,\rangle_a \vert\, n \,\rangle_b$ [238]	$\frac{1}{\sqrt{2n(n+1)}}$	HL	0	yes [147]
5.	$\vert\, n \,\rangle_a \vert\, n-1 \,\rangle_b$ [247]	$\frac{1}{\sqrt{2n^2-1}}$	HL	$\frac{1}{2}\cos\phi$	possible
6.*	NOON [242], [243]	$\frac{1}{n}$	HL	$\sim \cos(n\phi)^{(\ddagger)}$	unknown
7.	Yurke [236]	$\frac{1}{\sqrt{n(n+1)}}$	HL	$\frac{\cos\phi}{2} - \frac{\sin\phi}{4}\sqrt{n(n+2)}$	unknown
8.	This work	$\frac{1}{n}$	HL	$-\frac{n}{2}\sin\phi$	possible

Case 4 in Table 7.1 is the twin Fock state input first proposed by Holland and Burnett [238], and which is implementable, to a good approximation, with large photon numbers by using an optical parametric oscillator above threshold [147], [241], [253]–[255].

The input density operator is then of the form, in the absence of losses,

$$\rho = \sum_{n,n'} \rho_{n,n'} \,|\, nn \,\rangle \langle\, n'n' \,| \,, \tag{7.13}$$

which can be a pure state ($\rho_{n,n'} \mapsto \rho_n \rho^*_{n'}$), e.g. the two-mode squeezed state emitted by a lossless optical parametric oscillator (OPO) below threshold, or can be a general statistical mixture as emitted by a lossless OPO above threshold [4]. It thus also benefits from the same mature OPO-based squeezing technology, with a record 9.7 dB reduction on the intensity-difference noise [255]. Moreover, the phase difference between the twin beams is irrelevant (being actually very noisy from being anti-squeezed) and thus need not be controlled before the interferometer. The generalized [256] Hong-Ou-Mandel [257] quantum interference responsible for twin beams breaking the SNL was demonstrated experimentally in an ultrastable phase-difference-locked OPO above threshold [147], [258], [259], with several mW of CW power.

An inconvenient feature of the Holland-Burnett scheme, however, is that the direct interference fringe disappears ($\langle N_a - N_b \rangle = 0$ in Table 7.1, a property also shared by the classical input $|\,\alpha\,\rangle_a |\,\alpha\,\rangle_b$) in contrast to all previous cases for which the fringe signal is proportional to the total photon number. This inconvenience can be circumvented by the use of Bayesian reconstruction of the probability distribution [238], [240], [249]. However, this requires photon-number-resolved detection at large photon numbers, which isn't accessible experimentally yet. Another workaround is to use the variance of the photon-number difference, which is sensitive to ϕ [239] but whose signal-to-noise ratio is bounded by $\sqrt{2}$ [240]. Another idea is to use a heterodyne signal, which presents high visibility but is restricted to phase shifts ever closer to zero as the squeezing increases [260]. This was demonstrated experimentally as heterodyne polarimetry 4.8 dB below the SNL [241].

Case 5 in Table 7.1 is a variant of the twin Fock state, the "fraternal" twin Fock state [247], does provide a direct fringe signal which being Heisenberg-limited, but the fringe signal is still extremely small.

Case 6 stands out for several reasons. The "noon" state is not to an interferometer

[4] This is the most general mixture for which $\langle N_a - N_b \rangle = 0$ and $\Delta(N_a - N_b) = 0$.

input state but to a state inside the Mach-Zehnder interferometer [242], [243]. While it yields performance at the HL, its experimental generation isn't yet experimentally accessible for $n \gg 1$; previous experimental realizations have been using postselected outcomes for $n = 3$ [244] and 4 [245], a method which doesn't scale to large photon numbers, though a more scalable method using coherent state displacement was also demonstrated [246]. Last but not least, the use of a noon state with n photons requires n-photon detection, which isn't experimentally accessible optically for $n \gg 1$ (but may be easier to reach in atomic spectroscopy [242]).

Case 7 is the theoretical proposal of Yurke, McCall, and Klauder (YMCK) [236]. It features both performance at the HL and a strong fringe signal, but its experimental realization hasn't been figured out yet.

Case 8 features the input proposed in this chapter; it is the only one of the table that features HL performance, a clear interference fringe signal, and is experimentally feasible with demonstrated technology for large photon numbers. The state can be generated by using bright twin beams from which one photon has been indistinguishably subtracted (or added).

A similar approach was proposed by Carranza and Gerry [261], in which they propose to subtract equal photon numbers from the weak twin beams created by two-mode squeezing, in part to increase the average photon number by photon subtraction — a counterintuitive but well-known effect, already demonstrated for small photon numbers [262]. In this chapter, the proposal is different in several ways: first, we perform *indistinguishable* — rather than simultaneous in Ref. [261] — photon subtraction to obtain, as detailed below, the state of case 8, which is different from Ref. [261] ; second, we consider *bright* twin beams, such as emitted by an OPO above threshold, in order to start with large photon numbers and truly evidence the HL advantage over the SNL; third, the emphasis here is on a direct fringe measurement, allowed by our state, as opposed to the parity measurement considered in Ref. [261], and initially proposed by Anisimov et al. [263], a measurement that's not yet experimentally feasible for large photon numbers.

This chapter is organized as follows. In section 7.2, we examine the effect of various types of photon subtraction on twin beams for quantum interferometry and determine the optimum input. In section 7.3, we derive the interference signal and phase sensitivity that can be obtained with such states, and corresponding statistical mixtures, and show that the HL can be reached. We also analyze the effect of losses on performance, and confirm the general result of Escher et al. [248].

7.2 Study of indistinguishable photon subtraction processes on twin beams

As announced in Table 7.1 — and proven in the next section — the input state

$$|\,\phi^+\,\rangle = \frac{1}{\sqrt{2}}(|\,n\,\rangle_a\,|\,n-1\,\rangle_b + |\,n-1\,\rangle_a\,|\,n\,\rangle_b) \tag{7.14}$$

boasts Heisenberg-limited performance *as well as a strong fringe signal,* experimentally accessible with state-of-the-art technology. A casual examination of this state easily reveals why the process of indistinguishable photon subtraction from either mode a or mode b is being considered as a means to prepare such a state. However, one should be mindful of a crucial point: the output of multimode photon subtraction is, in general, not a pure state but a statistical mixture [264]. In the following, we consider two experimental protocols, both of which can be legitimately construed as "indistinguishable photon subtracting," and show that only the one that preserves quantum coherence can prepare the state of Eq. (7.14).

7.2.1 “Bucket” indistinguishable photon subtraction

We consider the situation depicted in Fig.7.2, in which a twin-beam input sees a photon subtracted from either mode by detection by a single photodetector. Adopting

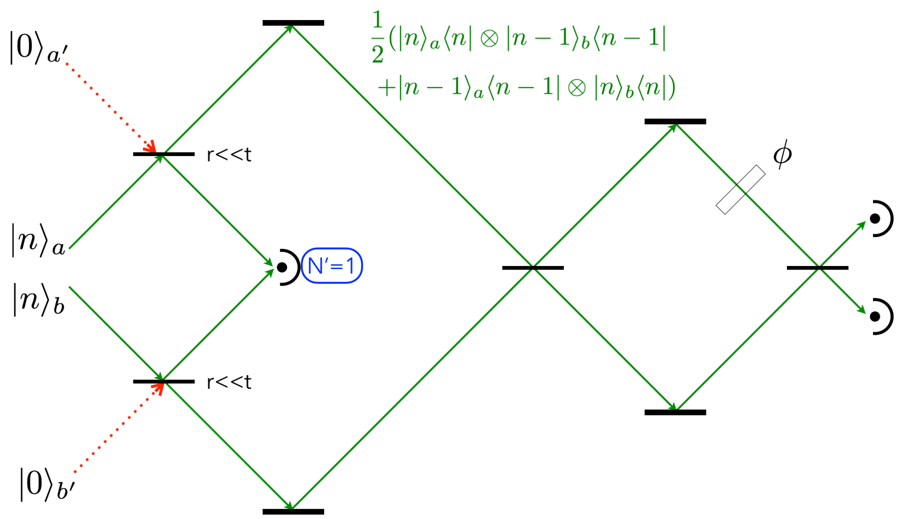

Figure 7.2: Indistinguishable single-photon subtraction producing a statistical mixture. All interferometer output measurements are conditioned by the single-photon detection event in blue.

the method introduced in Ref. 264, we now derive the quantum output of this “bucket” photon subtraction procedure. The formal description of photon subtraction uses a very unbalanced beam splitter. The unitary operator for a multimode beam splitter is

$$U_{BS} = \exp\left[i\sum_{n=1}^{m}\theta_n({a_n}^\dagger a'_n + {a'_n}^\dagger a_n)\right], \tag{7.15}$$

where θ_n is the beam splitter parameter such that $r_n = \sin\theta_n$ and $t_n = \cos\theta_n$, where r_n and t_n are the respective reflection and transmission coefficients, and a_n and a'_n are the annihilation operators for the signal and vacuum modes respectively. An unbalanced beam splitter features $\theta_n \ll 1$, which allows us to neglect the higher order terms in the power series. Therefore, we have

$$U_{BS} \simeq \mathbb{I} + i\sum_{n=1}^{m}\theta_n({a_n}^\dagger a'_n + {a'_n}^\dagger a_n). \tag{7.16}$$

As shown in Fig.7.2, one port of each beam splitter is being fed an n-photon Fock state and the other port a vacuum state:

$$\left|\,\psi^{in}\,\right\rangle = \left|\,n,n\,\right\rangle_{a,b} \otimes \left|\,0,0\,\right\rangle_{a',b'}. \tag{7.17}$$

We consider two distinct cases of single photon subtraction which are differentiated by conditioned photon detection process. In first case, we adopt the multimode single photon subtraction method introduced in [264].

The quantum state just after the two leftmost beam splitters in Fig.7.2 is, taking $\theta_1 = \theta_2 = \theta$,

$$\begin{aligned}
\left|\,\psi'\,\right\rangle &= U_{BS}\left|\,\psi_{in}\,\right\rangle \\
&= \left|\,n,n\,\right\rangle_{a,b} \otimes \left|\,0,0\,\right\rangle_{a',b'} + i\sqrt{n}\theta\left|\,n-1,n\,\right\rangle_{a,b} \otimes \left|\,1,0\,\right\rangle_{a',b'} \\
&+ i\sqrt{n}\theta\left|\,n,n-1\,\right\rangle_{a,b} \otimes \left|\,0,1\,\right\rangle_{a',b'}.
\end{aligned} \tag{7.18}$$

The subtracted single photon traveling in either arm gets absorbed at detector, and the Positive-Operator Valued-Measurement (POVM) for detecting one photon is

$$\mathbf{\Pi} = p\left|\,10\,\right\rangle_{a',b'}\left\langle\,10\,\right|_{a',b'} + (1-p)\left|\,01\,\right\rangle_{a',b'}\left\langle\,01\,\right|_{a',b'}, \tag{7.19}$$

where p is the probability of photon being present in mode a'. Due to indistinguishability we set $p = \frac{1}{2}$ and the POVM becomes

$$\mathbf{\Pi} = \frac{1}{2}\left|\,10\,\right\rangle_{a',b'}\left\langle\,10\,\right|_{a',b'} + \frac{1}{2}\left|\,01\,\right\rangle_{a',b'}\left\langle\,01\,\right|_{a',b'}. \tag{7.20}$$

The MZI input modes a, b are conditioned by the measurement of a single photon, which can be calculated by a partial trace over the two-mode Hilbert space of a', b':

$$\rho_{a,b} = Tr_{a',b'}[U_{BS}(\left|\,\psi^{in}\,\right\rangle\left\langle\,\psi^{in}\,\right|)U^{\dagger}_{BS}\mathbf{\Pi}] \tag{7.21}$$

$$= \frac{1}{2}\left|\,n, n-1\,\right\rangle_{a,b}\left\langle\,n, n-1\,\right|_{a,b} + \frac{1}{2}\left|\,n-1, n\,\right\rangle_{a,b}\left\langle\,n-1, n\,\right|_{a,b}, \tag{7.22}$$

as written in Fig.7.2. The density operator of Eq. (7.22) is a statistical mixture and is not the density operator of the state $|\,\psi_+\,\rangle$ (Eq. (7.14)). Moreover, it is not performing adequately in interferometry: indeed, it is straightforward to show that MZI input $\rho_{a,b}$ does not generate a direct interference fringe,

$$\langle J_z \rangle = Tr(\rho_{a,b} J_z) = 0, \tag{7.23}$$

which is the same shortcoming at the twin-Fock state input. It is therefore important to be precise as to how the indistinguishable photon subtraction is conducted, so that the pure state of Eq. (7.14) can be obtained. We now turn to the proper state preparation protocol.

7.2.2 Coherently indistinguishable photon subtraction

We now consider the experiment depicted in Fig.7.3, in which the two "subtraction" modes a', b' are made *coherently* indistinguishable by interference at a balanced beam splitter — rather than being equiprobably detected by a single detector as above. The photon numbers of the output ports of the balanced beam splitter are then detected and only one detection configuration, $(n_{a'} = 1, n_{b'} = 0)$, is considered for further

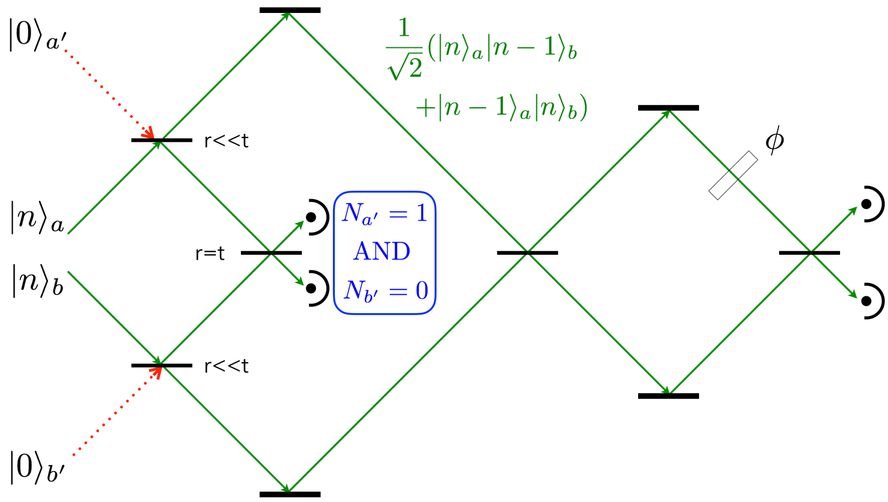

Figure 7.3: Indistinguishable single-photon subtraction producing a pure state. All interferometer output measurements are conditioned by the 1-0 joint photon detection event in blue (note that the 0-1 event would work as well, merely flipping the sign of the superposition).

heralding of the MZI input. The state after the balanced beam splitter is

$$\begin{aligned}\left|\psi''\right\rangle &= |n,n\rangle_{a,b}|0,0\rangle_{a',b'} \\ &\quad + i\theta\sqrt{\frac{n}{2}}|n-1,n\rangle_{a,b}[|1,0\rangle_{a',b'}+|0,1\rangle_{a',b'}] \\ &\quad + i\theta\sqrt{\frac{n}{2}}|n,n-1\rangle_{a,b}[|1,0\rangle_{a',b'}-|0,1\rangle_{a',b'}] \end{aligned} \tag{7.24}$$

$$\begin{aligned} &= |n,n\rangle_{a,b}|0,0\rangle_{a',b'} \\ &\quad + i\theta\sqrt{\frac{n}{2}}(|n,n-1\rangle_{a,b}+|n-1,n\rangle_{a,b})|1,0\rangle_{a',b'} \\ &\quad - i\theta\sqrt{\frac{n}{2}}(|n,n-1\rangle_{a,b}-|n-1,n\rangle_{a,b})|0,1\rangle_{a',b'} \end{aligned} \tag{7.25}$$

It is clear that the POVM elements for single-photon detection in this case are pure:,

$$\Pi_+ = |10\rangle_{a',b'}\langle 10|_{a',b'} \tag{7.26}$$

$$\Pi_- = |01\rangle_{a',b'}\langle 01|_{a',b'}\,, \tag{7.27}$$

and that the postselected state for MZI input modes a, b will therefore be also pure. Indeed, $|\,\psi''\,\rangle$ collapses to the respective states

$$|\,\psi^{\pm}\,\rangle = \frac{1}{\sqrt{2}}(|\,n, n-1\,\rangle_{a,b} \pm |\,n-1, n\,\rangle_{a,b}). \tag{7.28}$$

In the next section, we show that both these states achieve Heisenberg-limited interferometric performance, and that they also yield a direct interference fringe.

7.3 Interferometric sensitivity of photon-subtracted twin-beam interferometry

7.3.1 Schwinger representation

For the sake of convenience, we adopt for our calculation the Schwinger-spin SU(2) representation [265] initially proposed by Yurke et al. for quantum interferometers [236]. A fictitious spin $\vec{J}$ is defined from a pair of bosonic modes (a, b) as

$$J_x = \frac{1}{2}(a^\dagger b + b^\dagger a) \tag{7.29}$$
$$J_y = -\frac{i}{2}(a^\dagger b - b^\dagger a) \tag{7.30}$$
$$J_z = \frac{1}{2}(a^\dagger a - b^\dagger b) \tag{7.31}$$

where a and b are the annihilation operators of each mode. These operators satisfy the canonical angular momentum commutation relations of the su(2) algebra

$$[J_i, J_j] = i\epsilon_{ijk}J_k. \tag{7.32}$$

The operator J_z represents the photon number difference operator between the two modes whereas $J_{x,y}$ are interference terms. The total photon number of the two-mode field is represented by the operator

$$J^2 = \frac{a^\dagger a + b^\dagger b}{2}\left(\frac{a^\dagger a + b^\dagger b}{2} + 1\right). \tag{7.33}$$

The common eigenstates of J^2 and J_z are the two-mode Fock states

$$|\, jm \,\rangle_z = |\, n_a \,\rangle_a \,|\, n_b \,\rangle_b \,, \tag{7.34}$$

where the respective eigenvalues, $j(j+1)$ and m, are given by

$$j = \frac{n_a + n_b}{2}, \tag{7.35}$$

$$m = \frac{n_a - n_b}{2}. \tag{7.36}$$

The single photon-subtracted state of Eq. (7.28) therefore becomes, in the Schwinger representation,

$$|\, \psi^\pm \,\rangle = \frac{1}{\sqrt{2}}\left(|\, j, \tfrac{1}{2} \rangle \pm |\, j, -\tfrac{1}{2} \rangle\right). \tag{7.37}$$

7.3.2 Field evolution in the interferometer

In the Heisenberg picture, the action of the MZI amounts to the transformation of the J_i operators as the sequence of rotations of $\pi/2$ around x axis, ϕ around z axis, and $-\pi/2$ around x axis respectively resulting effective rotation of ϕ around y axis [236].

$$J_z^{out} = e^{i\frac{\pi}{2}J_x} e^{i\phi J_z} e^{-i\frac{\pi}{2}J_x} J_z e^{i\frac{\pi}{2}J_x} e^{-i\phi J_z} e^{-i\frac{\pi}{2}J_x}, \tag{7.38}$$

which yields

$$J_z^{\text{out}} = -\sin\phi J_x + \cos\phi J_z \tag{7.39}$$

$$(J_z^{\text{out}})^2 = \sin^2\phi J_x^2 + \cos^2\phi J_z^2 - \sin\phi\cos\phi(J_x J_z + J_z J_x) \tag{7.40}$$

For the input state $|\,\psi^{\pm}\,\rangle$, we obtain an interference fringe whose amplitude is of the order of the photon number,

$$\langle J_z \rangle = -\frac{\sin\phi}{2}\sqrt{j(j+1)+\frac{1}{4}}, \tag{7.41}$$

which is the result presented in Table 7.1. Turning now to the phase error, we first derive the mean square value $\langle J_z^2 \rangle$ for $|\,\psi^{\pm}\,\rangle$ is

$$\langle J_z^2 \rangle = \left[j(j+1)-\frac{1}{4}\right]\frac{\sin^2\phi}{2}+\frac{1}{4}\cos^2\phi\ . \tag{7.42}$$

If J_z is our phase estimator, the phase error is

$$\triangle\phi = \frac{\triangle J_z}{\left|\frac{d\langle J_z\rangle_{\rm out}}{d\phi}\right|}. \tag{7.43}$$

and we get

$$\triangle\phi = \frac{\sqrt{j(j+1)\sin^2\phi+\cos^2\phi-\frac{3}{4}\sin^2\phi}}{\cos\phi\sqrt{j(j+1)+\frac{1}{4}}} \tag{7.44}$$

which has its minimum value at $\phi = 0$,

$$\triangle\phi_{min} = \frac{1}{\sqrt{j(j+1)+\frac{1}{4}}} = \frac{1}{n}, \tag{7.45}$$

since $j = \frac{n}{2} - 1$. In the appendix 5, we show that the indistinguishable single photon subtraction protocol also works for the general twin-beam density operator input

$$\rho = \sum_{n,n'} \rho_{n,n'}\,|\,nn\,\rangle\,\langle\, n'n'\,|\,. \tag{7.46}$$

7.3.3 Quantum Fisher Information

The quantum Fisher information (QFI) is an important tool in quantum interferometry as it allows to obtain a lower bound of the phase measurement error [231]. The QFI is defined as

$$\mathcal{F}(\rho_\phi) = \mathrm{Tr}[\rho(\phi)\hat{L}_\phi^2], \tag{7.47}$$

where $\hat{L}_\phi$ is symmetric-logarithmic derivative (SLD), mathematically formulated as

$$\frac{\partial \rho(\phi)}{\partial \phi} = \frac{1}{2}[\rho_\phi \hat{L}_\phi + \hat{L}_\phi \rho_\phi]. \tag{7.48}$$

We now calculate the SLD for pure states, i.e., $\rho_\phi = \rho_\phi^2 = |\psi_\phi\rangle\langle\psi_\phi|$. A simple calculation shows that

$$\frac{\partial \rho_\phi}{\partial \phi} = \rho_\phi \frac{\partial \rho_\phi}{\partial \phi} + \frac{\partial \rho_\phi}{\partial \phi}\rho_\phi. \tag{7.49}$$

From Eqs. 7.48 and 7.49, we note that

$$L_\phi = 2\frac{\partial|\psi_\phi\rangle}{\partial \phi} = |\psi_\phi\rangle\frac{\partial|\psi_\phi\rangle}{\partial \phi} + \frac{\partial|\psi_\phi\rangle}{\partial \phi}|\psi_\phi\rangle, \tag{7.50}$$

where $|\psi_\phi\rangle$ is the output quantum state with the phase information encoded in the probability amplitudes. From Eqs. 7.47 and 7.50, we get

$$\mathcal{F}(\rho_\phi = \mathrm{Tr}[\rho(\phi)\hat{L}_\phi^2] = 4\left[\left\langle \frac{\partial\psi_\phi}{\partial\phi}\middle|\frac{\partial\psi_\phi}{\partial\phi}\right\rangle - \left|\left\langle\frac{\partial\psi_\phi}{\partial\phi}\middle|\psi\right\rangle\right|^2\right] \tag{7.51}$$

One can further express Eq. 7.51 in the Schwinger representation, where it turns out to be

$$\mathcal{F}(\rho_\phi) = 4\langle(\triangle J_y)^2\rangle_{|\psi^\pm\rangle} \tag{7.52}$$

As a result, we see that the calculation QFI for pure states in the quantum interferometry amounts to calculate the variance of J_y for the given quantum state, $|\psi^\pm\rangle$

from Eq. 7.28 in our case. With this state, the QFI leads to

$$\mathcal{F}(\rho_\phi) = 2n^2 - 1 \tag{7.53}$$

This quantity is then related to the phase error by [266]

$$(\Delta\phi)^2 \geq \frac{1}{\mathcal{F}(\rho_\phi)} \tag{7.54}$$

We then calculate the lower bound, i.e., quantum Cramér-Rao bound (QCRB) on the phase error, which is

$$\triangle\phi_{QCRB} \approx \frac{1}{\sqrt{2n^2 - 1}} \tag{7.55}$$

From Eq. 7.55, it is evident that phase error achieves the Heisenberg limit. In other words, the QFI is quadratic in mean photon-number for the proposed state.

7.3.4 Effect of losses

Losses in both modes are modeled by two beam splitters (t_1,r_1 and t_2,r_2) placed before detection. The expectation values of the spin operators become

$$\langle J_z \rangle = -\frac{1}{2}\left[n t_1 t_2 \sin\phi + \left(n - \frac{1}{2}\right)(t_1^2 - t_2^2)\cos\phi\right] \tag{7.56}$$

$$\langle J_z^2 \rangle_{in} = \frac{1}{4}\left[n(n-1)(t_1^2 - t_2^2)^2 + \frac{1}{2}(t_1^4 + t_2^4) + \frac{n}{2}(t_1 r_1^2 + t_2 r_2^2)\right] \tag{7.57}$$

$$= \frac{1}{4}\left[\left(n - \frac{1}{2}\right)(t_1^2 + t_2^2) + 2t_1^2 t_2^2 n(n-1)\right] \tag{7.58}$$

$$\langle J_x J_z + J_z J_x \rangle_{in} = \frac{n}{2}[(2n-1)t_1 t_2 (t_1^2 - t_2^2) + t_1 t_2 (r_1^2 - r_2^2)] \tag{7.59}$$

which yields

$$\triangle\phi = \frac{\sqrt{\left(\frac{c_1^2}{4} + \frac{c_3}{2}n\right)C^2 + [c_1(n - \frac{1}{2}) + nc_2(nc_2 - 4)]S^2}}{n\ c_2\ C + (n - \frac{1}{2})c_4\ S}, \tag{7.60}$$

where we posed

$$C = \cos\phi \tag{7.61}$$

$$S = \sin\phi \tag{7.62}$$

$$c_1 = (t_1^2 + t_2^2) \tag{7.63}$$

$$c_2 = t_1 t_2 \tag{7.64}$$

$$c_3 = (t_1 r_1^2 + t_2 r_2^2) \tag{7.65}$$

$$c_4 = (t_1^2 - t_2^2). \tag{7.66}$$

For $t_1 = t_2 = 1$, we recover the lossless case of Eq. (7.44). To simplify further, we assume identical beam splitters ($t_1 = t_2 = t$) and $\phi \to 0$, which yields

$$\triangle\phi \simeq \frac{1}{tn}\sqrt{1 + \frac{1-t^2}{t}n} \tag{7.67}$$

The first term in the square root on the right-hand side of Eq. (7.67) is the HL, reached for $t = 1$; the second term is the SNL, which dominates when $t \to 0$.

The tipping point for the losses is given by

$$1 = \frac{1-t^2}{t}n \tag{7.68}$$

which, solved for t in the limit of large n, yields the loss coefficient

$$1 - t^2 \simeq \frac{1}{n}, \tag{7.69}$$

consistent with the general result of Escher, de Matos Filho, and Davidovich [248].

7.4 Conclusions and outlook

In this chapter, we have proposed and studied a nontrivial modification of the twin-beam input for Heisenberg-limited quantum interferometry, which features coherently indistinguishable photon subtraction. This modification brings about a strong fringe signal — absent from the unmodified twin-beam input — while preserving Heisenberg-limited operation. The loss behavior is consistent with what is now well known about Heisenberg-limited interferometry. The experimental implementation should be feasible with state-of-the-art technology, for example using a stable OPO above threshold [147], [258], [259] and photodetectors with single-photon sensitivity. We believe it is possible to operate at no more than 10^6 photons per detection time bin, so as to be compatible with the lowest achievable optical losses and splitting ratios. Such an experimental endeavor is currently under progress in our laboratory. A underway direction employs macroscopically entangled states for quantum interferometry. One such state is

$$|\psi\rangle = \mathcal{N}(\hat{a_1}^\dagger|\alpha_1, \alpha_2\rangle + \hat{a_2}^\dagger|\alpha_1, \alpha_2\rangle) \tag{7.70}$$

These states can be experimentally generated by using an indistinguishable addition of a single-photon to two optical modes prepared in macroscopic coherent states.

Chapter 8

Conclusions and future directions

> Friends applaud, the comedy is over.
>
> — Ludwig van Beethoven

Since their original conception by Richard Feynman in the 1980s, quantum computers have evolved from a groundbreaking theoretical idea to physically realized devices on a variety of platforms including superconducting circuits, trapped ions, and optics. While there has been significant progress towards scaling qubit-based quantum computation, the continuous-variable implementations with quantum optics still remain the most scalable platforms for quantum computation. It is well understood that in order to achieve exponential speedup and fault tolerance in continuous-variable quantum computation the inclusion of a non-Gaussian element (states or operations, or measurements) is necessary. Therefore, the efficient characterization and development of these non-Gaussian elements is a key task in building a fault-tolerant quantum computer.

8.1 State tomography with PNR measurements

In *Chapter 2*, we demonstrate the WVBW scheme, which allows us to *directly* probe the Wigner quasiprobability distribution using PNR measurements. While we demonstrate the WVBW scheme for a single-photon Fock state, our tomography setup is state-independent, and hence can be used to characterize arbitrary quantum states prepared in a single-mode weak quantum field [267]. We observe the negativity of the Wigner function without using any numerical post-processing or correcting for losses. The WVBW scheme requires a phase space raster scan which can be experimentally demanding, particularly for quantum states, such as cat state or Gottesman-Kitaev-Preskill state, with rich phase space interference features. These states play an important role in bosonic quantum error correction [105], [106]. In addition to having to probe the phase space densely, the WVBW scheme is intrinsically lossy due to approximated implementations of phase space displacements.

In *Chapter 3*, we present a generalization of the WVBW scheme. The proposed scheme uses state overlap measurements between the unknown state and a small set of known coherent states to reconstruct the density matrix in the Fock space, as opposed to WVBW, which is a point-by-point phase-space Wigner function reconstruction technique. Our scheme requires considerably less data and laser power while allowing higher resolution of the phase space as compared with the WVBW scheme. We then consider experimental imperfections due to detection losses, noise, and mode mismatch between the fields of unknown state and coherent states. We devise techniques to deconvolve the deleterious effects of these experimental imperfections. Our deconvolution techniques are computationally efficient and lead to physically reliable reconstructions. We demonstrate the generalized overlap tomography for a weak-coherent state and a single-photon Fock state [268].

A natural direction for future work is to characterize a multimode quantum state with the WVBW and generalized overlap tomography schemes and see how these schemes compare to conventional balanced homodyne detection. Moreover, the reconstruction of a multimode Wigner function offers an interesting way to test the quantum nonlocality in phase space for commonly used entangled states such as the Bell state and Einstein-Podolsky-Rosen state [269], [270]. On the experimental front, an immediate step to improve the setup would be to lock the phase between the fields of the local oscillator and the unknown state. This will be particularly beneficial for characterizing phase-sensitive quantum states.

Finally, the generalized scheme can be employed for other physical platforms such as cavity and circuit quantum electrodynamics. We hope that it draws attention from researchers in these fields.

8.2 Spectral and temporal aspects of the segmented detector

In *Chapter 4*, we propose a new design for a room-temperature segmented waveguide PNR detector with click or no-click detectors such as single-photon avalanche-photodiodes (SPADs). While we split n photons over m modes, as in other spatial or temporal multiplexed methods [62], [162], the key advantage of our segmented detector is that the nonideal quantum efficiency of SPADs does not contribute to photon loss. In our design, SPADs are side-coupled to the same waveguide rather than terminally coupled, which allows photons that are not absorbed in the first SPAD to couple back into the waveguide to be absorbed by the next SPADs. We characterize the PNR performance by evaluating the purity of the POVM elements corresponding to the measurement outcomes of the detector. We find that reasonable levels of losses, dark counts, and cross-talk noise do not degrade performance as much as having a limited number of SPADs does. Therefore, the number of integrated SPADs is the dominant factor for high-quality PNR detection. We hope that this work offers enough motivation to invest in such a scalable integrated photonic technology, which has the potential for room-temperature high-quality PNR operations.

In this work, our analysis only focuses on the PNR measurements in that we ignore the spectral and temporal features of the detected photons. We assume that the signal field is extremely narrowband and all the detectors which register an event click at the same time. Recently, S.J. van Enk developed a formalism to determine the time-dependent POVM of a broadband single-photon field [188]. While Ref. [188] focuses on constructing the time-dependent POVM of a single-photon, it completely omits the multiphoton situation. An important next step would be to add the spectral and temporal features to the segmented detector, which will enable us to experimentally test fundamental trade-off relations between the different quantum figures-of-merit such as photon-number resolution, quantum efficiency, and dark noise [189]. One may also expect trade-off relations between the classical detector characteristics, namely, detector bandwidth, jitter time, and spectral resolution. A segmented device with spectral and temporal features may help us settle the conjecture that there are no fundamental trade-off relations between the quantum and classical detector characteristics [189].

Finally, our model considers the homogeneous radiative losses throughout the waveguide for simplicity. However, a realistic detector may have varying losses. In that case it becomes crucial to understand how the losses affect detector performance and be able to account for these effects in the device design.

8.3 Phase space characterization of quantum detectors

In *Chapter 5*, we devise a method to reconstruct the Wigner functions of the detector's POVM elements. The proposed method uses displaced-thermal mixtures as tomography probes and reconstructs the Wigner function point-by-point over the entire phase space. We further show that the resources required to fully characterize a PNR detector scale linearly with the detector saturation threshold. Finally, we make the method robust to experimental fluctuations by using quadratic convex optimizations.

We note that one can use any state that is diagonal in photon-number basis. One such state is a phase-averaged coherent state (PACS), which can be prepared by using a fast-modulated PZT mirror to randomize the optical phase of a coherent state. Since PACSs have less noise compared to the thermal mixtures, the reconstruction performance might be improved. Ongoing work is considering PACSs as the detector probes. Additionally, one can also look into including the mode mismatch between the fields of the local oscillator and probes.

Most of the quantum detector tomography schemes use classical states as their probes, mainly because these states are easy to prepare in the lab [91], [271]. Brida et al. demonstrated that using quantum resources such as twin-beam outperforms classical resources in statistical robustness in the POVM reconstruction [272]. It would be interesting to extend this work with such quantum resources and see what kinds of improvements it would lead to as compared to the classical resources. We are currently investigating such ideas.

8.4 Quantum interferometry with macroscopically-entangled states (MES)

Chapter 6 presents a Heisenberg-limited (HL) interferometer with coherently photon-subtracted twin beams. We propose an experimental realization using a stable optical parametric oscillator above threshold and detectors with single-photon sensitivity. This work provides motivation to investigate into quantum interferometry with coherently photon-added states. For instance, a coherent addition of a single-photon to two classical fields, say $|\alpha\rangle_1$ and $|\alpha\rangle_2$, allows us to prepare a macroscopically-entangled two-mode state. It would be intriguing to see how MESs perform in quantum interferometry, particularly under realistic scenarios with losses, and what kinds of measurements one needs to use in order to achieve the quantum Cramèr–Rao bound for the phase measurement. The MESs might offer advantages both due to their bright fields and the entanglement inside the interferometer.

Appendix A

Generalized overlap quantum state tomography

In the case of an unbalanced beamsplitter where the input probe is still a coherent state, $\alpha_j = \frac{1}{\sqrt{2}}(q_{\alpha_j} + ip_{\alpha_j})$, we recall that the overlap is

$$
\begin{aligned}
W_1'(0,0;r,t) &= \iint W_1(rq_2', rp_2')W_2(tq_2', tp_2')dq_2'dp_2' \\
&= \frac{1}{r^2}\iint W_1(q,p)W_2(\tfrac{t}{r}q, \tfrac{t}{r}p)dqdp. \qquad \text{(A.1)}
\end{aligned}
$$

A further simplification leads to

$$
\begin{aligned}
W_2(\tfrac{t}{r}q, \tfrac{t}{r}p) = W_{|\alpha_j\rangle\langle\alpha_j|}(\tfrac{t}{r}q, \tfrac{t}{r}p) &= \frac{1}{\pi}\exp\Big[-\big(\tfrac{t}{r}q + q_{\alpha_j}\big)^2 - \big(\tfrac{t}{r}p + p_{\alpha_j})\big)^2\Big] \qquad \text{(A.2)} \\
&= \frac{1}{\pi}\exp\left\{-\frac{1}{\sigma^2}\Big[\big(q + q_{\beta_j}\big)^2 + \big(p + p_{\beta_j}\big)^2\Big]\right\}, \qquad \text{(A.3)}
\end{aligned}
$$

where $\sigma = \frac{r}{t}$ and $\beta_j = \sigma\alpha_j$. The integral overlap from Eq. A.1 is then

$$
\frac{1}{t^2}\iint W_1(q,p)W_\sigma(q + q_{\beta_j}, p + p_{\beta_j})dqdp, \qquad \text{(A.4)}
$$

where $W_\sigma(q+q_{\beta_j}, p+p_{\beta_j}) = \frac{1}{\pi\sigma^2}\exp\left\{-\frac{1}{\sigma^2}\left[\left(q+q_{\beta_j}\right)^2+\left(p+p_{\beta_j}\right)^2\right]\right\}$. Note that when $\sigma > 1$, Eq. (A.4) gives a scaled overlap between ρ_{in} and a thermal state displaced by β^j with the Wigner function $W_\sigma(q+q_{\beta_j}, p+p_{\beta_j})$. When $\sigma < 1$, however, the overlap is between ρ_{in} and a mathematical object that approaches a displaced delta function in the limit where $\sigma \to 0$ and $|\alpha| \to \infty$, which exactly probes the Wigner function of unknown state, ρ point-by-point as in the unbalanced homodyne technique of Refs. [1] and [2].

One might also wonder about the outcome of a similar measurement performed on the other port of the beamsplitter. If we go back to Eq. (4.3) and now determine the value of the Wigner function of output mode 2 at the origin while tracing out over mode 1, we have

$$\int W'_{1,2}(\mathbf{x}')dq'_1dp'_1|_{q'_2,p'_2=0} = \int W_1(tq'_1, tp'_1)W_2(-rq'_1, -rp'_1)dq'_1dp'_1 \tag{A.5}$$

$$= \frac{1}{t^2}\int W_1(q,p)W_2(-\tfrac{r}{t}q, -\tfrac{r}{t}p)dqdp. \tag{A.6}$$

With $r = t$, the measured Wigner function overlap is between ρ_{in} and $|-\alpha^j\rangle\langle-\alpha^j|$, i.e., the very same coherent state probe with a phase factor of $e^{i\pi}$. From this, we can conclude that measuring the Wigner function at the origin of both beamsplitter outputs would yield the overlap between the signal and coherent-state probes at opposite phases. When performing the tomographic reconstruction, it is possible to utilize both outputs to collect overlap measurements and only externally vary the probe phases by half of the desired range; however, ensuring that both detection channels following the beamsplitter are identical in losses, detector efficiency, etc., is experimentally challenging, and this also imposes additional requirements on PNR detection capabilities. Therefore, it is simpler to utilize a single output mode to perform the tomographic reconstruction and correct for known losses as detailed in the main text.

A.0.1 Discussion on inverting Eq. 4 for a general beam splitter

In this section, we investigate an inversion scheme for an arbitrary beamsplitter with reflection and transmission coefficients of r and t, respectively. This elegant proof was done by Carlos González-Arciniegas (after a long "mathematical" wrestling) with some inputs, mainly in the form of encouragement, from me. We start with formally defining the Wigner function of an operator denoted by $\hat{T}$ as

$$W_{\hat{T}}(q,p) = \frac{1}{2\pi}\mathrm{Tr}[\hat{T}\hat{\Pi}(q,p)], \tag{A.7}$$

where $\hat{\Pi}(q,p)$ is the translated parity operator formally defined as

$$\hat{\Pi}(q,p) = \iint \frac{dq'dp'}{2\pi} e^{-i(qp'-pq')}\hat{D}\left(q',p'\right) = \int dq' e^{-ipq'} \left| q + \frac{q'}{2} \right\rangle \left\langle q - \frac{q'}{2} \right|, \tag{A.8}$$

where $\hat{D}(q,p)$ is the phase space displacement operator. For a given quantum state $\hat{T} = \rho$, Eq. (A.8) leads to the usual Wigner function of the state. However, this definition is general and may be extended to any arbitrary operator, $\hat{T} = T(\hat{q},\hat{p})$ in order to calculate the so called Weyl symbol representing the operator $\hat{T}$. This is achieved by inverting Eq. (A.7) which results to the operator $\hat{T}$ in Weyl symbol form as

$$\hat{T} = \iint dpdq W_T(q,p)\hat{\Pi}(q,p). \tag{A.9}$$

Here we have used the fact that $\mathrm{Tr}[\hat{\Pi}\left(q,p\right)\hat{\Pi}\left(q',p'\right)] = 2\pi\delta(q-q')\delta(p-p')$. Next, we calculate the matrix elements of the operator $\hat{T}$ as

$$T_{n,m} = \langle n \,|\, \hat{T} \,|\, m \rangle = \iint W_T(q,p) \, \langle n \,|\, \hat{\Pi}(q,p) \,|\, m \rangle \, dqdp, \tag{A.10}$$

where the matrix elements of the displaced parity operator can be determined using Eq. A.8 as

$$
\begin{aligned}
\langle\, n \,|\, \hat{\Pi}(p,q) \,|\, m \,\rangle &= \int dq' e^{-ipq'} \left\langle n \middle| q - \frac{q'}{2} \right\rangle \left\langle q + \frac{q'}{2} \middle| m \right\rangle \\
&= \frac{e^{-q^2}}{\sqrt{\pi 2^{m+n} n! m!}} \int dq' e^{-ipq'} e^{-q'^2/4} H_n\left(q + \frac{q'}{2}\right) H_m\left(q - \frac{q'}{2}\right) \\
&\overset{q' \to 2(x-ip)}{=} \frac{2e^{-\left(q^2+p^2\right)}}{\sqrt{\pi 2^{n+m} n! m!}} \int dx e^{-x^2} H_n(x + (q - ip))(-1)^m H_m(x - (q + ip)).
\end{aligned}
\tag{A.11}
$$

Note that $\langle x|n\rangle = \frac{1}{\pi^{1/4}} \frac{e^{-x^2/2}}{\sqrt{2^n n!}} H_n(x)$ and $H_n(-x) = (-1)^n H_n(x)$. Using these relations, we get

$$
\int dx e^{-x^2} H_m(x+\sigma) H_n(x+\rho) = \left\{ \begin{array}{ll} \sqrt{\pi} 2^n n! (2\sigma)^{m-n} L_n^{m-n}(-2\sigma\rho) & n < m \\ \sqrt{\pi} 2^m m! (2\rho)^{n-m} L_m^{n-m}(-2\sigma\rho) & m < n \end{array} \right\}
\tag{A.12}
$$

$$
\langle\, n \,|\, \hat{\Pi}(p,q) \,|\, m \,\rangle = \left\{ \begin{array}{ll} 2(-1)^n \sqrt{\frac{2^m n!}{2^n m!}} e^{-|\alpha|^2} \alpha^{m-n} L_n^{m-n}(2|\alpha|^2) & n < m \\ 2(-1)^m \sqrt{\frac{2^n m!}{2^m n!}} e^{-|\alpha|^2} \alpha^{*n-m} L_m^{n-m}(2|\alpha|^2) & m < n \end{array} \right\},
\tag{A.13}
$$

where $\alpha := q + ip$. For a general beamsplitter, the measured overlap is between the Wigner function of the unknown state and a Wigner function of the form given by Eq. (A.3)

$$
W_T(\alpha) = \frac{1}{\pi\sigma^2} \exp\left\{ -\frac{|\alpha - \beta|^2}{\sigma^2} \right\}.
\tag{A.14}
$$

Defining $\tau = 1/\sigma$ and using Eq. (A.13), we have that the matrix elements Eq. (A.10) of the operator given by the Wigner function above are for $m < n$:

$$\begin{aligned} T_{n,m} &= \int_{-\infty}^{\infty} 2(-1)^m \sqrt{\frac{2^n m!}{2^m n!}} e^{-|\alpha|^2} \alpha^{*n-m} L_m^{n-m}(2|\alpha|^2) \frac{1}{\pi\sigma^2} \exp\left\{-\frac{|\alpha-\beta|^2}{\sigma^2}\right\} d^2\alpha \\ &= C e^{-\tau^2|\beta|^2} \int_{-\infty}^{\infty} \alpha^{*n-m} L_m^{n-m}(2|\alpha|^2) e^{-(\tau^2+1)|\alpha|^2} e^{\tau^2(\alpha\beta^*+\alpha^*\beta)} d^2\alpha, \end{aligned} \tag{A.15}$$

where we define $C = \frac{2(-1)^m}{\pi\sigma^2}\sqrt{\frac{2^n m!}{2^m n!}}$. Now we we transform Eq. (A.15) using polar coordinate transformation $\alpha = re^{i\theta}$ and $d^2\alpha = rdrd\theta$ which leads to the matrix elements

$$\begin{aligned} T_{n,m} &= Ce^{-\tau^2|\beta|^2} \int_{-\infty}^{\infty} dr \int_0^{2\pi} d\theta r^{n-m+1} \Psi e^{-i(n-m)\theta} e^{-(\tau^2+1)r^2} e^{\tau^2 r\left(e^{i\theta}\beta^* + e^{-i\theta}\beta\right)} L_n^{n-m}\left(2r^2\right) \\ &= Ce^{-\tau^2|\beta|^2} \int_{-\infty}^{\infty} dr \int_0^{2\pi} d\theta r^{n-m+1} \Psi e^{-i(n-m)\theta} e^{-(\tau^2+1)r^2} L_n^{n-m}\left(2r^2\right) \sum_{k=0}^{\infty} \frac{\tau^{2k} r^k}{k!} \left(e^{i\theta}\beta^* + e^{-i\theta}\beta\right)^k \\ &= Ce^{-\tau^2|\beta|^2} \int_{-\infty}^{\infty} dr r^{n-m+1} e^{-(\tau^2+1)r^2} L_n^{n-m}\left(2r^2\right) \sum_{k=0}^{\infty} \frac{\tau^{2k} r^k}{k!} \sum_{l=0}^{k} \beta^{*l} \beta^{k-l} \binom{k}{l} \int_0^{2\pi} d\theta e^{i\theta(2l-k-n+m)}. \end{aligned} \tag{A.16}$$

The last integral is null for $l \neq \frac{1}{2}(k+n-m)$ and equals 2π for $l = \frac{1}{2}(k+n-m)$. Therefore, we can write $k = n-m+2s$ ($k+n-m$ must be even and $0 \leq l \leq k$), $s = 0, 1, ...$ which implies that $l = n-m+s$. This simplification leads to

$$\begin{aligned} T_{n,m} = 2\pi C e^{-\tau^2|\beta|^2} \sum_{s=0}^{\infty} \binom{n-m+2s}{s+n-m} \frac{\beta^{*s+n-m}\beta^s}{(n-m+2s)!} \tau^{2(n-m+2s)} \\ \times \int_{-\infty}^{\infty} dr\, r^{2(n-m+s)+1} e^{-(\tau^2+1)r^2} L_n^{n-m}\left(2r^2\right) e^{-sr^2}. \end{aligned}$$

To evaluate the last integral (which we will call I), we use the following identity [273]:

$$\int_0^\infty x^{\mu-1}e^{-\sigma x}L_{n_1}^{(\alpha_1)}(\lambda_1 x)\cdots L_{n_r}^{(\alpha_\nu)}(\lambda_\nu x)\,dx \overset{x=r^2}{=} 2\int_0^\infty r^{2\mu-1}e^{-\sigma r^2}L_{n_1}^{(\alpha_1)}\left(\lambda_1 r^2\right)\cdots L_{n_\nu}^{\alpha_\nu}\left(\lambda_\nu r^2\right)dr$$

$$= \left(\begin{array}{c} n_1+\alpha_1 \\ \\ n_1 \end{array}\right)\cdots\left(\begin{array}{c} n_\nu+\alpha_\nu \\ \\ n_\nu \end{array}\right)\frac{\Gamma(\mu)}{\sigma^\mu}F_A^{(r)}\left[\mu,-n_1,\ldots,-n_\nu;\alpha_1+1,\ldots,\alpha_\nu+1;\frac{\lambda_1}{\sigma},\ldots,\frac{\lambda_\nu}{\sigma}\right]$$

$$(Re(\mu)>0;\quad Re(\sigma)>0;\quad n_j\in\mathbb{N}_0;\quad j=1,\ldots,\nu),$$

where $F_A^{(\nu)}$ denotes the first of the four Lauricella's hypergeometric functions of ν variables defined by

$$F_A^{(\nu)}[a,b_1,\ldots,b_\nu;c_1,\ldots,c_\nu;z_1,\ldots,z_\nu] = \sum_{k_1,\ldots,k_\nu=0}^{\infty}\frac{(a)_{k_1+\cdots+k_\nu}(b_1)_{k_1}\cdots(b_\nu)_{k_\nu}}{(c_1)_{k_1}\cdots(c_\nu)_{k_\nu}}\frac{z_1^{k_1}}{k_1!}\cdots\frac{z_\nu^{k_\nu}}{k_\nu!}$$

$$(|z_1|+\cdots+|z_\nu|<1)\quad \text{and } (a)_n = \frac{\Gamma(a+n)}{\Gamma(a)},$$

where $\Gamma(a)=(a-1)!$ are standard gamma functions. Thus,

$$I = \frac{1}{2}\frac{n!}{(\tau^2+1)^{n-m+s+1}}\sum_{k=0}^{m}\frac{(-1)^k(n-m+s+k)!}{(m-k)!(n-m+k)!k!}\left(\frac{2}{\tau^2+1}\right)^k,$$

and the matrix elements to be calculated take the form

$$T_{n,m} = 2\pi Ce^{-\tau^2|\beta|^2}\beta^{*(n-m)}\frac{\tau^{2(n-m)}}{(1+\tau^2)^{n-m+1}}$$
$$\times\sum_{s=0}^{\infty}\binom{n-m+2s}{n-m+s}\frac{\left(\tau^4|\beta|^2\right)^s n!}{(n-m+2s)!(1+\tau^2)^s}\sum_{k=0}^{m}\frac{(-1)^k(n-m+s+k)!}{(m-k)!(n-m+k)!k!}\left(\frac{2}{\tau^2+1}\right)^k,$$

where the expression above can be rewritten as

$$T_{n,m} = 2\pi Ce^{-\tau^2|\beta|^2}n!\frac{\beta^{*(n-m)}}{1+\tau^2}\left(\frac{\tau^2}{1+\tau^2}\right)^{n-m}\sum_{k=0}^{m}\frac{(-1)^k\left(\frac{2}{\tau^2+1}\right)^k}{(m-k)!(n-m+k)!}$$
$$\times\sum_{s=0}^{\infty}\left(\frac{\tau^4|\beta|^2}{1+\tau^2}\right)^s\frac{1}{s!}\binom{n-m+s+k}{k}.$$

Using Vandermonde's identity, we may write the last binomial term as

$$\binom{n-m+s+k}{k} = \sum_{j=0}^{k} \binom{s}{j}\binom{n-m+k}{k-j}, \tag{A.17}$$

which gives us

$$\begin{aligned}
T_{n,m} = 2\pi C e^{-\tau^2|\beta|^2} \frac{\beta^{*(n-m)}}{1+\tau^2}\left(\frac{\tau^2}{1+\tau^2}\right)^{n-m} \sum_{k=0}^{m}\binom{n}{m-k}\left(\frac{-2}{\tau^2+1}\right)^{k} \sum_{j=0}^{k}\binom{n-m+k}{k-j} \\
\times \sum_{s=0}^{\infty}\left(\frac{\tau^4|\beta|^2}{1+\tau^2}\right)^{s}\frac{1}{s!}\binom{s}{j} \\
= 2\pi C e^{-\tau^2|\beta|^2} \frac{\beta^{*(n-m)}}{1+\tau^2}\left(\frac{\tau^2}{1+\tau^2}\right)^{n-m} \sum_{k=0}^{m}\binom{n}{m-k}\left(\frac{-2}{\tau^2+1}\right)^{k} \\
\times \sum_{j=0}^{k}\binom{n-m+k}{k-j}\left(\frac{\tau^4|\beta|^2}{1+\tau^2}\right)^{j}\frac{1}{j!}\exp\left(\frac{\tau^4|\beta|^2}{1+\tau^2}\right) \\
= 2\pi C \exp\left(-\frac{\tau^2|\beta|^2}{1+\tau^2}\right)\frac{\beta^{*(n-m)}}{1+\tau^2}\left(\frac{\tau^2}{1+\tau^2}\right)^{n-m} \sum_{k=0}^{m}\binom{n}{m-k}\left(\frac{-2}{\tau^2+1}\right)^{k} L_k^{n-m}\left(\frac{\tau^4|\beta|^2}{1+\tau^2}\right),
\end{aligned} \tag{A.18}$$

where we have used the additional identities

$$\sum_{s=0}^{\infty}\frac{x^s}{s!}\binom{s}{j} = \sum_{s=j}^{\infty}\frac{x^s}{s!}\binom{s}{j} = \frac{x^j e^x}{j!} \tag{A.19}$$

and the definitions of the generalized Laguerre's polynomials

$$\sum_{j=0}^{k}\binom{n-m+k}{k-j}\frac{x^j}{j!} = L_k^{n-m}(-x). \tag{A.20}$$

Finally, we can use the multiplication theorem of the generalized Laguerre's polynomials,

$$L_m^{\lambda}(yx) = \sum_{k=0}^{m}\binom{m+\lambda}{m-k} L_k^{\lambda}(y) x^k (1-x)^{m-k}, \tag{A.21}$$

written as

$$(1-x)^m L_m^{n-m}\left(\frac{-yx}{1-x}\right) = \sum_{k=0}^{m}\binom{n}{m-k} L_k^{n-m}(y)(-x)^k, \tag{A.22}$$

to derive a closed form for the photon-number basis matrix elements of the operator described by the general Gaussian Wigner function ((A.14)) as

$$T_{n,m} = \frac{2(-1)^m}{2+\tau^2}\sqrt{\frac{2^n m!}{2^m n!}}\beta^{*(n-m)}\left(\frac{\tau^2}{1+\tau^2}\right)^{n-m}\left(\frac{\tau^2-1}{\tau^2+1}\right)^m L_m^{n-m}\left(\frac{2\tau^4|\beta|^2}{\tau^4-1}\right). \tag{A.23}$$

This expression allows us to explicitly write down the overlap integral, even in the case of unbalanced beamsplitter, as

$$\mathcal{O} = \sum_{n=0}\sum_{m=0} T_{n,m}\rho_{m,n}, \tag{A.24}$$

where $T_{n,m}$'s are calculated in Eq. (A.23) and $\rho_{m,n}$'s are matrix elements of the unknown state.

A.0.2 Overlap tomography of a multimode state

For a multi-mode quantum state, we interfere each mode at a balanced beamsplitter followed by measuring the overall parity of the multi-mode state. For example, let's consider a two-mode state state. The Wigner function at the origin of phase space is then given by

$$W'_{1,2}(\gamma,\delta=0) = \frac{1}{\pi^2}\sum_{n_1,n_2=0}^{\infty}(-1)^{n_1+n_2}c_{n_1,n_2,n_1,n_2} = \frac{1}{\pi^2}\sum_{n_1,n_2=0}^{\infty}(-1)^N c_N, \tag{A.25}$$

where c_{n_1,n_2,n_1,n_2} are the diagonal elements of two-mode density matrix and $N = n_1+n_2$, thereby C_N being the probability of N-photon detection in two-mode state after the interference. The state overlap is given by

$$\mathcal{O} = \mathrm{Tr}[\rho_{1,2}(|\alpha_1\rangle\langle\alpha_1| \otimes |\alpha_2\rangle\langle\alpha_2|)], \tag{A.26}$$

where $|\alpha_1\rangle$ and α_2 are known coherent states. Consider the unknown two-mode state described by density matrix

$$\rho_{1,2} = \sum_{n_1,n_2,n_1',n_2'}^{\infty} \rho_{n_1,n_2,n_1',n_2'} |n_1, n_2\rangle\langle n_1', n_2'|. \tag{A.27}$$

The coherent states in the Fock basis are

$$\rho_{\alpha_1} = \sum_{m_1,m_1'}^{\infty} c^1_{m_1,m_1'} |m_1\rangle\langle m_1'| \tag{A.28}$$

$$\rho_{\alpha_2} = \sum_{m_2,m_2'}^{\infty} c^2_{m_2,m_2'} |m_2\rangle\langle m_2'| \tag{A.29}$$

Using Eqs.A.26,A.27, A.28, A.29, we get

$$\mathcal{O} = \sum_{n_1,n_2,n_1',n_2'=0}^{\infty} \rho_{n_1,n_2,n_1',n_2'} c^1_{n_1,n_1'} c^2_{n_2,n_2'}. \tag{A.30}$$

With the finite Hilbert space truncation, we have

$$\mathcal{O} = \sum_{n_1,n_2,n_1',n_2'=0}^{n_0} \rho_{n_1,n_2,n_1',n_2'} c^1_{n_1,n_1'} c^2_{n_2,n_2'} \tag{A.31}$$

One can then employ SDP programming to invert Eq. A.31 as in single-mode case. Furthermore, it could be extended to n-mode case where the measurement positive-valued-operator measures are defined as

$\{|\alpha_1, \alpha_2, \ldots \alpha_N\rangle\langle\alpha_1, \alpha_2, \ldots \alpha_N|, \alpha \in \mathbb{C}\}$. Although, the higher number of modes results in larger Hilbert space dimension as expected but due to *inherently* finite size of Hilbert space leads to finite size of POVM set. In the ideal case, $\mathcal{O}(d^{2N})$ POVM measurements would be required for a Hilbert space size of d per mode and N being number of modes.

Appendix B

Interferometric phase noise for a general twin-beam input

In this section, we show that our photon subtraction protocol also works for the most general statistical mixture, e.g. as produced by an OPO above threshold. The density operator in the Fock basis is given by

$$\rho = \sum_{n,n'} \rho_{n,n'} \,|\, nn \,\rangle \,\langle\, n'n' \,|\ \ . \tag{B.1}$$

After single photon subtraction, the density operator becomes

$$\rho^{\pm} = \frac{\sum_{n,n'} \sqrt{nn'}\rho_{n,n'}(|\, n-1, n \,\rangle \,\langle\, n'-1, n' \,| \pm |\, n-1, n \,\rangle \,\langle\, n', n'-1 \,|}{2\sum_n n\rho_{nn}}$$
$$\frac{\pm \,|\, n, n-1 \,\rangle \,\langle\, n'-1, n' \,| + |\, n, n-1 \,\rangle \,\langle\, n', n'-1 \,|)}{2\sum_n n\rho_{nn}} \tag{B.2}$$

Where ρ^{+} and ρ^{-} are referred to the conditioned detection by detectors D_1 and D_2. $\rho^{\pm}$ can be further simplified as

$$\rho^{\pm} = \frac{\sum_{n,n'} \sqrt{nn'}\rho_{n,n'}\left(\frac{|\, n-1,n \,\rangle \pm |\, n,n-1 \,\rangle}{\sqrt{2}}\right)\left(\frac{\langle\, n'-1,n' \,| \pm \langle\, n',n'-1 \,|}{\sqrt{2}}\right)}{\sum_n n\rho_{nn}} \tag{B.3}$$

The normalized density operator in Schwinger representation is

$$\rho^{\pm} = \sum_{j,j'} c_{j,j'} \left(\frac{|\, j, -1/2\,\rangle \pm |\, j, 1/2\,\rangle}{\sqrt{2}} \right) \left(\frac{\langle\, j', -1/2\,| \pm \langle\, j', 1/2\,|}{\sqrt{2}} \right), \tag{B.4}$$

where

$$c_{j,j'} = \frac{\sqrt{(j+1/2)(j'+1/2)}\rho_{j+1/2,j'+1/2}}{\sum_j (j+1/2)\rho_{j+1/2,j+1/2}}. \tag{B.5}$$

The mean values $\langle J_z \rangle$ and $\langle J_z^2 \rangle$ for $\rho^{\pm}$ as an input state of the MZI are

$$\langle J_z \rangle = -\frac{\sin\phi}{2} \sum_j c_{j,j} \sqrt{j(j+1) + \frac{1}{4}} \tag{B.6}$$

which shows that the direct fringe signal is still present. Turning now to the phase error, we have

$$\langle J_z^2 \rangle = \frac{\sin^2\phi}{2} \sum_j c_{j,j} \left(j(j+1) - \frac{1}{4} \right) + \frac{1}{4}\cos^2\phi, \tag{B.7}$$

and the phase uncertainty $\triangle\phi$ is

$$\triangle\phi = \frac{\sqrt{\frac{\cos^2\phi}{4} + \frac{\sin^2\phi}{2}\sum_j c_{j,j}\left(j(j+1) - \frac{1}{4}\right) - \frac{\sin^2\phi}{4}\left(\sum_j c_{j,j}\sqrt{j(j+1) + \frac{1}{4}} \right)^2}}{\frac{\cos\phi}{2}\sum_j c_{j,j}\sqrt{j(j+1) + \frac{1}{4}}}. \tag{B.8}$$

The minimum error is obtained, as before, for $\phi = 0$, and we have

$$\triangle\phi_{min} = \frac{1}{\sum_j c_{j,j}\sqrt{j(j+1) + \frac{1}{4}}} = \frac{1}{\langle N \rangle} \tag{B.9}$$

Appendix C

Multiplexing TES Channels for Higher Photon-Number-Resolved Measurements

In this section, we consider spatial multiplexing using a 50:50 beamsplitter, of two TES channels for performing PNR measurements at larger photon numbers. This is of importance when one needs to characterize a high energy state using PNR measurements with TESs. The detection efficiencies of TESs channels are η_1 and η_2 modeled by setting up fictitious beamsplitters of transmission η_1 and η_2 as shown in Fig. C.1. Input modes are $\hat{a}_1$ and $\hat{a}_2$ corresponding to the signal and vacuum field respectively. Vacuum modes for the fictitious BSs are a_3 and a_4 as shown in the figure.

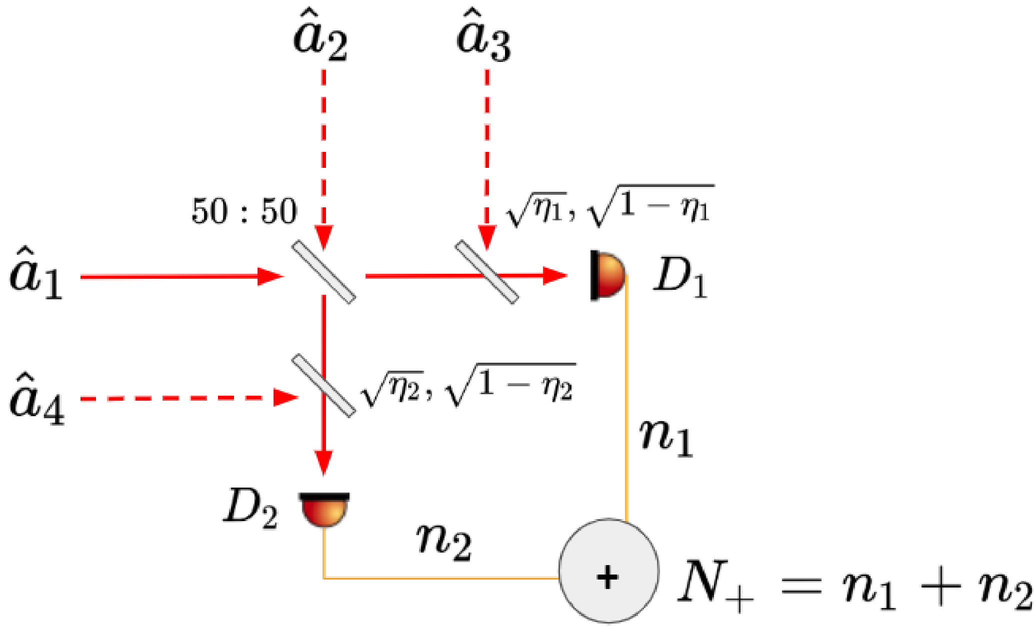

Figure C.1: Spatial multiplexing setup

We are interested in total photon number given by both TES channels. Therefore, we would like to determine the detection modes right before both the detectors D_1 and D_2. We adopt the Heisenberg picture and evolve the input modes under beamsplitter interactions. After the 50:50 BS, we get

$$\hat{a}_1 \to \frac{(\hat{a}_1 - \hat{a}_2)}{\sqrt{2}} = \hat{a}_1^{'}. \tag{C.1}$$

$$\hat{a}_2 \to \frac{(\hat{a}_1 + \hat{a}_2)}{\sqrt{2}} = \hat{a}_2^{'}. \tag{C.2}$$

Similarly, after $BS(\eta_1)$ and $BS(\eta_2)$:

$$\hat{a}_1^{'} \to \sqrt{\eta_1}\frac{(\hat{a}_1 - \hat{a}_2)}{\sqrt{2}} - \sqrt{1-\eta_1}\hat{a}_3 = \hat{a}_1^{''}. \tag{C.3}$$

$$\hat{a}_2^{'} \rightarrow \sqrt{\eta_2}\frac{(\hat{a}_1+\hat{a}_2)}{\sqrt{2}} - \sqrt{1-\eta_2}\hat{a}_4 = \hat{a}_2^{''} \tag{C.4}$$

As a result, the total photon-number operator right before the detectors is given by

$$N = \hat{a}_2^{''\dagger}\hat{a}_2^{''} + \hat{a}_1^{''\dagger}\hat{a}_1^{''}. \tag{C.5}$$

Using Eq.(C.19) and Eq. (C.20), we get

$$\hat{N} = \left(\frac{\eta_1}{2}+\frac{\eta_2}{2}\right)(\hat{a}_1^\dagger\hat{a}_1 + \hat{a}_2^\dagger\hat{a}_2) + (1-\eta_1)a_3^\dagger a_3 + (1-\eta_2)a_4^\dagger a_4 \tag{C.6}$$

$$- \frac{(\sqrt{1-\eta_1}\sqrt{\eta_1}(\hat{a}_1-\hat{a}_2)a_3^\dagger}{\sqrt{2}} - \frac{(\sqrt{1-\eta_1}\sqrt{\eta_1}(\hat{a}_1^\dagger-\hat{a}_2^\dagger)a_3}{\sqrt{2}} \tag{C.7}$$

$$- \frac{(\sqrt{1-\eta_2}\sqrt{\eta_2}(\hat{a}_1+\hat{a}_2)a_4^\dagger}{\sqrt{2}} - \frac{(\sqrt{1-\eta_2}\sqrt{\eta_2}(\hat{a}_1^\dagger+\hat{a}_2^\dagger)a_4}{\sqrt{2}} \tag{C.8}$$

Next, we calculate the expectation value of the total number operator given by Eq. (C.8) for a signal state prepared in n-photon Fock state. Thus, the input quantum state is given by

$$|\phi_{in}\rangle = |n\rangle \otimes |000\rangle \tag{C.9}$$

As a result, measured photon-count using Eq.(C.8) and Eq. (C.9) is

$$\langle N\rangle = Tr[|\phi_{in}\rangle\langle\phi_{in}|N] = \langle\phi_{in}|N|\phi_{in}\rangle = \left(\frac{\eta_1}{2}+\frac{\eta_2}{2}\right)n. \tag{C.10}$$

Note that we could define an effective photon-number operator given as

$$\hat{N}_{\text{effective}} := \left(\frac{\eta_1}{2}+\frac{\eta_2}{2}\right)\hat{a}_1^\dagger\hat{a}_1. \tag{C.11}$$

Here, we utilize the fact the expectation value of remaining terms in Eq. (C.8) results to zero. If we have $\eta_1 = \eta_2 = \eta$, Eq. (C.10) gives $\langle N\rangle = \eta n$, which means that the measured mean-photon number reduces by a factor determined by η. This is equivalent of having a single beamsplitter with transmission η put up in front of a single perfect PNR detector. Additionally, we consider another example where mode $\hat{a}_1$ is prepared in a coherent state. After the 50:50 BS, we get two coherent states of amplitudes $\frac{\alpha}{\sqrt{2}}$ and $\frac{\alpha}{\sqrt{2}}$, which are further fed to 2 BSs of transmissions η_1 and η_2 leading to the output coherent states of amplitudes $\frac{\sqrt{\eta_1}\alpha}{\sqrt{2}}$ and $\frac{\sqrt{\eta_2}\alpha}{\sqrt{2}}$. In this case, the photon-number in both coherent states is

$$\langle N\rangle = \left(\frac{\eta_1}{2} + \frac{\eta_2}{2}\right)|\alpha|^2. \tag{C.12}$$

Note that the result in Eq. (C.12) can be obtained using Eq. (C.10) with $|\phi_{in}\rangle = |\alpha\rangle$. We now measure the variance in total photon-number operator for an arbitrary single-mode quantum state given as

$$\rho = \sum_{n,n'=0} c_{n,n'}|n\rangle\langle n'|. \tag{C.13}$$

The standard deviation is

$$\triangle N = \sqrt{\langle \hat{N}^2\rangle - \langle \hat{N}\rangle^2}, \tag{C.14}$$

where N is given by Eq.C.24. A simple calculation shows that

$$\triangle N = \frac{\eta_1+\eta_2}{2}\sqrt{\sum_n n^2 c_{n,n} - \big(\sum_n n c_{n,n}\big)^2} = \frac{\eta_1+\eta_2}{2}\triangle N_o, \tag{C.15}$$

where $\triangle N_o$ is the photon-number variance of the input state. Here, we use the fact that number operator $\hat{N}_{\text{effective}}$ is diagonal in photon-number basis, and the expectation value for all the terms having vacuum modes is zero. Therefore, we see that multiplexing two TES channels with quantum efficiencies η_1 and η_2 is equivalent to having a single channel with overall efficiency of $\frac{\eta_1+\eta_2}{2}$.

C.1 Balanced Homodyne Detection with Photon-Number-Resolving Measurements

In this section, we formulate the conventional Balanced Homodyne Detection (BHD) tomography using PNR detectors in place of photodiodes as in Ref. [85]. In BHD tomography, the density matrix elements can be obtained using pattern functions as in Eq. (C.16) [85], [111]

$$\rho_{n,m} = \int_0^{\pi} d\phi \int_{-\infty}^{+\infty} dx \; P(X,\phi) F_{n,m}(X,\phi), \tag{C.16}$$

where $p(X,\phi) = \langle X_\phi|\rho|X_\phi\rangle$ is the probability distribution for quadrature X_ϕ, experimentally determined by setting up the local oscillator phase to ϕ.

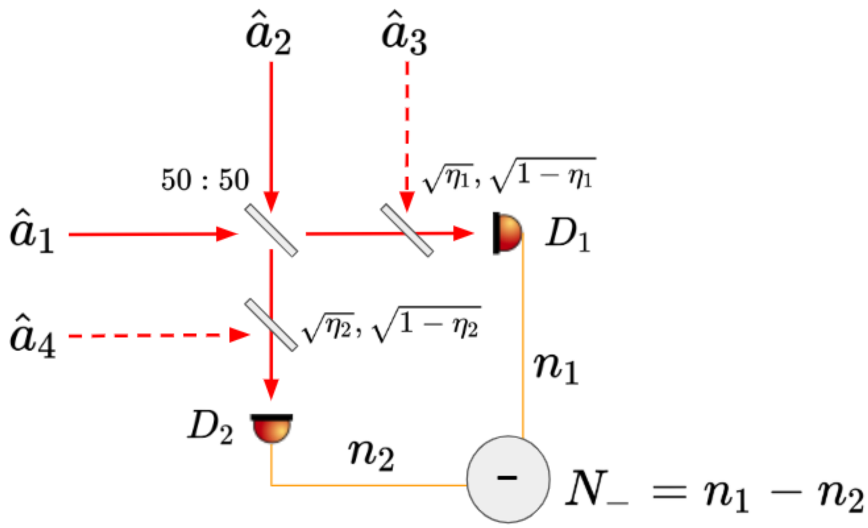

Figure C.2: Balanced homodyne detection with PNR detectors.

In Fig. C.2, we display BHD with PNR detectors of efficiencies η_1 and η_2. The input modes are signal mode, $\hat{a}_1$ and local oscillator mode $\hat{a}_2$. The vacuum modes of fictitious beamsplitters are denoted by $\hat{a}_3$ and $\hat{a}_4$. We are interested in the total photon-number difference operator. Therefore we would like to know the evolved modes right before both the detectors as in multiplexing setup. In the Heisenberg picture after the 50:50 BS, we have

$$\hat{a}_1 \rightarrow \frac{(\hat{a}_1 - \hat{a}_2)}{\sqrt{2}} = \hat{a}_1^{'}. \tag{C.17}$$

$$\hat{a}_2 \rightarrow \frac{(\hat{a}_1 + \hat{a}_2)}{\sqrt{2}} = \hat{a}_2^{'}. \tag{C.18}$$

Similarly, after $BS(\eta_1)$ and $BS(\eta_2)$:

$$\hat{a}_1^{'} \rightarrow \sqrt{\eta_1}\frac{(\hat{a}_1 - \hat{a}_2)}{\sqrt{2}} - \sqrt{1-\eta_1}\hat{a}_3 = \hat{a}_1^{''}. \tag{C.19}$$

$$\hat{a}_2^{'} \rightarrow \sqrt{\eta_2}\frac{(\hat{a}_1 + \hat{a}_2)}{\sqrt{2}} - \sqrt{1-\eta_2}\hat{a}_4 = \hat{a}_2^{''} \tag{C.20}$$

In the lab, we measure the expectation value of the photon-number difference operator given as

$$\hat{N}_- = \hat{a}_1^{''\dagger}\hat{a}_1^{''} + \hat{a}_2^{''\dagger}\hat{a}_2^{''}. \tag{C.21}$$

And the expectation value can be calculated as

$$\langle \hat{N}_- \rangle = \mathrm{Tr}[|\psi\rangle_{1,2,3,4}\langle\psi|_{1,2,3,4}\hat{N}_-], \tag{C.22}$$

where $|\psi\rangle_{1,2,3,4} = |\psi\rangle_{a_1} \otimes |\alpha\rangle_{a_2} \otimes |0,0\rangle_{a_3,a_4}$ is the four-mode input state. A simple algebra shows that

$$\langle N_- \rangle = \left(\frac{\eta_1}{2} - \frac{\eta_2}{2}\right)\langle(\hat{a}_1^\dagger\hat{a}_1 + \hat{a}_2^\dagger\hat{a}_2)\rangle_{|\psi\rangle_{a_1}\otimes|\alpha\rangle_{a_2}} + \underbrace{\left(\frac{\eta_1}{2} + \frac{\eta_2}{2}\right)\langle(\hat{a}_1^\dagger\hat{a}_2 + \hat{a}_2^\dagger\hat{a}_1)\rangle_{|\psi\rangle_{a_1}\otimes|\alpha\rangle_{a_2}}}\,. \tag{C.23}$$

Thus, the effective photon-number difference operator is

$$\hat{N}^{-}_{\text{effective}} := \left(\frac{\eta_1}{2} - \frac{\eta_2}{2}\right)(\hat{a}_1^\dagger \hat{a}_1 + \hat{a}_2^\dagger \hat{a}_2) + \underbrace{\left(\frac{\eta_1}{2} + \frac{\eta_2}{2}\right)(\hat{a}_1^\dagger \hat{a}_2 + \hat{a}_2^\dagger \hat{a}_1)} \tag{C.24}$$

Here, we again utilize the fact the expectation value of remaining terms in Eq. (C.21) results to zero because of vacuum inputs in modes $\hat{a}_3$ and $\hat{a}_4$. If we have $\eta_1 = \eta_2 = \eta$, only interference term under-brace contributes to the total photon-number difference operator. Thus, Eq. (C.22) gives

$$\langle N_- \rangle = \eta \langle (\hat{a}_1^\dagger \hat{a}_2 + \hat{a}_2^\dagger \hat{a}_1) \rangle. \tag{C.25}$$

A further simplification leads to

$$\langle N_- \rangle = \eta |\alpha_2| (\hat{a}_1^\dagger e^{i\phi} + e^{-i\phi} \hat{a}_1) = \sqrt{2}\eta |\alpha_2| \langle \hat{X}_\phi \rangle, \tag{C.26}$$

where we have used $\hat{a}_2 |\alpha_2\rangle = \alpha_2 |\alpha_2\rangle$. Next, let's define

$$\triangle := \sqrt{2}\eta |\alpha_2| \langle \hat{X}_\phi \rangle, \tag{C.27}$$

where $\hat{X}_\phi$ is the quadrature operator of the signal field and it's mean value is given by

$$\langle \hat{X}_\phi \rangle = \frac{\triangle}{\sqrt{2}\eta |\alpha_2|} \tag{C.28}$$

As a result, the continuous distributions, $P(X, \phi)$ are replaced by the discrete photon-number difference distributions, $P\big(\frac{\triangle}{\sqrt{2}\eta|\alpha_2|}, \phi\big)$, where $\triangle$ is the loss-degraded measured photon-number difference expectation values.

Appendix D

Python Codes

In this appendix, we provide the main python functions used for various purposes in this thesis. These functions use opensource Python libraries such as QuTIP [221], CVXPY [159], and Operation Research (OR)-Tools developed by Google, available at OR-Tools.

Quantum Optics Functions

July 29, 2020

[1]:
```
"""This notebook contains some functions commonly used in quantum optics, they␣
↪are written by Miller Eaton and me built on
QuTIPT: http://qutip.org/docs/3.1.0/index.html: """
"""Importing all the modules"""
import cmath, random, numpy
import functools
import  matplotlib.pyplot as plt
import sys
import os
from qutip import*
from sympy import*
from scipy import optimize
from mpl_toolkits.mplot3d import Axes3D
from matplotlib import cm
import math
from qutip import *
from qutip.ipynbtools import plot_animation
import numpy as np
import matplotlib.pyplot as plt
%matplotlib inline
import matplotlib.pylab as plt
import matplotlib as mpl
from mpl_toolkits.mplot3d import Axes3D
from matplotlib import cm
from IPython.display import display, Math, Latex
from mpl_toolkits.axes_grid1 import AxesGrid
from scipy.special import factorial as fac
xvec = np.arange(-80.,80.)*5./80 ##Mash for Surface plots
yvec = np.arange(-50.,50)*5/40
X,Y = np.meshgrid(xvec, xvec)  ##Some plotting params
X1,Y1 = np.meshgrid(yvec,yvec)
N_dim = 35 ##Dimenstion of the Hilbert space
"""Define single-mode annihilation  operators"""
a1 = destroy(N_dim)
a2 = destroy(N_dim)
a3 = destroy(N_dim)
```

```python
'''Displacement operator: accepts input density matrix and outputs displaced␣
↪density matrix'''
def D(state,alpha):
    Rho_new=displace(N_dim,alpha)*state*displace(N_dim,alpha).dag()
    return Rho_new
"""Phase shift operator"""
def Phase(theta):
    b=-1j*theta*a1.dag()*a1;
    return b.expm()
"""Balanced Beamsplitter"""
def BS_50_50(a1,a2):
    b = (np.pi/4)*(tensor(a1,a2.dag()) - tensor(a1.dag(),a2))
    return b.expm()
'''The function below creates a beamsplitter operation that acts on
two modes. The value for k determines what number Fock state could be
filtered out of the first state based on a single photon input for the
second BS port, followed by single photon detection.'''
def BS_operator_filtering(a1, a2, k):
    theta_k = np.arctan(1/np.sqrt(k))
    T = np.sin(theta_k)*np.sin(theta_k)
    R = np.cos(theta_k)*np.cos(theta_k)
    print('I am filtering', k, 'and:', theta_k*180/math.pi)
    print('BS T is : ', T, 'and : ', R)
    b = theta_k*(tensor(a1,a2.dag()) - tensor(a1.dag(),a2))
    return b.expm()
"""n-photon Fock state density matrix: http://qutip.org/docs/3.1.0/guide/
↪guide-states.html"""
def Fock_state(n, N_dim):
    return fock_dm(N_dim, n)
"""Coherent State: alpha is the amplitude"""
def coherent_state(alpha, N_dim):
    return coherent_dm(N_dim, alpha)
""" Phase-averaged coherent states"""
def PHAV(alpha, n_dim, n_trun):
    PHAV = 0;
    for i in range(n_trun):
        PHAV += ((math.pow(alpha, 2*i)/math.factorial(i))*fock_dm(n_dim, i))
    rho_PHAV = math.exp(-math.pow(alpha,2))*PHAV
    return Qobj(rho_PHAV)
"""Squeezed state: r is the squeezing parameter"""
def Sq(state,r):
    Rho_new=squeeze(N_dim,r)*state*squeeze(N_dim,r).dag();
    return Rho_new
"""Schrodinger cat states"""
def cat_plus(alpha):
    cat = (1/(np.sqrt(2)*np.sqrt(1+np.e**(-alpha*alpha.
↪conj()))))*(coherent(N_dim,-alpha)+(coherent(N_dim,alpha)))
```

```
    return cat
def cat_minus(alpha):
    cat = (1/(np.sqrt(2)*np.sqrt(1-np.e**(-alpha*alpha.
 ↪conj()))))*(-coherent(N_dim,-alpha)+(coherent(N_dim,alpha)))
    return cat
"""Utilize positive-operator value measurments (POVM) of the detector
to define a PNR detector with efficiency eta, n_truc is the detector saturation␣
 ↪threshold, please refer to:
 https://arxiv.org/abs/1909.10628 for more details"""
def pnr_resolution_detector(eta, click, n_truc):
    pi_n = 0;
    l = np.arange(click,n_truc)
    for i in l:
        pi_n +=  n_choose_k(i,click)*math.pow((1-eta),(i-click))*math.
 ↪pow(eta,click)*fock(N_dim,i)*fock(N_dim,i).dag()
        #print("The final Povm element is: ", pi_0)
    return Qobj(pi_n)
'''Performs photon catalysis with Fock state input.  Both inputs
are density matrices, and the returned output mode is a normalized
density matrix after the PNR detection'''
def Fock_Filter_povm(in_state,in_fock,refl,num_det,eta,n_truc):
    Projector = tensor(pnr_resolution_detector(eta, num_det,␣
 ↪n_truc),qeye(N_dim));
    Initial_state=tensor(in_state,ket2dm(fock(N_dim,in_fock)));
    theta_k=np.arccos(np.sqrt(refl));
    BS1= ((theta_k)*(tensor(a1,a2.dag()) - tensor(a1.dag(),a2))).expm()
    Rho=BS1*Initial_state*BS1.dag();
    Rho_filtered = ((Rho*Projector).ptrace(1))/((Rho*Projector).tr())
    '''The operation .ptrace(m) takes the partial trace over every mode
    EXCEPT m, where the numbering startes at 0.  So .ptrace(1) means
    you keep mode 1, which is actually the 2nd mode'''
    print('BS has reflectivity',refl,' and I am detecting the |',num,
          '> state,where my detector has efficiency', eta)
    return Rho_filtered
'''Performs photon catalysis with Fock state input and calculates
the probability of success.'''
def Fock_Filter_prob(in_state,in_fock,refl,num_det,eta,n_truc):
    Projector = tensor(pnr_resolution_detector(eta, num_det,␣
 ↪n_truc),qeye(N_dim));
    Initial_state=tensor(in_state,ket2dm(fock(N_dim,in_fock)));
    theta_k=np.arccos(np.sqrt(refl));
    BS1= ((theta_k)*(tensor(a1,a2.dag()) - tensor(a1.dag(),a2))).expm()
    Rho=BS1*Initial_state*BS1.dag();
    P=(Rho*Projector).tr()
    print('The probability of a sucessful detection is:',P)
    Rho_filtered = ((Rho*Projector).ptrace(1))/((Rho*Projector).tr())
    #Rho_filtered=Rho*Projector
```

```python
    '''The operation .ptrace(m) takes the partial trace over every mode
    EXCEPT m, where the numbering startes at 0.  So .ptrace(1) means you
    keep mode 1, which is actually the 2nd mode'''
    print('BS has reflectivity',refl,' and I am detecting the |',num,
          '> state, where my detector has efficiency', eta)
    return Rho_filtered
'''Generic photon catalysis where the two input states are allowed to be
arbitrary. Takes in two density matrices and returns a density matrix
along with success probability.'''
def catalysis(in1,in2,refl,num_det,eta,n_truc):
    Projector = tensor(pnr_resolution_detector(eta, num_det,␣
 ↪n_truc),qeye(N_dim));
    Initial_state=tensor(in1,in2);
    theta_k=np.arccos(np.sqrt(refl));
    BS1= ((theta_k)*(tensor(a1,a2.dag()) - tensor(a1.dag(),a2))).expm()
    Rho=BS1*Initial_state*BS1.dag();
    P=(Rho*Projector).tr()
    print('The probability of a sucessful detection is:',P)
    Rho_filtered = ((Rho*Projector).ptrace(1))/((Rho*Projector).tr())
    '''The operation .ptrace(m) takes the partial trace over every mode
    EXCEPT m, where the numbering startes at 0.  So .ptrace(1) means you
    keep mode 1, which is actually the 2nd mode'''
    print('BS has reflectivity',refl,' and I am detecting the |',num,
          '> state, where my detector has efficiency', eta)
    return Rho_filtered
'''Defines the fidelity between two arbitrary quantum states'''
def fid(state1,state2):
    F=np.absolute((state1.sqrtm()*state2*state1.sqrtm()).sqrtm().tr())
    return F
"""The Wigner function reconstruction from the parity measurements accessed␣
 ↪with PNR measurements"""
def Wigner_as_parity_expectation(rho):
    W = 0;
    prob_array = rho.diag()
    #print("length of prob_araay:", len(prob_array))
    for i in range(len(prob_array)):
        W+=math.pow(-1,i)*prob_array[i]
    print("Amplitude of Wigner function is: ", W/math.pi)
    return W/math.pi
```

Semi-definite program for the state tomography

July 29, 2020

[1]:
```
"""This SDP is built upon opensource python library for convex optimizations.␣
↪Please refer to:https://www.cvxpy.org/"""
import cvxpy as cp
import cvxopt
from scipy import linalg
import scipy as scp
```

[2]:
```
'''This functions minimized the l2 norm of [O-CM], please refer to: https://
↪arxiv.org/abs/1911.00173v2'''
def state_overlap_tomography(Matrix_prob, Measurements, gamma):
    M = Matrix_prob; # the coherent state coefficients matrix
    Q_measured = Measurements; #Overlab measurements and gamma is the adhoc␣
↪paremeter set according to noise level
    #P = cp.Variable((N_dim,N_dim), PSD = True) #To optimize over the real␣
↪space
    P = cp.Variable((N_dim,N_dim), hermitian = True)# To optimize over the␣
↪complex space
    #Error = cp.sum_squares(M*P - Q_measured)
    Error = cp.norm(M*cp.vec(P) - Q_measured,2)#second parameter gives norm␣
↪type
    Obj_detect = cp.Minimize(Error + gamma*cp.norm(cp.vec(P),2))#the overall␣
↪minimizer including the regularizer
    """Some other norms"""
    #Obj_detect = cp.Minimize(Error + gamma*cp.norm(smooth_regulizer(P), 1))
    #Obj_detect = cp.Minimize(Error + gamma*(smooth_regulizer(P)))
    #Obj_detect = cp.Minimize(Error + gamma*cp.norm(Diagonal_Matrix(N_dim,␣
↪N_dim)*P, 2))
    #Obj_detect = cp.Minimize(Error + gamma*cp.norm(np.ones(N_dim)*P,␣
↪2))#+2*gamma*(cp.norm(np.ones(N_dim)*P, 1)))
    #Obj_detect = cp.Minimize(Error + gamma*cp.sum_squares(cp.
↪diff(P)))#*gamma*cp.norm(cp.tv(P),1))
    #print(cp.norm(np.ones(N_dim)*P,2))
    #constraints = [(cp.reshape(P, 10)).trace()==1]
    constraints = [cp.trace(P)==1]# Normalization
    #for i in range(N_dim):
```

```
    #   constraints.append(cp.real(P[i][i]) >= 0) ##In case,one needs to more␣
↪constraints on the density matrix elements
   Prob_detect = cp.Problem(Obj_detect,constraints)
   Prob_detect.solve(verbose = False)
   #Prob_detect.solve(cp.CVXOPT)  ##Optimizers to solve
   p_values = (P.value)
   return p_values
```

Detector Tomography

July 29, 2020

[2]:
```python
"""These functions are used for characterizing quantum detectors by the Wigner␣
↪funtions, please refer to: https://arxiv.org/abs/1909.10628. To minimize the␣
↪l2 norm,
we employ the CVXPY"""
def thermal_state_prob(mu, N_dim, N_turn):
    Th_m = thermal_dm(N_dim, mu)
    Prob = Th_m.diag()
    return Prob
def thermal_state_displace_expectation(thermal_state, POVM):
    Exp = (D(thermal_state)*POVM).tr() #D(.) is the displacement operator
    return Exp
def phase_average_displace_expectation(PHAV, POVM):
    Exp = (D(PHAV)*POVM).tr() #D(.) is the displacement operator
    return Exp
def Convex_optimization(Matrix_prob, POVM_thermal, gamma):
    M = Matrix_prob;
    Q_measured = POVM_thermal;
    P = cp.Variable(len(POVM_thermal))
    Error = cp.norm(M*P - Q_measured,2)
    """Other norms to invert [MP-Q]"""
    #Obj_detect = cp.Minimize(Error + gamma*cp.norm(smooth_regulizer(P), 1))
    #Obj_detect = cp.Minimize(Error + gamma*(smooth_regulizer(P)))
    #Obj_detect = cp.Minimize(Error + gamma*cp.norm(Diagonal_Matrix(N_dim,␣
↪N_dim)*P, 2))
    #Obj_detect = cp.Minimize(Error + gamma*cp.norm(np.ones(N_dim)*P,␣
↪2))#+2*gamma*(cp.norm(np.ones(N_dim)*P, 1)))
    Obj_detect = cp.Minimize(Error + gamma*cp.norm(P,2))
   ## Obj_detect = cp.Minimize(Error + gamma*cp.sum_squares(cp.
↪diff(P)))#*gamma*cp.norm(cp.tv(P),1))
    #print(cp.norm(np.ones(N_dim)*P,2))
    #constraints = [0 <= P, P <= 1, cp.sum(P)<=1, -1<=␣
↪overall_P(P),overall_P(P)<=1]
    constraints = [0 <= P, P <= 1, -1<= overall_P(P),overall_P(P)<=1]
    Prob_detect = cp.Problem(Obj_detect, constraints)
    Prob_detect.solve(solver=cp.CVXOPT)
    p_values = (P.value)
```

```
    return p_values
```

PNR distributions for segmented detector

July 29, 2020

[1]:
```
"""This function was used to find the number of photon-splitting␣
↪configurations, please refer to, Optics Express 28 (3), 3660-3675
for details. Details on the opensource solver can be found:
https://developers.google.com/optimization/cp/original_cp_solver"""

from ortools.constraint_solver import pywrapcp
import matplotlib.pyplot as plt
from matplotlib import*
def CP_solver(num_input, num_mode, k_clicks):
    """num_input: number of photons
       num_mode : number of output modes or SPADs
       K : Solutions are stored in two-array
       k_clicks: the click number"""
    global  K, eta
    solver = pywrapcp.Solver("Photon_Detection")
    A = [solver.IntVar(0, num_input, "n%i" % i) for i in range(num_mode)]
    solver.Add(np.sum(A) == num_input)
    #for i in range(k_clicks):
     #   solver.Add(A[i]!=0)    ##This is used when eta is 1, i.e., no␣
↪radiative losses
    db = solver.Phase(A, solver.CHOOSE_FIRST_UNBOUND, solver.ASSIGN_MIN_VALUE)
    solution = solver.Assignment()
    solution.Add(A)
    collector = solver.AllSolutionCollector(solution)
    solver.Solve(db, [collector])
    print("Solutions found:", collector.SolutionCount())
    print("Time:", solver.WallTime(), "ms")
    K = np.zeros((collector.SolutionCount(),num_mode))
    for sol in range(collector.SolutionCount()):
        #print("Solution number" , sol, '\n')
        for i in range(num_mode):
            K[sol][i] = (collector.Value(sol, A[i]))
    return K
```

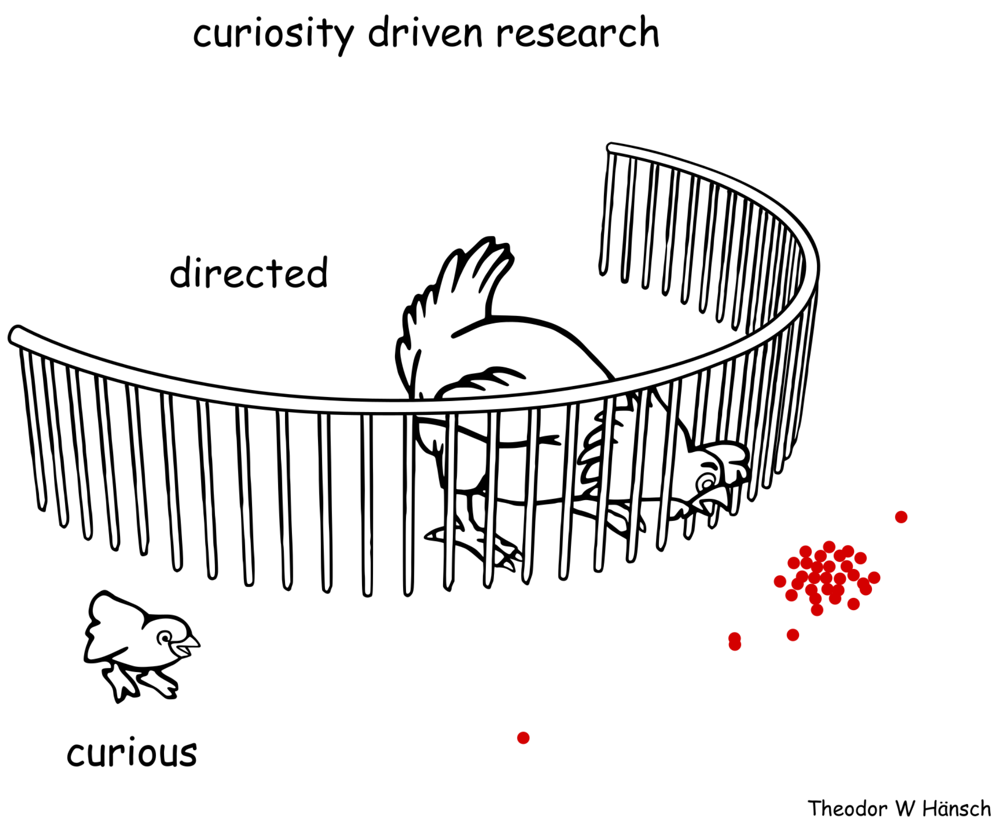
curiosity driven research
directed
curious
Theodor W Hänsch

Bibliography

[1] S. Wallentowitz and W. Vogel. Unbalanced homodyning for quantum state measurements. *Phys. Rev. A*, 53:4528–4533, Jun 1996.

[2] Konrad Banaszek and Krzysztof Wódkiewicz. Direct probing of quantum phase space by photon counting. *Phys. Rev. Lett.*, 76:4344, 1996.

[3] Kelsey M Morgan. Hot science with cool sensors. *Physics Today*, 71(Physics Today), 2018.

[4] Qianhuan Yu, Keye Sun, Qinglong Li, and Andreas Beling. Segmented waveguide photodetector with 90% quantum efficiency. *Opt. Express*, 26(10):12499–12505, May 2018.

[5] Jonathan P Dowling and Gerard J Milburn. Quantum technology: the second quantum revolution. *Philosophical Transactions of the Royal Society of London. Series A: Mathematical, Physical and Engineering Sciences*, 361(1809):1655–1674, 2003.

[6] Gordon E Moore. Cramming more components onto integrated circuits. *Proceedings of the IEEE*, 86(1):82–85, 1998.

[7] Frank Schwierz. Graphene transistors. *Nature nanotechnology*, 5(7):487, 2010.

[8] Jerome Bonnet, Peter Yin, Monica E. Ortiz, Pakpoom Subsoontorn, and Drew Endy. Amplifying genetic logic gates. *Science*, 340(6132):599–603, 2013.

[9] Richard P. Feynman. Simulating physics with computers. *Int. J. Theor. Phys.*, 21:467–488, 1982.

[10] S. Lloyd. Universal quantum simulators. *Science*, 273:1073, 1996.

[11] Joseph W Britton, Brian C Sawyer, Adam C Keith, C-C Joseph Wang, James K Freericks, Hermann Uys, Michael J Biercuk, and John J Bollinger. Engineered two-dimensional ising interactions in a trapped-ion quantum simulator with hundreds of spins. *Nature*, 484(7395):489–492, 2012.

[12] Chao-Yang Lu, Wei-Bo Gao, Otfried Gühne, Xiao-Qi Zhou, Zeng-Bing Chen, and Jian-Wei Pan. Demonstrating anyonic fractional statistics with a six-qubit quantum simulator. *Physical review letters*, 102(3):030502, 2009.

[13] B. P. Lanyon, T. J. Weinhold, N. K. Langford, M. Barbieri, D. F. V. James, A. Gilchrist, and A. G. White. Experimental demonstration of a compiled version of Shor's algorithm with quantum entanglement. *Phys. Rev. Lett.*, 99(25):250505, 2007.

[14] Xinhua Peng, Jingfu Zhang, Jiangfeng Du, and Dieter Suter. Quantum simulation of a system with competing two-and three-body interactions. *Physical review letters*, 103(14):140501, 2009.

[15] Andrew A Houck, Hakan E Türeci, and Jens Koch. On-chip quantum simulation with superconducting circuits. *Nature Physics*, 8(4):292, 2012.

[16] Hannes Bernien, Sylvain Schwartz, Alexander Keesling, Harry Levine, Ahmed Omran, Hannes Pichler, Soonwon Choi, Alexander S Zibrov, Manuel Endres, Markus Greiner, et al. Probing many-body dynamics on a 51-atom quantum simulator. *Nature*, 551(7682):579–584, 2017.

[17] Jiehang Zhang, Guido Pagano, Paul W Hess, Antonis Kyprianidis, Patrick Becker, Harvey Kaplan, Alexey V Gorshkov, Z-X Gong, and Christopher Mon-

roe. Observation of a many-body dynamical phase transition with a 53-qubit quantum simulator. *Nature*, 551(7682):601–604, 2017.

[18] Peter W Shor. Polynomial-time algorithms for prime factorization and discrete logarithms on a quantum computer. *SIAM review*, 41(2):303–332, 1999.

[19] Lieven MK Vandersypen, Matthias Steffen, Gregory Breyta, Costantino S Yannoni, Mark H Sherwood, and Isaac L Chuang. Experimental realization of shor's quantum factoring algorithm using nuclear magnetic resonance. *Nature*, 414(6866):883–887, 2001.

[20] Chao-Yang Lu, Daniel E Browne, Tao Yang, and Jian-Wei Pan. Demonstration of a compiled version of shors quantum factoring algorithm using photonic qubits. *Physical Review Letters*, 99(25):250504, 2007.

[21] Erik Lucero, Rami Barends, Yu Chen, Julian Kelly, Matteo Mariantoni, Anthony Megrant, Peter OMalley, Daniel Sank, Amit Vainsencher, James Wenner, et al. Computing prime factors with a josephson phase qubit quantum processor. *Nature Physics*, 8(10):719–723, 2012.

[22] Lov K Grover. A fast quantum mechanical algorithm for database search. In *Proceedings of the twenty-eighth annual ACM symposium on Theory of computing*, pages 212–219, 1996.

[23] Caroline Figgatt, Dmitri Maslov, KA Landsman, Norbert M Linke, S Debnath, and C Monroe. Complete 3-qubit grover search on a programmable quantum computer. *Nature communications*, 8(1):1–9, 2017.

[24] Frank Arute, Kunal Arya, Ryan Babbush, Dave Bacon, Joseph C Bardin, Rami Barends, Rupak Biswas, Sergio Boixo, Fernando GSL Brandao, David A Buell, et al. Quantum supremacy using a programmable superconducting processor. *Nature*, 574(7779):505–510, 2019.

[25] John Clarke and Frank K Wilhelm. Superconducting quantum bits. *Nature*, 453(7198):1031–1042, 2008.

[26] Jeremy L O'brien, Akira Furusawa, and Jelena Vučković. Photonic quantum technologies. *Nature Photonics*, 3(12):687, 2009.

[27] Juan I Cirac and Peter Zoller. Quantum computations with cold trapped ions. *Physical review letters*, 74(20):4091, 1995.

[28] A. Imamoglu, D. D. Awschalom, G. Burkard, D. P. DiVincenzo, D. Loss, M. Sherwin, and A. Small. Quantum information processing using quantum dot spins and cavity qed. *Phys. Rev. Lett.*, 83:4204–4207, Nov 1999.

[29] Mark Saffman, Thad G Walker, and Klaus Mølmer. Quantum information with rydberg atoms. *Reviews of modern physics*, 82(3):2313, 2010.

[30] Richard J Hughes, George L Morgan, and C Glen Peterson. Quantum key distribution over a 48 km optical fibre network. *Journal of Modern Optics*, 47(2-3):533–547, 2000.

[31] Wolfgang Tittel, Jürgen Brendel, Nicolas Gisin, and Hugo Zbinden. Long-distance bell-type tests using energy-time entangled photons. *Physical Review A*, 59(6):4150, 1999.

[32] E. Knill, R. Laflamme, and G. J. Milburn. A scheme for efficient quantum computation with linear optics. *Nature*, 409(6816):46–52, 01 2001.

[33] TB Pittman, MJ Fitch, BC Jacobs, and JD Franson. Experimental controlled-not logic gate for single photons in the coincidence basis. *Physical Review A*, 68(3):032316, 2003.

[34] Jeremy L O'Brien, Geoffrey J Pryde, Andrew G White, Timothy C Ralph, and David Branning. Demonstration of an all-optical quantum controlled-not gate. *Nature*, 426(6964):264–267, 2003.

[35] Sara Gasparoni, Jian-Wei Pan, Philip Walther, Terry Rudolph, and Anton Zeilinger. Realization of a photonic controlled-not gate sufficient for quantum computation. *Physical review letters*, 93(2):020504, 2004.

[36] Dik Bouwmeester, Jian-Wei Pan, Klaus Mattle, Manfred Eibl, Harald Weinfurter, and Anton Zeilinger. Experimental quantum teleportation. *Nature*, 390(6660):575–579, 1997.

[37] Ryo Okamoto, Jeremy L OBrien, Holger F Hofmann, and Shigeki Takeuchi. Realization of a knill-laflamme-milburn controlled-not photonic quantum circuit combining effective optical nonlinearities. *Proceedings of the National Academy of Sciences*, 108(25):10067–10071, 2011.

[38] Seth Lloyd and Samuel L. Braunstein. Quantum computation over continuous variables. *Phys. Rev. Lett.*, 82:1784, 1999.

[39] Daniel F Walls and Gerard J Milburn. *Quantum optics*. Springer Science & Business Media, 2007.

[40] Luis Ortiz-Gutiérrez, Bruna Gabrielly, Luis F Muñoz, Kainã T Pereira, Jefferson G Filgueiras, and Alessandro S Villar. Continuous variables quantum computation over the vibrational modes of a single trapped ion. *Optics Communications*, 397:166–174, 2017.

[41] Robert Raussendorf and Hans J. Briegel. A one-way quantum computer. *Phys. Rev. Lett.*, 86:5188–5191, May 2001.

[42] Jing Zhang and Samuel L. Braunstein. Continuous-variable Gaussian analog of cluster states. *Phys. Rev. A*, 73(3):032318, 2006.

[43] Nicolas C. Menicucci, Peter van Loock, Mile Gu, Christian Weedbrook, Timothy C. Ralph, and Michael A. Nielsen. Universal quantum computation with continuous-variable cluster states. *Phys. Rev. Lett.*, 97:110501, Sep 2006.

[44] Philip Walther, Kevin J Resch, Terry Rudolph, Emmanuel Schenck, Harald Weinfurter, Vlatko Vedral, Markus Aspelmeyer, and Anton Zeilinger. Experimental one-way quantum computing. *Nature*, 434(7030):169–176, 2005.

[45] Nikolai Kiesel, Christian Schmid, Ulrich Weber, Géza Tóth, Otfried Gühne, Rupert Ursin, and Harald Weinfurter. Experimental analysis of a four-qubit photon cluster state. *Phys. Rev. Lett.*, 95:210502, Nov 2005.

[46] Olaf Mandel, Markus Greiner, Artur Widera, Tim Rom, Theodor W Hänsch, and Immanuel Bloch. Controlled collisions for multi-particle entanglement of optically trapped atoms. *Nature*, 425(6961):937–940, 2003.

[47] Peter van Loock, Christian Weedbrook, and Mile Gu. Building Gaussian cluster states by linear optics. *Phys. Rev. A*, 76:032321, 2007.

[48] Xiaolong Su, Aihong Tan, Xiaojun Jia, Jing Zhang, Changde Xie, and Kunchi Peng. Experimental preparation of quadripartite cluster and greenberger-horne-zeilinger entangled states for continuous variables. *Phys. Rev. Lett.*, 98:070502, Feb 2007.

[49] Olivier Pfister, Sheng Feng, Gregory Jennings, Raphael Pooser, and Daruo Xie. Multipartite continuous-variable entanglement from concurrent nonlinearities. *Phys. Rev. A*, 70:020302, Aug 2004.

[50] Nicolas C. Menicucci, Steven T. Flammia, and Olivier Pfister. One-way quantum computing in the optical frequency comb. *Phys. Rev. Lett.*, 101:130501, 2008.

[51] Moran Chen, Nicolas C. Menicucci, and Olivier Pfister. Experimental realization of multipartite entanglement of 60 modes of a quantum optical frequency comb. *Phys. Rev. Lett.*, 112:120505, Mar 2014.

[52] Rafael N Alexander, Shota Yokoyama, Akira Furusawa, and Nicolas C Menicucci. Universal quantum computation with temporal-mode bilayer square lattices. *Physical Review A*, 97(3):032302, 2018.

[53] Shota Yokoyama, Ryuji Ukai, Seiji C. Armstrong, Chanond Sornphiphatphong, Toshiyuki Kaji, Shigenari Suzuki, Jun-ichi Yoshikawa, Hidehiro Yonezawa, Nicolas C. Menicucci, and Akira Furusawa. Ultra-large-scale continuous-variable cluster states multiplexed in the time domain. *Nat. Photon.*, 7:982, 2013.

[54] Mikkel V Larsen, Xueshi Guo, Casper R Breum, Jonas S Neergaard-Nielsen, and Ulrik L Andersen. Fiber-coupled epr-state generation using a single temporally multiplexed squeezed light source. *npj Quantum Information*, 5(1):1–7, 2019.

[55] Warit Asavanant, Yu Shiozawa, Shota Yokoyama, Baramee Charoensombutamon, Hiroki Emura, Rafael N. Alexander, Shuntaro Takeda, Jun-ichi Yoshikawa, Nicolas C. Menicucci, Hidehiro Yonezawa, and Akira Furusawa. Generation of time-domain-multiplexed two-dimensional cluster state. *Science*, 366(6463):373–376, 2019.

[56] Mikkel V. Larsen, Xueshi Guo, Casper R. Breum, Jonas S. Neergaard-Nielsen, and Ulrik L. Andersen. Deterministic generation of a two-dimensional cluster state. *Science*, 366(6463):369–372, 2019.

[57] Xuan Zhu, Chun-Hung Chang, Carlos González-Arciniegas, Jacob Higgins, Avi Pe'er, and Olivier Pfister. Graph state engineering by phase modulation of the quantum optical frequency comb. *arXiv preprint arXiv:1912.11215*, 2019.

[58] Adriana E. Lita, Aaron J. Miller, and Sae Woo Nam. Counting near-infrared single-photons with 95% efficiency. *Opt. Express*, 16(5):3032–3040, Mar 2008.

[59] Peter C Humphreys, Benjamin J Metcalf, Thomas Gerrits, Thomas Hiemstra, Adriana E Lita, Joshua Nunn, Sae Woo Nam, Animesh Datta, W Steven

Kolthammer, and Ian A Walmsley. Tomography of photon-number resolving continuous-output detectors. *New J. Phys.*, 17(10):103044, oct 2015.

[60] Leonardo Assis Morais, Marcelo Pereira de Almeida, Geoff Gillett, and Andrew G. White. Revealing the number of single photons in real time. In *Frontiers in Optics + Laser Science APS/DLS*, page JTu4A.42. Optical Society of America, 2019.

[61] Pieter Kok and Samuel L. Braunstein. Detection devices in entanglement-based optical state preparation. *Phys. Rev. A*, 63:033812, Feb 2001.

[62] Daryl Achilles, Christine Silberhorn, Cezary Śliwa, Konrad Banaszek, and Ian A. Walmsley. Fiber-assisted detection with photon number resolution. *Opt. Lett.*, 28(23):2387–2389, Dec 2003.

[63] M. J. Fitch, B. C. Jacobs, T. B. Pittman, and J. D. Franson. Photon-number resolution using time-multiplexed single-photon detectors. *Phys. Rev. A*, 68:043814, Oct 2003.

[64] F. Piacentini, M. P. Levi, A. Avella, M. López, S. Kück, S. V. Polyakov, I. P. Degiovanni, G. Brida, and M. Genovese. Positive operator-valued measure reconstruction of a beam-splitter tree-based photon-number-resolving detector. *Opt. Lett.*, 40(7):1548–1551, Apr 2015.

[65] Francesco Mattioli, Zili Zhou, Alessandro Gaggero, Rosalinda Gaudio, Saeedeh Jahanmirinejad, Döndü Sahin, Francesco Marsili, Roberto Leoni, and Andrea Fiore. Photon-number-resolving superconducting nanowire detectors. *Superconductor Science and Technology*, 28(10):104001, 2015.

[66] Kaisa Laiho, Katiúscia N. Cassemiro, David Gross, and Christine Silberhorn. Probing the negative Wigner function of a pulsed single photon point by point. *Phys. Rev. Lett.*, 105:253603, Dec 2010.

[67] Josef Hloušek, Michal Dudka, Ivo Straka, and Miroslav Ježek. Accurate detection of arbitrary photon statistics. *Phys. Rev. Lett.*, 123:153604, Oct 2019.

[68] Rajveer Nehra, Chun-Hung Chang, Qianhuan Yu, Andreas Beling, and Olivier Pfister. Photon-number-resolving segmented detectors based on single-photon avalanche-photodiodes. *Optics Express*, 28(3):3660–3675, 2020.

[69] Young-Sik Ra, Adrien Dufour, Mattia Walschaers, Clément Jacquard, Thibault Michel, Claude Fabre, and Nicolas Treps. Non-gaussian quantum states of a multimode light field. *Nature Physics*, 16(2):144–147, 2020.

[70] M. Dakna, L. Knöll, and D.-G. Welsch. Quantum state engineering using conditional measurement on a beam splitter. *Eur. Phys. J. D*, 3(3):295–308, September 1998.

[71] A. Ourjoumtsev, R. Tualle-Brouri, J. Laurat, and P. Grangier. Generating optical Schrödinger kittens for quantum information processing. *Science*, 312:83–86, 2006.

[72] Alessandro Zavatta, Silvia Viciani, and Marco Bellini. Quantum-to-classical transition with single-photon–added coherent states of light. *Science*, 306:660, 2004.

[73] Miller Eaton, Rajveer Nehra, and Olivier Pfister. Non-gaussian and gottesman-kitaev-preskill state preparation by photon catalysis. *New Journal of Physics, in press; arxiv:1903.01925 [quant-ph].*, 2019.

[74] K. J. Resch, J. L. O'Brien, T. J. Weinhold, K. Sanaka, B. P. Lanyon, N. K. Langford, and A. G. White. Entanglement generation by fock-state filtration. *Phys. Rev. Lett.*, 98:203602, May 2007.

[75] Shohini Ghose and Barry C. Sanders. Non-gaussian ancilla states for continuous variable quantum computation via gaussian maps. *Journal of Modern Optics*, 54(6):855–869, 2007.

[76] Daiqin Su, Casey R Myers, and Krishna Kumar Sabapathy. Conversion of gaussian states to non-gaussian states using photon-number-resolving detectors. *Physical Review A*, 100(5):052301, 2019.

[77] J. S. Bell. *Speakable and unspeakable in quantum mechanics*, chapter 21, *"EPR correlations and EPW distributions"*, pages 196–200. Cambridge University Press, 1987.

[78] A. Furusawa, J. L. Sørensen, S. L. Braunstein, C. A. Fuchs, H. J. Kimble, and E. S. Polzik. Unconditional quantum teleportation. *Science*, 282:706, 1998.

[79] Marissa Giustina, Marijn A. M. Versteegh, Sören Wengerowsky, Johannes Handsteiner, Armin Hochrainer, Kevin Phelan, Fabian Steinlechner, Johannes Kofler, Jan-Åke Larsson, Carlos Abellán, Waldimar Amaya, Valerio Pruneri, Morgan W. Mitchell, Jörn Beyer, Thomas Gerrits, Adriana E. Lita, Lynden K. Shalm, Sae Woo Nam, Thomas Scheidl, Rupert Ursin, Bernhard Wittmann, and Anton Zeilinger. Significant-loophole-free test of bell's theorem with entangled photons. *Phys. Rev. Lett.*, 115:250401, Dec 2015.

[80] Julien Niset, Jaromír Fiurášek, and Nicolas J. Cerf. No-go theorem for Gaussian quantum error correction. *Phys. Rev. Lett.*, 102:120501, 2009.

[81] J. Eisert, S. Scheel, and M. B. Plenio. Distilling Gaussian states with Gaussian operations is impossible. *Phys. Rev. Lett.*, 89(13):137903, Sep 2002.

[82] J. P. Dowling. Correlated input-port, matter-wave interferometer: Quantum-noise limits to the atom-laser gyroscope. *Phys. Rev. A*, 57:4736, 1998.

[83] Alan Migdall, Sergey Polyakov, Jingyun Fan, and Joshua Bienfang, editors. *Single-Photon Generation and Detection*, volume 45 of *Experimental Methods in the Physical Sciences*. Academic Press, 2013.

[84] Joanne C Zwinkels, Erkki Ikonen, Nigel P Fox, Gerhard Ulm, and Maria Luisa Rastello. Photometry, radiometry and 'the candela': evolution in the classical and quantum world. *Metrologia*, 47(5):R15, 2010.

[85] Stefano Olivares, Alessia Allevi, Giovanni Caiazzo, Matteo GA Paris, and Maria Bondani. Quantum tomography of light states by photon-number-resolving detectors. *New J. Phys*, 21:103045, 2019.

[86] Rajveer Nehra, Miller Eaton, Carlos Gonzalez-Arciniegas, MS Kim, and Olivier Pfister. Loss tolerant quantum state tomography by number-resolving measurements without approximate displacements. *arXiv preprint arXiv:1911.00173*, 2019.

[87] GS Thekkadath, DS Phillips, JFF Bulmer, WR Clements, A Eckstein, BA Bell, J Lugani, TAW Wolterink, A Lita, SW Nam, et al. Tuning between photon-number and quadrature measurements with weak-field homodyne detection. *arXiv preprint arXiv:1908.04765*, 2019.

[88] J Sperling, DS Phillips, JF F Bulmer, GS Thekkadath, A Eckstein, TAW Wolterink, J Lugani, SW Nam, A Lita, T Gerrits, et al. Detector-agnostic phase-space distributions. *Physical Review Letters*, 124(1):013605, 2020.

[89] Rajveer Nehra, Aye Win, Miller Eaton, Reihaneh Shahrokhshahi, Niranjan Sridhar, Thomas Gerrits, Adriana Lita, Sae Woo Nam, and Olivier Pfister. State-independent quantum state tomography by photon-number-resolving measurements. *Optica*, 6(10):1356–1360, Oct 2019.

[90] Rajveer Nehra and Kevin Valson Jacob. Characterizing quantum detectors by wigner functions. *arXiv preprint arXiv:1909.10628*, 2019.

[91] J. S. Lundeen, A. Feito, H. Coldenstrodt-Ronge, K. L. Pregnell, Ch. Silberhorn, T. C. Ralph, J. Eisert, M. B. Plenio, and I. A. Walmsley. Tomography of quantum detectors. *Nat Phys*, 5(1):27–30, 01 2009.

[92] Lijian Zhang, Animesh Datta, Hendrik B Coldenstrodt-Ronge, Xian-Min Jin, Jens Eisert, Martin B Plenio, and Ian A Walmsley. Recursive quantum detector tomography. *New Journal of Physics*, 14(11):115005, nov 2012.

[93] E. Wigner. On the quantum correction for thermodynamic equilibrium. *Phys. Rev.*, 40:749–759, Jun 1932.

[94] R. L. Hudson. When is the Wigner quasi-probability density non-negative? *Rep. Math. Phys.*, 6(2):249–252, 1974.

[95] Derek Harland, M. J. Everitt, Kae Nemoto, T. Tilma, and T. P. Spiller. Towards a complete and continuous wigner function for an ensemble of spins or qubits. *Phys. Rev. A*, 86:062117, Dec 2012.

[96] Nicolas C. Menicucci, Steven T. Flammia, and Peter van Loock. Graphical calculus for Gaussian pure states with applications to continuous-variable cluster states. *Phys. Rev. A*, 83:042335, 2011.

[97] Kôdi HUSIMI. Some formal properties of the density matrix. *Proceedings of the Physico-Mathematical Society of Japan. 3rd Series*, 22(4):264–314, 1940.

[98] NG Walker. Quantum theory of multiport optical homodyning. *Journal of Modern Optics*, 34(1):15–60, 1987.

[99] Dirk-Gunnar Welsch, Werner Vogel, and Tomáš Opatrnỳ. Ii homodyne detection and quantum-state reconstruction. In *Progress in Optics*, volume 39, pages 63–211. Elsevier, 1999.

[100] Olivier Pfister. Continuous-variable quantum computing in the quantum optical frequency comb. *Journal of Physics B: Atomic, Molecular and Optical Physics*, 53(1):012001, nov 2019.

[101] Christian Weedbrook, Stefano Pirandola, Raúl García-Patrón, Nicolas J Cerf, Timothy C Ralph, Jeffrey H Shapiro, and Seth Lloyd. Gaussian quantum information. *Reviews of Modern Physics*, 84(2):621, 2012.

[102] Mile Gu, Christian Weedbrook, Nicolas C. Menicucci, Timothy C. Ralph, and Peter van Loock. Quantum computing with continuous-variable clusters. *Phys. Rev. A*, 79:062318, 2009.

[103] Stephen D. Bartlett, Barry C. Sanders, Samuel L. Braunstein, and Kae Nemoto. Efficient classical simulation of continuous variable quantum information processes. *Phys. Rev. Lett.*, 88:097904, 2002.

[104] G. N. Gol'tsman, O. Okunev, G. Chulkova, A. Lipatov, A. Semenov, K. Smirnov, B. Voronov, A. Dzardanov, C. Williams, and Roman Sobolewski. Picosecond superconducting single-photon optical detector. *Appl. Phys. Lett.*, 79(6):705–707, 2001.

[105] Daniel Gottesman, Alexei Kitaev, and John Preskill. Encoding a qubit in an oscillator. *Phys. Rev. A*, 64:012310, 2001.

[106] Ben Q Baragiola, Giacomo Pantaleoni, Rafael N Alexander, Angela Karanjai, and Nicolas C Menicucci. All-gaussian universality and fault tolerance with the gottesman-kitaev-preskill code. *Physical Review Letters*, 123(20):200502, 2019.

[107] David Gross, Yi-Kai Liu, Steven T Flammia, Stephen Becker, and Jens Eisert. Quantum state tomography via compressed sensing. *Physical review letters*, 105(15):150401, 2010.

[108] Dylan H Mahler, Lee A Rozema, Ardavan Darabi, Christopher Ferrie, Robin Blume-Kohout, and AM Steinberg. Adaptive quantum state tomography improves accuracy quadratically. *Physical review letters*, 111(18):183601, 2013.

[109] D. T. Smithey, M. Beck, M. G. Raymer, and A. Faridani. Measurement of the Wigner distribution and the density matrix of a light mode using optical homodyne tomography: Application to squeezed states and the vacuum. *Phys. Rev. Lett.*, 70:1244, 1993.

[110] A. I. Lvovsky and M. G. Raymer. Continuous-variable optical quantum-state tomography. *Rev. Mod. Phys.*, 81:299, 2009.

[111] Ulf Leonhardt. *Measuring the Quantum State of Light*. Cambridge University Press, Cambridge, U.K., 1997.

[112] Stefano Olivares, Alessia Allevi, Giovanni Caiazzo, Matteo G A Paris, and Maria Bondani. Quantum tomography of light states by photon-number-resolving detectors. *New Journal of Physics*, 21(10):103045, oct 2019.

[113] Alexander I Lvovsky and Michael G Raymer. Continuous-variable optical quantum-state tomography. *Reviews of Modern Physics*, 81(1):299, 2009.

[114] Steven T Flammia, David Gross, Yi-Kai Liu, and Jens Eisert. Quantum tomography via compressed sensing: error bounds, sample complexity and efficient estimators. *New Journal of Physics*, 14(9):095022, 2012.

[115] D. F. Walls and G. J. Milburn. *Quantum Optics*. Springer, Berlin, 1994.

[116] Seth Lloyd and Samuel L. Braunstein. Quantum computation over continuous variables. *Phys. Rev. Lett.*, 82:1784, 1999.

[117] Stephen D. Bartlett, Barry C. Sanders, Samuel L. Braunstein, and Kae Nemoto. Efficient classical simulation of continuous variable quantum information processes. *Phys. Rev. Lett.*, 88:097904, 2002.

[118] Daniel Gottesman, Alexei Kitaev, and John Preskill. Encoding a qubit in an oscillator. *Phys. Rev. A*, 64:012310, 2001.

[119] N. C. Menicucci, P. van Loock, M. Gu, C. Weedbrook, T. C. Ralph, and M. A. Nielsen. Universal quantum computation with continuous-variable cluster states. *Phys. Rev. Lett.*, 97:110501, 2006.

[120] Nicolas C. Menicucci. Fault-tolerant measurement-based quantum computing with continuous-variable cluster states. *Phys. Rev. Lett.*, 112:120504, Mar 2014.

[121] Shohini Ghose and Barry C. Sanders. Non-gaussian ancilla states for continuous variable quantum computation via gaussian maps. *J. Mod. Opt.*, 54:855–869, 2007.

[122] A. I. Lvovsky, H. Hansen, T. Aichele, O. Benson, J. Mlynek, and S. Schiller. Quantum state reconstruction of the single-photon Fock state. *Phys. Rev. Lett.*, 87:050402, 2001.

[123] Olivier Morin, Virginia D'Auria, Claude Fabre, and Julien Laurat. High-fidelity single-photon source based on a type ii optical parametric oscillator. *Opt. Lett.*, 37(17):3738–3740, Sep 2012.

[124] Antoine Royer. Wigner function as the expectation value of a parity operator. *Phys. Rev. A*, 15:449–450, Feb 1977.

[125] Matteo G. A. Paris. Displacement operator by beam splitter. *Phys. Lett. A*, 217(2):78–80, July 1996.

[126] A. Furusawa, J. L. Sørensen, S. L. Braunstein, C. A. Fuchs, H. J. Kimble, and E. S. Polzik. Unconditional quantum teleportation. *Science*, 282:706, 1998.

[127] K. E. Cahill and R. J. Glauber. Density operators and quasiprobability distributions. *Phys. Rev.*, 177:1882–1902, Jan 1969.

[128] D. Leibfried, D. M. Meekhof, B. E. King, C. Monroe, W. M. Itano, and D. J. Wineland. Experimental determination of the motional quantum state of a trapped atom. *Phys. Rev. Lett.*, 77:4281–4285, Nov 1996.

[129] P. Bertet, A. Auffeves, P. Maioli, S. Osnaghi, T. Meunier, M. Brune, J. M. Raimond, and S. Haroche. Direct measurement of the wigner function of a one-photon fock state in a cavity. *Phys. Rev. Lett.*, 89:200402, Oct 2002.

[130] Brian Vlastakis, Gerhard Kirchmair, Zaki Leghtas, Simon E. Nigg, Luigi Frunzio, S. M. Girvin, Mazyar Mirrahimi, M. H. Devoret, and R. J. Schoelkopf. Deterministically encoding quantum information using 100-photon schrödinger cat states. *Science*, 342(6158):607–610, 2013.

[131] K. Banaszek, C. Radzewicz, K. Wódkiewicz, and J. S. Krasiński. Direct measurement of the Wigner function by photon counting. *Phys. Rev. A*, 60:674–677, Jul 1999.

[132] Maria Bondani, Alessia Allevi, and Alessandra Andreoni. Wigner function of pulsed fields by direct detection. *Opt. Lett.*, 34(9):1444–1446, May 2009.

[133] Niranjan Sridhar, Reihaneh Shahrokhshahi, Aaron J. Miller, Brice Calkins, Thomas Gerrits, Adriana Lita, Sae Woo Nam, and Olivier Pfister. Direct measurement of the Wigner function by photon-number-resolving detection. *J. Opt. Soc. Am. B*, 31(10):B34–B40, 2014.

[134] W. P. Grice and I. A. Walmsley. Spectral information and distinguishability in type-ii down-conversion with a broadband pump. *Phys. Rev. A*, 56:1627–1634, Aug 1997.

[135] Andreas Christ and Christine Silberhorn. Limits on the deterministic creation of pure single-photon states using parametric down-conversion. *Phys. Rev. A*, 85:023829, Feb 2012.

[136] Nicolas Gisin and Rob Thew. Quantum communication. *Nature Photonics*, 1:165, March 2007.

[137] J. F. Clauser and A. Shimony. Bell's theorem. Experimental tests and implications. *Rep. Prog. Phys.*, 41(12):1881, 1978.

[138] Z. Y. Ou and Y. J. Lu. Cavity enhanced spontaneous parametric down-conversion for the prolongation of correlation time between conjugate photons. *Phys. Rev. Lett.*, 83:2556–2559, Sep 1999.

[139] Y. Jeronimo-Moreno, S. Rodriguez-Benavides, and A. B. U'Ren. Theory of cavity-enhanced spontaneous parametric downconversion. *Laser Physics*, 20(5):1221–1233, May 2010.

[140] Stéphane Virally, Suzanne Lacroix, and Nicolas Godbout. Limits of heralded single-photon sources based on parametric photon-pair generation. *Phys. Rev. A*, 81:013808, Jan 2010.

[141] M. Scholz, L. Koch, R. Ullmann, and O. Benson. Single-mode operation of a high-brightness narrow-band single-photon source. *Appl. Phys. Lett.*, 94(20):201105, 2009.

[142] David Höckel, Lars Koch, and Oliver Benson. Direct measurement of heralded single-photon statistics from a parametric down-conversion source. *Phys. Rev. A*, 83:013802, Jan 2011.

[143] Xiao-Hui Bao, Yong Qian, Jian Yang, Han Zhang, Zeng-Bing Chen, Tao Yang, and Jian-Wei Pan. Generation of narrow-band polarization-entangled photon pairs for atomic quantum memories. *Phys. Rev. Lett.*, 101:190501, Nov 2008.

[144] Christopher E. Kuklewicz, Eser Keskiner, Franco N. C. Wong, and Jeffrey H. Shapiro. A high-flux entanglement source based on a doubly resonant optical parametric amplifier. *J. Opt. B: Quantum Semiclass. Opt.*, 4:S162–S168, 2002.

[145] R. W. P. Drever, J. L. Hall, F. V. Kowalski, J. Hough, G. M. Ford, A. J. Munley, and H. Ward. Laser phase and frequency stabilization using an optical resonator. *Appl. Phys. B*, 31:97–105, 1983.

[146] S. Feng and O. Pfister. Stable nondegenerate optical parametric oscillation at degenerate frequencies in Na:KTP. *J. Opt. B: Quantum Semiclass. Opt.*, 5:262, 2003.

[147] S. Feng and O. Pfister. Quantum interference of ultrastable twin optical beams. *Phys. Rev. Lett.*, 92:203601, 2004.

[148] S. Feng and O. Pfister. Realization of an ultrastable twin-beam source for continuous-variable entanglement of bright beams. In *Quantum Communication and Quantum Imaging*, volume 5161 of *SPIE Proceedings*, page 109, Washington, D.C., 2004. SPIE.

[149] Adriana E. Lita, Aaron J. Miller, and Sae Woo Nam. Counting near-infrared single-photons with 95% efficiency. *Opt. Expr.*, 16:3032–3040, 2008.

[150] Dietrich Marcuse. *Theory of dielectric optical waveguides.* Elsevier, 2013.

[151] U. Fano. Description of states in quantum mechanics by density matrix and operator techniques. *Rev. Mod. Phys.*, 29:74–93, Jan 1957.

[152] Matteo Paris and Jaroslav Řeháček, editors. *Quantum State Estimation*, volume 649. Springer-Verlag Berlin Heidelberg, 2004.

[153] Marcus Cramer, Martin B. Plenio, Steven T. Flammia, Rolando Somma, David Gross, Stephen D. Bartlett, Olivier Landon-Cardinal, David Poulin, and Yi-Kai Liu. Efficient quantum state tomography. *Nat. Commun.*, 1:149, 2010.

[154] M. Hillery, R.F. O'Connell, M.O. Scully, and E.P. Wigner. Distribution functions in physics: Fundamentals. *Physics Reports*, 106(3):121 – 167, 1984.

[155] Egor S Tiunov, VV Tiunova, Alexander E Ulanov, AI Lvovsky, and AK Fedorov. Experimental quantum homodyne tomography via machine learning. *Optica*, 7(5):448–454, 2020.

[156] Xun Gao and Lu-Ming Duan. Efficient representation of quantum many-body states with deep neural networks. *Nature communications*, 8(1):1–6, 2017.

[157] MS Kim, Jinhyoung Lee, and William J Munro. Experimentally realizable characterizations of continuous-variable Gaussian states. *Physical Review A*, 66(3):030301, 2002.

[158] J Robert Johansson, Paul D Nation, and Franco Nori. Qutip 2: A python framework for the dynamics of open quantum systems. *Computer Physics Communications*, 184(4):1234–1240, 2013.

[159] Steven Diamond and Stephen Boyd. CVXPY: A Python-embedded modeling language for convex optimization. *Journal of Machine Learning Research*, 17(83):1–5, 2016.

[160] Ching Tsung Lee. External photodetection of cavity radiation. *Physical Review A*, 48(3):2285, 1993.

[161] Daryl Achilles, Christine Silberhorn, and Ian A Walmsley. Direct, loss-tolerant characterization of nonclassical photon statistics. *Physical review letters*, 97(4):043602, 2006.

[162] Josef Hloušek, Michal Dudka, Ivo Straka, and Miroslav Ježek. Accurate detection of arbitrary photon statistics. *Phys. Rev. Lett.*, 123:153604, Oct 2019.

[163] T. Kiss, U. Herzog, and U. Leonhardt. Compensation of losses in photodetection and in quantum-state measurements. *Phys. Rev. A*, 52:2433–2435, Sep 1995.

[164] P. L. Kelley and W. H. Kleiner. Theory of electromagnetic field measurement and photoelectron counting. *Phys. Rev.*, 136:A316–A334, Oct 1964.

[165] Konrad Banaszek, Andrzej Dragan, Krzysztof Wódkiewicz, and Czesław Radzewicz. Direct measurement of optical quasidistribution functions: Multimode theory and homodyne tests of bells inequalities. *Physical Review A*, 66(4):043803, 2002.

[166] Chao Shen, Reinier W Heeres, Philip Reinhold, Luyao Jiang, Yi-Kai Liu, Robert J Schoelkopf, and Liang Jiang. Optimized tomography of continuous variable systems using excitation counting. *Physical Review A*, 94(5):052327, 2016.

[167] Albert Tarantola. *Inverse problem theory and methods for model parameter estimation*, volume 89. siam, 2005.

[168] Andrey Nikolayevich Tikhonov. On the stability of inverse problems. In *Dokl. Akad. Nauk SSSR*, volume 39, pages 195–198, 1943.

[169] Steven T Flammia, David Gross, Yi-Kai Liu, and Jens Eisert. Quantum tomography via compressed sensing: error bounds, sample complexity and efficient estimators. *New Journal of Physics*, 14(9):095022, 2012.

[170] Thiago O Maciel, André T Cesário, and Reinaldo O Vianna. Variational quantum tomography with incomplete information by means of semidefinite programs. *International Journal of Modern Physics C*, 22(12):1361–1372, 2011.

[171] N. Boulant, T. F. Havel, M. A. Pravia, and D. G. Cory. Robust method for estimating the lindblad operators of a dissipative quantum process from measurements of the density operator at multiple time points. *Phys. Rev. A*, 67:042322, Apr 2003.

[172] Mirko Lobino, Dmitry Korystov, Connor Kupchak, Eden Figueroa, Barry C. Sanders, and A. I. Lvovsky. Complete characterization of quantum-optical processes. *Science*, 322(5901):563–566, 2008.

[173] Alexei Ourjoumtsev, Rosa Tualle-Brouri, and Philippe Grangier. Quantum homodyne tomography of a two-photon Fock state. *Phys. Rev. Lett.*, 96:213601, 2006.

[174] Yvonne Y Gao, Brian J Lester, Yaxing Zhang, Chen Wang, Serge Rosenblum, Luigi Frunzio, Liang Jiang, SM Girvin, and Robert J Schoelkopf. Programmable interference between two microwave quantum memories. *Physical Review X*, 8(2):021073, 2018.

[175] Rajibul Islam, Ruichao Ma, Philipp M Preiss, M Eric Tai, Alexander Lukin, Matthew Rispoli, and Markus Greiner. Measuring entanglement entropy in a quantum many-body system. *Nature*, 528(7580):77, 2015.

[176] Danna Rosenberg, Adriana E. Lita, Aaron J. Miller, and Sae Woo Nam. Noise-free high-efficiency photon-number-resolving detectors. *Phys. Rev. A*, 71:061803, Jun 2005.

[177] Marco Ramilli, Alessia Allevi, Valery Chmill, Maria Bondani, Massimo Caccia, and Alessandra Andreoni. Photon-number statistics with silicon photomultipliers. *J. Opt. Soc. Am. B*, 27(5):852–862, May 2010.

[178] Aleksander Divochiy, Francesco Marsili, David Bitauld, Alessandro Gaggero, Roberto Leoni, Francesco Mattioli, Alexander Korneev, Vitaliy Seleznev, Nataliya Kaurova, Olga Minaeva, Gregory Gol'tsman, Konstantinos G. Lagoudakis, Moushab Benkhaoul, Francis Levy, and Andrea Fiore. Superconducting nanowire photon-number-resolving detector at telecommunication wavelengths. *Nat Photon*, 2(5):302–306, 05 2008.

[179] Chandra M. Natarajan, Lijian Zhang, Hendrik Coldenstrodt-Ronge, Gaia Donati, Sander N. Dorenbos, Val Zwiller, Ian A. Walmsley, and Robert H. Hadfield. Quantum detector tomography of a time-multiplexed superconducting nanowire

single-photon detector at telecom wavelengths. *Opt. Express*, 21(1):893–902, Jan 2013.

[180] Kathryn L. Nicolich, Clinton Cahall, Nurul T. Islam, Gregory P. Lafyatis, Jungsang Kim, Aaron J. Miller, and Daniel J. Gauthier. Universal model for the turn-on dynamics of superconducting nanowire single-photon detectors. *Phys. Rev. Applied*, 12:034020, Sep 2019.

[181] B. E. Kardynał, S. S. Hees, A. J. Shields, C. Nicoll, I. Farrer, and D. A. Ritchie. Photon number resolving detector based on a quantum dot field effect transistor. *Applied Physics Letters*, 90(18):181114, 2007.

[182] A. J. Shields, M. P. O'Sullivan, I. Farrer, D. A. Ritchie, R. A. Hogg, M. L. Leadbeater, C. E. Norman, and M. Pepper. Detection of single photons using a field-effect transistor gated by a layer of quantum dots. *Applied Physics Letters*, 76(25):3673–3675, 2000.

[183] J. Sperling, W. Vogel, and G. S. Agarwal. True photocounting statistics of multiple on-off detectors. *Phys. Rev. A*, 85:023820, Feb 2012.

[184] J. Sperling, W. Vogel, and G. S. Agarwal. Sub-binomial light. *Phys. Rev. Lett.*, 109:093601, Aug 2012.

[185] Regina Kruse, Johannes Tiedau, Tim J. Bartley, Sonja Barkhofen, and Christine Silberhorn. Limits of the time-multiplexed photon-counting method. *Phys. Rev. A*, 95:023815, Feb 2017.

[186] Filippo M. Miatto, Akbar Safari, and Robert W. Boyd. Explicit formulas for photon number discrimination with on/off detectors. *Appl. Opt.*, 57(23):6750–6754, Aug 2018.

[187] John von Neumann. *Mathematical Foundations of Quantum Mechanics*. Princeton University Press, isbn 10: 0691178569 edition, 2018.

[188] S. J. van Enk. Time-dependent spectrum of a single photon and its positive-operator-valued measure. *Phys. Rev. A*, 96:033834, Sep 2017.

[189] S. J. van Enk. Photodetector figures of merit in terms of POVMs. *Journal of Physics Communications*, 1(4):045001, nov 2017.

[190] Peter C Humphreys, Benjamin J Metcalf, Thomas Gerrits, Thomas Hiemstra, Adriana E Lita, Joshua Nunn, Sae Woo Nam, Animesh Datta, W Steven Kolthammer, and Ian A Walmsley. Tomography of photon-number resolving continuous-output detectors. *New Journal of Physics*, 17(10):103044, 2015.

[191] Y. Wang, Z. Wang, Q. Yu, X. Xie, T. Posavitz, M. Jacob-Mitos, A. Ramaswamy, E. J. Norberg, G. A. Fish, and A. Beling. High-power photodiodes with 65 GHz bandwidth heterogeneously integrated onto silicon-on-insulator nano-waveguides. *IEEE Journal of Selected Topics in Quantum Electronics*, 24(2):1–6, March 2018.

[192] Qianhuan Yu, Nan Ye, Junyi Gao, Keye Sun, Linli Xie, Kartik Srinivasan, Michael Zervas, Gabriele Navickaite, Michael Geiselmann, and Andreas Beling. High-responsivity photodiodes heterogeneously integrated on silicon nitride waveguides. In *OSA Advanced Photonics Congress (AP) 2019 (IPR, Networks, NOMA, SPPCom, PVLED)*, page IW3A.5. Optical Society of America, 2019.

[193] Jan Philipp Höpker, Moritz Bartnick, Evan Meyer-Scott, Frederik Thiele, Stephan Krapick, Nicola Montaut, Matteo Santandrea, Harald Herrmann, Sebastian Lengeling, Raimund Ricken, Viktor Quiring, Torsten Meier, Adriana Lita, Varun Verma, Thomas Gerrits, Sae Woo Nam, Christine Silberhorn, and Tim J. Bartley. Towards integrated superconducting detectors on lithium niobate waveguides. In Cesare Soci, Mario Agio, and Kartik Srinivasan, editors, *Quantum Photonic Devices*, volume 10358, pages 21 – 27. International Society for Optics and Photonics, SPIE, 2017.

[194] Jan Philipp Höpker, Thomas Gerrits, Adriana Lita, Stephan Krapick, Harald Herrmann, Raimund Ricken, Viktor Quiring, Richard Mirin, Sae Woo Nam, Christine Silberhorn, and Tim J. Bartley. Integrated transition edge sensors on titanium in-diffused lithium niobate waveguides. *APL Photonics*, 4(5):056103, 2019.

[195] Changhyoup Lee, Simone Ferrari, Wolfram H. P. Pernice, and Carsten Rockstuhl. Sub-poisson-binomial light. *Phys. Rev. A*, 94:053844, Nov 2016.

[196] Pascual Munoz, Paulus WL van Dijk, Douwe Geuzebroek, Michael Geiselmann, Carlos Dominguez, Andim Stassen, José David Doménech, Michael Zervas, Arne Leinse, Chris GH Roeloffzen, et al. Foundry developments toward silicon nitride photonics from visible to the mid-infrared. *IEEE Journal of Selected Topics in Quantum Electronics*, 25(5):1–13, 2019.

[197] Domenico D'Agostino, Giuseppe Carnicella, Caterina Ciminelli, Peter Thijs, Petrus J Veldhoven, Huub Ambrosius, and Meint Smit. Low-loss passive waveguides in a generic inp foundry process via local diffusion of zinc. *Optics express*, 23(19):25143–25157, 2015.

[198] Marlan O. Scully and Willis E. Lamb. Quantum theory of an optical maser. iii. theory of photoelectron counting statistics. *Phys. Rev.*, 179:368–374, Mar 1969.

[199] J Sperling, W Vogel, and GS Agarwal. True photocounting statistics of multiple on-off detectors. *Physical Review A*, 85(2):023820, 2012.

[200] Jared F. Bauters, Martijn J. R. Heck, Demis D. John, Jonathon S. Barton, Christiaan M. Bruinink, Arne Leinse, René G. Heideman, Daniel J. Blumenthal, and John E. Bowers. An ultra-low-loss (<0.1 dB/m) planar silica waveguide platform. *IEEE Photon. Soc. Newslett.*, (12):4, December 2011.

[201] Ivan Rech, Antonino Ingargiola, Roberto Spinelli, Ivan Labanca, Stefano Marangoni, Massimo Ghioni, and Sergio Cova. Optical crosstalk in single pho-

ton avalanche diode arrays: a new complete model. *Opt. Express*, 16(12):8381–8394, Jun 2008.

[202] Chockalingam Veerappan and Edoardo Charbon. A low dark count pin diode based spad in cmos technology. *IEEE transactions on electron devices*, 63(1):65–71, 2015.

[203] Danilo Bronzi, Federica Villa, Simone Tisa, Alberto Tosi, and Franco Zappa. Spad figures of merit for photon-counting, photon-timing, and imaging applications: A review. *IEEE Sensors Journal*, 16(1):3–12, 2015.

[204] Xudong Jiang, Mark Itzler, Kevin O'Donnell, Mark Entwistle, Mark Owens, Krystyna Slomkowski, and Sabbir Rangwala. Inp-based single-photon detectors and geiger-mode apd arrays for quantum communications applications. *IEEE Journal of Selected Topics in Quantum Electronics*, 21(3):5–16, 2014.

[205] Robert H. Hadfield. Single-photon detectors for optical quantum information applications. *Nature Photonics*, 3:696 EP –, 12 2009.

[206] Christine Silberhorn. Detecting quantum light. *Contemporary Physics*, 48(3):143–156, 2007.

[207] E Knill, R Laflamme, and G J Milburn. A scheme for efficient quantum computation with linear optics. *Nature (London)*, 409:46–52, January 2001.

[208] Jeremy L. O'Brien. Optical quantum computing. *Science*, 318(5856):1567, 12 2007.

[209] Pieter Kok, W. J. Munro, Kae Nemoto, T. C. Ralph, Jonathan P. Dowling, and G. J. Milburn. Linear optical quantum computing with photonic qubits. *Rev. Mod. Phys.*, 79:135–174, Jan 2007.

[210] J. F. Clauser and A. Shimony. Bell's theorem. Experimental tests and implications. *Rep. Prog. Phys.*, 41(12):1881, 1978.

[211] Alain Aspect, Philippe Grangier, and Gérard Roger. Experimental realization of Einstein-Podolsky-Rosen-Bohm gedankenexperiment: A new violation of Bell's inequalities. *Phys. Rev. Lett.*, 49(2):91–94, Jul 1982.

[212] C. W. Helstrom. *Quantum Detection and Estimation Theory.* Mathematics in Science and Engineering, 123, Academic Press, New York, 1976.

[213] S J van Enk. Photodetector figures of merit in terms of POVMs. *Journal of Physics Communications*, 1(4):045001, nov 2017.

[214] Samuele Grandi, Alessandro Zavatta, Marco Bellini, and Matteo G A Paris. Experimental quantum tomography of a homodyne detector. *New J. Phys.*, 19(5):053015, may 2017.

[215] Giorgio Brida, Luigi Ciavarella, Ivo Pietro Degiovanni, Marco Genovese, Lapo Lolli, Maria Griselda Mingolla, Fabrizio Piacentini, Mauro Rajteri, Emanuele Taralli, and Matteo G A Paris. Quantum characterization of superconducting photon counters. *New J. Phys.*, 14(8):085001, 2012.

[216] Eugene P. Wigner. *Quantum Theory of Angular Momentum.* Academic Press, (New York, 1965).

[217] Christopher Gerry and Peter Knight. *Introductory Quantum Optics.* Cambridge University Press, 2004.

[218] Maria Bondani, Alessia Allevi, and Alessandra Andreoni. Self-consistent phase determination for wigner function reconstruction. *J. Opt. Soc. Am. B*, 27(2):333–337, Feb 2010.

[219] V. D'Auria, N. Lee, T. Amri, C. Fabre, and J. Laurat. Quantum decoherence of single-photon counters. *Phys. Rev. Lett.*, 107:050504, Jul 2011.

[220] F. T. Arecchi. Measurement of the statistical distribution of gaussian and laser sources. *Phys. Rev. Lett.*, 15:912–916, Dec 1965.

[221] J. R. Johansson, P. D. Nation, and Franco Nori. Qutip 2: A python framework for the dynamics of open quantum systems. *Computer Physics Communications*, 184:1234–1240, 2013.

[222] Mariano Gasca and Thomas Sauer. Polynomial interpolation in several variables. *Advances in Computational Mathematics*, 12(4):377, Mar 2000.

[223] V A Ilin. TIKHONOVs WORK ON METHODS OF SOLVING ILL-POSED PROBLEMS. *Russian Mathematical Surveys*, 22(2):142–149, apr 1967.

[224] Bill Triggs, Philip F. McLauchlan, Richard I. Hartley, and Andrew W. Fitzgibbon. Bundle adjustment — a modern synthesis. In Bill Triggs, Andrew Zisserman, and Richard Szeliski, editors, *Vision Algorithms: Theory and Practice*, pages 298–372, Berlin, Heidelberg, 2000. Springer Berlin Heidelberg.

[225] C. M. Caves. Quantum-mechanical radiation-pressure fluctuations in an interferometer. *Phys. Rev. Lett.*, 45:75, 1980.

[226] Carlton M. Caves, Kip S. Thorne, Ronald W. P. Drever, Vernon D. Sandberg, and Mark Zimmermann. On the measurement of a weak classical force coupled to a quantum-mechanical oscillator. I. Issues of principle. *Rev. Mod. Phys.*, 52:341–392, Apr 1980.

[227] Vladimir B. Braginsky and Farid Ya. Khalili. *Quantum Measurement*. Cambridge University Press, 1992.

[228] Jean-Marc Lévy-Leblond and Françoise Balibar. *Quantics: Rudiments of Quantum Physics*. North-Holland, 1990.

[229] Rafal Demkowicz-Dobrzański, Marcin Jarzyna, and Jan Kołodyński. *Progress in Optics*, volume 60, chapter 4 - Quantum Limits in Optical Interferometry, pages 345–435. Elsevier, 2015.

[230] C. M. Caves. Quantum-mechanical noise in an interferometer. *Phys. Rev. D*, 23:1693, 1981.

[231] Matthias D. Lang and Carlton M. Caves. Optimal quantum-enhanced interferometry using a laser power source. *Phys. Rev. Lett.*, 111:173601, Oct 2013.

[232] P. Grangier, R. E. Slusher, B. Yurke, and A. LaPorta. Squeezed-light-enhanced polarization interferometer. *Phys. Rev. Lett.*, 59:2153, 1987.

[233] M. Xiao, L. A. Wu, and H. J. Kimble. Precision measurement beyond the shot-noise limit. *Phys. Rev. Lett.*, 59:278, 1987.

[234] The LIGO Collaboration. A gravitational wave observatory operating beyond the quantum shot-noise limit. *Nat Phys*, 7(12):962–965, 12 2011.

[235] The LIGO Collaboration. Enhanced sensitivity of the LIGO gravitational wave detector by using squeezed states of light. *Nat. Photon.*, 7:613, 2013.

[236] B. Yurke, S. L. McCall, and J. R. Klauder. SU(2) and SU(1,1) interferometers. *Phys. Rev. A*, 33:4033, 1986.

[237] A. Luis and L.L. Sánchez-Soto. Quantum phase difference, phase measurements and Stokes operators. *Prog. Opt.*, 41:421, 2000.

[238] M. J. Holland and K. Burnett. Interferometric detection of optical phase shifts at the Heisenberg limits. *Phys. Rev. Lett.*, 71:1355, 1993.

[239] P. Bouyer and M. A. Kasevich. Heisenberg-limited spectroscopy with degenerate Bose-Einstein gases. *Phys. Rev. A*, 56:1083, 1997.

[240] T. Kim, O. Pfister, M. J. Holland, J. Noh, and J. L. Hall. Influence of decorrelation on Heisenberg-limited interferometry using quantum correlated photons. *Phys. Rev. A*, 57:4004, 1998.

[241] S. Feng and O. Pfister. Sub-shot-noise heterodyne polarimetry. *Opt. Lett.*, 29:2800, 2004.

[242] J. J . Bollinger, Wayne M. Itano, D. J. Wineland, and D. J. Heinzen. Optimal frequency measurements with maximally correlated states. *Phys. Rev. A*, 54:R4649–R4652, Dec 1996.

[243] Agedi N. Boto, Pieter Kok, Daniel S. Abrams, Samuel L. Braunstein, Colin P. Williams, and Jonathan P. Dowling. Quantum interferometric optical lithography: Exploiting entanglement to beat the diffraction limit. *Phys. Rev. Lett.*, 85:2733, 2000.

[244] M. W. Mitchell, J. S. Lundeen, and A. M. Steinberg. Super-resolving phase measurements with a multiphoton entangled state. *Nature*, 429(6988):161–164, 05 2004.

[245] Philip Walther, Jian-Wei Pan, Markus Aspelmeyer, Rupert Ursin, Sara Gasparoni, and Anton Zeilinger. De broglie wavelength of a non-local four-photon state. *Nature*, 429(6988):158–161, 05 2004.

[246] Itai Afek, Oron Ambar, and Yaron Silberberg. High-NOON states by mixing quantum and classical light. *Science*, 328(5980):879–881, 2010.

[247] Matthias D. Lang and Carlton M. Caves. Optimal quantum-enhanced interferometry. *Phys. Rev. A*, 90:025802, Aug 2014.

[248] B. M. Escher, R. L. de Matos Filho, and L. Davidovich. General framework for estimating the ultimate precision limit in noisy quantum-enhanced metrology. *Nat. Phys.*, 7(5):406–411, 05 2011.

[249] Raphael C. Pooser and Olivier Pfister. Particle-number scaling of the phase sensitivity in realistic Bayesian twin-mode Heisenberg-limited interferometry. *Phys. Rev. A*, 69(4):043616, Apr 2004.

[250] The LIGO Scientific Collaboration. Advanced ligo. *arXiv:1411.4547 [gr-qc]*, 2014.

[251] Henning Vahlbruch, Moritz Mehmet, Karsten Danzmann, and Roman Schnabel. Detection of 15 dB squeezed states of light and their application for the absolute calibration of photoelectric quantum efficiency. *Phys. Rev. Lett.*, 117:110801, Sep 2016.

[252] Henning Vahlbruch, Simon Chelkowski, Boris Hage, Alexander Franzen, Karsten Danzmann, and Roman Schnabel. Coherent control of vacuum squeezing in the gravitational-wave detection band. *Phys. Rev. Lett.*, 97:011101, Jul 2006.

[253] A. Heidmann, R. J. Horowicz, S. Reynaud, E. Giacobino, C. Fabre, and G. Camy. Observation of quantum noise reduction on twin laser beams. *Phys. Rev. Lett.*, 59(22):2555–2557, Nov 1987.

[254] J. Mertz, T. Debuisschert, A. Heidmann, C. Fabre, and E. Giacobino. Improvements in the observed intensity correlation of optical parametric oscillator twin beams. *Opt. Lett.*, 16:1234, 1991.

[255] Julien Laurat, Laurent Longchambon, Claude Fabre, and Thomas Coudreau. Experimental investigation of amplitude and phase quantum correlations in a type ii optical parametric oscillator above threshold: from nondegenerate to degenerate operation. *Opt. Lett.*, 30:1177, 2005.

[256] R. A. Campos, B. E. A. Saleh, and M. C. Teich. Quantum-mechanical lossless beam splitter: Su(2) symmetry and photon statistics. *Phys. Rev. A*, 40:1371, 1989.

[257] C. K. Hong, Z. Y. Ou, and L. Mandel. Measurement of subpicosecond time intervals between two photons by interference. *Phys. Rev. Lett.*, 59:2044, 1987.

[258] J. Jing, S. Feng, R. Bloomer, and O. Pfister. Experimental continuous-variable entanglement from a phase-difference-locked optical parametric oscillator. *Phys. Rev. A*, 74:041804(R), 2006.

[259] M. Pysher, Y. Miwa, R. Shahrokhshahi, and O. Pfister. A new way to lock the signal-field phase difference in a type-II optical parametric oscillator above threshold. *Opt. Expr.*, 18:27858, 2010.

[260] J. J. Snyder, E. Giacobino, C. Fabre, A. Heidmann, and M. Ducloy. Sub-shot-noise measurements using the beat note between quantum-correlated photon beams. *J. Opt. Soc. Am. B*, 7(10):2132–2136, Oct 1990.

[261] Raul Carranza and Christopher C. Gerry. Photon-subtracted two-mode squeezed vacuum states and applications to quantum optical interferometry. *J. Opt. Soc. Am. B*, 29(9):2581–2587, Sep 2012.

[262] Seyed Mohammad Hashemi Rafsanjani, Mohammad Mirhosseini, Omar S. Maga na Loaiza, Bryan T. Gard, Richard Birrittella, B. E. Koltenbah, C. G. Parazzoli, Barbara A. Capron, Christopher C. Gerry, Jonathan P. Dowling, and Robert W. Boyd. Quantum-enhanced interferometry with weak thermal light. *Optica*, 4(4):487–491, Apr 2017.

[263] Petr M. Anisimov, Gretchen M. Raterman, Aravind Chiruvelli, William N. Plick, Sean D. Huver, Hwang Lee, and Jonathan P. Dowling. Quantum metrology with two-mode squeezed vacuum: Parity detection beats the heisenberg limit. *Phys. Rev. Lett.*, 104:103602, Mar 2010.

[264] V. Averchenko, C. Jacquard, V. Thiel, C. Fabre, and N. Treps. Multimode theory of single-photon subtraction. *New J. Phys.*, 18(8):083042, 2016.

[265] Julian Schwinger. On angular momentum. *U.S. Atomic Energy Commission Report. No. NYO–3071 (1952), reprinted in Quantum Theory of Angular Mo-*

mentum, edited by L. C. Biedenharn and H. van Dam (Academic Press, New York, 1965), pp. 229–279.

[266] Samuel L. Braunstein and Carlton M. Caves. Statistical distance and the geometry of quantum states. *Phys. Rev. Lett.*, 72:3439–3443, May 1994.

[267] Rajveer Nehra, Aye Win, Miller Eaton, Reihaneh Shahrokhshahi, Niranjan Sridhar, Thomas Gerrits, Adriana Lita, Sae Woo Nam, and Olivier Pfister. State-independent quantum state tomography by photon-number-resolving measurements. *Optica*, 6(10):1356–1360, Oct 2019.

[268] Rajveer Nehra, Miller Eaton, Carlos González-Arciniegas, M.S. Kim, and Olivier Pfister. Loss tolerant quantum state tomography by number-resolving measurements without approximate displacements. *arXiv:1911.00173 [quant-ph]*, 2019.

[269] Konrad Banaszek and Krzysztof Wódkiewicz. Testing quantum nonlocality in phase space. *Phys. Rev. Lett.*, 82:2009–2013, Mar 1999.

[270] Konrad Banaszek and Krzysztof Wodkiewicz. Nonlocality of the einstein-podolsky-rosen state in the phase space. *arXiv preprint quant-ph/9904071*, 1999.

[271] Giorgio Brida, Luigi Ciavarella, Ivo Pietro Degiovanni, Marco Genovese, Lapo Lolli, Maria Griselda Mingolla, Fabrizio Piacentini, Mauro Rajteri, Emanuele Taralli, and Matteo G A Paris. Quantum characterization of superconducting photon counters. *New Journal of Physics*, 14(8):085001, 2012.

[272] G. Brida, L. Ciavarella, I. P. Degiovanni, M. Genovese, A. Migdall, M. G. Mingolla, M. G. A. Paris, F. Piacentini, and S. V. Polyakov. Ancilla-assisted calibration of a measuring apparatus. *Phys. Rev. Lett.*, 108:253601, Jun 2012.

[273] Lee Poh-aun, Seng hung Ong, and H. M. Srivastava. Some integrals of the products of laguerre polynomials. *International Journal of Computer Mathematics*, 78(2):303–321, 2001.